# NONLINEAR FLUTTER OF A CANTILEVER WING INCLUDING THE INFLUENCE OF STRUCTURE UNCERTAINTIES

by

**STEFAN CRISTIAN CASTRAVETE**

**DISSERTATION**

Submitted to the Graduate School

of Wayne State University,

Detroit, Michigan

in partial fulfillment of the requirements

for the degree of

**DOCTOR OF PHILOSOPHY**

2007

MAJOR: MECHANICAL ENGINEERING

Approved by:

_____

Advisor Date

_____

_____

_____

_____

## DEDICATION

To my wife Liliana, my daughters Joanne Daria and Eva Antonia, and my parents Ion and Irina.

## ACKNOWLEDGMENTS

First, I would like to express my gratitude and appreciation to my adviser Dr. Raouf Ibrahim whose guidance, assistance, and encouragement led me to fulfill the greatest educational accomplishment, a doctoral degree. Next, I would like to thank to Dr. Sergio Preidikman whose guidance and advice helped me to continue his work done on his Ph.D. dissertation. Without his help my work would take a longer time to complete.

Special thanks to my wife, Liliana, who supported, encouraged, and endured me over the last years. Her love and support helped me go over the hard periods of my work and without her I might not have succeed to finish my dissertation. Also, I would like to thank my daughter Daria for her love and patience even though I didn't have too much time to spend with her.

Last, but not least, I would like to thank my parents who encouraged me to continue my education even though they suffered a lot when I left my country. Also I would like to thank them for taking care of my daughter Daria over the period I was involved in my work.

The thesis was supported by AFOSR under grant number FA9550-04-1-0042.

## TABLE OF CONTENTS

**List of Figures** **Page**

List of Figures ..... viii

**Chapter** **Page**

CHAPTERS

CHAPTER 1 – A review of literature and background ..... 1

1.1 Introduction ..... 1

1.2 Aerodynamic modeling ..... 2

1.2.1. Analytical schemes (linear) ..... 2

1.2.2. Numerical schemes ..... 9

1.2.2.1. Fluid field equations ..... 10

1.2.2.2. Vortex lattice method ..... 15

1.2.2.3. Doublet lattice method ..... 17

1.2.2.4. Sources of aerodynamic nonlinearities ..... 19

1.3 Structural modeling ..... 22

1.3.1. Types of structural nonlinearities ..... 22

1.3.2. The effect of concentrated nonlinearities ..... 22

1.3.2. The effect of distributed nonlinearities ..... 24

1.4 Systems with parameter uncertainties ..... 27

1.4.1. Stochastic finite element methods ..... 29

1.4.1.1. Karhunen-Loeve expansion (K-L) ..... 30

1.4.1.2. Monte Carlo simulation ..... 35

1.4.1.3. Perturbation method ..... 35

1.4.1.4. Neumann expansion method ..... 37
1.4.2. Nonlinear aeroelastic models with parameter uncertainties ..... 39
1.5 Stabilization of unstable systems via parametric excitation ..... 43
1.5.1. Stabilization evidence in aeroelastic structures..... 44
1.5.2. Stabilization of the inverted pendulum ..... 45
1.6 Scope of the present research ..... 47
CHAPTER 2 – Flutter suppression of a plate-like wing via parametric excitation ..... 58
2.1. Introduction ..... 58
2.2. Analytical modeling of a plate-like wing ..... 60
2.3. Modal analysis and parametric stability ..... 67
2.4. Nonlinear analysis..... 72
2.4.1. Resonance conditions..... 72
2.4.2. Response at zero flow speed..... 75
2.4.3. Response at critical and post-critical flutter speeds ..... 78
2.4.3.1. Response at critical flutter speed ..... 81
2.4.3.2. Response at post-critical flutter speed ..... 85
2.5. Numerical simulations ..... 88
2.5.1. Zero flow speed ..... 88
2.5.2. Critical flutter speed ..... 89
2.5.3. Post-critical flutter speed..... 90
2.6. Closing remarks ..... 90

CHAPTER 3 – Influence of parameter uncertainties on the flutter of a cantilever wing ..... 135
3.1. Introduction ..... 135
3.2. Aerodynamic modeling ..... 136
3.3. Structural modeling ..... 141
3.4. Modeling of material uncertainties ..... 145
3.5. System modeling ..... 150
3.6. Perturbation analysis ..... 153
3.6.1. Results in the absence of uncertainties ..... 156
3.6.2. The influence of bending stiffness uncertainty ..... 156
3.6.3. The influence of torsion stiffness uncertainty ..... 158
3.6.4. The influence of combination bending-torsion stiffness uncertainty ..... 159
3.7. Monte Carlo simulation ..... 160
3.8. Closing remarks ..... 163
CHAPTER 4 – Conclusions and recommendations ..... 230
APPENDICES
Appendix A ..... 235
Appendix B ..... 236
Appendix C ..... 237
Appendix D ..... 238
Appendix E ..... 264
REFERENCES ..... 265

ABSTRACT ..... 291

AUTOBIOGRAPHICAL STATEMENT ..... 293

## LIST OF FIGURES

**FIGURE** **PAGE**

Figure 1.1. Schematic diagram showing a two-dimensional analytical airfoil model ..... 50

Figure 1.2. Streamlines for a uniform flow parallel to the x-axis ..... 50

Figure 1.3. Equipotential lines and streamlines for flow from a two-dimensional source ..... 50

Figure 1.4. Equipotential lines and streamlines for a doublet ..... 51

Figure 1.5. Equipotential lines and streamlines for a potential vortex ..... 51

Figure 1.6. Vortex ring model for a thin lifting surface ..... 52

Figure 1.7. Model of self-sustained shock oscillations ..... 53

Figure 1.8. A 3D representation of the computed wakes using the unsteady vortex lattice method ..... 53

Figure 1.9. Boundary layer separation. (a) At low angles of attack, the boundary layer leaves as a wake at the trailing edge; (b) At higher angles of attack, the boundary layer on the upper surface separates; (c) As the angle of attack increases, the separation position moves forward. ..... 54

Figure 1.10. Force versus displacement curve for. (a) Cubic hardening spring. (b) Cubic softening spring ..... 55

Figure 1.11. Force vs. Displacement. (a) Flat spot without preload. (b) General bilinear spring ..... 55

Figure 1.12. Inverted pendulum under parametric excitation ..... 56

Figure 1.13. Indian rope trick ..... 57

Figure 2.1. Schematic diagram of the analytical model, coordinates axes, and deformations. (a) Plate-like cantilever wing showing the coordinate frame. (b) Locations of different axes and deformations in bending, torsion, and longitudinal ..... 92

Figure 2.2. Dependence of eigenvalue components on the flow speed parameter showing: (a) the influence of the imaginary component of circulation function, $G \neq 0$ and (b) its absence, $G = 0$. ——— Eigenvalue components in the presence of aerodynamic and structure damping. …….. Eigenvalue components in the absence of aerodynamic and structure damping ..... 93

Figure 2.3. Stability boundaries in the neighborhood of parametric combination resonance at zero flow speed and at critical flow speed ..... 94

Figure 2.4. Time histories, phase diagrams, and FFTs at zero flow speed, $\Omega = \omega_1 + \omega_2$, $\omega_1 = 0.5\omega_2$, $\sigma_e = 0$, $\bar{u}(0) = 0.1$, $\alpha(0) = 0.1$, $\bar{u}'(0) = 0$, $\alpha'(0) = 0$. (a) $Y_0 = 0.0015$; (b) $Y_0 = 0.005$; (c) $Y_0 = 0.01$ .... 97

Figure 2.5. Bifurcation diagram at zero flow speed estimated at $\Omega = \omega_1 + \omega_2$, $\omega_1 = 0.5\omega_2$, for $\sigma_e = 0$, $\bar{u}(0) = 0.1$, $\alpha(0) = 0.1$, $\bar{u}'(0) = 0$, $\alpha'(0) = 0$. ..... 98

Figure 2.6. Domains of attractions for different values of excitation amplitude. (a) $Y_0 = 0$; (b) $Y_0 = 0.00875$; (c) $Y_0 = 0.01$; (d) $Y_0 = 0.014$; (e) $Y_0 = 0.015$; (f) $Y_0 = 0.017$ ..... 99

Figure 2.7. Time histories at critical flow speed $U_\infty / b\omega_\alpha = 4.965$, $Y_0 = 0$, $\Omega = \omega_1 + \omega_2$, $\omega_1 = \omega_2$, $\sigma_e = 0$, $\sigma_i = 0.061$, $\bar{u}(0) = 0.45$, $\alpha(0) = 0.01$, $\bar{u}'(0) = 0$, $\alpha'(0) = 0$ ..... 100

Figure 2.8. Time histories records at critical flow speed $U_\infty / b\omega_\alpha = 4.965$, $Y_0 = 0.00875$; $\Omega = \omega_1 + \omega_2$, $\omega_1 = \omega_2$, $\sigma_e = 0$, $\sigma_i = 0.061$. (a) $\bar{u}(0) = 0.5$, $\alpha(0) = 0.04$, $\bar{u}'(0) = 0$, $\alpha'(0) = 0$. (b) $\bar{u}(0) = 0.5$, $\alpha(0) = 0.05$, $\bar{u}'(0) = 0$, $\alpha'(0) = 0$. (c) $\bar{u}(0) = 0.5$, $\alpha(0) = 0.07$, $\bar{u}'(0) = 0$, $\alpha'(0) = 0$. (d) $\bar{u}(0) = 0.5$, $\alpha(0) = 0.1$, $\bar{u}'(0) = 0$, $\alpha'(0) = 0$ ..... 101

Figure 2.9. Time histories at critical flow speed $U_\infty / b\omega_\alpha = 4.965$, $Y_0 = 0.01$, $\Omega = \omega_1 + \omega_2$, $\omega_1 = \omega_2$, $\sigma_e = 0$, $\sigma_i = 0.061$, $\bar{u}(0) = 0.5$, $\alpha(0) = 0.1$, $\bar{u}'(0) = 0$, $\alpha'(0) = 0$ ..... 101

Figure 2.10. Time histories, phase diagrams, and FFTs at critical flow speed $U_\infty / b\omega_\alpha = 4.965$, $Y_0 = 0.014$; $\Omega = \omega_1 + \omega_2$, $\omega_1 = \omega_2$, $\sigma_e = 0$, $\sigma_i = 0.061$. (a) $\bar{u}(0) = 0.5$, $\alpha(0) = -0.1$, $\bar{u}'(0) = 0$, $\alpha'(0) = 0$. (b) $\bar{u}(0) = 0.5$, $\alpha(0) = 0.1$, $\bar{u}'(0) = 0$, $\alpha'(0) = 0$ ..... 103

Figure 2.11. Time histories, phase diagrams, and FFTs at critical flow speed $U_\infty / b\omega_\alpha = 4.965$, $Y_0 = 0.015$; $\Omega = \omega_1 + \omega_2$, $\omega_1 = \omega_2$, $\sigma_e = 0$, $\sigma_i = 0.061$. (a) $\bar{u}(0) = 0.5$, $\alpha(0) = -0.1$, $\bar{u}'(0) = 0$, $\alpha'(0) = 0$. (b) $\bar{u}(0) = 0.5$, $\alpha(0) = 0.1$, $\bar{u}'(0) = 0$, $\alpha'(0) = 0$ ..... 105

Figure 2.12. Time histories, phase diagrams, and FFTs at critical flow speed $U_\infty / b\omega_\alpha = 4.965$, $Y_0 = 0.016$; $\Omega = \omega_1 + \omega_2$, $\omega_1 = \omega_2$, $\sigma_e = 0$, $\sigma_i = 0.061$. (a) $\bar{u}(0) = 0.5$, $\alpha(0) = -0.1$, $\bar{u}'(0) = 0$, $\alpha'(0) = 0$. (b) $\bar{u}(0) = 0.5$, $\alpha(0) = 0.1$, $\bar{u}'(0) = 0$, $\alpha'(0) = 0$ ..... 107

Figure 2.13. Time histories, Poincare maps, phase diagrams, and FFTs at critical flow speed $U_\infty / b\omega_\alpha = 4.965$, $Y_0 = 0.017$, $\Omega = \omega_1 + \omega_2$, $\omega_1 = \omega_2$, $\sigma_e = 0$, $\sigma_i = 0.061$. (a) $\bar{u}(0) = 0.5$, $\alpha(0) = -0.1$, $\bar{u}'(0) = 0$, $\alpha'(0) = 0$. (b) $\bar{u}(0) = 0.5$, $\alpha(0) = 0.1$, $\bar{u}'(0) = 0$, $\alpha'(0) = 0$ ..... 109

Figure 2.14. Bifurcation diagrams at critical flow speed $U_\infty / b\omega_\alpha = 4.965$, $\Omega = \omega_1 + \omega_2$, $\omega_1 = \omega_2$, $\sigma_e = 0$, $\sigma_i = 0.061$. (a) Dependence of bending amplitude on excitation amplitude. (b) Dependence of torsion amplitude on excitation amplitude..... 110

Figure 2.15. Stabilization effect of parametric excitation at critical flow speed $U_\infty / b\omega_\alpha = 4.965$ showing the percentage of domains of attraction for large amplitude response (solid diamond curve)

and large plus small amplitude responses (dotted solid circle curve). ..... 111

Figure 2.16. Domains of attraction at post-critical flow speed $U_\infty / b\omega_\alpha = 5.02$ for $\Omega = \omega_1 + \omega_2$, $\omega_1 = \omega_2$, $\sigma_e = 0$, $\sigma_i = 0.061$, and different values of excitation amplitude. (a) $Y_0 = 0$; (b) $Y_0 = 0.013$; (c) $Y_0 = 0.014$ ..... 112

Figure 2.17. Time histories at post-critical flow speed $U_\infty / b\omega_\alpha = 5.02$, $Y_0 = 0$; $\Omega = \omega_1 + \omega_2$, $\omega_1 = \omega_2$, $\sigma_e = 0$, $\sigma_i = 0.061$. (a) $\bar{u}(0) = 0.2$, $\alpha(0) = 0.01$, $\bar{u}'(0) = 0$, $\alpha'(0) = 0$. (b) $\bar{u}(0) = 0.5$, $\alpha(0) = 0.1$, $\bar{u}'(0) = 0$, $\alpha'(0) = 0$. ..... 113

Figure 2.18. Time histories, Poincare maps, phase diagrams, and FFTs at post-critical flow speed $U_\infty / b\omega_\alpha = 5.02$, $Y_0 = 0.0025$; $\Omega = \omega_1 + \omega_2$, $\omega_1 = \omega_2$, $\sigma_e = 0$, $\sigma_i = 0.061$. (a) $\bar{u}(0) = 0.2$, $\alpha(0) = 0.01$, $\bar{u}'(0) = 0$, $\alpha'(0) = 0$. (b) $\bar{u}(0) = 0.5$, $\alpha(0) = 0.1$, $\bar{u}'(0) = 0$, $\alpha'(0) = 0$ ..... 115

Figure 2.19. Time histories, Poincare maps, phase diagrams, and FFTs at post-critical flow speed $U_\infty / b\omega_\alpha = 5.02$, $Y_0 = 0.004$, $\Omega = \omega_1 + \omega_2$, $\omega_1 = \omega_2$, $\sigma_e = 0$, $\sigma_i = 0.061$. (a) $\bar{u}(0) = 0.2$, $\alpha(0) = 0.01$, $\bar{u}'(0) = 0$, $\alpha'(0) = 0$. (b) $\bar{u}(0) = 0.5$, $\alpha(0) = 0.1$, $\bar{u}'(0) = 0$, $\alpha'(0) = 0$ ..... 117

Figure 2.20. Time histories, Poincare maps, phase diagrams, and FFTs at post-critical flow speed $U_\infty / b\omega_\alpha = 5.02$, $Y_0 = 0.0075$; $\Omega = \omega_1 + \omega_2$, $\omega_1 = \omega_2$, $\sigma_e = 0$, $\sigma_i = 0.061$. (a) $\bar{u}(0) = 0.2$, $\alpha(0) = 0.01$, $\bar{u}'(0) = 0$, $\alpha'(0) = 0$. (b) $\bar{u}(0) = 0.5$, $\alpha(0) = 0.1$, $\bar{u}'(0) = 0$, $\alpha'(0) = 0$ ..... 119

Figure 2.21. Time histories at post-critical flow speed $U_\infty / b\omega_\alpha = 5.02$, $Y_0 = 0.01$, $\Omega = \omega_1 + \omega_2$, $\omega_1 = \omega_2$, $\sigma_e = 0$, $\sigma_i = 0.061$. (a) $\bar{u}(0) = 0.2$, $\alpha(0) = 0.01$, $\bar{u}'(0) = 0$, $\alpha'(0) = 0$. (b) $\bar{u}(0) = 0.5$, $\alpha(0) = 0.1$, $\bar{u}'(0) = 0$, $\alpha'(0) = 0$ ..... 120

Figure 2.22. Time histories at post-critical flow speed $U_\infty / b\omega_\alpha = 5.02$, $Y_0 = 0.013$; $\Omega = \omega_1 + \omega_2$, $\omega_1 = \omega_2$, $\sigma_e = 0$, $\sigma_i = 0.061$. (a) $\bar{u}(0) = 0.1$, $\alpha(0) = 0.01$, $\bar{u}'(0) = 0, \alpha'(0) = 0$. (b) $\bar{u}(0) = 0.1$, $\alpha(0) = 0.02$, $\bar{u}'(0) = 0, \alpha'(0) = 0$. (c) $\bar{u}(0) = 0.2$, $\alpha(0) = 0.02$, $\bar{u}'(0) = 0, \alpha'(0) = 0$. (d) $\bar{u}(0) = 0.4$, $\alpha(0) = 0.1$, $\bar{u}'(0) = 0$, $\alpha'(0) = 0$ ..... 121

Figure 2.23. Time histories at post-critical flow speed $U_\infty / b\omega_\alpha = 5.02$, $Y_0 = 0.014$; $\Omega = \omega_1 + \omega_2$, $\omega_1 = \omega_2$, $\sigma_e = 0$, $\sigma_i = 0.061$. (a) $\bar{u}(0) = 0.3$, $\alpha(0) = 0.02$, $\bar{u}'(0) = 0, \alpha'(0) = 0$. (b) $\bar{u}(0) = 0.35$, $\alpha(0) = 0.02$, $\bar{u}'(0) = 0, \alpha'(0) = 0$. (c) $\bar{u}(0) = 0.25$, $\alpha(0) = 0.07$, $\bar{u}'(0) = 0, \alpha'(0) = 0$ ..... 122

Figure 2.24. Bifurcation diagrams showing different regions of response behavior at post-critical flow speed $U_\infty / b\omega_\alpha = 5.02$, $\Omega = \omega_1 + \omega_2$, $\omega_1 = \omega_2$, $\sigma_e = 0$, $\sigma_i = 0.061$. (a) Dependence of bending amplitude on excitation amplitude. (b) Dependence of torsion amplitude on excitation amplitude ..... 123

Figure 2.25. Stabilization effect of parametric excitation at post-critical flow speed $U_\infty / b\omega_\alpha = 5.02$ showing the percentage of domains of attraction for large amplitude response (diamond-solid curve) and large plus small amplitude responses (star-dotted curve). .... 124

Figure 2.26. Response time history records according to numerical simulation at zero flow speed for different values of excitation amplitude and for the same initial conditions $\bar{u}(0) = 0.5$, $\alpha(0) = 0.1$, $\bar{u}'(0) = 0$, $\alpha'(0) = 0$. (a) $Y_0 = 0.001$; (b) $Y_0 = 0.005$; (c) $Y_0 = 0.01$; (d) $Y_0 = 0.015$ ..... 125

Figure 2.27. Bifurcation diagram according to the numerical simulation of equations of motion at zero flow speed and $\Omega = \omega_1 + \omega_2$, $\omega_1 = 0.5\omega_2$, $\bar{u}(0) = 0.5$, $\alpha(0) = 0.1$, $\bar{u}'(0) = 0$, $\alpha'(0) = 0$. (a) Dependence of bending response amplitude on excitation amplitude. (b) Dependence of torsion response amplitude on excitation amplitude ..... 126

Figure 2.28. Numerical solution time histories, phase diagrams (d, f, g, h), Poincare maps (f, g, h), and FFT (d, f, g, h) at flutter speed

$U_\infty / b\omega_\alpha = 4.965$, $\Omega = \omega_1 + \omega_2$, $\omega_2 = \omega_1 + 0.061$. (a) $Y_0 = 0$,

$\bar{u}(0) = 0.05$, $\alpha(0) = 0.01$, $\bar{u}'(0) = 0$, $\alpha'(0) = 0$. (b) $Y_0 = 0$,

$\bar{u}(0) = 0.5$, $\alpha(0) = 0.1$, $\bar{u}'(0) = 0$, $\alpha'(0) = 0$. (c) $Y_0 = 0.00875$,

$\bar{u}(0) = 0.4$, $\alpha(0) = 0.02$, $\bar{u}'(0) = 0$, $\alpha'(0) = 0$. (d) $Y_0 = 0.00875$,

$\bar{u}(0) = 0.5$, $\alpha(0) = 0.04$, $\bar{u}'(0) = 0$, $\alpha'(0) = 0$. (e) $Y_0 = 0.014$,

$\bar{u}(0) = 0.2$, $\alpha(0) = 0.1$, $\bar{u}'(0) = 0$, $\alpha'(0) = 0$. (f) $Y_0 = 0.014$,

$\bar{u}(0) = 0.5$, $\alpha(0) = 0.1$, $\bar{u}'(0) = 0$, $\alpha'(0) = 0$. (g) $Y_0 = 0.016$,

$\bar{u}(0) = 0.6$, $\alpha(0) = 0.1$, $\bar{u}'(0) = 0$, $\alpha'(0) = 0$. (h) $Y_0 = 0.017$,

$\bar{u}(0) = 0.6$, $\alpha(0) = 0.1$, $\bar{u}'(0) = 0$, $\alpha'(0) = 0$ ..... 131

Figure 2.29. Numerical solution time histories, phase diagrams (a, g), and FFTs (a, g) at post critical flow speed $U_\infty / b\omega_\alpha = 5.02$,

$\Omega = \omega_1 + \omega_2$, $\omega_2 = \omega_1 + 0.061$. (a) $Y_0 = 0$, $\bar{u}(0) = 0.1$, $\alpha(0) = 0.01$,

$\bar{u}'(0) = 0$, $\alpha'(0) = 0$. (b) $Y_0 = 0.001$, $\bar{u}(0) = 0.1$, $\alpha(0) = 0.01$,

$\bar{u}'(0) = 0$, $\alpha'(0) = 0$. (c) $Y_0 = 0.005$, $\bar{u}(0) = 0.1$, $\alpha(0) = 0.01$,

$\bar{u}'(0) = 0$, $\alpha'(0) = 0$. (d) $Y_0 = 0.0075$, $\bar{u}(0) = 0.1$, $\alpha(0) = 0.01$,

$\bar{u}'(0) = 0$, $\alpha'(0) = 0$. (e) $Y_0 = 0.01$, $\bar{u}(0) = 0.1$, $\alpha(0) = 0.01$,

$\bar{u}'(0) = 0$, $\alpha'(0) = 0$. (f) $Y_0 = 0.015$, $\bar{u}(0) = 0.2$, $\alpha(0) = 0.01$,

$\bar{u}'(0) = 0$, $\alpha'(0) = 0$. (g) $Y_0 = 0.015$, $\bar{u}(0) = 0.3$, $\alpha(0) = 0.01$,

$\bar{u}'(0) = 0$, $\alpha'(0) = 0$. ..... 134

Figure 3.1. Lifting surface discretization ..... 166

Figure 3.2. The position of an arbitrary point $P$ on the lifting surface caused by the wing structure deformation ..... 166

Figure 3.3(a). Bound and free vortex lattices ..... 167

Figure 3.3(b). Representation of a general bound lattice element ..... 167

Figure 3.4. A portion of the lattice with representation of the aerodynamic loads ..... 168

Figure 3.5. Wing structure model ..... 168

Figure 3.6(a). Finite elements discretization ..... 169

Figure 3.6(b). A finite element representation ..... 169

Figure 3.7(a). Structural grid superimposed to the aerodynamic grid ..... 170

Figure 3.7(b). Connection of an aerodynamic grid point to an internal point of the structural grid point ..... 170

Figure 3.8. Dependence of wing response variances on the number of terms *N* in the Karhunen-Loeve expansion showing the convergence is achieved for $N \geq 2$. ..... 171

Figure 3.9. Time history records of bending and torsion responses and their variances for $V_\infty = 120m/s$, $\sigma_{EI_x} / \overline{EI}_x = 0$, $\sigma_{GJ} / \overline{GJ} = 0$, $\alpha_a = 5°$, $q_{ben}(0) = -0.05$, $\dot{q}_{ben}(0) = 0$, $q_{tor}(0) = 0.01$, $\dot{q}_{tor}(0) = 0$ ..... 172

Figure 3.10. Time history records of bending and torsion responses and their variances for $V_\infty = 140m/s$, $\sigma_{EI_x} / \overline{EI}_x = 0$, $\sigma_{GJ} / \overline{GJ} = 0$, $\alpha_a = 5°$, $q_{ben}(0) = -0.05$, $\dot{q}_{ben}(0) = 0$, $q_{tor}(0) = 0.01$, $\dot{q}_{tor}(0) = 0$ ..... 173

Figure 3.11. Time history records of bending and torsion responses and their variances for flutter speed $V_\infty = 143m/s$, $\sigma_{EI_x}/\overline{EI}_x = 0$, $\sigma_{GJ}/\overline{GJ} = 0$, $\alpha_a = 5°$, $q_{ben}(0) = -0.05$, $\dot{q}_{ben}(0) = 0$, $q_{tor}(0) = 0.01$, $\dot{q}_{tor}(0) = 0$ ..... 174

Figure 3.12. Time history records of bending and torsion responses and their variances for $V_\infty = 145m/s$, $\sigma_{EI_x}/\overline{EI}_x = 0$, $\sigma_{GJ}/\overline{GJ} = 0$, $\alpha_a = 5°$, $q_{ben}(0) = -0.05$, $\dot{q}_{ben}(0) = 0$, $q_{tor}(0) = 0.01$, $\dot{q}_{tor}(0) = 0$ ..... 175

Figure 3.13. Time history records of bending and torsion responses and their variances for $V_\infty = 120m/s$, $\sigma_{EI_x}/\overline{EI}_x = 0.09$, $\sigma_{GJ}/\overline{GJ} = 0$, $\alpha_a = 5°$, $q_{ben}(0) = -0.05$, $\dot{q}_{ben}(0) = 0$, $q_{tor}(0) = 0.01$, $\dot{q}_{tor}(0) = 0$ ..... 176

Figure 3.14. Time history records of bending and torsion responses and their variances for $V_\infty = 120m/s$, $\sigma_{EI_x}/\overline{EI}_x = 0.1$, $\sigma_{GJ}/\overline{GJ} = 0$, $\alpha_a = 5°$, $q_{ben}(0) = -0.05$, $\dot{q}_{ben}(0) = 0$, $q_{tor}(0) = 0.01$, $\dot{q}_{tor}(0) = 0$ ..... 177

Figure 3.15. Time history records of bending and torsion responses and their variances for $V_\infty = 125m/s$, $\sigma_{EI_x}/\overline{EI}_x = 0.07$, $\sigma_{GJ}/\overline{GJ} = 0$, $\alpha_a = 5°$, $q_{ben}(0) = -0.05$, $\dot{q}_{ben}(0) = 0$, $q_{tor}(0) = 0.01$, $\dot{q}_{tor}(0) = 0$ ..... 178

Figure 3.16. Time history records of bending and torsion responses and their variances for $V_\infty = 125m/s$, $\sigma_{EI_x}/\overline{EI}_x = 0.08$, $\sigma_{GJ}/\overline{GJ} = 0$, $\alpha_a = 5°$, $q_{ben}(0) = -0.05$, $\dot{q}_{ben}(0) = 0$, $q_{tor}(0) = 0.01$, $\dot{q}_{tor}(0) = 0$ ..... 179

Figure 3.17. Time history records of bending and torsion responses and their variances for $V_\infty = 125m/s$, $\sigma_{EI_x}/\overline{EI}_x = 0.09$, $\sigma_{GJ}/\overline{GJ} = 0$, $\alpha_a = 5°$, $q_{ben}(0) = -0.05$, $\dot{q}_{ben}(0) = 0$, $q_{tor}(0) = 0.01$, $\dot{q}_{tor}(0) = 0$ ..... 180

Figure 3.18. Time history records of bending and torsion responses and their variances for $V_\infty = 130m/s$, $\sigma_{EI_x}/\overline{EI}_x = 0.05$, $\sigma_{GJ}/\overline{GJ} = 0$, $\alpha_a = 5°$, $q_{ben}(0) = -0.05$, $\dot{q}_{ben}(0) = 0$, $q_{tor}(0) = 0.01$, $\dot{q}_{tor}(0) = 0$ ..... 181

Figure 3.19. Time history records of bending and torsion responses and their variances for $V_\infty = 130m/s$, $\sigma_{EI_x}/\overline{EI}_x = 0.06$, $\sigma_{GJ}/\overline{GJ} = 0$, $\alpha_a = 5°$, $q_{ben}(0) = -0.05$, $\dot{q}_{ben}(0) = 0$, $q_{tor}(0) = 0.01$, $\dot{q}_{tor}(0) = 0$ ..... 182

Figure 3.20. Time history records of bending and torsion responses and their variances for $V_\infty = 130m/s$, $\sigma_{EI_x}/\overline{EI}_x = 0.07$, $\sigma_{GJ}/\overline{GJ} = 0$, $\alpha_a = 5°$, $q_{ben}(0) = -0.05$, $\dot{q}_{ben}(0) = 0$, $q_{tor}(0) = 0.01$, $\dot{q}_{tor}(0) = 0$ ..... 183

Figure 3.21. Time history records of bending and torsion responses and their variances for $V_\infty = 135m/s$, $\sigma_{EI_x}/\overline{EI}_x = 0.03$, $\sigma_{GJ}/\overline{GJ} = 0$, $\alpha_a = 5°$, $q_{ben}(0) = -0.05$, $\dot{q}_{ben}(0) = 0$, $q_{tor}(0) = 0.01$, $\dot{q}_{tor}(0) = 0$ ..... 184

Figure 3.22. Time history records of bending and torsion responses and their variances for $V_\infty = 135m/s$, $\sigma_{EI_x}/\overline{EI}_x = 0.04$, $\sigma_{GJ}/\overline{GJ} = 0$, $\alpha_a = 5°$, $q_{ben}(0) = -0.05$, $\dot{q}_{ben}(0) = 0$, $q_{tor}(0) = 0.01$, $\dot{q}_{tor}(0) = 0$ ..... 185

Figure 3.23. Time history records of bending and torsion responses and their variances for $V_\infty = 135m/s$, $\sigma_{EI_x}/\overline{EI}_x = 0.05$, $\sigma_{GJ}/\overline{GJ} = 0$, $\alpha_a = 5°$, $q_{ben}(0) = -0.05$, $\dot{q}_{ben}(0) = 0$, $q_{tor}(0) = 0.01$, $\dot{q}_{tor}(0) = 0$ ..... 186

Figure 3.24. Time history records of bending and torsion responses and their variances for $V_\infty = 140m/s$, $\sigma_{EI_x}/\overline{EI}_x = 0.01$, $\sigma_{GJ}/\overline{GJ} = 0$, $\alpha_a = 5°$, $q_{ben}(0) = -0.05$, $\dot{q}_{ben}(0) = 0$, $q_{tor}(0) = 0.01$, $\dot{q}_{tor}(0) = 0$ ..... 187

Figure 3.25. Time history records of bending and torsion responses and their variances for $V_\infty = 140m/s$, $\sigma_{EI_x}/\overline{EI}_x = 0.015$, $\sigma_{GJ}/\overline{GJ} = 0$, $\alpha_a = 5°$, $q_{ben}(0) = -0.05$, $\dot{q}_{ben}(0) = 0$, $q_{tor}(0) = 0.01$, $\dot{q}_{tor}(0) = 0$ ..... 188

Figure 3.26. Time history records of bending and torsion responses and their variances for $V_\infty = 140m/s$, $\sigma_{EI_x}/\overline{EI}_x = 0.02$, $\sigma_{GJ}/\overline{GJ} = 0$, $\alpha_a = 5°$, $q_{ben}(0) = -0.05$, $\dot{q}_{ben}(0) = 0$, $q_{tor}(0) = 0.01$, $\dot{q}_{tor}(0) = 0$ ..... 189

Figure 3.27. Stability bifurcation diagram $V_\infty$ vs. $\sigma_{EI_x}/\overline{EI}_x$ ..... 190

Figure 3.28. Time history records of bending and torsion responses and their variances for $V_\infty = 120m/s$, $\sigma_{EI_x}/\overline{EI}_x = 0$, $\sigma_{GJ}/\overline{GJ} = 0.03$, $\alpha_a = 5°$, $q_{0,ben}(0) = -0.05$, $\dot{q}_{0,ben}(0) = 0$, $q_{0,tor}(0) = 0.01$, $\dot{q}_{0,tor}(0) = 0$ . 191

Figure 3.29. Time history records of bending and torsion responses and their variances for $V_\infty = 120m/s$, $\sigma_{EI_x}/\overline{EI}_x = 0$, $\sigma_{GJ}/\overline{GJ} = 0.035$, $\alpha_a = 5°$, $q_{0,ben}(0) = -0.05$, $\dot{q}_{0,ben}(0) = 0$, $q_{0,tor}(0) = 0.01$, $\dot{q}_{0,tor}(0) = 0$ . 192

Figure 3.30. Time history records of bending and torsion responses and their variances for $V_\infty = 120m/s$, $\sigma_{EI_x}/\overline{EI}_x = 0$, $\sigma_{GJ}/\overline{GJ} = 0.04$, $\alpha_a = 5°$, $q_{0,ben}(0) = -0.05$, $\dot{q}_{0,ben}(0) = 0$, $q_{0,tor}(0) = 0.01$, $\dot{q}_{0,tor}(0) = 0$ . 193

Figure 3.31. Time history records of bending and torsion responses and their variances for $V_\infty = 130m/s$, $\sigma_{EI_x}/\overline{EI}_x = 0$, $\sigma_{GJ}/\overline{GJ} = 0.03$, $\alpha_a = 5°$, $q_{0,ben}(0) = -0.05$, $\dot{q}_{0,ben}(0) = 0$, $q_{0,tor}(0) = 0.01$, $\dot{q}_{0,tor}(0) = 0$ . 194

Figure 3.32. Time history records of bending and torsion responses and their variances for $V_\infty = 135m/s$, $\sigma_{EI_x}/\overline{EI}_x = 0$, $\sigma_{GJ}/\overline{GJ} = 0.02$, $\alpha_a = 5°$, $q_{0,ben}(0) = -0.05$, $\dot{q}_{0,ben}(0) = 0$, $q_{0,tor}(0) = 0.01$, $\dot{q}_{0,tor}(0) = 0$ . 195

Figure 3.33. Time history records of bending and torsion responses and their variances for $V_\infty = 140m/s$, $\sigma_{EI_x}/\overline{EI}_x = 0$, $\sigma_{GJ}/\overline{GJ} = 0.01$, $\alpha_a = 5°$, $q_{0,ben}(0) = -0.05$, $\dot{q}_{0,ben}(0) = 0$, $q_{0,tor}(0) = 0.01$, $\dot{q}_{0,tor}(0) = 0$ . 196

Figure 3.34. Stability bifurcation diagram $V_\infty$ vs. $\sigma_{GJ}/\overline{GJ}$ ..... 197

Figure 3.35. Time history records of bending and torsion responses and their variances for $V_\infty = 120m/s$, $\sigma_{EI_x}/\overline{EI}_x = 0.01$, $\sigma_{GJ}/\overline{GJ} = 0.0325$, $\alpha_a = 5°$, $q_{0,ben}(0) = -0.05$, $\dot{q}_{0,ben}(0) = 0$, $q_{0,tor}(0) = 0.01$, $\dot{q}_{0,tor}(0) = 0$ ..... 198

Figure 3.36. Time history records of bending and torsion responses and their variances for $V_\infty = 120m/s$, $\sigma_{EI_x}/\overline{EI}_x = 0.03$,

$\sigma_{GJ}/\overline{GJ}=0.025$, $\alpha_a=5°$, $q_{0,ben}(0)=-0.05$,

$\dot{q}_{0,ben}(0)=0$, $q_{0,tor}(0)=0.01$, $\dot{q}_{0,tor}(0)=0$ ..... 199

Figure 3.37. Time history records of bending and torsion responses and their variances for $V_\infty=120m/s$, $\sigma_{EI_x}/\overline{EI}_x=0.05$, $\sigma_{GJ}/\overline{GJ}=0.02$, $\alpha_a=5°$, $q_{0,ben}(0)=-0.05$, $\dot{q}_{0,ben}(0)=0$, $q_{0,tor}(0)=0.01$, $\dot{q}_{0,tor}(0)=0$ ..... 200

Figure 3.38. Time history records of bending and torsion responses and their variances for $V_\infty=120m/s$, $\sigma_{EI_x}/\overline{EI}_x=0.07$, $\sigma_{GJ}/\overline{GJ}=0.015$, $\alpha_a=5°$, $q_{0,ben}(0)=-0.05$, $\dot{q}_{0,ben}(0)=0$, $q_{0,tor}(0)=0.01$, $\dot{q}_{0,tor}(0)=0$ ..... 201

Figure 3.39. Time history records of bending and torsion responses and their variances for $V_\infty=120m/s$, $\sigma_{EI_x}/\overline{EI}_x=0.09$, $\sigma_{GJ}/\overline{GJ}=0.01$, $\alpha_a=5°$, $q_{0,ben}(0)=-0.05$, $\dot{q}_{0,ben}(0)=0$, $q_{0,tor}(0)=0.01$, $\dot{q}_{0,tor}(0)=0$ . 202

Figure 3.40. Time history records of bending and torsion responses and their variances for $V_\infty=130m/s$, $\sigma_{EI_x}/\overline{EI}_x=0.01$, $\sigma_{GJ}/\overline{GJ}=0.025$, $\alpha_a=5°$, $q_{0,ben}(0)=-0.05$, $\dot{q}_{0,ben}(0)=0$, $q_{0,tor}(0)=0.01$, $\dot{q}_{0,tor}(0)=0$ ..... 203

Figure 3.41. Time history records of bending and torsion responses and their variances for $V_\infty=130m/s$, $\sigma_{EI_x}/\overline{EI}_x=0.02$,

$\sigma_{GJ}/\overline{GJ}=0.021$, $\alpha_a=5°$, $q_{0,ben}(0)=-0.05$,

$\dot{q}_{0,ben}(0)=0$, $q_{0,tor}(0)=0.01$, $\dot{q}_{0,tor}(0)=0$ ..... 204

Figure 3.42. Time history records of bending and torsion responses and their variances for $V_\infty=130m/s$, $\sigma_{EI_x}/\overline{EI}_x=0.03$, $\sigma_{GJ}/\overline{GJ}=0.015$, $\alpha_a=5°$, $q_{0,ben}(0)=-0.05$, $\dot{q}_{0,ben}(0)=0$, $q_{0,tor}(0)=0.01$, $\dot{q}_{0,tor}(0)=0$ ..... 205

Figure 3.43. Time history records of bending and torsion responses and their variances for $V_\infty=130m/s$, $\sigma_{EI_x}/\overline{EI}_x=0.04$, $\sigma_{GJ}/\overline{GJ}=0.01$, $\alpha_a=5°$, $q_{0,ben}(0)=-0.05$, $\dot{q}_{0,ben}(0)=0$, $q_{0,tor}(0)=0.01$, $\dot{q}_{0,tor}(0)=0$ . 206

Figure 3.44. Time history records of bending and torsion responses and their variances for $V_\infty=130m/s$, $\sigma_{EI_x}/\overline{EI}_x=0.05$, $\sigma_{GJ}/\overline{GJ}=0.0075$, $\alpha_a=5°$, $q_{0,ben}(0)=-0.05$, $\dot{q}_{0,ben}(0)=0$, $q_{0,tor}(0)=0.01$, $\dot{q}_{0,tor}(0)=0$ ..... 207

Figure 3.45. Time history records of bending and torsion responses and their variances for $V_\infty=140m/s$, $\sigma_{EI_x}/\overline{EI}_x=0.01$, $\sigma_{GJ}/\overline{GJ}=0.005$, $\alpha_a=5°$, $q_{0,ben}(0)=-0.05$, $\dot{q}_{0,ben}(0)=0$, $q_{0,tor}(0)=0.01$, $\dot{q}_{0,tor}(0)=0$ ..... 208

Figure 3.46. Stability boundaries $\sigma_{EI_x}/\overline{EI}_x$ vs. $\sigma_{GJ}/\overline{GJ}$ at different flow speeds (a) 2D representation and (b) 3D representation ..... 209

Figure 3.47. Time history records of bending and torsion responses and their variances from Monte Carlo Simulation; $V_\infty = 120m/s$, $\sigma_{EI_x}/\overline{EI}_x = 0.1$, $\sigma_{GJ}/\overline{GJ} = 0$, $\alpha_a = 5°$, $q_{ben}(0) = -0.05$, $\dot{q}_{ben}(0) = 0$, $q_{tor}(0) = 0.01$, $\dot{q}_{tor}(0) = 0$ ..... 211

Figure 3.48. Time history records of bending and torsion responses and their variances from Monte Carlo Simulation; $V_\infty = 125m/s$, $\sigma_{EI_x}/\overline{EI}_x = 0.08$, $\sigma_{GJ}/\overline{GJ} = 0$, $\alpha_a = 5°$, $q_{ben}(0) = -0.05$, $\dot{q}_{ben}(0) = 0$, $q_{tor}(0) = 0.01$, $\dot{q}_{tor}(0) = 0$ ..... 213

Figure 3.49. Time history records of bending and torsion responses and their variances from Monte Carlo Simulation; $V_\infty = 130m/s$, $\sigma_{EI_x}/\overline{EI}_x = 0.06$, $\sigma_{GJ}/\overline{GJ} = 0$, $\alpha_a = 5°$, $q_{ben}(0) = -0.05$, $\dot{q}_{ben}(0) = 0$, $q_{tor}(0) = 0.01$, $\dot{q}_{tor}(0) = 0$ ..... 215

Figure 3.50. Time history records of bending and torsion responses and their variances from Monte Carlo Simulation; $V_\infty = 135m/s$, $\sigma_{EI_x}/\overline{EI}_x = 0.04$, $\sigma_{GJ}/\overline{GJ} = 0$, $\alpha_a = 5°$, $q_{ben}(0) = -0.05$, $\dot{q}_{ben}(0) = 0$, $q_{tor}(0) = 0.01$, $\dot{q}_{tor}(0) = 0$ ..... 217

Figure 3.51. Time history records of bending and torsion responses and their variances from Monte Carlo Simulation; $V_\infty = 140m/s$, $\sigma_{EI_x}/\overline{EI}_x = 0.015$, $\alpha_a = 5°$, $q_{ben}(0) = -0.05$, $\dot{q}_{ben}(0) = 0$, $q_{tor}(0) = 0.01$, $\dot{q}_{tor}(0) = 0$ ..... 219

Figure 3.52. Stability bifurcation diagram $V_\infty$ vs. $\sigma_{EI_x} / \overline{EI}_x$ for Monte Carlo Simulation ..... 220

Figure 3.53. Perturbation method convergence ..... 221

Figure 3.54. Time history records of bending and torsion responses and their variances from Monte Carlo Simulation; $V_\infty = 120 m/s$, $\sigma_{EI_x} / \overline{EI}_x = 0$, $\sigma_{GJ} / \overline{GJ} = 0.05$, $\alpha_a = 5°$, $q_{ben}(0) = -0.05$, $\dot{q}_{ben}(0) = 0$, $q_{tor}(0) = 0.01$, $\dot{q}_{tor}(0) = 0$ ..... 223

Figure 3.55. Time history records of bending and torsion responses and their variances from Monte Carlo Simulation; $V_\infty = 130 m/s$, $\sigma_{EI_x} / \overline{EI}_x = 0$, $\sigma_{GJ} / \overline{GJ} = 0.03$, $\alpha_a = 5°$, $q_{ben}(0) = -0.05$, $\dot{q}_{ben}(0) = 0$, $q_{tor}(0) = 0.01$, $\dot{q}_{tor}(0) = 0$ ..... 225

Figure 3.56. Time history records of bending and torsion responses and their variances from Monte Carlo Simulation; $V_\infty = 140 m/s$, $\sigma_{EI_x} / \overline{EI}_x = 0$, $\sigma_{GJ} / \overline{GJ} = 0.01$, $\alpha_a = 5°$, $q_{ben}(0) = -0.05$, $\dot{q}_{ben}(0) = 0$, $q_{tor}(0) = 0.01$, $\dot{q}_{tor}(0) = 0$ ..... 227

Figure 3.57. Stability bifurcation diagram $V_\infty$ vs. $\sigma_{GJ} / \overline{GJ}$ for Monte Carlo Simulation ..... 228

Figure 3.58. Perturbation method convergence ..... 229

Figure D.1. The relationship between line and surface integrals ..... 256

Figure D.2. Fluid-structure boundary ..... 256

Figure D.3. Vortex tube ..... 257

Figure D.4. Velocity estimated at point $P$ due to vorticity distribution ..... 257

Figure D.5. Velocity estimated at point $P$ due to a vortex filament ..... 258

Figure D.6. Velocity induced by a straight vortex element ..... 258

Figure D.7. Velocity induced by a straight vortex segment ..... 259

Figure D.8. The position of an arbitrary point $P$ in the airflow ..... 259

Figure D.9. A $3 \times 4$ elements lattice ..... 260

Figure D.10. Vortex loops ..... 260

Figure D11. Influence coefficients interpretation ..... 261

Figure D.12. Vortex loops at time $t = \Delta t$ ..... 261

# CHAPTER 1

# A REVIEW OF LITERATURE AND BACKGROUND

## 1.1 Introduction

Flutter of aeroelastic structures refers to the interaction between aerodynamic, inertia, and elastic forces. It is characterized by unstable oscillations at a critical airflow speed. Above that flutter speed, the oscillations grow until the amplitude reaches a value above which the nonlinearities bring the flutter into limit cycle oscillations (LCO). The role of nonlinearities on the flutter boundary depends on the system parameters, airflow conditions, speed, turbulence, gust, etc. The coupling of several degrees of freedom (DOF) is also an essential feature of flutter. With reference to the flutter of a cantilever wing, the coupling between bending and torsional deflection is predominant.

An accurate analytical or numerical modeling requires a strong background of aerodynamic loading and its interaction with structural mechanics. For this reason this chapter provides different approaches of describing aerodynamic forces and moments. This overview is followed by different combined models of structural-flow interaction. Based on findings that will be covered in chapter 2 (stabilization of the wing under parametric excitation), a review of stabilization of different mechanical systems under parametric excitation will be presented.

In some cases two identical aeroelastic structures may exhibit different flutter characteristics. For example, the flutter speed may not be the same for each structure. The main reason for this unexpected observation owes its origin

to the structure parameter uncertainties. This chapter will also provide an assessment of the influence of parameter uncertainties on aeroelastic structures and will identify the unresolved problems.

## 1.2 Aerodynamic Modeling

Different approaches are developed in the literature to determine the aerodynamic loading acting on aeroelastic structures. These methods are either analytical or numerical. The analytical approaches are based on restricted assumptions which lead to linear descriptions. Numerical schemes are versatile and include flexibility to account for the nonlinear flow and provide more realistic representation of aerodynamic loading. The next subsections briefly describe the two approaches.

### 1.2.1 ANALYTICAL SCHEMES (LINEAR)

The analysis of aeroelastic flutter usually depends on the methods of aerodynamic loading. Linear modeling is based on linear representations of aerodynamic, elastic, and inertia forces. Nonlinear modeling, on the other hand, considers the inherent nonlinearity of any of these forces or combination of them. Ashley [1] presented the state-of-the-art up to 1978 of solved and unsolved problems of aeroelastic stability. Resolved problems included the torsional and flexural-torsional divergence of conventional lifting surfaces, and subsonic and supersonic flutter of isolated lifting surfaces. The unresolved problems included deterministic and stochastic flutter of nonlinear aeroelastic structures in the

presence of time-varying in-plane excitations. This in addition to the stochastic flutter of linear and nonlinear aeroelastic structures in transonic and supersonic flow regimes.

For the calculation of the aerodynamic loads, several analytical theories have been developed. These include (a) the Wagner theory [2-4], (b) the modified strip analysis [5], (c) the modified two-dimensional loading [6], (d) the subsonic kernel function [7], and (e) the rectangular wing theory [8]. Among the methods stated above, the first two (a) and (b) are the most utilized in aeroelastic analytical formulations. Also the modified strip analysis (b) was frequently adopted to calculate the flutter speed in industry up to the late 1960's. Because of that, only these two methods will be discussed in detail below. In the analytical theories the lift force and aerodynamic moment are eventually obtained in a closed form.

It is believed that the early analysis of wing flutter in an incompressible subsonic flow was based on a quasi-stationary formulation. Theodorsen [9] and Wagner [2] developed non-stationary formulations that account for the lag effects of the unsteady aerodynamics for different frequencies. Later, Theodorsen and Garrick [10] conducted an experimental investigation to examine the validity of the predicted flutter speed and frequency.

The Wagner theory and the modified strip theory give the unsteady aerodynamic loads for two-dimensional incompressible potential flow at subsonic speeds. The modified strip theory, based on Theodorsen's work [9], includes alterations in the expressions of lift, moment, and circulation function in order to

approximate the effects of the span finite length. In both theories the aerodynamic loads contain a non-circulatory flow component that contributes to the lift and moment with a virtual mass and a circulatory component that takes into account the vortex caused by the wake. The non-circulatory component is the same in both theories but the circulatory component uses the Wagner's function [2] in the first case and Theodorsen's function [9] in the second case. The aerodynamic loads according to Theodorsen's theory can be obtained from Wagner's theory under the assumption of harmonic motion of the wing.

The derivations of the unsteady aerodynamic loads using Wagner's theory as they are described by Fung [4] are presented in this section. First we consider a two-degree-of-freedom airfoil describing a vertical translation $u$ (*plunge*), taken positive downward, and a rotation $\alpha$ (*pitch* angle) about the elastic axis located at a distance $\delta_1 = ab$ from the mid-chord, positive nose up as shown in Figure 1.1. Assuming two-dimensional flow with constant flow speed $U_\infty$, the lift force is composed of a circulatory part and non-circulatory part which is caused by "apparent mass" forces.

For plunge and pitch oscillations, the circulation[1] about the airfoil is determined by the downwash[2] velocity at the ¾-chord point from the leading edge of the airfoil. The downwash at ¾-chord point due to both plunge and pitch contains:

a) a uniform downwash $w_1$ corresponding to the pitch, $w_1 = U_\infty \sin\alpha \simeq U_\infty \alpha$, where $U_\infty$ is the speed of undisturbed flow;

[1] Circulation is the line integral of fluid velocity around a closed curve

b) a uniform downwash $w_2$ due to vertical translation, $w_2 = \frac{du}{ds}\frac{ds}{dt} = \frac{U_\infty}{b}u'$ $= U_\infty \bar{u}'$, where prime denotes a differentiation with respect to the non-dimensional time $s = U_\infty t/b$, $\bar{u} = u/b$ the non-dimensional plunge, $t$ is dimensional time, and $b$ is the half-chord;

c) a non-uniform downwash $w_3$ due to $\frac{d\alpha}{dt}$, its value at the ¾-chord being $w_3 = \left(\frac{1}{2} - a\right) b \frac{d\alpha}{ds}\frac{ds}{dt} = \left(\frac{1}{2} - a\right) U_\infty \alpha'$, where $\alpha' = \frac{d\alpha}{ds}$.

Adding a), b), and c), the total downwash $w(u, \alpha, t)$ is:

$$w(u,\alpha,t) = w_1 + w_2 + w_3 = U_\infty \alpha(t) + \dot{u}(t) + \left(\frac{1}{2} - a\right) b\dot{\alpha}(t) \tag{1.1}$$

This expression can be written in terms of the non-dimensional time parameter $s$ as:

$$w(u,\alpha,s) = U_\infty \alpha(s) + U_\infty \bar{u}'(s) + \left(\frac{1}{2} - a\right) U_\infty \alpha'(s) \tag{1.2}$$

In the time interval $(s_0, s_0 + ds_0)$, the downwash is increased by $dw(s_0)/ds_0$. If $ds_0$ is sufficiently small, it may be regarded as impulsive increment and the circulatory lift per unit span is given by [4]:

---

[2] Downwash refers to the flow of air behind a wing. The downwash behind a wing is a consequence of the wing trailing vortex system. (www.wikipedia.com)

$$dL_1(\bar{u},\alpha,s) = 2\pi\rho_\infty b U_\infty \phi(s-s_0)\frac{dw(\bar{u},\alpha,s_0)}{ds_0}ds_0, \text{ over } ds_0 \text{ for } s \geq s_0 \qquad (1.3)$$

where $\rho_\infty$ is the air density, $\phi(s)$ is Wagner's function which describes the growth of circulation about the airfoil due to the sudden increase of downwash. Approximate expression for the Wagner's function is given by Jones [11]:

$$\phi(s) = 1 - \psi_1 e^{-\varepsilon_1 s} - \psi_2 e^{-\varepsilon_2 s} \qquad (1.4)$$

where $\psi_1 = 0.165$, $\psi_2 = 0.335$, $\varepsilon_1 = 0.0455$, $\varepsilon_2 = 0.3$.

The total circulatory lift per unit span at time $s$ is obtained by integrating equation (1.3) with respect to $s$:

$$L_1(\bar{u},\alpha,s) = 2\pi\rho_\infty b U_\infty \int_{-\infty}^{s} \phi(s-s_0)\frac{dw(\bar{u},\alpha,s_0)}{ds_0}ds_0 \qquad (1.5)$$

If the motion starts from $s = 0$, equation (1.5) becomes:

$$L_1(\bar{u},\alpha,s) = 2\pi\rho_\infty b U_\infty \left[ w_0\phi(s) + \int_0^s \phi(s-s_0)\frac{dw(\bar{u},\alpha,s_0)}{ds_0}ds_0 \right] \qquad (1.6)$$

where $w_0 = U_\infty\left(\alpha(0) + \bar{u}'(0) + \left(\frac{1}{2} - a\right)\alpha'(0)\right)$ is the initial value of downwash.

The lift and moment of the non-circulatory flow include the following components:

a) a lift force having the center of pressure at the mid-chord generated by apparent mass $\pi\rho_\infty b^2$:

$$L_2 = \pi\rho_\infty b^2\left(\ddot{u}(t) - ab\ddot{\alpha}(t)\right) = \pi\rho_\infty bU_\infty^2\left(\bar{u}''(s) - a\alpha''(s)\right) \tag{1.7}$$

b) a lift force (of centrifugal nature) having the center of pressure at ¾-chord point generated also by apparent mass $\pi\rho_\infty b^2$:

$$L_3 = \pi\rho_\infty b^2 U_\infty \dot{\alpha}(t) = \pi\rho_\infty bU_\infty^2\alpha'(s) \tag{1.8}$$

c) a nose down moment generated by apparent moment of inertia $\rho_\infty \pi b^2\left(b^2/8\right)$:

$$M_\alpha = -\pi\rho_\infty b^4 U_\infty^2 \frac{1}{8}\ddot{\alpha}(t) = -\pi\rho_\infty b^2 U_\infty^2 \frac{1}{8}\alpha''(s) \tag{1.9}$$

The total lift per unit span is given by:

$$L(\bar{u}, \alpha, s) = L_1 + L_2 + L_3 \tag{1.10}$$

The total moment per unit span about the elastic axis is given by:

$$M(\bar{u}, \alpha, s) = \left(\frac{1}{2} + a\right)bL_1 + abL_2 - \left(\frac{1}{2} - a\right)bL_3 + M_\alpha \tag{1.11}$$

Combining (1.2) with (1.6), and introducing the full expression for each component, the aerodynamic lift per unit span become:

$$L(\bar{u}, \alpha, s) = \pi\rho_\infty bU_\infty^2\left(\bar{u}''(s) - a\alpha''(s) + \alpha'(s)\right) + 2\pi\rho_\infty bU_\infty^2\left[\alpha(0) + \bar{u}'(0)\right.$$

$$\left. + \left(\frac{1}{2} - a\right)\alpha'(0)\right]\phi(s) + 2\pi\rho_\infty bU_\infty^2\int_0^s \phi(s - s_0)\left(\alpha'(s_0) + \bar{u}''(s_0) + \left(\frac{1}{2} - a\right)\alpha''(s_0)\right)ds_0 \tag{1.12}$$

The aerodynamic moment about the elastic axis, per unit span is given by:

$$M(\bar{u},\alpha,s)=\pi\rho_\infty b^2U_\infty^2\left(a\left[\bar{u}''(s)-a\alpha''(s)\right]-\left(\frac{1}{2}-a\right)\alpha'(s)-\frac{1}{8}\alpha''(s)\right)$$
$$+2\pi\rho_\infty b^2U_\infty^2\left(\frac{1}{2}+a\right)\left(\alpha(0)+\bar{u}'(0)+\left(\frac{1}{2}-a\right)\alpha'(0)\right)\phi(s)$$
$$+2\pi\rho_\infty b^2U_\infty^2\left(\frac{1}{2}+a\right)\int_0^s\phi(s-s_0)\left(\alpha'(s_0)+\bar{u}''(s_0)+\left(\frac{1}{2}-a\right)\alpha''(s_0)\right)ds_0 \qquad (1.13)$$

Assuming harmonic motion of the wing, the aerodynamic loads given in equations (1.12) and (1.13) according to the Theodorsen's theory[3] are:

$$L(u,\alpha,t)=2\pi\rho_\infty U_\infty bB(k)\,w(u,\alpha,t)+\pi\rho_\infty b^2(\ddot{u}-ba\ddot{\alpha})+\pi\rho_\infty b^2U_\infty\dot{\alpha} \qquad (1.14)$$

$$M(u,\alpha,t)=2\pi\rho_\infty U_\infty b^2\left(\frac{1}{2}+a\right)B(k)\,w(u,\alpha,t)$$
$$+\pi\rho_\infty ab^3(\ddot{u}-ba\ddot{\alpha})-\left(\frac{1}{2}-a\right)\pi\rho_\infty b^3U_\infty\dot{\alpha}-\frac{\pi\rho_\infty b^4}{8}\ddot{\alpha} \qquad (1.15)$$

where $w(u,\alpha,t)$ is the downwash and its expression is given in the equation (1.1), $B(k)$ is called the Theodorsen's or circulation function, which is a function of the reduced frequency, $k=b\omega/U_\infty$ ($\omega$ is the natural frequency of the wing structure). Generally, the Theodorsen's function is a complex function whose real part modifies the load component in-phase with the angle of attack, while its imaginary part accounts for the out-of-phase load component. Jones (see, e.g.

[3] Note that the aerodynamic loads given by equations (1.14) and (1.15) are in dimensional form

[4, 11]) introduced an approximation, stated below, to Theodorsen's function in order to predict the wing dynamic behavior in unsteady aerodynamic field:

$$B(k) = F(k) + iG(k) \tag{1.16}$$

where

$$F(k) = 1 - \frac{0.165k^2}{k^2 + 0.00207} - \frac{0.335k^2}{k^2 + 0.09} \text{ and } G(k) = -\frac{0.0075k}{k^2 + 0.00207} - \frac{0.1005k}{k^2 + 0.09}$$

Although it would seem straightforward to use the real and imaginary parts directly in the flutter analysis, this procedure was found to give poor results in comparison with experimental results as reported by Yates [5]. The large phase angles of complex circulation functions associated with two-dimensional flow were found to be inappropriate for three-dimensional wings. Yates found that if the phase angles remained moderately small the calculated flutter speed would be relatively insensitive to changes in the magnitude of the imaginary part.

The real part of the circulation function is usually given in terms of the first eigenvalue of the coupled modes and Mach number for different values of a frequency parameter (non-dimensional flow speed). Small disturbances to the flow are assumed, which imply that the resultant fluid speed differs only slightly from the free stream speed.

### 1.2.2 NUMERICAL SCHEMES

There are two ways to numerically model the aerodynamic loads. One way is to model the entire flow by one of the computational fluid dynamics

schemes based on finite difference or finite volume methods to directly solve the fluid flow equations. This approach is the most accurate yet and it is considered the ultimate approach. Unfortunately the method is very expensive in computational time because it needs to grid the entire flow. Another way to numerically model the aerodynamic loads is to use potential flow models based on singularity elements. Singularity element models are based on a general method for calculating the incompressible potential flow about arbitrary body shapes [12-24]. A general description of singularity element models is given below, starting with the fluid field equations.

*1.2.2.1 Fluid Field Equations*

In an inviscid, incompressible and irrotational[4] flow, the velocity field can be expressed in terms of a potential function $\Phi$ whose gradient gives the flow velocity vector as (e.g. [23]):

$$\mathbf{V} = \nabla\Phi \tag{1.17}$$

where $\mathbf{V}$ is the fluid velocity vector, and $\nabla = \frac{\partial}{\partial x}\hat{i} + \frac{\partial}{\partial x}\hat{j} + \frac{\partial}{\partial x}\hat{k}$, where $\hat{i}$, $\hat{j}$, $\hat{k}$ are the unit vectors of Cartesian coordinates $x$, $y$, and $z$ respectively. In this case the governing equation for the velocity field is given by the continuity equation (Laplace's equation) (see Appendix D for further details):

[4] In an irrotational flow the fluid does not move in circular or helical motions; it does not form vortices (www.wikipedia.com)

$$\nabla^2 \Phi = 0 \tag{1.18a}$$

If the flow is passing over a solid body the following boundary condition is imposed:

$$\nabla \Phi \cdot \mathbf{n} = 0 \tag{1.18b}$$

where $\mathbf{n}$ represents the unit vector normal to the solid body. Another condition requires that the resultant velocity of the flow at points far away from the solid boundary has to be equal to the undisturbed velocity of the flow.

Now it is necessary to define some elementary flows such as: uniform flow, source or sink, doublet, and potential vortex [23]:

- A two dimensional *uniform flow* parallel to the x-direction is shown in Figure 1.2. The potential function for this flow in cylindrical coordinates is:

$$\Phi = U_\infty r \cos\theta \tag{1.19}$$

  where $r$ is the radial coordinate from the origin and $\theta$ is the angle made with the x-axis.

- A *source* is defined as a point from which fluid is generated and flows radially outward as seen in Figure 1.3. The potential function for a two-dimensional source centered at the origin is given by:

$$\Phi = \frac{K}{2\pi} \ln r \tag{1.20}$$

where $K$ is the source's strength. As we can see from equation (1.20), there is a singularity at the source's center ($r = 0$). For this reason a source is called singularity.

- A *sink* is a negative source. This implies the fluid flows into a sink along radial streamlines[5]. The potential function is given by

$$\Phi = -\frac{K}{2\pi}\ln r \tag{1.21}$$

- A *doublet* (see Figure 1.4) is the singularity which results when a source and a sink of equal strength approach each other such that the product of their strength ($K$) and their distance apart remains constant in the limit as the distance between them approaches zero. The line along which the approach is made is called the *axis of the doublet* and it has a positive direction when oriented from sink to source. The potential for a doublet is given by:

$$\Phi = \frac{\tilde{B}}{r}\cos\theta \tag{1.22}$$

where $\tilde{B}$ is a constant.

- A *potential vortex* is a singularity about which fluid flows with concentric streamlines as seen in Figure 1.5. The potential for a vortex centered at the origin is given by:

[5] Streamlines are a family of curves that are instantaneously tangent to the velocity vector of the flow (www.wikipedia.com).

$$\Phi = -\frac{\Gamma\theta}{2\pi} \tag{1.23}$$

where $\Gamma$, which is called circulation, is the strength of the vortex.

The singularity element methods use singularities distribution over the wing body and calculates this distribution as the solution of an integral equation [25]. Most of these methods specify a *source* distribution of variable strength (e.g. source-panel models), a *dipole* distribution of variable strength (e.g. doublet-lattice, and doublet-panel methods), or a *vortex* distribution of variable circulation (e.g. vortex-lattice methods, and vortex-panel methods). From the above mentioned methods, doublet-lattice and vortex-lattice methods have been extensively used over the years in the calculation of the aerodynamic loads in potential flows.

An example of discretization using singularity elements is presented in Figure 1.6(a). In this case the singularities are vortex rings used by vortex-lattice and vortex-panel methods [24]. Some typical ring elements are shown in Figure 1.6(b) (where L.E. is wing leading edge, T.E. is wing trailing edge, $U_\infty$ is speed of airflow, $\Gamma$ is circulation around a vortex line, and collocation points are the points where the lift force is calculated).

The purpose of the singularity elements methods is to find the velocity field $\mathbf{V}$ needed in the Bernoulli's equation to calculate the airflow pressure necessary to compute the aerodynamic loads. The Bernoulli's equation in

unsteady form for a point $P$, which belongs to discretized wing (see Figure 1.6b), is given by:

$$\frac{\partial \Phi}{\partial t} + \frac{1}{2}V_P^2 + \frac{p_P}{\rho_P} = \frac{1}{2}U_\infty^2 + \frac{p_\infty}{\rho_\infty} \tag{1.24}$$

where $\Phi$ is the total velocity potential function, $V_P$ is the fluid velocity at point $P$ in the flow, $p$ is the pressure at point $P$, $\rho$ is the fluid density at point $P$, $p_\infty$ is the pressure of the undisturbed airflow, $U_\infty$ is speed of undisturbed airflow. The nonlinearity in the flow is given by the unsteady term $\frac{\partial \Phi}{\partial t}$ and the $\frac{1}{2}V_P^2$ term. Some models drop the unsteady term and linearize the $\frac{1}{2}V_P^2$ term in order to simplify the model.

Next step is to calculate the pressure difference across the airfoil as follows:

$$\Delta p_P = p_{PL} - p_{PU} \tag{1.25}$$

where $p_{PL}$ is the pressure below the wing body and $p_{PU}$ is the pressure above the wing body. The pressures $p_{PL}$ and $p_{PU}$ are calculated using Bernoulli's equation (1.24).

The lift force, $L_P$ (see Figure 1.6b), for a discrete point $P$ is then obtained integrating the pressure as follows:

$$L_P = \Delta p_P \Delta A_P \tag{1.26}$$

where $\Delta A_p$ is the area of the element that encloses $P$. A detailed description of the aerodynamic loads obtained to the unsteady vortex lattice method is given in the Chapter 3.

*1.2.2.2 Vortex Lattice Method*

Early developments of numerical algorithms based on vortex lattice method were done by several authors [26-28]. For example Mook and Maddox [26] modified the vortex lattice method to include the effects of leading-edge separation and this modified method was applied to calculate the aerodynamic loads on high swept delta wings. Asfar, et al. [28] developed a numerical method that predicts the potential flow-field past arbitrary bodies. The method uses a combination of a vortex lattice and sources. For blunt bodies, the method appeared to be superior to either vortex lattice or the sources acting alone while for slender bodies there is no visible advantage comparing to vortex lattice alone, and vortex lattice appears to be superior to the sources.

A general unsteady vortex lattice method was developed by Konstadinopoulos, et al. [29]. The method is an extension of the vortex-lattice technique and is not limited by aspect ratio, camber, or angle of attack, as long as vortex breakdown does not occur above the surface of the wing and separation occurs only along sharp edges. The procedure treats steady flows more efficiently than the specialized steady flow vortex lattice. The comparison with experimental results showed that the developed procedure accurately predicted the aerodynamic loads.

Since then, the general unsteady vortex lattice method was used in many other studies [25, 30-38]. For example, Strganac and Mook [34] coupled the equations of motion of the structure with the governing equations of the fluid obtained by the general unsteady vortex lattice method and treated the fluid and structure as a single system which was integrated by a predictor-corrector algorithm. The results predict simultaneously and interactively the motion of the structure and the fluid in the time domain. Two models were used to demonstrate the technique: a rigid wing on an elastic support and an elastic wing rigidly supported at the root chord. Nuhait and Mook [35] included the steady and unsteady ground effects in the wing modeling. It was found that the aerodynamic coefficients increase near the ground and the ground effect increases when the aspect ratio increases. Also the steady ground effect increases the rolling moment and side force.

Preidikman and Mook [36] found that when the speed is low, the responses to initial disturbances contain many frequencies and decay. As the speed or the angle of attack increases the responses become more organized (energy concentrates around a few frequencies). It appeared that the flutter is a supercritical Hopf bifurcation[6]. At and above the critical flutter speed LCO were encountered. The amplitudes of the LCOs grew as the speed increased. Then LCO experienced a secondary supercritical Hopf bifurcation and become unstable.

[6] Supercritical Hopf bifurcation is characterized by connecting the static equilibria with periodic motion in a branching form as one of the system control parameters reaches a critical value.

Luton and Mook [37] implemented a feedback control system to suppress the flutter. The results showed that the suppression of flutter by means of active control is possible at velocities well beyond the flutter speed and that limit cycle oscillations might exist near flutter speed. To suppress flutter, Hall [38] used a classical linear control strategy based on proportional-integral (PI) feedback and a novel nonlinear controller based on the phenomenon of saturation that exists as a result of a specific internal resonance. It was shown that linear control method provides excellent flutter suppression and probably gust-load alleviation while the nonlinear controller is only effective when the controller is actively tuned to the structural response.

Soviero and Bortolus [39] and Soviero [40] developed a numerical method to calculate the unsteady pressure distribution on harmonically oscillating lifting surfaces in subsonic flow. The method is a generalization of the vortex lattice method applied to a two-dimensional case of a harmonically oscillating plate. The unsteady vortex lattice method is also used in some commercial computer codes such as HESS, VSAERO, QUADPAN, MCAERO, and PAN AIR [25].

*1.2.2.3 Doublet Lattice Method*

The doublet lattice method was the primary method used in industry to predict flutter for the last 30 years. It replaced the modified strip theory [5] which formed the basis for the flutter in the late 1960s. A survey up to 1971 of developments of the vortex- and doublet- lattice methods in steady and oscillatory motion at subsonic speeds was made by Kalman, et al. [41]. A review

of the doublet lattice method as well as the status of the unsteady aerodynamic prediction in industry was made by Yurkovich [42].

An early development of the doublet lattice method was done by Albano and Rodden [43] who obtained approximate solutions for the aerodynamic loads by idealizing the wing surface as a set of lifting elements which are short line segments of acceleration-potential doublets. Load on each element is determined by satisfying the normal velocity boundary condition at a set of points on the surface (normal velocity must be zero at the boundary).

Later, Rodden, et al. [44] modified the doublet lattice method to extend its frequency limits for applications to higher frequency flutter. A hybrid doublet-lattice / double-point method was developed by Eversman and Pitt [45]. The hybrid code handle unequal strip widths and nonparallel intersecting lifting surfaces and increases the computational efficiency in comparison to classical doublet lattice code. Also two quasi-doublet-lattice methods for oscillating thin airfoils in subsonic flow were developed by Ando and Ichikawa [46]. One method contain a special device for a chord-wise logarithmic singularity resulting from the kernel function while the other does not. It was shown the device drastically improves the convergence of the solution.

An application of the doublet lattice method to delta wings was given by van Zyl [47]. A generalization of a doublet lattice method was used by Edwards and Wieseman [48] to calculate the root loci[7] for the wing model for

[7] In control theory, the root locus is the locus of the poles of a transfer function as the system gain is varied on some interval (www.wikipedia.com).

incompressible flow conditions. The scope of this research was to illustrate the nature of the flutter and divergence instabilities.

The sources of the aerodynamic nonlinearities will be discussed in the following paragraph.

*1.2.2.4 Sources of Aerodynamic Nonlinearities*

A good description of aerodynamic nonlinearities was given by Lee, et al., [49]. The aerodynamic nonlinearities are caused by the unsteady forces, wing-tip vortex formation, or flow separation. If the flow is assumed inviscid so the flow separation cannot take place, the presence of shock waves in transonic flow generates unsteady forces that destabilize the airfoil pitching motion and affect the bending-torsional flutter by lowering the flutter speed. Ashley [50] showed that the shock waves have an oscillatory motion in addition to the wing oscillatory motion. Between the motion of the shock wave and the motion of the wing there is a large phase lag. This phase lag is a source of instability. A model of shock wave oscillations is shown in the Figure 1.7.

The aerodynamic nonlinearities associated to the unsteady behavior and wing-tip vortex formation can be modeled by the unsteady vortex lattice method [36]. A detailed description of the unsteady vortex lattice method is given in the Appendix D. An example of the wakes obtained by the vortex lattice method is shown in the Figure 1.8.

When viscosity is taken into account, the flow separation occurs due to shock-boundary layer interaction. In an incompressible flow, only the laminar flow

is present. When the flow separation occurs, turbulence appears. The flow separation results in single DOF flutter, control surface buzz[8] and buffeting[9] [49]. At low speeds, the aerodynamic nonlinearities caused by flow separation are found in dynamic stall. In this case the leading edge separation begins at a certain critical angle of attack. An example of flow separation is revealed in the Figure 1.9 [51]. A wing section under normal flight condition is shown in Figure 1.9(a). As the angle of attack increases (see Figure 1.9(b)), the boundary layer starts to separate. If the angle of attack is increased further, the separation position moves forward as seen in the Figure 1.9(c).

The aerodynamic nonlinearity that arise from stall has been considered in several studies [52-58]. For example Gilliatt et al. [52] found that nonlinear modal interaction of aeroelastic structures can result in the occurrence of internal resonance. As the free stream speed increases the nonlinear solution reveals a LCO close to the initial conditions. For the flow speed at which the aeroelastic frequencies are in 3:1 internal resonance, the root-mean-square amplitude of plunge degree-of-freedom was found to increase. Near 1:1 internal resonance, the response grows without limit. It was also found that for an aeroelastic system with cubic nonlinearity, large response amplitudes were predicted as the system frequencies pass through a 3:1 internal resonance. Abdel-Rahim et.al. [53] and Hwang and Fang [54] studied the stall flutter for a cascade of blades used in turbomachinery. It was found that the flutter of the blade may occur when the

[8] buzz is the noise made by the vibration of the control surface.
[9] buffeting is a succession of blows; continued violence, as of winds or waves (www.hyperdictionary.com)

stall propagation frequency is close to the natural frequency of the blade. The influence of structural nonlinearities in addition to stall was analyzed by Sarkar and Bijl [58]. Period-three oscillations and super-harmonic and quasi-harmonic responses have been reported. Experiments on stall flutter have been reported in [59-61].

An investigation of how a nonlinear aerodynamics can affect the divergence, flutter, and LCO characteristics of a transonic airfoil configuration was made by Thomas et al. [62]. A computational fluid dynamic (CFD) method was used to model the nonlinear steady and unsteady transonic flows. A harmonic balance method in conjunction with the CFD solver was used to determine the aerodynamics for finite amplitude unsteady excitations of a prescribed frequency. The nonlinear aerodynamic effects produced a favorable transonic divergence trend as well as unstable and stable LCO solutions for flutter models.

Yang and Lee [63] performed transonic aeroelastic analyses for a flap of airfoil. For the aerodynamic calculation, the Euler's equations were solved by a finite volume method. The time domain unsteady aerodynamic loads were transformed in the frequency domain using a transient pulse technique. It was found that the flutter region increases as the Mach number increases. Also the instability region increases as the initial flap angle increases (valid for flap angles smaller than $4^{\circ}$).

## 1.3 Structural Modeling

### 1.3.1 TYPES OF STRUCTURAL NONLINEARITIES

Lee, et al., [49] classified structural nonlinearities as distributed governed by electrodynamics deformations that affect the whole structure, or concentrated that act locally and are found in control mechanisms or the connecting parts between wing, pylon, engine or external stores. The distributed nonlinearities can be modeled as cubic spring while concentrated nonlinearities can be modeled as bilinear spring, solid friction, and hysteresis.

Cubic springs can be hardening or softening. A twisted thin wing will behave as a cubic hardening spring that becomes stiffer as the angle of twist increases (Figure 1.10a). The effect of buckling can be approximated by a softening spring whose stiffness decreases when displacement is increased (Figure 1.10b).

Backlash is the most frequent cause for nonlinearity in power-operated and spring-tab systems and it can be modeled as bilinear spring (see Figure 1.11). Backlash induces a flat spot nonlinearity in the force displacement characteristic (Figure 1.11a). If the spring is preloaded, a modified form of the flat spot appears (Figure 1.11b). Solid friction is another type of structural nonlinearity. Hysteresis is encountered if both backlash and friction appears.

### 1.3.2 THE EFFECT OF CONCENTRATED NONLINEARITIES

Concentrated nonlinearity acts locally in control mechanisms or connecting parts between wing and external stores. This nonlinearity results from

backlash in linkage elements of the control system, dry friction in control cable and push rod ducts, kinematic limitation of the control surface deflection, and application of spring tab systems provided for relieving pilot operation. Breitbach [64] determined the flutter boundaries for three different configurations distinguished by different types of nonlinearities in the rudder and aileron control system of a sailplane. The hysteretic damping was found to result in a considerable stabilizing effect and increase of flutter speed. Similar effects of nonlinearities due to friction and backlash on the dynamic behavior of aircraft were reported by De Ferrari et al [65].

The effects of control system nonlinearities, such as actuator force or deflection limits, on the performance of an active flutter suppression system were examined in [66-68]. Reed et al [67] showed that a nonlinear system which is stable with respect to small disturbances may be unstable with respect to large ones. Another important feature was that a store mounted on a pylon with low pitch stiffness can provide a substantial increase in flutter speed and reduce the dependency of flutter on the mass and inertia of stores relative to that of stiff-mounted stores. A detailed review of structural and aerodynamic nonlinearities with more emphasis on concentrated structural nonlinearities is given by Lee et al [49].

Free-play nonlinearity effects have been the subject several studies [69-73]. For example, Laurenson and Trn [71] investigated the flutter of a missile with control surfaces having free-play nonlinearity. At a particular flight speed, the amplitude of oscillation, caused by external excitation, starts to build up. Due to

the presence of free-play nonlinearity in combination with increasing amplitude of oscillation, the effective stiffness of the system increases and the motion becomes stable at some limited amplitude. Kim and Lee [70] found that responses involving LCO and chaotic motion are highly influenced by the pitch-to-plunge frequency ratio in an airfoil with free-play nonlinearity. Experimental studies [73] of a wing model with free-play nonlinearity in pitch showed the appearance of double LCO. Alighanbari [69] studied three-degree-of-freedom airfoil-aileron dynamics with free-play nonlinearity in the aileron hinge moment. Bifurcation analysis indicated various LCO solutions for velocities well below the linear flutter boundary. Depending on the initial conditions and air speed, quasi-periodic and chaotic oscillations were reported for the aileron motion.

A series of papers [74-77] considered the influence of structural non-linearities, represented by free-play and bilinear, on various types of LCO and periodic motions. The subsonic unsteady aerodynamic forces were modeled using the doublet-hybrid method originally proposed by Ueda and Dowell [78]. Zhao and Hu [79] considered similar structural nonlinearities and used unsteady vortex lattice model to predict the LCO of an airfoil section.

### 1.3.3 THE EFFECT OF DISTRIBUTED NONLINEARITIES

The analysis of two-dimensional airfoil with cubic stiffness nonlinearities was conducted in references [80-84]. Lee et al [80] found that the flutter boundary was dependent on the initial conditions for a soft spring, while for a hard spring flutter was independent of initial conditions, and both linear and

nonlinear flutter speeds were identical. Further, LCO was observed for velocities greater than the flutter speed. A jump phenomenon in the pitch amplitude was numerically detected by Lee et al [81], and its location was found to depend on the given initial conditions. A frequency relation was derived by Liu et al [82] who observed that the frequency and amplitude of limit cycle oscillations do not depend on the choice of initial conditions. A secondary bifurcation after the primary Hopf bifurcation was detected by Liu and Dowell [83]. Furthermore, starting from different initial conditions, the motion may jump from one limit cycle to another for different values of fluid flow speeds. A chaotic region was found by Zhao and Yang [84] for certain elastic axis positions, and the chaotic motion appeared only at air flow speed higher than the linear divergent speed.

Price at al [85] studied the response of a two-dimensional airfoil with bilinear and cubic stiffness nonlinearities. LCO with period one was obtained at velocities well below the flutter boundary. In some cases, where the airfoil was subjected to small pre-loads, the motion is chaotic for both bilinear and cubic nonlinearities. This was confirmed for cubic nonlinearity using Lyapunov exponents. Singh and Brenner [86] observed asymmetric LCO for certain values of flow speed and elastic axis location.

A singular perturbation technique based on normal-form method was used to analyze the stability of limit cycles of wing-flap flutter [87-89]. For example, Dessi and Mastroddi [87] analyzed limit-cycle stability reversal via singular perturbation and wing-flap flutter. A three-degree-of-freedom aeroelastic typical section with a trailing-edge control surface was modeled by including nonlinear

springs in torsional stiffness and hinge elastic moment. The numerical analysis revealed the presence of stable and unstable LCOs, along with stability reversal in the neighborhood of Hopf bifurcation. Coller and Chamara [88] investigated the sub-critical and supercritical nature of the flutter Hopf bifurcation of a two-degree-of-freedom system with nonlinear restoring forces. Under certain conditions, the instability gave rise to stable LCOs while for other conditions unstable periodic orbits emerged.

Marzocca et al [90] considered the determination of the sub-critical aeroelastic response and flutter instability of a two-dimensional wing section. The analytical model includes the stiffness and damping nonlinearities in plunging and pitching degrees of freedom. In addition to the aerodynamic loads, an arbitrary time-dependent external pressure pulse was considered. At zero flow speed the plunging amplitudes were found slightly larger than those at the small flow speeds. However, this trend is reversed when the flow speed is further increased and in such case larger amplitudes are experienced near the flutter speed. For the flow speed greater than the flutter speed the response becomes unbounded. Recently, Tang and Dowell [91] examined the influence of geometric structural nonlinear coupling among the bending deflection, chord-wise bending deflection, and twist about the deformed axis on flutter speed and LCO of high-aspect-ratio wings. They found that LCO above and below the perturbation flutter boundary generally occurs over a limited range of flow speed, depending on initial conditions.

A high fidelity tool that accurately predicts LCOs of an aeroelastic system with combined structural and aerodynamic nonlinearities was developed by Sheta, et al., [92]. The aeroelastic computations predicted LCO amplitudes and frequencies in very close agreement with the experimental data. Patil, et al., [93] presented results obtained for LCOs in high-aspect-ratio wings caused by structural and aerodynamic nonlinearities. The analysis was based on geometrically exact structural analysis and finite-state unsteady aerodynamics with stall. The results indicated that stall limits the amplitude of post-flutter unstable oscillations. At speeds below the linear flutter speed, LCOs could be observed if the stable steady state was disturbed by a finite-amplitude disturbance. A critical disturbance magnitude at a given speed and a critical speed at a given disturbance magnitude was required to initiate LCOs. The LCO got more complex with increasing speed. Period doubling was observed at low speeds and as the speed increased the oscillation lost periodicity and become chaotic.

The influence of parameter uncertainties on aeroelastic structures as well as the methods used to solve the systems with parameter uncertainties are shown in the next paragraph.

### 1.4 Systems with Parameter Uncertainties

Recent trends of studying structural mechanics involve randomness. These structures are usually modeled by linear differential equations with random

coefficients. From a mathematic point of view, a system can be modeled by the following equation [94]:

$$\Lambda u = f \tag{1.27}$$

where $\Lambda$ is a stochastic differential operator, e.g. $\Lambda = \left( m\frac{d^2}{dt^2} + c\frac{d}{dt} + k \right)$, where $m$, $c$, $k$ are random variables, $u$ is the random response and $f$ is the excitation which can be deterministic or random. The case of deterministic linear operator $\Lambda$ and random excitation $f$ has been widely studied in the literature (e.g. [95-97]). The case when $\Lambda$ is stochastic is more difficult and only approximate solutions are available. The systems which involve random operators ($\Lambda$) are called systems with parameter uncertainties.

Parameter uncertainties owe their origin to a number of sources, which include

(i) randomness in material properties due to variations in material composition;

(ii) randomness in structural dimensions due to manufacturing variations and thermal effects;

(iii) randomness in boundary conditions due to preload and relaxation variations in mechanical joints;

(iv) randomness of external excitations.

The major tools for analytical and numerical solutions of systems with parameter uncertainties are direct Monte Carlo simulation [98-102], perturbation

method [103-107], and Neumann expansion method [94, 105, 107-110]. These tools when are combined with deterministic finite element method, are called stochastic finite element methods.

Due to the large number of samples which require a high computational time, the Monte Carlo simulation is used mainly to verify other approaches. The perturbation method and Neumann expansion method proved acceptable results for small random variation in the material properties. It was found that the methods are comparable in accuracy but the most efficient solution procedure is the perturbation finite element method which requires a single simulation. However, perturbation methods require the system uncertainty to be small enough to guarantee convergence and accurate results.

### 1.4.1 STOCHASTIC FINITE ELEMENT METHODS

In this section, the Monte Carlo simulation, perturbation method, and Neumann expansion method will be briefly described. The methods are chosen because their popularity and their compatibility with the finite element method. The methods are based on direct operation on the following equation [94]:

$$\left[L(\mathrm{x})+\Pi\left(\alpha(\mathrm{x},\theta),\mathrm{x}\right)\right]u\left(\alpha(\mathrm{x},\theta),\mathrm{x}\right)=f(\mathrm{x},\theta) \tag{1.28}$$

where $L(\mathrm{x})$ is a deterministic differential operator, $\Pi\left(\alpha(\mathrm{x},\theta),\mathrm{x}\right)$ is a differential operator whose coefficients are zero-mean random processes, $\alpha(\mathrm{x},\theta)$ is a zero-mean random process, $\theta$ is a parameter that belongs to the space of random events, and $\mathrm{x}$ is a variable that belongs to the deterministic domain, e.g., $D$.

Equation (1.28) is derived from equation (1.27) under the assumption that the random coefficients which belong to operator $\Lambda$ can be decomposed into a purely deterministic component and a purely random component in the following way [94]:

$$a_k(\mathrm{x},\theta) = \bar{a}_k(\mathrm{x}) + \alpha_k(\mathrm{x},\theta) \tag{1.29}$$

where $a_k$ is a random coefficient which belongs to $\mathbf{\Lambda}$, $\bar{a}_k$ is the mathematical expectation of $a_k$, and $\alpha_k$ is a zero-mean random process with the same covariance function as $a_k$.

Before describing the above mentioned methods, it is necessary to illustrate the Karhunen-Loeve expansion, an expansion of the Fourier type which is utilized to discretize the continuous random field.

*1.4.1.1 Karhunen-Loeve Expansion (K-L)*

In finite element modeling, the uncertainties are usually introduced into the stiffness parameters. These parameters are usually modeled by a Markov[10] random field. One of the major problems of incorporating the random field into finite element analyses is to deal with abstract spaces which have limited physical support [94, 107]. The difficulty involves the treatment of random variables defined on these abstract spaces. Usually the problem is solved by Monte Carlo simulation which requires a large number of points to be sampled.

Another way is to discretize the random field into a series of Fourier type called Karhunen-Loeve expansion.

Let the random field be denoted by the function $\chi(\mathrm{x},\theta)$, where $\theta$ is a parameter that belongs to the space of random events. The random field $\chi(\mathrm{x},\theta)$ can be expressed by the truncated Karhunen-Loeve (K-L) expansion [94]:

$$\chi(\mathrm{x},\theta) = \overline{\chi}(\mathrm{x}) + \sum_{n=1}^{N} \alpha_n(\theta)\sqrt{\lambda_n}\, f_n(\mathrm{x}) \tag{1.30}$$

where $\overline{\chi}(\mathrm{x})$ is the mean value of $\chi(\mathrm{x},\theta)$, $\lambda_n$ is some constant, $f_n(\mathrm{x})$ is a set of deterministic functions, and $\xi_n(\theta)$ is a set of random variables with zero mean and $E\left[\xi_n(\theta)\xi_m(\theta)\right] = \delta_{nm}$, $\delta_{nm}$ is the Kronecker delta. Ghanem and Spanos [94] showed that $\lambda_n$ and $f_n(\mathrm{x})$ are given by the solution of the integral equation

$$\int_D C(\mathrm{x},\mathrm{x}_1) f_n(\mathrm{x}_1) d\mathrm{x}_1 = \lambda_n f_n(\mathrm{x}) \tag{1.31}$$

where $C(\mathrm{x},\mathrm{x}_1)$ is the covariance kernel of the random field $\chi(\mathrm{x},\theta)$.

Ghanem and Spanos [94] and Loeve [111] showed that for a Gaussian process the K-L expansion is convergent. For a one-dimensional Gaussian process, the covariance kernel of the random field $\chi(x,\theta)$ is given by:

$$C(\mathrm{x},\mathrm{x}_1) = \sigma_\chi^2 e^{-|\mathrm{x}-\mathrm{x}_1|/l_{cor}} \tag{1.32}$$

---

[10] A Markov field is characterized by a random spatial structure whose probability at location *n*

where $\sigma_\chi^2$ is the variance of the random field $\chi$, $l_{cor}$ is the correlation length such that $l_{cor} \to L$, and $L$ is the length of the one-dimensional domain which will be discretized. For the case of one-dimensional problem equation (1.31) can be written after introducing equation (1.32) as:

$$\int_{-L/2}^{L/2} \sigma_\chi^2 e^{-|\mathrm{x}-\mathrm{x}_1|/l_{cor}} f_n(\mathrm{x}_1) d\mathrm{x}_1 = \lambda_n f_n(\mathrm{x}) \tag{1.33}$$

Equation (1.33) can be solved analytically for one dimensional case [94]:

$$\int_{-L/2}^{\mathrm{x}} \sigma_\chi^2 e^{-(\mathrm{x}-\mathrm{x}_1)/l_{cor}} f(\mathrm{x}_1) d\mathrm{x}_1 + \int_{\mathrm{x}}^{L/2} \sigma_\chi^2 e^{(\mathrm{x}-\mathrm{x}_1)/l_{cor}} f(\mathrm{x}_1) d\mathrm{x}_1 = \lambda f(\mathrm{x}) \tag{1.34}$$

Differentiating equation (1.34) with respect to $\mathrm{x}$, gives:

$$-\frac{\sigma_\chi^2}{l_{cor}} \int_{-L/2}^{\mathrm{x}} e^{-(\mathrm{x}-\mathrm{x}_1)/l_{cor}} f(\mathrm{x}_1) d\mathrm{x}_1 + \frac{\sigma_\chi^2}{l_{cor}} \int_{\mathrm{x}}^{L/2} e^{(\mathrm{x}-\mathrm{x}_1)/l_{cor}} f(\mathrm{x}_1) d\mathrm{x}_1 = \lambda f'(\mathrm{x}) \tag{1.35}$$

Differentiating equation (1.35) with respect to $\mathrm{x}$, the following equation is obtained:

$$\lambda_n f_n''(\mathrm{x}) + \left( 2\frac{1}{l_{cor}} \sigma_\chi^2 - \frac{1}{l_{cor}^2} \lambda_n \right) f_n(\mathrm{x}) = 0 \tag{1.36}$$

Introducing

---

depends on its state at *n* - 1 regardless of the previous state *n* - 2, *n* - *m*, *m* > 1.

$$\omega^2 = \left( 2\frac{\sigma_\chi^2}{l_{cor}} - \frac{1}{l_{cor}^2}\lambda \right)\frac{1}{\lambda} \tag{1.37}$$

equation (1.36) becomes

$$f''(\mathrm{x}) + \omega^2 f(\mathrm{x}) = 0 \tag{1.38}$$

Evaluating equations (1.34) and (1.35) at $\mathrm{x} = -L/2$, and $\mathrm{x} = L/2$, and rearrange, the boundary conditions for equation (1.38) are obtained:

$$\frac{1}{l_{cor}} f(L/2) + f'(L/2) = 0 \tag{1.39.a}$$

$$\frac{1}{l_{cor}} f(-L/2) - f'(-L/2) = 0 \tag{1.39.b}$$

The solution of equation (1.38) is:

$$f(\mathrm{x}) = a_1 \cos(\omega \mathrm{x}) + a_2 \sin(\omega \mathrm{x}) \tag{1.40}$$

Introducing equation (1.40) into (1.38) and applying the boundary conditions (1.39) the following equations are obtained:

$$a_1\left( \frac{1}{l_{cor}} - \omega \tan\left( \omega \frac{L}{2} \right) \right) + a_2\left( \omega + \frac{1}{l_{cor}} \tan\left( \omega \frac{L}{2} \right) \right) = 0 \tag{1.41.a}$$

$$a_1\left( \frac{1}{l_{cor}} - \omega \tan\left( \omega \frac{L}{2} \right) \right) - a_2\left( \omega + \frac{1}{l_{cor}} \tan\left( \omega \frac{L}{2} \right) \right) = 0 \tag{1.41.b}$$

Setting the determinant to zero the following transcendental equations are obtained:

$$\frac{1}{l_{cor}} - \omega \tan\left(\omega \frac{L}{2}\right) = 0 \,;\; \omega + \frac{1}{l_{cor}} \tan\left(\omega \frac{L}{2}\right) \qquad (1.42.a,b)$$

Denoting the solution of the equation (42.b) by $\omega^*$, the eigenfunctions are:

$$f_n(\mathrm{x}) = \frac{\cos(\omega_n \mathrm{x})}{\sqrt{\frac{L}{2} + \frac{\sin(2\omega_n L/2)}{2\omega_n}}} \,;\; f_n{}^*(\mathrm{x}) = \frac{\sin(\omega_n{}^* \mathrm{x})}{\sqrt{\frac{L}{2} - \frac{\sin(2\omega_n{}^* L/2)}{2\omega_n{}^*}}} \qquad (1.43.a,b)$$

for even $n$ and odd $n$ respectively. The corresponding eigenvalues are:

$$\lambda_n = \frac{2\sigma_\chi^2 / l_{cor}}{\omega_n^2 + 1/l_{cor}^2} \,;\; \lambda_n{}^* = \frac{2\sigma_\chi^2 / l_{cor}}{\omega_n^2{}^* + 1/l_{cor}^2} \qquad (1.44.a,b)$$

for even $n$ and odd $n$ respectively.

Introducing expressions (1.43) and (1.44) into (1.30) the random field takes the form:

$$\chi(\mathrm{x},\theta) = \bar{\chi}(\mathrm{x}) + \sum_{n=1}^{N} 2\alpha_n(\theta)\sigma_\chi \sqrt{\frac{\omega_n / l_{cor}}{\left(\omega_n^2 + 1/l_{cor}^2\right)\left[L\omega_n + \sin(2\omega_n L/2)\right]}} \cos(\omega_n \mathrm{x}) \qquad (1.45)$$

The expression (1.45) is the Karhunen-Loeve expansion for a one-dimensional random field. Next, three best known methods that deal with uncertainty modeling and their integration into finite element analysis, will be described.

*1.4.1.2 Monte Carlo Simulation*

In the absence of analytical solution of the probability density function (PDF) of a given random variable, one has an alternative to use Monte Carlo simulation. The method consists of numerically simulating a population corresponding to the random quantities in the physical problem, solving the deterministic problem associated with each member of that population, and obtaining a population corresponding to the random response quantities. This population can be used to obtain the statistics of the response variables.

The Monte Carlo simulation is a very powerful tool and it is the most accurate. Unfortunately, the method requires very large population so it is very expensive in computational time. It is mainly used to validate other approaches. Monte Carlo simulation involves numerically generating the random process $\alpha_k(x,\theta)$ and $f(x,\theta)$ which appear in equation (1.28) for a fixed value of $\theta$. Equation (1.28) is solved as a deterministic equation, then the procedure is repeated a number of times for different values of $\theta$.

*1.4.1.3 Perturbation Method*

The perturbation method applied in problems that involve random variables is an extension of the method used in nonlinear dynamics [112]. If certain smoothness conditions are fulfilled, the variables and operators can be expanded into Taylor series about their mean values. If a system is modeled by

$r$ random variables and if the excitation is deterministic, then equation (1.28) will be:

$$\left[L(\mathrm{x})+\Pi\left(\alpha(\theta),\mathrm{x}\right)\right]u\left(\alpha(\theta),\mathrm{x}\right)=f(\mathrm{x}) \tag{1.46}$$

Expanding $\Pi$ and $u$ in a Taylor series about their mean values gives:

$$\Pi\left(\alpha(\theta),\mathrm{x}\right)=\sum_{i=1}^{r}\alpha_i(\theta)\frac{\partial}{\partial\alpha_i(\theta)}\Pi\left(\alpha(\theta),\mathrm{x}\right)$$

$$+\sum_{i=1}^{r}\sum_{j=1}^{r}\alpha_i(\theta)\alpha_j(\theta)\frac{\partial^2}{\partial\alpha_i(\theta)\partial\alpha_j(\theta)}\Pi\left(\alpha(\theta),\mathrm{x}\right)+\ldots \tag{1.47a}$$

$$u\left(\alpha(\theta),\mathrm{x}\right)=\bar{u}(\mathrm{x})+\sum_{i=1}^{r}\alpha_i(\theta)\frac{\partial}{\partial\alpha_i(\theta)}u\left(\alpha(\theta),\mathrm{x}\right)$$

$$+\sum_{i=1}^{r}\sum_{j=1}^{r}\alpha_i(\theta)\alpha_j(\theta)\frac{\partial^2}{\partial\alpha_i(\theta)\partial\alpha_j(\theta)}u\left(\alpha(\theta),\mathrm{x}\right)+\ldots \tag{1.47b}$$

Introducing equations (1.47) into equation (1.46) and collecting terms of the same $\alpha_i(\theta)$ order, the following perturbation equations are obtained:

$\alpha_i^0$ order:

$$L(\mathrm{x})\bar{u}(\mathrm{x})=f(\mathrm{x}) \tag{1.48a}$$

$\alpha_i^1$ order:

$$L(\mathrm{x})\left[\frac{\partial}{\partial\alpha_i(\theta)}u\left(\alpha(\theta),\mathrm{x}\right)\right]+\left[\frac{\partial}{\partial\alpha_i(\theta)}\Pi\left(\alpha(\theta),\mathrm{x}\right)\right]\bar{u}(\mathrm{x})=0 \tag{1.48b}$$

Note that in this example only terms up to first order are shown.

Once the solutions of the equations (1.49) are obtained, the response of the process can be written as:

$$u\left(\alpha\left(\theta\right),\mathrm{x}\right)=\overline{u}\left(\mathrm{x}\right)+\sum_{i=1}^{r}\alpha_i\left(\theta\right)\frac{\partial}{\partial\alpha_i\left(\theta\right)}u\left(\alpha\left(\theta\right),\mathrm{x}\right)+\ldots \qquad (1.49)$$

In order to introduce the perturbation method into finite element analysis, either the variational principle or Galerkin method can be used directly on equations (1.48), yielding a sequential system of algebraic equations to be solved for the successive derivatives of the response.

The perturbation method was originally used for static analyses. However, Liu, et al., [106] showed that the perturbation method is suitable for dynamic and nonlinear systems. The advantage of the method is that equations (1.48) need to be solved only once because they do not depend on random variables.

Because the perturbation method uses the Taylor series expansion, its accuracy decreases with the increase of level of uncertainty. Improved accuracy will be obtained if the K-L expansion is used to expand the operator $\Pi$ [113]. This method will be further discussed in the Chapter 3.

*1.4.1.4 Neumann Expansion Method*

The Neumann expansion method is based on the assumption that equation (1.28) can be solved by computing the inverse of a given operator. It is known that when it exists, the inverse of an operator can be expanded into a

convergent series in terms of iterated kernels [94, 114]. The theory was developed by Neumann and further studied by Fredholm [115]. Further extension of the theory which includes the concept of generalized inverse [116], was applied to the solution of stochastic operator equations by Bharrucha-Reid [117]. The concept was later improved by Adomian [118] and Adomian and Malakin [110]. The concept was purely theoretical until Shinozouka and Nomoto [109] introduced the concept into structural mechanics. The Neumann expansion method consists of expressing the solution of equation (1.28) in the series form [94]:

$$u\left(\alpha(\theta),\mathrm{x}\right)=\sum_{i=0}^{\infty}(-1)^{i}\left[L^{-1}(\mathrm{x})\Pi\left(\alpha(\mathrm{x},\theta),\mathrm{x}\right)\right]^{i} f(\mathrm{x},\theta) \tag{1.50}$$

Series (1.50) is convergent if satisfies the following condition:

$$\left\|L^{-1}(\mathrm{x})\Pi\left(\alpha(\mathrm{x},\theta),\mathrm{x}\right)\right\|<1 \tag{1.51}$$

Note that the inclusion of higher order terms, even the second order terms, in the expansion implies cumbersome algebraic manipulation. In order to obtain more accurate results, Yamazaki et al. [119] suggested to apply a Monte Carlo simulation to equation (1.50). With this implementation, only the deterministic operator $L$ needs to be inverted. However, the method requires several runs in order to obtain reliable results. Because the deterministic operator needs to be inverted the method is applicable only on linear systems.

### 1.4.2 NONLINEAR AEROELASTIC MODELS WITH PARAMETER UNCERTAINTIES

Some recent results on the sensitivity and variability of the response and eigenvalues of structural stochasticity have been reviewed by Ibrahim [120] and Manohar and Ibrahim [121]. These reviews showed that the early developments relied on Monte Carlo simulation and later on first- and second-order perturbation methods to compute second-order moments of structure response. Furthermore, these reviews focused on the results pertaining to parametric approaches. On the other hand, non-parametric approaches, based on the use of the maximum entropy principle [122] were considered by Soize [123-127] for modeling random uncertainties in linear and nonlinear elasto-dynamics in the low frequency range. Soize [125] introduced a new ensemble of random matrices constituted of symmetric positive-definite real random matrices.

Regarding the randomness in boundary conditions due to preload and relaxation variations in mechanical joints, Ibrahim and Pettit [128] presented an assessment of dynamic problems associated with joint relaxation and uncertainties. Fasteners and joints subjected to vibration often lose much of their preload; this is known as relaxation. First there is a slow loss of pre-load caused by some of the relaxation mechanisms. Vibration increases relaxation because wear and hammering take place during vibration. Vibration-induced loosening and relaxation effects cause time-dependent boundary conditions and depend on the level of structural vibration.

Perturbation stochastic finite element method (SFEM) has been adopted by Nieuwenhof and Coyette [113] using the K-L expansion to discretize random fields arising from structure mechanical properties. An alternative method for the dynamic analysis of linear structural systems with parameter uncertainties subjected to either deterministic or random excitation was developed by Jensen [129]. His method was an extension of the deterministic finite element method to the space of random function. A Neumann dynamic SFEM of vibration for structures with stochastic parameters to random excitation was described by Lei and Chen [130]. The equation of motion was transformed into quasi-static equilibrium equation for the solution of displacement in the time domain. Neumann expansion method was applied to the equation for deriving the statistical solution of the dynamic response within the framework of Monte Carlo simulation.

Free vibration and reliability of composite cantilever beams featuring uncertain properties was analyzed by Oh and Librescu [131]. Klosner et al. [132] studied the influence of uncertainty of stiffness nonlinearity of Duffing oscillator and two coupled Duffing oscillators on the response statistics using equivalent linearization technique and Monte Carlo simulation. It was found that the response variances are essentially independent of the variances of the random parameters. The variance errors were found to decrease with increasing parameter variances.

Structural and material uncertainties have a direct impact on the flutter characteristics of aeroelastic structures and they have attracted some attention in

the literature. They were considered in studying the flutter of panels and shells by several authors [133-137]. Liaw and Yang [133, 134] quantified the effect of parameter uncertainties on the reduction of the structural reliability and stability boundaries of initially compressed laminated plates and shells. For buckling analysis, the uncertainties were included in the modulus of elasticity, thickness, and fiber orientation of individual lamina, as well as geometric imperfections. For flutter analysis, further uncertainties such as mass density, air density, and in-plane load were also considered. Kuttenkeuler and Ringertz [135] performed an optimization study of the onset of flutter, with respect to material and structural uncertainties, using finite element analysis and the doublet-lattice method. Lindsley et al. [136, 137] considered uncertainties in the modulus of elasticity and boundary conditions for a nonlinear panel in supersonic flow. The probabilistic response distributions were obtained using Monte Carlo simulation. It was observed that uncertainties have the greatest nonlinear influence on limit cycle oscillation (LCO) amplitude near the deterministic point of LCO.

Recently, Pettit and Beran [138, 139], Ueda [140], and Attar and Dowell [141] considered the influence of parameter uncertainties on the aeroelastic response of typical airfoil sections. The effect of parametric uncertainty on the response of a nonlinear aeroelastic system was studied by Attar and Dowell [141] using a response surface method to map the random input parameters to the root-mean square wing tip response.

Ostenfeld-Rosenthal, et al. [142], Ge, et al. [143], and Jakobsen and Tanaka [144] considered the influence of uncertainties of structural properties (in

particular damping) on the reliability analysis of flutter of the bridge girder and a flat plate. The prediction of the flutter wind speed was found to be associated with a number of uncertainties such that the critical wind speed can be treated as a stochastic variable. The probability of the bridge failure due to flutter was defined as the probability of the flutter speed exceeding the extreme wind speed at the bridge site for a given period of time.

A ground vibration test was used by Potter and Lind [145] to obtain uncertainty models, such as natural frequencies and their associated variations, which can update analytical models for the purpose of predicting robust flutter speeds. Different norm approaches were used to formulate uncertainty models that cover the entire range of observed variations. It was found that the $\infty - \text{norm}$ produces the smallest uncertainty and the least conservative robust flutter speed. Lind and Brenner [146] introduced a tool referred to as the “flutterometer” for predicting the onset of flutter during a flight test. The flutterometer computes a flutter for an analytical model with respect to an uncertainty description. Brenner [147] considered a technique that identifies model parameters and their associated variances from flight data. Later, Prazenica, et al. [148] introduced a technique for estimating uncertainty descriptions based on a wavelet approach, but relies on Volterra kernels.

An adaptive control of a supersonic airfoil with flap was proposed by Rao, et al. [149]. The control objective is to stabilize the pitch angle while adaptively compensating for uncertainties in all of the aeroelastic model parameters. It was shown that all the states of the closed-loop system are asymptotically stable.

Reddy, et al. [150] described a probabilistic approach for aeroelastic analysis of turbo-machinery blade rows. The analysis accounts for uncertainties in structural and aerodynamic design variables. The results showed that the probabilistic approach provides a more realistic way to assess the effect of design variables on the aeroelastic instability.

Next paragraph includes a review of stabilization of mechanical systems in the presence of parametric excitation.

### 1.5 Stabilization of Unstable Systems via Parametric Excitation

Stabilization of unstable systems using deterministic or random parametric excitation, in the absence of feedback control, has been extensively studied in different mechanical, chemical, optical, or neuroscience models. A recent detailed review about systems stabilized via parametric excitation as well as noise-enhanced stability is documented by Ibrahim [151, 152]. The purpose of this section is to present a review of the main results reported in the literature. This review is valuable in interpreting and understanding the influence of parametric excitation on the system considered in the present study. With reference to aeroelastic structures only few studies have been reported in the literature. On the other hand, the inverted pendulum has received extensive analytical and experimental studies.

### 1.5.1 STABILIZATION EVIDENCE IN AEROELASTIC STRUCTURES

Parametric excitation of aeroelastic structures has been considered for a limited number of studies [153-156]. For example, Lumbantobing and Haaker [153] considered the parametric excitation of two one-degree-of-freedom nonlinear aeroelastic oscillators in cross-flow. A nonlinear Mathieu equation describes the motion of the oscillators. The origin of nonlinearity is the dependence on the flow angle of attack. In the absence of parametric excitation, there is a critical wind speed above which the system exhibits periodic oscillations. It was found that by increasing the air flow speed above the critical value the equilibrium position is re-stabilized. However, if the parametric excitation is due to longitudinal turbulence, the frequency of coalescence occurs at a lower air flow speed [151, 157, 158]. Chin, et al., [154, 155] obtained the modulated equations of a simply supported panel in a supersonic flow to calculate the equilibrium solutions and their stability. In the neighborhood of combination parametric resonance, they identified the excitation parameters that suppress flutter and those that lead to complex motions. A general solution for dynamic stability of the fluttered systems subjected to parametric random excitations was proposed by Young, et al., [156]. The numerical results showed that a beam or a panel in the flutter mode remain stable in the sense of asymptotic sample stability due to white noise excitation.

### 1.5.2. STABILIZATION OF THE INVERTED PENDULUM

The stabilization of mechanical systems using parametric excitation was first time observed by Stephenson [159] on an inverted pendulum. A schematic diagram of an inverted pendulum is shown in Figure 1.12. The equation of motion for this system written in standard Mathieu form is [151]:

$$\theta'' + (\alpha + \beta \cos \tau)\theta = 0 \tag{1.52}$$

where $\theta$ is the angle measured from the vertical upward position, prime denotes differentiation with respect to the non-dimensional time $\tau = \Omega t$, $\alpha = -\omega_n^2 / \Omega^2$, $\beta = -Z_0 \omega_n^2 / g$, $Z_0$ is the amplitude of the support excitation, $\Omega$ is the frequency of the excitation, $\omega_n$ is the natural frequency of the system, and $g$ represents the gravitational acceleration.

Stephenson [159] showed that the inverted pendulum can be stabilized by applying the following parametric excitation:

$$z(t) = Z_0 \cos \Omega t \tag{1.53}$$

with sufficiently small amplitude and sufficiently high frequency, i.e.,

$$\Omega > \sqrt{2g\ell} / Z_0 \tag{1.54}$$

where $\ell$ is the pendulum length. However, later studies [160] revealed that the inverted state can be stabilized with lower excitation frequency and larger excitation amplitude provided that these lie within the stability region. Different

versions of inverted pendulum were analyzed in [161-166]. The studies demonstrated that the pendulum becomes unstable on upward acceleration of its support while the stability state is obtained on downward acceleration. Depending on the physical parameters, the periodic exchange between the two situations the system can be globally stable or unstable [151].

Experimental work involving stabilization of inverted pendulum was done in [167-169]. The influence of the tilt of the excitation from the gravity direction on the stabilization of the inverted pendulum has been the subject of analytical and experimental studies [170-172]. It was discovered that the angle of inclination of the pendulum in the stable position differs from the angle of parametric excitation. However, if the excitation frequency increases then both angles approach each other. A pendulum with bilinear hysteresis was studied by Tso [173] who found that bilinear hysteresis limits the growth of the amplitude response during parametric resonance.

Stabilization of a double pendulum with linear viscoelastic joints was considered by Agafonov [174, 175] and Agafonov and Shcheglov [176]. It was found that small dissipation can destabilize the system. Also the stabilization is effective at high frequency. Studies involving a chain of inverted pendulums have been done by Otterbein [177] and Acheson [160, 178]. Acheson [178] used modal analysis to find the stability of N inverted pendulums modeled by N uncoupled Mathieu equations with different parameters. If the frequency for each mode is chosen sufficiently high and amplitude sufficiently small, the chain can be stabilized by parametric excitation. The numerical simulation [178] and

experimental tests [179] for two and three pendulums showed that the stability is remarkably robust even to quite large disturbances.

The limiting case for a chain on inverted pendulums, $N \to \infty$, was used by Hurst [180] as a possible explanation of the "*Indian rope trick*" [11] (see Figure 1.13). Unfortunately they found that the stable region is insignificant, and the explanation fails. However, experiments done by Acheson [160] and Acheson and Mullin [181] showed that a piece of "bending curtain wire" clamped at the bottom and free at the top, can be stabilized by the parametric excitation. This phenomenon was called by Galán et al. [182] the "Indian rod trick".

Galán, et al., [182] proposed a discrete model in which small amounts of damped elastic constraints were added to the bottom joint and the joints between N identical pendulums. In the limit, $N \to \infty$, the system approaches the case of a continuously flexible rod after including realistic material damping. Their analysis revealed that damping has the effect of removing most of instability regions for fixed amplitude of parametric excitation. The shape of instability curves and mode shapes of the corresponding instabilities were found in agreement with those of an experiment on curtain wire.

### 1.6 Scope of the Present Research

This chapter provides an overview of the work published in the literature pertaining to stabilization of aeroelastic structures and systems with parametric

[11] This legend involves an Indian magician who throws a rope to the sky, but the rope does not fall back to the ground. Instead it mysteriously rises until the top disappears into thin air. Unfortunately, this claim has never been substantiated.

uncertainties. These results include the stabilization of the initially unstable systems in the absence of feedback control which has been studied for several years on inverted pendulum or a chain of inverted pendulums. Few other systems have also been consulted. However, to the best of my knowledge, the role of parametric excitation on the stabilization of the aeroelastic structures has not yet been well understood. In aeroelasticity the most common way to suppress flutter is active feedback control.

Furthermore, the present Chapter has also presented various models of aeroelastic structures that involve nonlinearities and parameter uncertainties. To the best of my knowledge very few papers considered the effect of both nonlinearities and uncertainties in aeroelastic systems and most of them were formulated for plates at supersonic flow speeds. Furthermore, few studies considered perturbation method to model an aeroelastic wing in the presence of parameter uncertainties. The implementation of perturbation method has been considered a very important tool because it is very cheap in computational time and requires only a single simulation.

However, these results do not address other issues which are considered in the present work. The main objectives of the present research are:

- To investigate the role of parametric excitation on the flutter behavior of a cantilever beam. This task will explore the possibility of suppressing flutter of a cantilever wing via parametric excitation in the neighborhood of combination parametric resonance of summed-type. This type of excitation owes its origin to a possible longitudinal vibration of aircraft

engines. The sources of nonlinearities are due to the small in-plane displacement and nonlinear curvature. This task is completely developed in Chapter 2.

- To develope a numerical algorithm to study the influence of stiffness uncertainties on the flutter behavior of an aeroelastic wing. The numerical algorithm originally developed by Predikman and Mook [36] will be adopted. This algorithm has been originally developed to simulate unsteady, nonlinear, incompressible flow interacting with linear aeroelastic wing in the absence of uncertainties. The uncertainties in the structure are modeled using a modified first order stochastic perturbation method together with a truncated Karhunen-Loeve expansion instead of Taylor series. The method was developed by Nieuwenhof and Coyette [113] and it was used for a linear dynamic system which was analyzed in frequency domain. The method has never been used in time domain and for an aeroelastic system. However, the Taylor series is used for displacement vector expansion. The perturbation method will be integrated into a finite element method in order to model the wing structure. The air flow and wing structure will be treated as elements of a single dynamic system. Next the perturbation stochastic method will be compared to Monte Carlo simulation. Chapter 3 presents the modeling of the system and the results of the two approaches.

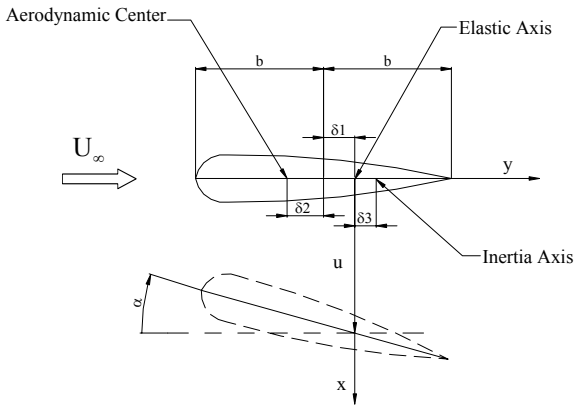


Figure 1.1. Schematic diagram showing a two-dimensional analytical airfoil model

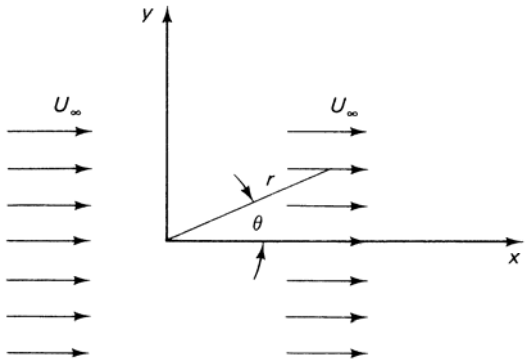


Figure 1.2. Streamlines for a uniform flow parallel to the x-axis [23]

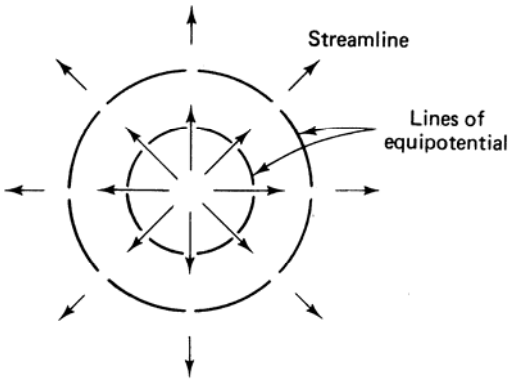


Figure 1.3. Equipotential lines and streamlines for flow from a two-dimensional source [23]

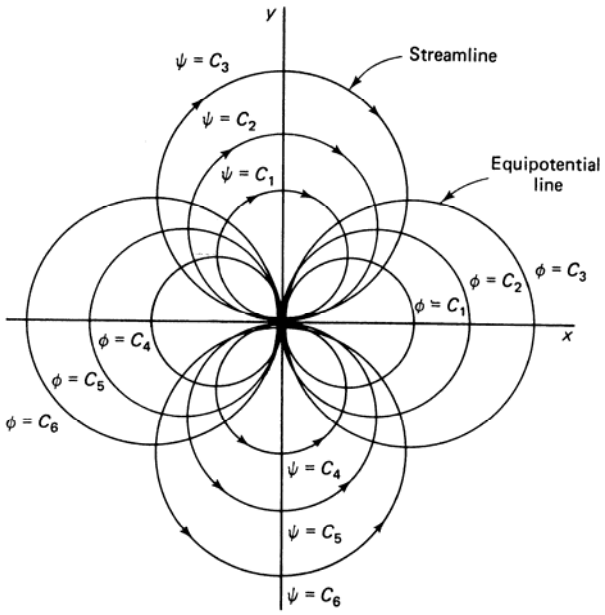


Figure 1.4. Equipotential lines and streamlines for a doublet [23]

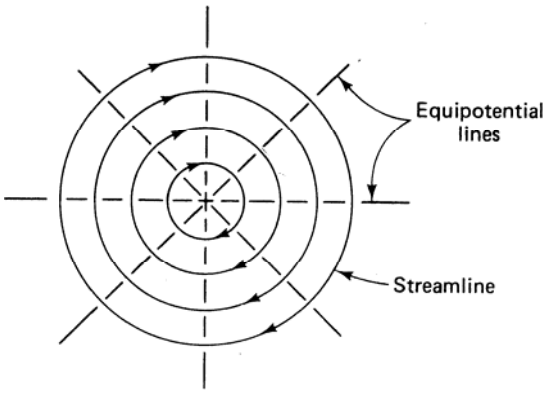


Figure 1.5. Equipotential lines and streamlines for a potential vortex [23]

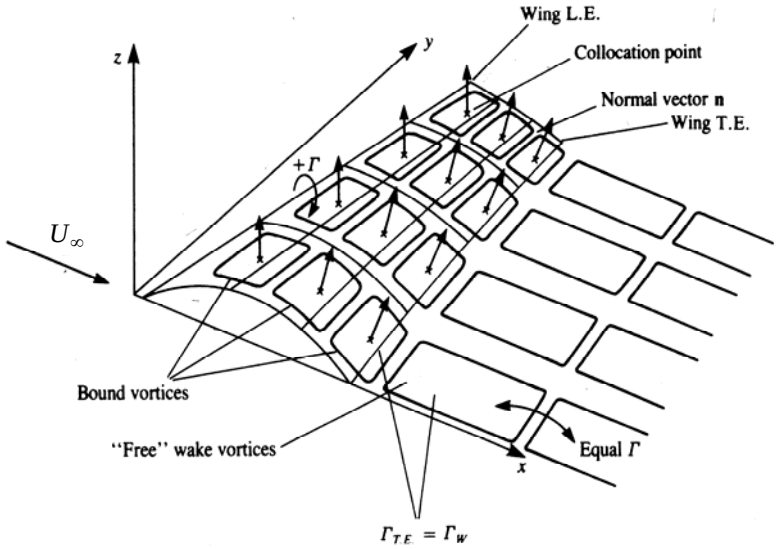


(a)

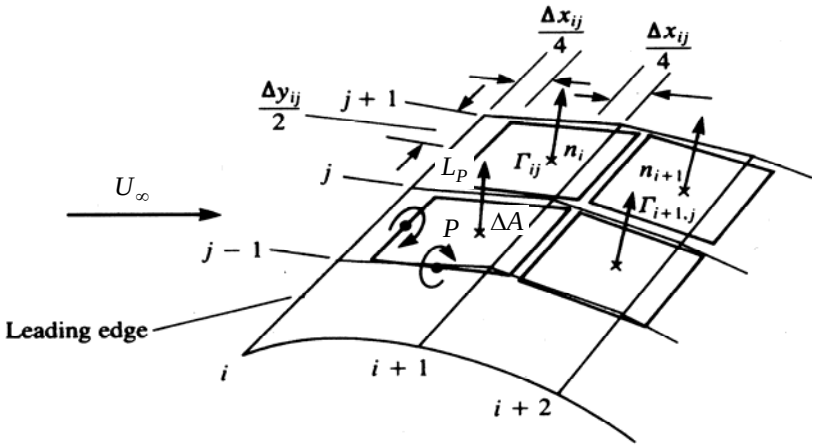


(b)

Figure 1.6. Vortex ring model for a thin lifting surface [24]

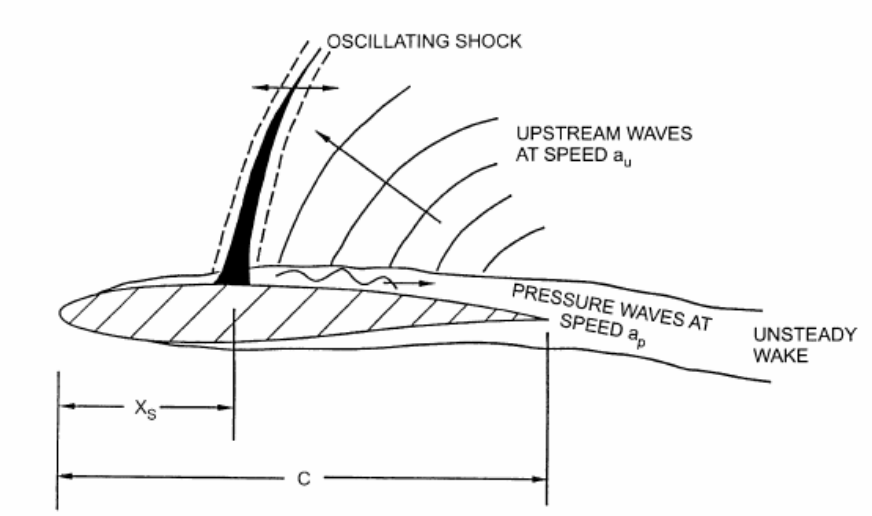


Figure 1.7. Model of self-sustained shock oscillations [49, 183]

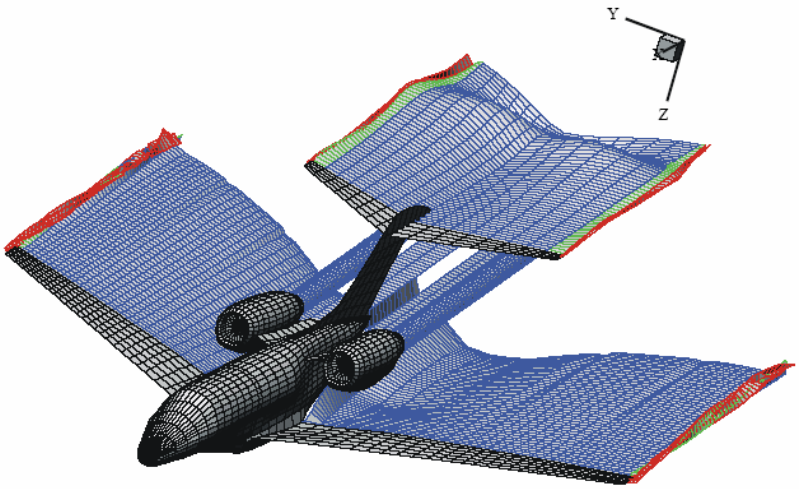


Figure 1.8. A 3D representation of the computed wakes using the unsteady vortex lattice method [25]

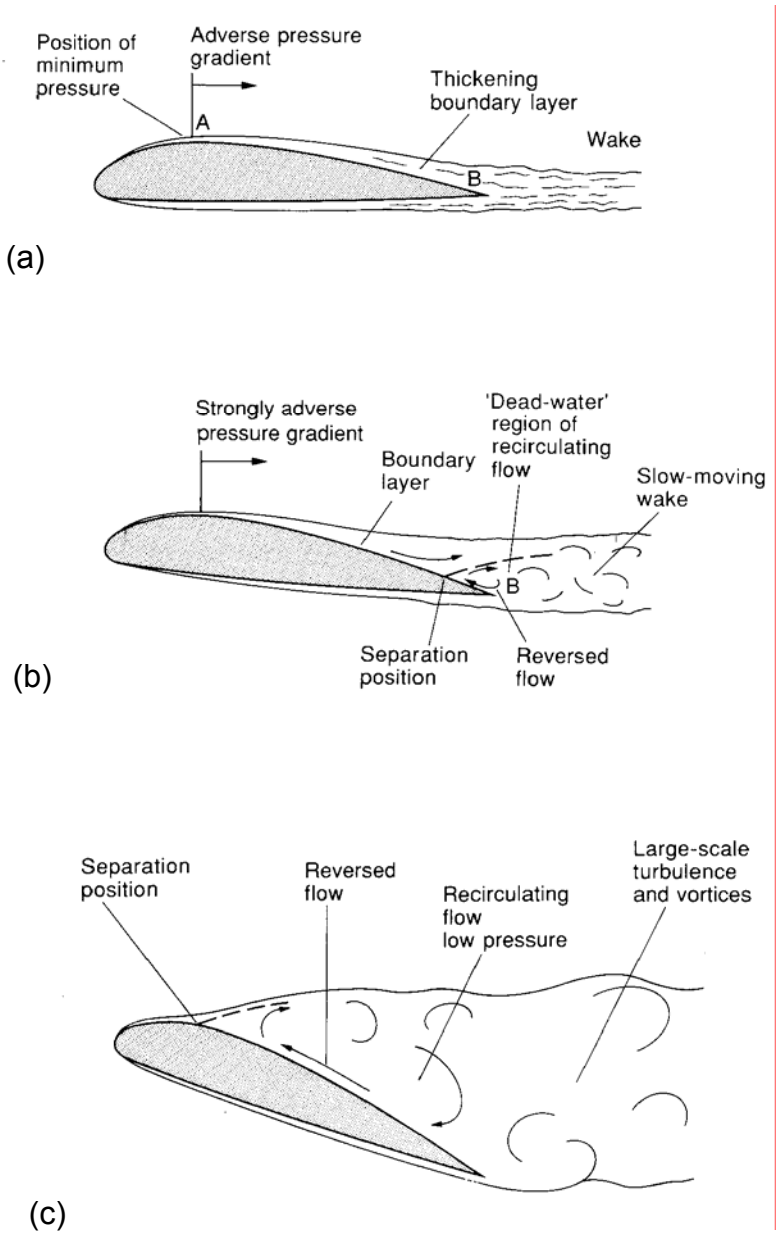


Figure 1.9. Boundary layer separation [51].

(a) At low angles of attack, the boundary layer leaves as a wake at the trailing edge; (b) At higher angles of attack, the boundary layer on the upper surface separates; (c) As the angle of attack increases, the separation position moves forward.

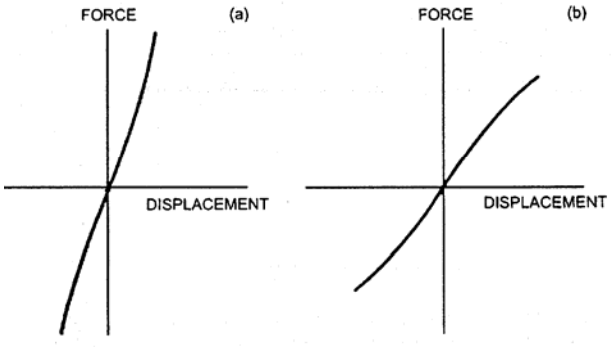


Figure 1. 10. Force versus displacement curve for

a) cubic hardening spring, b) cubic softening spring [49]

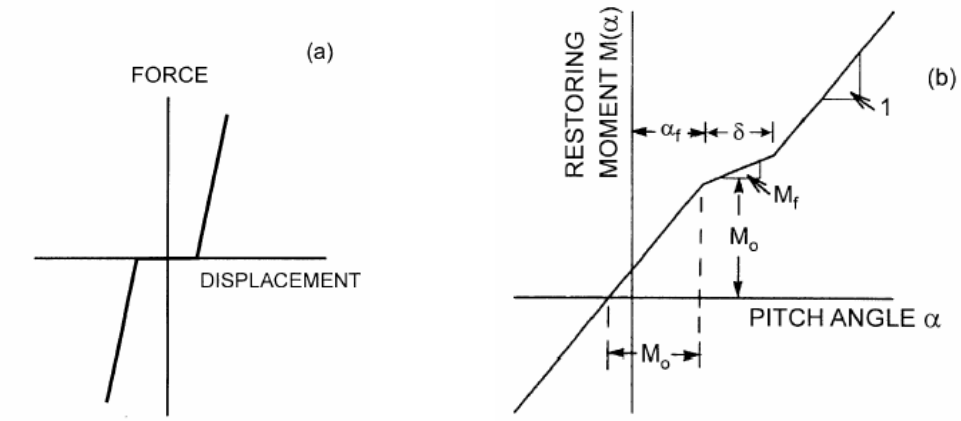


Figure 1.11. Force vs. Displacement: (a) flat spot without preload; (b) general bilinear spring [49]

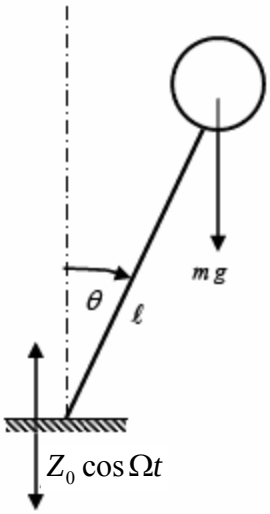


Figure 1.12. Inverted pendulum under parametric excitation [151]

Figure 1.13. Indian rope trick

# CHAPTER 2

# FLUTTER SUPPRESSION OF A PLATE-LIKE WING VIA PARAMETRIC EXCITATION

## 2.1 Introduction

The purpose of the present study is to explore the possibility of suppressing flutter of a cantilever wing via parametric excitation in the neighborhood of combination parametric resonance of summed-type. The excitation of the clamped end is applied in the plane of largest rigidity such that the bending and torsion modes are cross-coupled through the excitation. This type of excitation owes its origin to a possible longitudinal vibration of aircraft engines. The sources of nonlinearities are due to the small in-plane displacement and nonlinear curvature. Section 2.2 deals with developing the analytical modeling of the nonlinear wing under aerodynamic loading. The aerodynamic lift and moment are modeled based on Theodorsen's theory and the equations of motion are developed using Hamilton's principle. The reference axis is taken to pass through the elastic axis of the wing. This will result in a linear coupling in the equations of motion in addition to the inherent nonlinear coupling. Thus the equations of motion differ from those derived by Ibrahim and Hijawi [184] due to the presence of linear coupling and aerodynamic loading. Section 2.3 presents a linear analysis of the system normal modes and parametric stability boundaries in the absence and presence of airflow at the flutter speed. In the absence of aerodynamic forces, the response dynamic behavior is determined using multiple

scales method in the neighborhood of combination resonance. The parametric excitation at the critical flutter speed and at slightly higher value than the flutter speed is considered in Section 2.4. Section 2.5 presents numerical simulation of the original coupled bending and torsion equations of motion of the wing. It is interesting to find out that the parametric excitation results in stabilization of the flutter wing when the excitation amplitude exceeds a critical value.

Lindner, et al., [185] presented an assessment of the dynamic behavior of some specific models driven by Gaussian white noise. The systems considered possess a single stable rest state which can be simply an equilibrium (or fixed) point or a small-amplitude (sub-threshold) limit cycle. The large excursions of the system's variables produced by strong enough perturbations of this state are often called spikes, and their occurrence is referred as a "*firing*". This terminology is borrowed from neuroscience and the associated scenarios are well described in reference [185]. In neuroscience, the electrical discharge of a nerve cell's membrane potential is commonly called an action potential or a firing of a spike. The generation of a spike is considered as a one-way passage through a sequence of stable and unstable states. The resting state, being dynamically stable, can be left only by a sufficiently strong external excitation. The *firing* and the following *refractory* (recovery) states are unstable in the sense that the system escapes from them even in the absence of external excitations. While the escape from the resting state strongly depends on the external input, the passage through the firing and refractory states possesses only a weak dependence on the external excitation.

Since the occurrence of stable spiking trajectories requires a dynamical system close to a bifurcation toward a limit cycle regime, the system must possess at least two variables obeying a nonlinear dynamics. Models exhibiting this property were first proposed for neuronal spike generation [186-188]. In these models a fast variable is driven by an external excitation above a threshold level. After that it keeps growing and approaching a second metastable state due to a nonlinear dynamics: the system is excited, i.e., in the firing state. Another variable, a recovery variable, acting on a slower time scale, destabilizes the excited state of the fast voltage variable, bringing it back to its rest state by means of negative feedback. When the recovery variable relaxes, the initial state is reestablished. The *firing* and the following *refractory* states where encountered in the present work at the airflow speed slightly higher than the flutter speed.

The main results of this chapter have been published in reference [189].

## 2.2 Analytical Modeling of a Plate-Like Wing

Consider a cantilever wing having a straight elastic axis, $z$, perpendicular to the fuselage as shown in Figure 2.1(a). The wing deformation can be measured by the bending deflection, $u(z,t)$, and torsional angle, $\alpha(z,t)$, about the elastic axis. The displacements of the elastic axis along $y$, and $z$ axes are $\mathrm{v}(z,t)$ and $w(z,t)$, respectively. The deflection, $u(z,t)$, is considered positive downward and $\alpha(z,t)$ is positive when the leading edge is up (clockwise). The chord-wise distortion will be neglected. The airfoil is exposed to an incompressible fluid flow of speed $U_\infty$. Figure 2.1(b) shows the projections of the

model where $b$ is half of the chord, $\delta_1$ is the distance between the elastic axis and mid-chord, $\delta_2$ is the distance between the aerodynamic center and mid-chord, and $\delta_3$ is the distance between the elastic and inertia axes.

The cantilever wing is modeled as a plate-like beam subjected to periodic base excitation, $Y(t)$, in the plane of largest rigidity and involves nonlinear coupling between bending and torsion modes. This coupling arises mainly from the fact that the centers of mass of cross-sections undergo a small but important displacement, $\mathrm{v}$, in the plane of excitation. This displacement is measured in terms of the second-order of the fundamental bending, $u$, and torsion, $\alpha$, displacements. Under an initial bending displacement, $\Delta u$, with a slight twist, $\alpha$, of the beam cross-section, there will be an inevitable very small displacement $\Delta \mathrm{v} << \Delta u$ associated with these displacements. When the beam is released from this state, the inertia force acting through the bending displacement, $u(z,t)$, will give a torque to the beam cross-section. Similarly, because of the small rotation of the principal planes of the cross-section, the inertia force contributes a bending moment about the local plane of minimum bending stiffness proportional to the twist angle, $\alpha$. The bending-torsion coupling of the wing can be realized by considering the curvatures, $\kappa_x$, $\kappa_y$, and $\kappa_z$ about $x$, $y$, and $z-$axes, [190],

$$\kappa_x = -\frac{\partial^2 \mathrm{v}}{\partial z^2} + \frac{\partial^2 u}{\partial z^2}\alpha, \quad \kappa_y = \frac{\partial^2 \mathrm{v}}{\partial z^2}\alpha + \frac{\partial^2 u}{\partial z^2}, \quad \kappa_z = -\frac{\partial \alpha}{\partial z} + \frac{\partial \mathrm{v}}{\partial z}\frac{\partial^2 u}{\partial z^2} \tag{2.1}$$

Note that the curvature $\kappa_x$ is very small and can be set to zero and thus one can write

$$\frac{\partial^2 \mathrm{v}}{\partial z^2} = \frac{\partial^2 u}{\partial z^2}\alpha \tag{2.2}$$

This relationship represents the projection of the curvature of the beam in the plane Oxz on the Oy-axis, which gives the curvature in the plane Oyz, see Figure 2.1. It is clear that the displacement $\mathrm{v}$ can be expressed in terms of $u$ and $\alpha$ through double integration of relation (2.2). Furthermore, one can approximate the curvature about z-axis by the linear relationship $\kappa_z = -\partial\alpha/\partial z$. Neglecting the extension of the beam elastic axis, the lateral displacement, $\mathrm{v}(z,t)$, and axial drop, $w(z,t)$, may be expressed in terms of the bending deflection and the twist angle in the form:

$$\mathrm{v}(z,t) = \int_0^z (l-\xi)\frac{\partial^2 u(\xi,t)}{\partial \xi^2}\alpha d\xi \tag{2.3}$$

$$w(z,t) = \int_0^z \frac{1}{2}\left(\frac{\partial u(\xi,t)}{\partial \xi}\right)^2 d\xi \tag{2.4}$$

The kinetic energy is:

$$T = \frac{1}{2}\iiint \rho\left[\left(\frac{\partial u}{\partial t} + \delta_3\frac{\partial \alpha}{\partial t}\right)^2 + \left(\frac{\partial w}{\partial t}\right)^2 + \left(\frac{\partial \mathrm{v}}{\partial t} + \frac{\partial Y}{\partial t}\right)^2\right] dxdydz + \frac{1}{2}\int_0^l I_0\left(\frac{\partial \alpha}{\partial t}\right)^2 dz \tag{2.5}$$

where, $\rho$ is the wing density, $I_0$ is the mass moment of inertia (about the inertia axis) per unit length and $l$ is the wing length. The strain potential energy due to bending and torsion is

$$V = \frac{1}{2}EI\int_0^l \left\{\frac{\partial^2 u}{\partial z^2}\left[1+\left(\frac{\partial u}{\partial z}\right)^2\right]\right\}^2 dz + \frac{1}{2}cGJ\int_0^l \left(\frac{\partial \alpha}{\partial z}\right)^2 dz \tag{2.6}$$

where $E$ is Young's modulus, $I$ is the area moment of inertia of the wing cross-section about $y$ axis, $J$ is the polar moment of inertia of the wing cross-section about $z$ axis, $G$ is the modulus of rigidity, and $c$ is a correction constant due to the noncircular cross-section of the wing. The curvature will be expressed up to cubic order.

For incompressible flow, the aerodynamic lift per unit span is obtained based on Theodorsen's theory [9] in the form

$$L = 2\pi\rho_\infty U_\infty bB(k)\left[U_\infty\alpha + \frac{\partial u}{\partial t} + b\left(\frac{1}{2}-a\right)\frac{\partial\alpha}{\partial t}\right] + \pi\rho_\infty b^2\left(\frac{\partial^2 u}{\partial t^2} - ba\frac{\partial^2\alpha}{\partial t^2}\right) + \pi\rho_\infty b^2 U_\infty\frac{\partial\alpha}{\partial t} \tag{2.7}$$

The aerodynamic moment about the elastic axis, $z$, per unit span is

$$M = 2\pi\rho_\infty U_\infty b^2\left(\frac{1}{2}+a\right)B(k)\left(U_\infty\alpha + \frac{\partial u}{\partial t} + b\left(\frac{1}{2}-a\right)\frac{\partial\alpha}{\partial t}\right) +$$

$$+\pi\rho_\infty ab^3\left(\frac{\partial^2 u}{\partial t^2} - ba\frac{\partial^2\alpha}{\partial t^2}\right) - \left(\frac{1}{2}-a\right)\pi\rho_\infty b^3 U_\infty\frac{\partial\alpha}{\partial t} - \frac{\pi\rho_\infty b^4}{8}\frac{\partial^2\alpha}{\partial t^2} \tag{2.8}$$

where $\rho_\infty$ is the air density, $a = \delta_1 / b$, $B(k)$ is the circulation function, which depends on the reduced frequency parameter, $k = b\omega / U_\infty$, $\omega$ is the natural frequency of the wing coupled modes and will be determined later. The circulation function is a complex quantity represented by [4, 11]:

$$B(k) = F(k) + iG(k) \tag{2.9}$$

where $F(k)$ and $G(k)$ are given by the following expression [11]:

$$F(k) = 1 - \frac{0.165k^2}{k^2+0.00207} - \frac{0.335k^2}{k^2+0.09},\quad G(k) = -\frac{8.837\times10^{-4}k + 0.108k^3}{1.863\times10^{-4} + 9.207\times10^{-2}k^2 + k^4}$$

Applying Hamilton's principle

$$\int_{t_0}^{t_1}\delta(T-V)\,dt+\int_{t_0}^{t_1}\left[-\int_0^l L\delta u\,dz+\int_0^l M\,\delta\alpha\,dz\right]dt=0 \tag{2.10}$$

and carrying out the variational process, gives the equations of motion and associated boundary conditions:

$$-m\frac{\partial^2 u}{\partial t^2}-m\delta_3\frac{\partial^2\alpha}{\partial t^2}-m\left[\frac{\partial u}{\partial z}\frac{\partial^2}{\partial t^2}\left(\int_0^z\frac{1}{2}\left(\frac{\partial u}{\partial\xi}\right)^2 d\xi\right)-\frac{\partial^2 u}{\partial z^2}\int_z^l\frac{\partial^2}{\partial t^2}\left(\int_0^\xi\frac{1}{2}\left(\frac{\partial u}{\partial\zeta}\right)^2 d\zeta\right)d\xi\right]+$$

$$m\left[\left(\alpha-2(l-z)\frac{\partial\alpha}{\partial z}\right)\frac{\partial^2}{\partial t^2}\left(\int_0^z(l-\xi)\frac{\partial^2 u}{\partial\xi^2}\alpha d\xi\right)+(l-z)\alpha\frac{\partial^3}{\partial t^2\partial z}\left(\int_0^z(l-\xi)\frac{\partial^2 u}{\partial\xi^2}\alpha d\xi\right)\right]-$$

$$m\alpha\frac{\partial^2}{\partial t^2}\left(\int_0^\xi(l-\xi)\frac{\partial^2 u}{\partial\xi^2}\alpha d\xi\right)-m\left[-2\frac{\partial\alpha}{\partial z}+(l-z)\frac{\partial^2\alpha}{\partial z^2}\right]\left(\int_z^l\frac{\partial^2}{\partial t^2}\left(\int_0^\xi(l-\zeta)\frac{\partial^2 u}{\partial\zeta^2}\alpha d\zeta\right)d\xi\right)+$$

$$m\frac{\partial^2 Y}{\partial t^2}\left[-\alpha+(l-z)\frac{\partial\alpha}{\partial z}\right]+m\frac{\partial^2 Y}{\partial t^2}(l-z)\frac{\partial\alpha}{\partial z}-m\frac{\partial^2 Y}{\partial t^2}\alpha-m(l-z)\frac{\partial^2 Y}{\partial t^2}\left[-2\frac{\partial\alpha}{\partial z}+(l-z)\frac{\partial^2\alpha}{\partial z^2}\right]-$$

$$EI\left[\frac{\partial^4 u}{\partial z^4}\left[1+\left(\frac{\partial u}{\partial z}\right)^2\right]^2+4\frac{\partial^3 u}{\partial z^3}\left[1+\left(\frac{\partial u}{\partial z}\right)^2\right]\frac{\partial u}{\partial z}\frac{\partial^2 u}{\partial z^2}\right]-4EI\left(\frac{\partial^2 u}{\partial z^2}\right)^3\left[1+\left(\frac{\partial u}{\partial z}\right)^2\right]-$$

$$4EI\left[2\frac{\partial u}{\partial z}\frac{\partial^2 u}{\partial z^2}\frac{\partial^3 u}{\partial z^3}\left[1+\left(\frac{\partial u}{\partial z}\right)^2\right]+2\left(\frac{\partial u}{\partial z}\right)^2\left(\frac{\partial^2 u}{\partial z^2}\right)^3\right]+4EI\frac{\partial^3 u}{\partial z^3}\frac{\partial^2 u}{\partial z^2}\left[1+\left(\frac{\partial u}{\partial z}\right)^2\right]\frac{\partial u}{\partial z}+$$

$$2EI\left(\frac{\partial^2 u}{\partial z^2}\right)^3\left[1+\left(\frac{\partial u}{\partial z}\right)^2\right]+4EI\left(\frac{\partial^2 u}{\partial z^2}\right)^3\left(\frac{\partial u}{\partial z}\right)^2-L=0 \tag{2.11a}$$

$$m\delta_3\frac{\partial^2 u}{\partial t^2}+m\delta_3^2\frac{\partial^2\alpha}{\partial t^2}+m(l-z)\frac{\partial^2 u}{\partial z^2}\left(\int_z^l\frac{\partial^2}{\partial t^2}\left(\int_0^\xi(l-\zeta)\frac{\partial^2 u}{\partial\zeta^2}\alpha d\zeta\right)d\xi\right)+$$

$$m\frac{\partial^2 Y}{\partial t^2}(l-z)^2\frac{\partial^2 u}{\partial z^2}+I_0\frac{\partial^2\alpha}{\partial t^2}-\frac{\partial}{\partial z}\left(cGJ\frac{\partial\alpha}{\partial z}\right)-M=0 \tag{2.11b}$$

where $m=\iint\rho dxdy$ is the wing mass per unit length. The boundary conditions are:

$$\alpha|_{z=0}=\frac{\partial\alpha}{\partial z}|_{z=0}=\frac{\partial\alpha}{\partial z}|_{z=l}=0,\ u|_{z=0}=\frac{\partial u}{\partial z}|_{z=0}=0,\qquad \frac{\partial^2 u}{\partial z^2}|_{z=l}=\frac{\partial^3 u}{\partial z^3}|_{z=l}=0 \tag{2.11c}$$

We will consider only the first mode in bending and the first mode in torsion. Furthermore the solutions are expanded in terms of the generalized coordinates and mode shapes

$$u(z,t)=u_0(t)f(z);\qquad \alpha(z,t)=\alpha_0(t)\phi(z) \tag{2.12a,b}$$

where

$f(z)=\cosh(1.875z/l)-\cos(1.875z/l)-0.734\left[\sinh(1.875z/l)-\sin(1.875z/l)\right]$, and

$\phi(z)=\sin(\pi z/2l)$.

Applying Galerkin's method gives the following two coupled nonlinear ordinary differential equations

$$m\left[1+\frac{\pi b^2\rho_\infty}{m}+\frac{c_1}{l^2}u_0^2(t)+c_2\alpha_0^2(t)\right]\ddot{u}_0(t)+2\pi b\rho_\infty B(k)U_\infty\dot{u}_0(t)+\left[K_u+m\frac{c_1}{l^2}\dot{u}_0^2(t)\right]u_0(t)+$$

$$K_{u3}u_0^3(t)+\left[c_6\left(S_\alpha-a\pi b^3\rho_\infty\right)+c_2mu_0(t)\alpha_0(t)\right]\ddot{\alpha}_0(t)+$$

$$\left[2\pi b\rho_\infty c_6B(k)U_\infty^2+2c_2m\dot{u}_0(t)\dot{\alpha}_0(t)\right]\alpha_0(t)+c_6\pi b^2\rho_\infty\left[1+(1-2a)B(k)\right]U_\infty\dot{\alpha}_0(t)+$$

$$c_3m\alpha_0(t)\ddot{Y}(t)=0 \tag{2.13}$$

$$\left[I_\alpha+\left(\frac{1}{8}+a^2\right)\pi b^4\rho_\infty+c_4mu_0^2(t)\right]\ddot{\alpha}_0(t)+\left(\frac{1}{2}-a\right)\left[1-(1+2a)B(k)\right]\pi b^3\rho_\infty U_\infty\dot{\alpha}_0(t)+$$

$$\left[K_\alpha-(1+2a)B(k)\pi b^2\rho_\infty U_\infty^2\right]\alpha_0(t)+\left[c_7\left(S_\alpha-a\pi b^3\rho_\infty\right)+c_4mu_0(t)\alpha_0(t)\right]\ddot{u}_0(t)-$$

$$c_7(1+2a)\pi b^2\rho_\infty B(k)U_\infty\dot{u}_0(t)+2c_4m\dot{u}_0(t)\dot{\alpha}_0(t)u_0(t)+c_5mu_0(t)\ddot{Y}(t)=0 \tag{2.14}$$

where $m$ is the wing mass per unit length, $I_\alpha = I_0 + m\delta_3^2$, $I_\alpha$ is the wing mass moment of the inertia (about the elastic axis) per unit length, $S_\alpha = m\delta_3$, $K_u = 12.3596EI_y / l^4$, $K_\alpha = \pi^2 cGJ / 4l^2$, $K_{u3} = 80.8579EI_y / l^6$, $c_1 = 4.597$, $c_2 = 0.222567$, $c_3 = 0.42$, $c_4 = 0.4552$, $c_5 = 0.84129$, $c_6 = 0.677861$, and $c_7 = 1.3557$.

Introducing the non-dimensional parameters $\bar{u} = u_0 / b$, $\bar{Y} = Y / b$, $\tau = \omega_\alpha t$, and linear viscous damping with damping factors $\zeta_u$ and $\zeta_\alpha$, equations (2.13) and (2.14) take the non-dimensional form

$$\left(1+\mu+c_1 d^2\bar{u}^2+c_2\bar{\alpha}^2\right)\bar{u}'' + \left(c_6\left(x_\alpha - a\mu\right)+c_2\bar{u}\alpha\right)\alpha'' + 2\left(r\zeta_u + \frac{\mu}{k_\alpha}B(k)\right)\bar{u}' +$$

$$c_6\frac{\mu}{k_\alpha}\left[1+B(k)(1-2a)\right]\alpha' + \left[r^2 + c_1 d^2\bar{u}'^2\right]\bar{u} + 2\left(c_6\frac{\mu B(k)}{k_\alpha^2} + c_2\bar{u}'\alpha'\right)\alpha$$

$$+c_8 d^2 r^2\bar{u}^3 + c_3\alpha\bar{Y}''(\tau) = 0 \qquad (2.15)$$

$$\left(c_7\left(x_\alpha - a\mu\right)+c_4\bar{u}\alpha\right)\frac{1}{r_\alpha^2}\bar{u}'' + \left(1+\frac{\mu}{r_\alpha^2}\left(\frac{1}{8}+a^2\right)+\frac{c_4}{r_\alpha^2}\bar{u}^2\right)\alpha'' - c_7(1+2a)\frac{\mu}{k_\alpha r_\alpha^2}B(k)\bar{u}' +$$

$$+\left[2\zeta_\alpha - \left(\frac{1}{2}-2a^2\right)\frac{\mu}{k_\alpha r_\alpha^2}B(k) + \left(\frac{1}{2}-a\right)\frac{\mu}{k_\alpha r_\alpha^2}\right]\alpha' + \frac{2c_4}{r_\alpha^2}\bar{u}'\alpha'\bar{u} +$$

$$\left[1-(1+2a)\frac{\mu}{k_\alpha^2 r_\alpha^2}B(k)\right]\alpha + \frac{c_5}{r_\alpha^2}\bar{u}\bar{Y}''(\tau) = 0 \qquad (2.16)$$

where a prime denotes differentiation with respect to the non-dimensional time $\tau$, the subscript $0$ is dropped, $k_\alpha = \frac{b\omega_\alpha}{U_\infty}$, $\mu = \frac{\pi b^2\rho_\infty}{m}$, $d = \frac{b}{l}$, $x_\alpha = \frac{S_\alpha}{mb}$, $r_\alpha = \sqrt{\frac{I_\alpha}{mb^2}}$, $a = \frac{\delta_1}{b}$, $r = \frac{\omega_u}{\omega_\alpha}$, $\omega_u = \sqrt{K_u / m}$, $\omega_\alpha = \sqrt{K_\alpha / I_\alpha}$, and $c_8 = 6.5421$

Equations (2.15) and (2.16) will be solved for linear modal analysis, parametric stability boundaries, and response LCO in the absence and presence of air flow.

### 2.3. Modal Analysis and Parametric Stability

The purpose of the linear analysis is to determine the critical flutter speed and the corresponding coupled frequencies on the system parameters and airflow speed. Under parametric excitation it is important to determine stability boundaries in the neighborhood of combination parametric resonance at the flutter speed. The linearized equations of motion are:

$$(1+\mu)\bar{u}'' + c_6(x_\alpha - a\mu)\alpha'' + 2\left(r\zeta_u + \frac{\mu}{k_\alpha}B(k)\right)\bar{u}' + c_6\frac{\mu}{k_\alpha}\left[1+B(k)(1-2a)\right]\alpha' +$$

$$r^2\bar{u} + 2c_6\frac{\mu B(k)}{k_\alpha^2}\alpha + c_3\alpha\bar{Y}''(\tau) = 0 \qquad (2.17)$$

$$c_7(x_\alpha - a\mu)\frac{1}{r_\alpha^2}\bar{u}'' + \left[1+\frac{\mu}{r_\alpha^2}\left(\frac{1}{8}+a^2\right)\right]\alpha'' - c_7(1+2a)\frac{\mu}{k_\alpha r_\alpha^2}B(k)\bar{u}' +$$

$$\left[2\zeta_\alpha - \left(\frac{1}{2}-2a^2\right)\frac{\mu}{k_\alpha r_\alpha^2}B(k) + \left(\frac{1}{2}-a\right)\frac{\mu}{k_\alpha r_\alpha^2}\right]\alpha' +$$

$$\left[1-(1+2a)\frac{\mu}{k_\alpha^2 r_\alpha^2}B(k)\right]\alpha + \frac{c_5}{r_\alpha^2}\bar{u}\bar{Y}''(\tau) = 0 \qquad (2.18)$$

In the absence of parametric excitation, equations (2.17) and (2.18) are linearly coupled and may be solved for the eigenvalues for the following parameters: air mass parameter $\mu = 1/38$, elastic axis location $a = -0.36$, inertia axis location $x_\alpha = 0.024$, inertia ratio $r_\alpha = 0.62$, bending-to-torsion frequency

ratio $r = 0.5$, and damping factors $\zeta_\alpha = 0.001$, $\zeta_u = 0.001$. To estimate the critical flutter speed, the solution of equations (2.17) and (2.18) is expressed in the form:

$$\bar{u} = u_a e^{i\bar{\omega}\tau} \quad \text{and} \quad \alpha = \alpha_a e^{i\bar{\omega}\tau} \tag{2.19}$$

where $\bar{\omega} = \omega / \omega_\alpha$ is the nondimensional natural frequency of the wing coupled modes.

Substituting equations (2.19) into equations (2.17) and (2.18), and setting the parametric excitation to zero, gives

$$\left[ -(1+\mu)\bar{\omega}^2 + 2i\left( \zeta_u r + \frac{\mu}{k_\alpha} B(k) \right)\bar{\omega} + r^2 \right] u_a +$$

$$\left\{ -c_6 (x_\alpha - a\mu)\bar{\omega}^2 + ic_6 \frac{\mu}{k_\alpha}\left[ 1 + B(k)(1-2a) \right]\bar{\omega} + 2c_6 \frac{\mu B(k)}{k_\alpha^2} \right\} \alpha_a = 0 \tag{2.20}$$

$$\left[ -c_7 (x_\alpha - a\mu)\bar{\omega}^2 - ic_7 (1+2a)\frac{\mu}{k_\alpha} B(k)\bar{\omega} \right] u_a + \left\{ -1 - \frac{\mu}{r_\alpha^2}\left( \frac{1}{8} + a^2 \right)\bar{\omega}^2 + \right.$$

$$\left. i\left[ 2\zeta_\alpha - \left( \frac{1}{2} - 2a^2 \right)\frac{\mu B(k)}{k_\alpha r_\alpha^2} + \left( \frac{1}{2} - a \right)\frac{\mu}{k_\alpha r_\alpha^2} \right]\bar{\omega} + \left[ 1 - (1+2a)\frac{\mu B(k)}{k_\alpha^2 r_\alpha^2} \right] \right\} \alpha_a = 0 \tag{2.21}$$

Substituting for $B(k)$ from the equation (2.9), replacing $k = k_\alpha \bar{\omega}$, and rearranging, gives the characteristic equation:

$$\begin{vmatrix} AA(k_\alpha, \bar{\omega}) & BB(k_\alpha, \bar{\omega}) \\ DD(k_\alpha, \bar{\omega}) & EE(k_\alpha, \bar{\omega}) \end{vmatrix} = 0 \tag{2.22}$$

where the elements of the determinant are given in Appendix A. Traditionally, (see e.g., [4]), the flutter speed and flutter frequencies are determined by setting the real and imaginary parts of the determinant (2.22) to zero. By giving a series of values of $k$ the corresponding values of $\bar{\omega}$ were determined from the real and

imaginary parts of the determinant. The intersection of the curves corresponding to the two parts establishes the flutter frequency and flutter speed. Instead, we will numerically solve the determinant (2.22) as a function of the flow speed. In view of the presence of $\bar{\omega}$ up to forth-order in the denominators of circulation functions $F$ and $G$, the resulting frequency equation is found to be of order 12. Careful inspection of this equation reveals that the free terms (coefficient of $\bar{\omega}^0$) and coefficients of lower order terms $\bar{\omega}$, $\bar{\omega}^2$ up to fourth or fifth-order are extremely small, resulting in almost zero roots. The numerical solution gives two different complex roots and their conjugates. The values of the remaining roots were found to be almost near zero. The real components $\left(\omega_{re}/\omega_\alpha\right)_1$ and $\left(\omega_{re}/\omega_\alpha\right)_2$ represent dimensionsless natural frequencies of the coupled modes, and the imaginary components $\left(\zeta_{im}\right)_1/\omega_\alpha$ and $\left(\zeta_{im}\right)_2/\omega_\alpha$ stand for the corresponding damping factors. The dependence of the eigenvalue components on the airflow speed parameter $U_\infty/b\omega_\alpha$ is shown in Figure 2.2(a) when both circulation functions $F$ and $G$ are considered. It is seen that $-\left(\zeta_{im}\right)_1/\omega_\alpha$ is always negative while $-\left(\zeta_{im}\right)_2/\omega_\alpha$ switches to a positive value at the critical airflow speed $U_\infty/b\omega_\alpha = 5.04$ indicating the occurrence of flutter.

If one ignores the imaginary component of the circulation function, i.e., $G=0$, the resulting natural frequencies shown in Figure 2.2(b) are found very close to those shown in Figure 2.2(a). For the case of Figure 2.2(a) the critical flutter speed ratio is $\left(U_\infty/b\omega_\alpha\right)_{G\neq 0} = 5.04$, while for the case of Figure 2.2(b)

$\left(U_\infty / b\omega_\alpha\right)_{G=0} = 4.965$. The error between the two flutter speeds obtained in both cases is 1.5%. Since this error is less than $2\%$ we will ignore the contribution of $G$.

It is interesting to note that at zero flow speed, the two natural frequencies possess the ratio $0.5$.

Under parametric excitation, $\bar{Y} = Y_0 \cos(\bar{\Omega}\tau)$, where $\bar{\Omega} = \Omega / \omega_\alpha$, equations (2.17) and (2.18) are considered for stability analysis. Consider the solution of equations (2.17) and (2.18) in the form

$$\bar{u} = a_1 \sin\left(\frac{\bar{\Omega}\tau}{2}\right) + b_1 \cos\left(\frac{\bar{\Omega}\tau}{2}\right); \qquad \alpha = A_1 \sin\left(\frac{\bar{\Omega}\tau}{2}\right) + B_1 \cos\left(\frac{\bar{\Omega}\tau}{2}\right) \quad \text{(2.23a,b)}$$

Substituting equations (2.23) into equations (2.17) and (2.18) and equating the coefficients of $\sin(\bar{\Omega}\tau/2)$ and $\cos(\bar{\Omega}\tau/2)$ gives a set of four linear homogeneous algebraic equations. The determinant of the coefficients of these equations establishes the frequency equation:

$$\begin{vmatrix} \frac{\bar{\Omega}^2}{4}(1+\mu) - r^2 & \frac{c_6\bar{\Omega}^2}{4}(x_\alpha - a\mu) - \frac{1}{2}c_3 Y_0 \bar{\Omega}^2 - c_6 \frac{2B(k)\mu}{k_\alpha^2} \\ \bar{\Omega}\left(\frac{B(k)\mu}{k_\alpha} + r\zeta_u\right) & \frac{c_6\bar{\Omega}\mu}{2k_\alpha}\left(1 + B(k)(1-2a)\right) \\ -\frac{c_7\bar{\Omega}^2}{4}(x_\alpha - a\mu) + \frac{1}{2}c_5 Y_0 \bar{\Omega}^2 & r_\alpha^2 - \frac{r_\alpha^2\bar{\Omega}^2}{4} - \frac{B(k)\mu}{k_\alpha^2}(1+2a) - \frac{\bar{\Omega}^2\mu}{32} - \frac{1}{4}a^2\bar{\Omega}^2\mu \\ -\frac{c_7 B(k)\bar{\Omega}\mu}{2k_\alpha}(1+2a) & \frac{\bar{\Omega}\mu}{4k_\alpha}\left(1 - 2a - B(k)\left(1-4a^2\right)\right) + r_\alpha^2\bar{\Omega}\zeta_\alpha \end{vmatrix}$$

$$\begin{vmatrix} \bar{\Omega}\left(\frac{B(k)\mu}{k_\alpha}+r\zeta_u\right) & \frac{c_6\bar{\Omega}\mu}{2k_\alpha}\left(1+B(k)(1-2a)\right) \\ r^2-\frac{\bar{\Omega}^2}{4}(1+\mu) & -\frac{c_6\bar{\Omega}^2}{4}\left(x_\alpha-a\mu\right)-\frac{1}{2}c_3Y_0\bar{\Omega}^2+\frac{2c_6B(k)\mu}{k_\alpha^2} \\ \frac{c_6B(k)\bar{\Omega}\mu}{2k_\alpha}(1+2a) & -\left(\frac{\bar{\Omega}\mu}{4k_\alpha}\left(1-2a-B(k)\left(1-4a^2\right)\right)+r_\alpha^2\bar{\Omega}\zeta_\alpha\right) \\ -\frac{c_6\bar{\Omega}^2}{4}\left(x_\alpha-a\mu\right)-\frac{1}{2}c_5Y_0\bar{\Omega}^2 & r_\alpha^2-\frac{r_\alpha^2\bar{\Omega}^2}{4}-\frac{B(k)\mu}{k_\alpha^2}(1+2a)-\frac{\bar{\Omega}^2\mu}{32}-\frac{1}{4}a^2\bar{\Omega}^2\mu \end{vmatrix} = 0 \quad (2.24)$$

The roots of this equation depend on the excitation amplitude and airflow speed. These roots are known to be the boundary frequencies of the instability regions. The instability regions are bounded by periodic solutions of period $2T$, where $T$ is the period of parametric excitation. The stability boundaries belonging to zero airflow speed, $U_\infty/b\omega_\alpha=0$, are given by the solid curves in Figure 2.3, while those belonging to the critical flow speed, $U_\infty/b\omega_\alpha=4.965$, are shown by the dashed curves. At the critical airflow speed, the stability boundary touches the frequency axis at excitation frequency ratio $\Omega/(\omega_\alpha+\omega_u)=1.04$ regardless of the damping of the structure. In the absence of airflow, there are two instability regions, a narrow region at excitation frequency ratio less than 1 and a wider one at excitation frequency greater than one. At and above the critical speed there is only one instability region and it is wider than those below the critical speed. The bottom of each instability regions at zero air speed moves away from the frequency axis. Inside instability regions, one should consider the system inherent nonlinearities that are responsible to bring the response amplitude into a bounded limit cycle oscillation (LCO).

## 2.4. Nonlinear Analysis

### 2.4.1 RESONANCE CONDITIONS

The nonlinear modal interaction is examined by considering the coupled nonlinear equations of motion (2.15) and (2.16) using multiple scales method [112]. The equations of motion are first written in terms of the linearized principal coordinates. Consider the equations of motion in the non-dimensional matrix form:

$$\mathbf{M}\left(\mathbf{u}(\tau)\right)\mathbf{u}''(\tau)+\mathbf{K}(k)\mathbf{u}(\tau)=\mathbf{F_{nl}}\left(\mathbf{u}(\tau),\mathbf{u}'(\tau),\bar{Y}''(\tau),k\right) \tag{2.25}$$

where $\mathbf{u}(\tau)=\begin{Bmatrix}\bar{u}(\tau)\\ \alpha(\tau)\end{Bmatrix}$, $\mathbf{F_{nl}}=\begin{Bmatrix}f_{n1}\\ f_{n2}\end{Bmatrix}$, $\bar{Y}(\tau)=Y_0\sin\left(\bar{\Omega}\tau\right)$, $\bar{\Omega}=\dfrac{\Omega}{\omega_\alpha}$,

$$\mathbf{M}=\begin{pmatrix}1+\mu+c_1d^2\bar{u}^2-c_2\alpha^2 & c_6\left(x_\alpha-a\mu\right)-c_2\bar{u}\alpha\\ \dfrac{c_7\left(x_\alpha-a\mu\right)+c_4\bar{u}\alpha}{r_\alpha^2} & 1+\dfrac{\mu}{r_\alpha^2}\left(\dfrac{1}{8}+a^2\right)+\dfrac{c_4}{r_\alpha^2}\bar{u}^2\end{pmatrix},\quad \mathbf{K}=\begin{pmatrix}r^2 & 2c_6\dfrac{\mu B(k)}{k_\alpha^2}\\ 0 & 1-\left(1+2a\right)\dfrac{\mu}{k_\alpha^2r_\alpha^2}B(k)\end{pmatrix}$$

$$f_{n1}=-2\left(r\zeta_u+\frac{\mu}{k_\alpha}B(k)\right)\bar{u}'-\frac{c_6\mu}{k_\alpha}\left[1+B(k)\left(1-2a\right)\right]\alpha'-c_1d^2\bar{u}'^2\bar{u}$$

$$+2c_2\bar{u}'\alpha'\alpha-c_8d^2r^2\bar{u}^3-c_3\alpha\bar{Y}''$$

$$f_{n2}=\left(1+2a\right)\frac{c_7\mu}{k_\alpha r_\alpha^2}B(k)\bar{u}'-\left[2\zeta_\alpha-\left(\frac{1}{2}-2a^2\right)\frac{\mu}{k_\alpha r_\alpha^2}B(k)+\left(\frac{1}{2}-a\right)\frac{\mu}{k_\alpha r_\alpha^2}\right]\alpha'$$

$$-2\frac{c_4}{r_\alpha^2}\bar{u}'\alpha'\bar{u}-\frac{c_5}{r_\alpha^2}\bar{u}\bar{Y}''$$

Multiplying equation (2.25) by the inverse of mass matrix, gives

$$\mathbf{I}\mathbf{u}''+\mathbf{M}^{-1}\mathbf{K}\mathbf{u}=\mathbf{M}^{-1}\mathbf{F_{nl}} \tag{2.26}$$

where $\mathbf{I}$ is the identity matrix. The inverse of the mass matrix is then expanded into a Taylor series up to cubic order. The normal mode natural frequencies are determined from the conservative system, $\mathbf{Iu}'' + \tilde{\mathbf{K}}\mathbf{u} = 0$, and are given by:

$$\bar{\omega}_1^2(k) = \frac{p_3(k) - \sqrt{p_4(k)}}{2\left[8r_\alpha^2(1+\mu) + (1+8a^2)(1+\mu)\mu - 8c_6c_7(x_\alpha - a\mu)^2\right]} \tag{2.27a}$$

$$\bar{\omega}_2^2(k) = \frac{p_3(k) + \sqrt{p_4(k)}}{2\left[8r_\alpha^2(1+\mu) + (1+8a^2)(1+\mu)\mu - 8c_6c_7(x_\alpha - a\mu)^2\right]} \tag{2.27b}$$

where $p_3(k)$ and $p_4(k)$ are given in Appendix B. $\bar{\omega}_1 = \omega_1/\omega_\alpha$, and $\bar{\omega}_2 = \omega_2/\omega_\alpha$. The corresponding modal matrix is:

$$\mathbf{P}(k) = \begin{pmatrix} 1 & 1 \\ p_1(k) & p_2(k) \end{pmatrix} \tag{2.28}$$

where $p_1(k)$ and $p_2(k)$ are the modal ratios given in Appendix B. The following coordinate transformation is introduced:

$$\mathbf{u}(\tau) = \mathbf{P}(k)\mathbf{v}(\tau) \tag{2.29}$$

where $\mathbf{v}(\tau) = \begin{Bmatrix} \mathrm{v}_1(\tau) \\ \mathrm{v}_2(\tau) \end{Bmatrix}$ are the principal coordinates. The equations of motion become:

$$\mathbf{I}\mathbf{v}''(\tau) + \mathbf{\Lambda}(k)\mathbf{v}(\tau) = \hat{\mathbf{F}}_{\mathbf{nl}}\left(\mathrm{v}_1(\tau), \mathrm{v}_2(\tau), \mathrm{v}_1'(\tau), \mathrm{v}_2'(\tau), k\right) \tag{2.30}$$

where $\mathbf{\Lambda}(k) = \begin{pmatrix} \bar{\omega}_1^2(k) & 0 \\ 0 & \bar{\omega}_2^2(k) \end{pmatrix}$, $\hat{\mathbf{F}}_{\mathbf{nl}}\left(\mathrm{v}_1, \mathrm{v}_2, \mathrm{v}_1', \mathrm{v}_2', k\right) = \begin{Bmatrix} \hat{F}_{nl1} \\ \hat{F}_{nl2} \end{Bmatrix}$, $Y_{0u} = Y_0\bar{\Omega}^2$,

$$\hat{F}_{nl1} = \varepsilon\Big\{\left(q_3\mathrm{v}_2^2 + q_4\mathrm{v}_1'^2 + q_5\mathrm{v}_2'^2 + q_6\mathrm{v}_1'\mathrm{v}_2' + q_7\mathrm{v}_1'\mathrm{v}_2 + q_8\mathrm{v}_2'\mathrm{v}_2\right)\mathrm{v}_1$$

$$+\left(q_9\mathrm{v}_1'^2 + q_{10}\mathrm{v}_1'\mathrm{v}_2' + q_{11}\mathrm{v}_2'^2\right)\mathrm{v}_2 + q_{12}\mathrm{v}_1' + q_{13}\mathrm{v}_2' + q_{14}\mathrm{v}_1^3 + q_{15}\mathrm{v}_2^3$$

$$+\left(q_{16}\mathrm{v}_2+q_{17}\mathrm{v}_1'+q_{18}\mathrm{v}_2'\right)\mathrm{v}_1^2+\left(q_{19}\mathrm{v}_1'+q_{20}\mathrm{v}_2'\right)\mathrm{v}_2^2-\left(q_1\mathrm{v}_2+q_2\mathrm{v}_1\right)Y_{0u}\sin\left(\bar{\Omega}\tau\right)\Big\}$$

$$\hat{F}_{nl2}=\varepsilon\Big\{\left(s_3\mathrm{v}_2^2+s_4\mathrm{v}_1'^2+s_5\mathrm{v}_2'^2+s_6\mathrm{v}_1'\mathrm{v}_2'+s_7\mathrm{v}_1'\mathrm{v}_2+s_8\mathrm{v}_2'\mathrm{v}_2\right)\mathrm{v}_1$$

$$+\left(s_9\mathrm{v}_1'^2+s_{10}\mathrm{v}_1'\mathrm{v}_2'+s_{11}\mathrm{v}_2'^2\right)\mathrm{v}_2+s_{12}\mathrm{v}_1'+s_{13}\mathrm{v}_2'+s_{14}\mathrm{v}_1^3+s_{15}\mathrm{v}_2^3$$

$$+\left(s_{16}\mathrm{v}_2+s_{17}\mathrm{v}_1'+s_{18}\mathrm{v}_2'\right)\mathrm{v}_1^2+\left(s_{19}\mathrm{v}_1'+s_{20}\mathrm{v}_2'\right)\mathrm{v}_2^2-\left(s_1\mathrm{v}_2+s_2\mathrm{v}_1\right)Y_{0u}\sin\left(\bar{\Omega}\tau\right)\Big\}$$

and a prime denotes differentiation with respect to the non-dimensional time $\tau$. $q_1 \ldots q_{20}$, and $s_1 \ldots s_{20}$ are coefficients that depend on the airflow speed. The solution of these equations is obtained using the multiple-scales method [112]. The method requires to express the solution in terms of two time scales $T_0=\tau$ and $T_1=\varepsilon\tau$

$$\mathrm{v}_1(\tau,\varepsilon)=\mathrm{v}_{10}(T_0,T_1)+\varepsilon\mathrm{v}_{11}(T_0,T_1)+\ldots,\ \mathrm{v}_2(\tau,\varepsilon)=\mathrm{v}_{20}(T_0,T_1)+\varepsilon\mathrm{v}_{21}(T_0,T_1)+\ldots \quad (2.31a,b)$$

Substituting equations (2.31) into equations (2.30) and collecting terms of the same order of $\varepsilon$, the following equations are obtained:

Equations of order $\varepsilon^0$ are:

$$D_0^2\mathrm{v}_{10}+\bar{\omega}_1^2\mathrm{v}_{10}=0 \quad (2.32a)$$

$$D_0^2\mathrm{v}_{20}+\bar{\omega}_2^2\mathrm{v}_{20}=0 \quad (2.32b)$$

Equations of order $\varepsilon$ are:

$$D_0^2\mathrm{v}_{11}+\bar{\omega}_1^2\mathrm{v}_{11}=\left(q_3\mathrm{v}_{20}^2+q_4D_0\mathrm{v}_{10}^2+q_5D_0\mathrm{v}_{20}^2+q_6D_0\mathrm{v}_{10}D_0\mathrm{v}_{20}+q_7D_0\mathrm{v}_{10}\mathrm{v}_{20}+q_8D_0\mathrm{v}_{20}\mathrm{v}_{20}\right)\mathrm{v}_{10}$$

$$+\left(q_9D_0\mathrm{v}_{10}^2+q_{10}D_0\mathrm{v}_{10}D_0\mathrm{v}_{20}+q_{11}D_0\mathrm{v}_{20}^2\right)\mathrm{v}_{20}+q_{12}D_0\mathrm{v}_{10}+q_{14}\mathrm{v}_{10}^3+q_{13}D_0\mathrm{v}_{20}+q_{15}\mathrm{v}_{20}^3$$

$$+\left(q_{16}\mathrm{v}_{20}+q_{17}D_0\mathrm{v}_{10}+q_{18}D_0\mathrm{v}_{20}\right)\mathrm{v}_{10}^2+\left(q_{19}D_0\mathrm{v}_{10}+q_{20}D_0\mathrm{v}_{20}\right)\mathrm{v}_{20}^2$$

$$-\frac{1}{2}i\left(q_1 \mathrm{v}_{20}+q_2 \mathrm{v}_{10}\right)Y_{0u}\left(e^{-i\bar{\Omega}T_0}-e^{i\bar{\Omega}T_0}\right)-2D_0D_1\mathrm{v}_{10}\Big\} \tag{2.33a}$$

$$\begin{aligned}D_0^2\mathrm{v}_{21}+\bar{\omega}_1^2\mathrm{v}_{21}=&\left(s_3\mathrm{v}_{20}^2+s_4D_0\mathrm{v}_{10}^2+s_5D_0\mathrm{v}_{20}^2+s_6D_0\mathrm{v}_{10}D_0\mathrm{v}_{20}+s_7D_0\mathrm{v}_{10}\mathrm{v}_{20}+s_8D_0\mathrm{v}_{20}\mathrm{v}_{20}\right)\mathrm{v}_{10}\\&+\left(s_9D_0\mathrm{v}_{10}^2+s_{10}D_0\mathrm{v}_{10}D_0\mathrm{v}_{20}+s_{11}D_0\mathrm{v}_{20}^2\right)\mathrm{v}_{20}+s_{12}D_0\mathrm{v}_{10}+s_{14}\mathrm{v}_{10}^3+s_{13}D_0\mathrm{v}_{20}+s_{15}\mathrm{v}_{20}^3\\&+\left(s_{16}\mathrm{v}_{20}+s_{17}D_0\mathrm{v}_{10}+s_{18}D_0\mathrm{v}_{20}\right)\mathrm{v}_{10}^2+\left(s_{19}D_0\mathrm{v}_{10}+s_{20}D_0\mathrm{v}_{20}\right)\mathrm{v}_{20}^2\\&-\frac{1}{2}i\left(s_1\mathrm{v}_{20}+s_2\mathrm{v}_{10}\right)Y_{0u}\left(e^{-i\bar{\Omega}T_0}-e^{i\bar{\Omega}T_0}\right)-2D_0D_1\mathrm{v}_{10}\Big\}\end{aligned} \tag{2.33b}$$

The zeroth-order solution is:

$$\mathrm{v}_{10}\left(T_0,T_1\right)=A\left[T_1\right]e^{i\bar{\omega}_1T_0}+\bar{A}\left[T_1\right]e^{-i\bar{\omega}_1T_0};\quad \mathrm{v}_{20}\left(T_0,T_1\right)=Q\left[T_1\right]e^{i\bar{\omega}_2T_0}+\bar{Q}\left[T_1\right]e^{-i\bar{\omega}_2T_0} \tag{2.34a,b}$$

Equations (2.33) contain secular terms, which give rise to following resonance conditions:

(a) Combination parametric resonance $\bar{\Omega}=\bar{\omega}_1+\bar{\omega}_2$, i.e., $\Omega=\omega_1+\omega_2$

(b) One-to-one internal resonance $\omega_1=\omega_2$

(c) One-to-three internal resonance $\omega_1=3\omega_2$

(d) Three-to-one internal resonance $3\omega_1=\omega_2$

The third and fourth resonance conditions are excluded because Theodorsen's theory is only applicable near flutter speed, i.e., when $\omega_1\approx\omega_2$. The first two cases will be considered.

### 2.4.2 RESPONSE AT ZERO FLOW SPEED

The results of the previous section revealed that the normal mode frequencies in the absence of air flow are not equal and possess the ratio

$\omega_1/\omega_2 = 0.5$. Setting secular terms[12] corresponding to the combination parametric resonance, $\bar{\Omega} = \bar{\omega}_1 + \bar{\omega}_2$, to zero and introducing the detuning parameter $\sigma_e$, defined by $\bar{\Omega} = \bar{\omega}_1 + \bar{\omega}_2 + \varepsilon\sigma_e$, gives the solvability conditions

$$\frac{1}{2} iq_1 \bar{Q} Y_{0u} e^{i\sigma_e T_1} + iq_{12}\bar{\omega}_1 A + \left(3q_{14} + iq_{17}\omega_1 + q_4\bar{\omega}_1^2\right) A^2 \bar{A} + 2\left(q_3 + iq_{19}\omega_1 + q_5\bar{\omega}_2^2\right) AQ\bar{Q} - 2i\bar{\omega}_1 A' = 0 \tag{2.35a}$$

$$\frac{1}{2} is_2 \bar{A} Y_{0u} e^{i\sigma_e T_1} + is_{13}\bar{\omega}_2 Q + \left(3s_{15} + is_{20}\omega_2 + s_{11}\bar{\omega}_2^2\right) Q^2 \bar{Q} + 2\left(s_{16} + is_{18}\omega_2 + s_9\bar{\omega}_1^2\right) QA\bar{A} - 2i\bar{\omega}_2 Q' = 0 \tag{2.35b}$$

Introducing the following polar transformations

$$A = b_1 e^{i\beta_1}; \qquad Q = b_2 e^{i\beta_2} \tag{2.36a,b}$$

and separating imaginary and real parts gives the following first-order differential equations:

$$2b_1' = q_{12} b_1 + q_{17} b_1^3 + 2q_{19} b_2^2 b_1 + \frac{q_1}{2\bar{\omega}_1} b_2 Y_{0u} \cos\left(\sigma_e T_1 - \beta_1 - \beta_2\right) \tag{2.37a}$$

$$2\bar{\omega}_1 b_1 \beta_1' = -\left(3q_{14} + q_4\bar{\omega}_1^2\right) b_1^3 - 2\left[q_3 + q_5\bar{\omega}_2^2\right] b_1 b_2^2 + \frac{q_1}{2} b_2 Y_{0u} \sin\left(\sigma_e T_1 - \beta_1 - \beta_2\right) \tag{2.37b}$$

$$2b_2' = s_{13} b_2 + s_{20} b_2^3 + 2s_{18} b_1^2 b_2 + \frac{s_2}{2\bar{\omega}_2} b_1 Y_{0u} \cos\left(\sigma_e T_1 - \beta_1 - \beta_2\right) \tag{2.37c}$$

$$2\bar{\omega}_2 b_2 \beta_2' = -2\left(s_{16} + s_9\bar{\omega}_1^2\right) b_2 b_1^2 - \left(3s_{15} + s_{11}\bar{\omega}_2^2\right) b_2^3 + \frac{s_2}{2} b_1 Y_{0u} \sin\left(\sigma_e T_1 - \beta_1 - \beta_2\right) \tag{2.37d}$$

The above four algebraic equations contain three unknowns and the dependence on the detuning parameter will not appear explicitly. In this case, it is

[12] Secular terms are those terms with small divisor

possible to combine two of these equations into one through the following transformation:

$$\gamma_e = \sigma_e T_1 - \beta_1 - \beta_2 \qquad \text{and} \qquad \beta_1' + \beta_2' = \sigma_e - \gamma_e' \tag{2.38}$$

where a prime denotes differentiation with respect to $T_1$. The resulting equations are:

$$2b_1' = q_{12}b_1 + q_{17}b_1^3 + 2q_{19}b_2^2 b_1 + \frac{q_1}{2\bar{\omega}_1} b_2 Y_{0u} \cos(\gamma_e) \tag{2.39a}$$

$$2b_2' = s_{13}b_2 + s_{20}b_2^3 + 2s_{18}b_1^2 b_2 + \frac{s_2}{2\bar{\omega}_2} b_1 Y_{0u} \cos(\gamma_e) \tag{2.39b}$$

$$\gamma_e' = \sigma_e - \left[\frac{q_1}{4\bar{\omega}_1}\frac{b_2}{b_1} + \frac{s_2}{4\bar{\omega}_2}\frac{b_1}{b_2}\right] Y_{0u} \sin\gamma_e + \left[\frac{3q_{14} + q_4\bar{\omega}_1^2}{2\bar{\omega}_1} + \frac{s_{16} + s_9\bar{\omega}_1^2}{\bar{\omega}_2}\right] b_1^2$$

$$+ \left[\frac{3s_{15} + s_{11}\bar{\omega}_2^2}{2\bar{\omega}_2} + \frac{q_3 + q_5\bar{\omega}_2^2}{\bar{\omega}_1}\right] b_2^2 \tag{2.39c}$$

Equations (2.39) are numerically integrated for different values of excitation amplitude in the neighborhood of combination parametric resonance, i.e., $\Omega \approx \omega_1 + \omega_2$, internal frequency ratio $\omega_1 / \omega_2 = 0.5$, and the external excitation detuning parameter $\sigma_e = 0$.

- Over a very small range of excitation amplitude, $0 < Y_0 < 0.0008$, the zero equilibrium is dynamically stable and the damping energy overcomes input energy. At a threshold value of excitation amplitude the equilibrium position loses its stability and both bending and torsion amplitudes achieve steady state values over the excitation amplitude range $0.0008 < Y_0 < 0.0018$. Time

histories, phase diagrams, and FFTs for excitation level of $Y_0 = 0.0015$ are shown in the Figure 2.4(a) which reveals harmonic oscillations.

- Over the region $0.0018 < Y_0 < 0.003$, the response amplitudes experience Hopf bifurcation.
- The response then experiences another bifurcation in the form of period doubling over the region, $0.003 < Y_0 < 0.0055$ as shown in the Figure 2.4(b) for an amplitude of excitation $Y_0 = 0.005$.
- Above that region, the response exhibits regular periodic (but not harmonic) oscillations (see Figure 2.4(c) for $Y_0 = 0.01$).
- Figure 2.5 shows the bifurcation diagram using the initial conditions $\bar{u}(0) = 0.1$, $\alpha(0) = 0.1$, $\bar{u}'(0) = 0$, $\alpha'(0) = 0$, and system parameters $\mu = 1/38$, $a = -0.36$, $x_\alpha = 0.024$, $r_\alpha = 0.62$, $r = 0.5$, $\zeta_\alpha = 0.001$, $\zeta_u = 0.001$, and $d = 0.1$. The bifurcation diagram reveals the upper and lower pairs of local maxima and minima by taking the excitation amplitude as the control parameter.

### 2.4.3 RESPONSE AT CRITICAL AND POST-CRITICAL FLUTTER SPEEDS

Introducing the external, $\sigma_e$, and internal, $\sigma_i$, detuning parameters, defined such that $\bar{\Omega} = \bar{\omega}_1 + \bar{\omega}_2 + \varepsilon\sigma_e$ and $\bar{\omega}_2 = \bar{\omega}_1 + \varepsilon\sigma_i$, gives the solvability conditions:

$$\frac{1}{2} i\left(q_1 \bar{Q} e^{i\sigma_e T_1} + q_2 \bar{A} e^{i(\sigma_e+\sigma_i)T_1}\right) Y_{0u} + i q_{13}\bar{\omega}_2 e^{i\sigma_i T_1} Q + i q_{12}\bar{\omega}_1 A + \left(3q_{14} + i q_{17}\bar{\omega}_1 + q_4 \bar{\omega}_1^2\right) A^2 \bar{A}$$

$$+\left(q_{16} + i q_7 \bar{\omega}_1 - q_9 \bar{\omega}_1^2 - i q_{18}\bar{\omega}_2 + q_6 \bar{\omega}_1 \bar{\omega}_2\right) e^{-i\sigma_i T_1} A^2 \bar{Q} + \left(q_3 - i q_{19}\bar{\omega}_1 + i q_8 \bar{\omega}_2\right)$$

$$+q_{10}\bar{\omega}_1\bar{\omega}_2-q_5\bar{\omega}_2^2\Big)e^{2i\sigma_i T_1}Q^2\bar{A}+\Big(3q_{15}+iq_{20}\bar{\omega}_2+q_{11}\bar{\omega}_2^2\Big)e^{i\sigma_i T_1}Q^2\bar{Q}$$

$$+2\Big(q_{16}+q_9\bar{\omega}_1^2+iq_{18}\bar{\omega}_2\Big)e^{i\sigma_i T_1}QA\bar{A}+2\Big(q_3+iq_{19}\bar{\omega}_1+q_5\bar{\omega}_2^2\Big)AQ\bar{Q}-2i\bar{\omega}_1A'=0 \tag{2.40a}$$

$$\frac{1}{2}i\Big(s_2\bar{A}e^{i\sigma_e T_1}+s_a\bar{Q}e^{i(\sigma_e+\sigma_i)T_1}\Big)Y_{0u}+is_{12}\bar{\omega}_1e^{-i\sigma_i T_1}A+is_{13}\bar{\omega}_2Q+\Big(3s_{15}+is_{20}\bar{\omega}_2+s_{11}\bar{\omega}_2^2\Big)Q^2\bar{Q}$$

$$+\Big(s_3+is_8\bar{\omega}_2-s_5\bar{\omega}_2^2-is_{19}\bar{\omega}_1+s_{10}\bar{\omega}_1\bar{\omega}_2\Big)e^{i\sigma_i T_1}Q^2\bar{A}+\Big(s_{16}-is_{18}\bar{\omega}_2+is_7\bar{\omega}_1$$

$$+s_6\bar{\omega}_1\bar{\omega}_2-s_9\bar{\omega}_1^2\Big)e^{-2i\sigma_i T_1}A^2\bar{Q}+\Big(3s_{14}+is_{17}\bar{\omega}_1+s_4\bar{\omega}_1^2\Big)e^{-i\sigma_i T_1}A^2\bar{A}$$

$$+2\Big(s_3+s_5\bar{\omega}_2^2+is_{19}\bar{\omega}_1\Big)e^{-i\sigma_i T_1}AQ\bar{Q}+2\Big(s_{16}+is_{18}\bar{\omega}_2+s_9\bar{\omega}_1^2\Big)QA\bar{A}-2i\bar{\omega}_2Q'=0 \tag{2.40b}$$

Introducing the following polar transformations

$$A=b_1e^{i\beta_1};\qquad Q=b_2e^{i\beta_2} \tag{2.41a,b}$$

and separating imaginary and real parts gives four first-order differential equations. By setting the left-hand sides of these equations to zero, one obtains four algebraic equations containing three unknowns, since the two phase angles are combined in one unknown. In addition, the dependency on the detuning parameter does not explicitly appear. In this case, one may introduce the following transformation:

$$\gamma_e=\sigma_eT_1-\beta_1-\beta_2,\ \gamma_i=\sigma_iT_1-\beta_1+\beta_2,\ \beta_1'+\beta_2'=\sigma_e-\gamma_e',\beta_1'-\beta_2'=\sigma_i-\gamma_i' \tag{2.42}$$

where a prime denotes differentiation with respect to $T_1$. The resulting equations are:

$$2b_1'=q_{12}b_1+q_{17}b_1^3+2q_{19}b_2^2b_1+\frac{q_1}{2\bar{\omega}_1}b_2Y_{0u}\cos\gamma_e+\frac{q_{13}\bar{\omega}_2}{\bar{\omega}_1}b_2\cos\gamma_i$$

$$+\frac{b_2^3}{\bar{\omega}_1}\left[q_{20}\bar{\omega}_2\cos\gamma_i + C_1\sin\gamma_i\right] + \frac{b_1^2 b_2}{\bar{\omega}_1}\left[C_2\cos\gamma_i + C_3\sin\gamma_i\right]$$

$$+\frac{b_1}{2\bar{\omega}_1}q_2 Y_{0u}\cos\left(\gamma_e+\gamma_i\right) + C_4 b_1 b_2^2\cos 2\gamma_i + C_5 b_1 b_2^2\sin 2\gamma_i \qquad (2.43a)$$

$$2b_2' = s_{13}b_2 + s_{20}b_2^3 + 2s_{18}b_1^2 b_2 + \frac{s_2}{2\bar{\omega}_2}b_1 Y_{0u}\cos\left(\gamma_e\right) + \frac{s_{12}\bar{\omega}_1}{\bar{\omega}_2}b_1\cos\gamma_i$$

$$+\frac{b_1^3}{\bar{\omega}_2}\left[s_{17}\bar{\omega}_1\cos\gamma_i - C_6\sin\gamma_i\right] + \frac{b_2^2 b_1}{\bar{\omega}_2}\left[C_7\cos\gamma_i - C_8\sin\gamma_i\right]$$

$$+\frac{b_2}{2\bar{\omega}_2}s_1 Y_{0u}\cos\left(\gamma_e-\gamma_i\right) - b_2 b_1^2\left(C_9\cos 2\gamma_i + C_{10}\sin 2\gamma_i\right) \qquad (2.43b)$$

$$\gamma_e' = \sigma_e + \frac{1}{4\bar{\omega}_1\bar{\omega}_2 b_1 b_2}\left\{-2q_{13}\bar{\omega}_2^2 b_2^2\sin\gamma_i + b_1^4\left[C_{11}\bar{\omega}_1\cos\gamma_i + 2s_{17}\bar{\omega}_1^2\sin\gamma_i\right]\right.$$

$$+2s_{12}\bar{\omega}_1^2 b_1^2\sin\gamma_i + b_2^4\left(C_{12}\bar{\omega}_2\cos\gamma_i - 2q_{20}\bar{\omega}_2^2\sin\gamma_i\right) + C_{13}b_1^2 b_2^2\cos\gamma_i$$

$$+C_{14}b_1^2 b_2^2\sin\gamma_i + 2C_{15}b_1^3 b_2 + 2C_{16}b_1^3 b_2\cos 2\gamma_i + 2C_{17}b_1^3 b_2\sin 2\gamma_i$$

$$+2C_{18}b_2^3 b_1 + 2C_{19}b_2^3 b_1\cos 2\gamma_i - 2C_{20}b_2^3 b_1\sin 2\gamma_i - C_{21}Y_{0u}\sin\gamma_e$$

$$\left.-Y_{0u}b_1 b_2\left[s_1\bar{\omega}_1\sin\left(\gamma_e-\gamma_i\right) + q_2\bar{\omega}_2\sin\left(\gamma_e+\gamma_i\right)\right]\right\} \qquad (2.43c)$$

$$\gamma_i' = \sigma_i + \frac{1}{4\bar{\omega}_1\bar{\omega}_2 b_1 b_2}\left\{-2q_{13}\bar{\omega}_2^2 b_2^2\sin\gamma_i - b_1^4\left[C_{22}\bar{\omega}_1\cos\gamma_i + 2s_{17}\bar{\omega}_1^2\sin\gamma_i\right]\right.$$

$$-2s_{12}\bar{\omega}_1^2 b_1^2\sin\gamma_i + b_2^4\left(C_{23}\bar{\omega}_2\cos\gamma_i - 2q_{20}\bar{\omega}_2^2\sin\gamma_i\right) + C_{24}b_1^2 b_2^2\cos\gamma_i$$

$$+C_{25}b_1^2 b_2^2\sin\gamma_i + 2C_{26}b_1^3 b_2 + 2b_1^3 b_2\left(C_{27}\cos 2\gamma_i + C_{28}\sin 2\gamma_i\right)$$

$$+2C_{29}b_2^3 b_1 + 2b_2^3 b_1\left(C_{30}\cos 2\gamma_i - C_{31}\sin 2\gamma_i\right)$$

$$\left.+C_{32}Y_{0u}\sin\gamma_e + Y_{0u}b_1 b_2\left[s_1\bar{\omega}_1\sin\left(\gamma_e-\gamma_i\right) - q_2\bar{\omega}_2\sin\left(\gamma_e+\gamma_i\right)\right]\right\} \qquad (2.43d)$$

where the coefficients $C_i$ are defined in Appendix C. Note that equations (2.43) contain four unknowns namely the response amplitudes, $b_1$, and $b_2$, and the two phase angles, $\gamma_e$ and $\gamma_i$. Furthermore, the dependency on the external and

internal detuning parameters explicitly appears in equations (2.43c) and (2.43d). The solution of these equations is obtained numerically for different values of excitation amplitude, at the critical and post-critical flutter speeds. In both cases, the response is estimated in the neighborhood of combination parametric resonance, i.e., $\Omega \approx \omega_1 + \omega_2$, internal frequency ratio, $\omega_1 / \omega_2 \approx 1$, external excitation detuning parameter, $\sigma_e = 0$, internal resonance detuning parameter $\sigma_i = 0.061$, and system parameters $\mu = 1/38$, $a = -0.36$, $x_\alpha = 0.024$, $r_\alpha = 0.62$, $r = 0.5$, $\zeta_\alpha = 0.001$, $\zeta_u = 0.001$, $d = 0.1$.

#### *2.4.3.1 Response at Critical Flutter Speed*

In the absence of parametric excitation, the solution of these equations reveals the coexistence of different fixed points implying LCO. Each fixed point is created from a certain domain of initial conditions. There are three possible values of the fixed point and each is achieved for certain values of initial conditions. The three fixed points are $\{u, \alpha\} = \{0, 0\}$, $\{0.15, -0.11\}$, and $\{1.4, 0.325\}$. The domains of attraction of each of the above fixed points are shown in Figure 2.6(a), where the empty space is belonging to the zero fixed point.

- Under parametric excitation, the same scenario is preserved up to an excitation level $Y_0 = 0.00875$ at which the response experiences Hopf

bifurcation[13] around each fixed point in addition to a new fixed point that also experiences Hopf bifurcation. At $Y_0 = 0.00875$, there are four different values of initial conditions, which lead to four different attractors. These initial conditions are: $\{u_0, \alpha_0, u_0', \alpha_0'\} = \{0.5, 0.04, 0, 0\}$, $\{0.5, 0.05, 0, 0\}$, $\{0.5, 0.7, 0, 0\}$, and $\{0.45,\ 0.07,\ \ 0, 0\}$. The domains of attraction corresponding to this case are shown in Figure 2.6(b).

- Over another range of excitation amplitude, $0.00875 < Y_0 < 0.0125$, the response experiences Hopf bifurcation for relatively high range of initial conditions below which the response settles at the static equilibrium position. For example, under excitation amplitude, $Y_0 = 0.01$, the basin of attraction of this response is shown in Figure 2.6(c) and reveals that the basin of initial conditions that leads to non-zero response is shifted away to either higher positive values or negative values.
- At excitation amplitude $Y_0 = 0.0125$ an additional bifurcation around a new point takes place depending on the initial conditions. For example, the two sets of initial conditions $\{0.3, -0.1, 0, 0\}$ and $\{0.5, 0.1, 0, 0\}$, yield two different periodic attractors under $Y_0 = 0.014$. Figure 2.6(d) shows the basins of attraction. In the first and third quadrants the basins of attraction are diminished to one positive or negative point, i.e., $\{0.5, 0.1, 0, 0\}$ or $\{-0.5, -0.1, 0, 0\}$. These two sets of initial conditions lead to large amplitude

[13] Hopf bifurcation implies the beginning of oscillatory motion

oscillations. Another two basins of attraction located in the second and fourth quadrants lead to another attractor of very small amplitude. As the excitation amplitude increases, additional bifurcations take place in the form of cascade of period doubling depending on initial conditions.

- Figure 2.7 shows samples of time history records under no excitation, $Y_0 = 0$, and initial conditions $\{0.45, -0.01, 0, 0\}$. The response shows steady state.
- Figures 2.8(a-d) show samples of time history records under excitation amplitude of $Y_0 = 0.00875$ and different initial conditions. The plots show four harmonic attractors of different amplitude levels.
- Figure 2.9 shows samples of time history records under excitation amplitude of $Y_0 = 0.01$ and initial conditions $\{0.5, 0.1, 0, 0\}$. Harmonic oscillations are obtained.
- Figures 2.10 show samples of time history records, phase diagrams, and FFT plots under excitation amplitude $Y_0 = 0.014$, and initial conditions $\{0.5, -0.1, 0, 0\}$ (Figure 2.10(a)) and $\{0.5, 0.1, 0, 0\}$ (Figure 2.10(a)). Two single periodic domains of attraction of different amplitude levels are obtained. Also it is seen that this is the critical point of bifurcation and any slight increase in amplitude will produce period doubling.
- Figure 2.11(a) shows samples of time history records, phase diagrams, and FFT plots under excitation amplitude $Y_0 = 0.015$, and initial conditions $\{0.5, -0.1, 0, 0\}$. It is seen that the bifurcation takes place in the form of period doubling. The domain of attraction of this attractor is slightly enlarged than the

corresponding case of Figure 2.6(d). There is another periodic attractor of period two shown in Figure 2.11(b), which oscillates with larger amplitude than the first attractor and emanates from one point of initial conditions in the first and third quadrants shown in Figure 2.6(e).

- Under excitation amplitude $Y_0 = 0.016$, the response experiences another bifurcation of period four as seen in the Figures 2.12(a, b). There are two different attractors similar to those displayed in Figure 2.6(e).
- Any further increase of excitation amplitude results in chaotic motion as shown in Figures 2.13(a, b), which is generated under excitation amplitude $Y_0 = 0.017$ and different domains of attraction. The spectrum of the time history records is continuous.
- The Poincaré maps displayed in Figures 2.13(a) and (b) do not cover a smooth closed curve but constitute a set of randomly scattered points implying that the motion turned out to be chaotic. The Poincaré maps are obtained based on the period of the first return. The domains of attraction corresponding to the small amplitude oscillation attractor are expanded as shown in Figure 2.6(f).
- Figure 2.14 presents the bifurcation diagram by taking the excitation amplitude as the control parameter. It is seen that for a region of initial conditions, the parametric excitation acts as a stabilizer source of the wing flutter where under these regions the response achieves its static equilibrium position. Outside this domain of initial conditions, the equilibrium position loses its stability and the response may possess fixed points, Hopf

bifurcation, cascade of period doubling, and eventually chaotic motion. It is seen that at each bifurcation point, branches of symmetric and asymmetric periodic solutions meet in the form of supercritical symmetry-breaking bifurcation.

It is obvious that the response exhibits multiple attractors, each with its own domain of attraction. One or two of these attractors, namely the zero response or small amplitude LCO about a small mean, are superior and desirable in the post flutter region. In order to achieve that desirable performance one may use one of the current techniques used to control chaos (see, e.g., [191]). For the present case, the domains of attractions of undesirable performance can be shifted away only by increasing the parametric excitation amplitude. Figure 2.15 shows the dependence of the percentage of domains of attraction that lead to non-zero flutter oscillation on the excitation amplitude. It is seen that as the excitation amplitude increases both the domains of attraction for low and large response amplitude decrease until critical excitation amplitude, $Y_{cr} \approx 0.01375$, above which the parametric excitation suppresses the wing flutter.

#### *2.4.3.2 Response at Post-Critical Flutter Speed*

At a flow speed that is slightly higher than the critical flutter speed, $U_\infty / b\omega_\alpha = 5.02$, the wing enters in the post flutter region. In the absence of parametric excitation the wing experiences Hopf bifurcation of different amplitude oscillations depending on initial conditions. For all values of initial conditions occupied in Figure 16(a), there are two domains of response amplitudes. Low

oscillation amplitudes shown by the region of small solid triangles, ▲, exemplified by the time histories shown the Figure 2.17(a); and large amplitudes shown by solid squares, ■, exemplified by the time histories shown the Figure 2.17(b). Under very small excitation amplitude, the response experiences multi-periods.

- Over the excitation amplitude range, $0.001 \le Y_0 < 0.003$, the response experiences multi-periods with growing amplitudes. For example, under excitation amplitude, $Y_0 = 0.0025$, Figures 2.18(a) and (b) show time history records, phase portraits, Poincaré mapping and FFT plots for two different sets of boundary conditions.
- Over another excitation amplitude range, $0.003 < Y_0 < 0.005$, there are two domains of attraction one of them leads to small amplitude oscillations with multi-period as in the previous range, while the other leads to periodic then cascade of period doubling with high amplitude oscillations. Figures 2.19(a) and (b) show samples of time history records, phase diagram, and FFT for the two cases under excitation amplitude $Y_0 = 0.004$. Figure 2.19(a) includes also Poincaré maps.
- The next region of excitation amplitude, $0.005 < Y_0 < 0.01$, is characterized by chaotic motion for all possible initial conditions. However, one set of initial conditions leads to a chaotic attractor with small amplitude oscillations, while the other set leads to large amplitude oscillations as shown in Figures 2.20(a) and (b), respectively for $Y_0 = 0.0075$. There is a small window around $Y_0 = 0.01$ characterized by period doubling for all possible initial conditions. Sample

time histories for $Y_0 = 0.01$ under two sets of initial conditions are shown in the Figure 2.21.

- A new regime of response behavior emerges at excitation level range, $0.01 < Y_0 < 0.014$ characterized by a train of spikes known as the "*firing*" state [185] for certain regions of initial conditions. The remaining initial conditions lead to periodic attractor. For example, under excitation amplitude, $Y_0 = 0.013$, Figures 2.22(a) and (b) show typical time history records of the firing state. Figures 2.22(c) and (d) show the periodic regime. Figure 2.16(b) show the domains of attraction of these four attractors. Note the period between the spikes in the firing state varies substantially. As the excitation amplitude increases the period between the spikes (called the "*refractory*" or "*recovery*" period) increases and for the some initial condition the recovery period becomes infinitely large declaring a stabilization effect. Figures 2.23(a)-(c) show samples of time history records belonging to these regimes. Figure 2.16(c) shows the domains of attraction that lead to these different attractors. At excitation levels, $Y_0 \geq 0.015$, the response achieves the zero equilibrium position.

Figures 2.24(a) and (b) show the bifurcation diagram which summarizes all the above stated regimes. In order to appreciate the stabilization effect of parametric excitation, Figure 2.25 gives the dependence of the percentage of the area of domain of attraction on the excitation amplitude.

## 2.5. Numerical Simulations

The purpose of the numerical simulation of the original equations of motion is to validate the multiple scales predictions. Equations (2.15) and (2.16) are numerically integrated for different values of excitation amplitude. The numerical integration is carried out in the absence of air flow and in the presence of air flow at the critical flutter speed for $\mu = 1/38$, $a = -0.36$, $x_\alpha = 0.024$, $r_\alpha = 0.62$, $r = 0.5$, $\zeta_\alpha = 0.001$, $\zeta_u = 0.001$, $d = 0.1$. The following subsections present just representative samples of the numerical simulation and are not considered exhaustive.

### 2.5.1 ZERO FLOW SPEED

Under parametric excitation with frequency close to the sum of the first two modes, $\Omega \approx \omega_1 + \omega_2$, and normal modal frequencies ratio $\omega_1 / \omega_2 \approx 0.5$, the wing response is obtained for different excitation amplitudes. Under all values of excitation amplitude, the response of both bending and torsion exhibits periodic modulated signals as shown in Figures 2.26(a)-(d). At relatively low excitation amplitude, the modulation effect is very weak as demonstrated in Figure 2.26(a) and becomes significant as the excitation amplitude increases. The simulations are carried out for initial conditions $\bar{u}(0) = 0.5$, $\alpha(0) = 0.1$, $\bar{u}'(0) = 0$, $\alpha'(0) = 0$. The bifurcation diagram is shown in Figure 2.27 which is obtained for initial conditions $\bar{u}(0) = 0.5$, $\alpha(0) = 0.1$, $\bar{u}'(0) = 0$, $\alpha'(0) = 0$.

2.5.2 CRITICAL FLUTTER SPEED

Under flutter flow speed $U_\infty / b\omega_\alpha = 4.965$ and parametric excitation with frequency close to the sum of the first two mode frequencies, $\Omega = \omega_1 + \omega_2$, and internal frequencies having the relationship $\omega_2 = \omega_1 + 0.061$, the wing response is obtained for different values of excitation amplitudes and initial conditions. Under zero excitation amplitude, and depending on initial conditions, there exist two different LCOs as shown in the Figures 2.28(a, b). At excitation amplitude $Y_0 = 0.00875$, and depending on initial conditions the response either preserves the zero equilibrium as shown in Figure 2.28(c), or possesses multi-period oscillations as shown in Figure 2.28(d). These two attractors are maintained up to excitation amplitude 0.013 above which the response is attracted to either the zero response as shown in Figure 2.28(e) or to a chaotic motion as shown in Figure 2.28(f) for $Y_0 = 0.014$. Note that the shown Poincaré maps are obtained based on the excitation period. As the excitation amplitude increases, say to $Y_0 = 0.016$, the chaotic regime is characterized by occasional spikes followed by relaxation period as shown in Figure 2.28(g). The zero response is not shown for this case. At excitation amplitude $Y_0 = 0.017$ the non-zero response becomes more ordered after experiencing spiky transition period as shown in Figure 2.28(h).

2.5.3 POST-CRITICAL SPEED

At slightly higher value of flow speed than the critical flutter speed, say, $U_\infty / b\omega_\alpha = 5.02$, the numerical simulation is presented for selected values of excitation amplitude. At zero excitation amplitude the wing experiences LCOs in bending and torsion as shown in Figure 2.29(a). The zero attractor disappears for all excitation levels up to excitation amplitude of 0.013. As the excitation level increases from a low value up to 0.013, the response time history records experience multi-periods and Figures 2.29(b-e) show the sequence of development of the response time history records for different values of excitation amplitude. For excitation levels of 0.014, and above, the zero attractor emerges for certain domain of attraction in addition to a multi-period attractor depending on the initial conditions. For example, Figures 2.29(f) and (g) show time history records at excitation level 0.015 for two different sets of initial conditions. The domains of attraction that lead to zero attractor are enlarged as the excitation amplitude increases and this confirms the results predicted by the multiple scales method.

## 2.6. Closing Remarks

The nonlinear flutter of a cantilever wing is studied analytically and numerically in the absence and presence of parametric excitation. In the absence of nonlinearities, the regions of parametric instability are obtained for different values of flow speed. At the critical flutter speed the bottom of instability region touches the frequency axis. Below and above the critical speed the instability

regions move away from the frequency axis. The nonlinear flutter is studied using the method of multiple scales in the neighborhood of combination parametric resonance at the critical flutter speed and at flow speed that is slightly higher than the critical one. At critical flutter speed the response was found to possess more than one attractor each is obtained from a certain domain of initial conditions. As the excitation amplitude increases the responses experiences a cascade of period doubling and eventually chaotic motion. At critical excitation amplitude the response exhibits stabilization state to the zero equilibrium attractor over a wide range of initial conditions. The stabilization effect was also manifested at a flow speed that is slightly higher than the critical flutter speed. However, the stabilization effect was preceded by new phenomena such as firing and recovery states. The numerical simulation of the original equations of motion has confirmed the multiple scales findings. Because of the limitation of Theodorsen's theory (valid only at flutter speed), the vortex lattice method proposed by Predikman [36] will be used to model aerodynamic loads in the next chapter. The aerodynamic loads will possess nonlinearities caused by the wakes. In addition, the wing structure, which is modeled linear, will have uncertainty in bending and torsion stiffnesses.

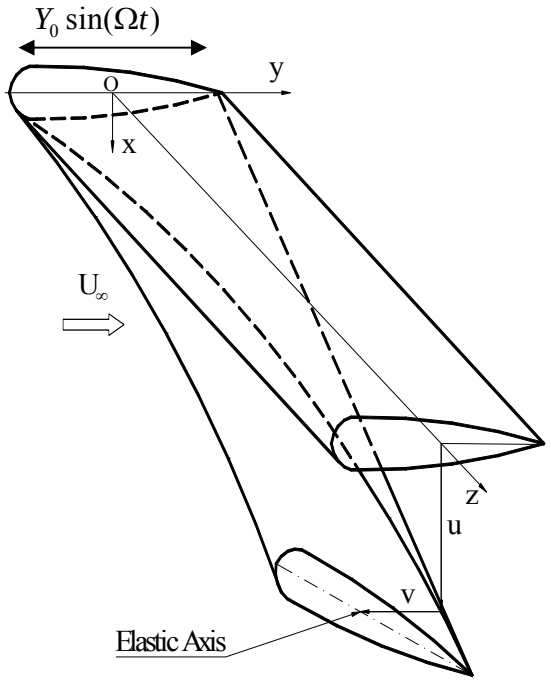


(a) Plate-like cantilever wing showing the coordinate frame

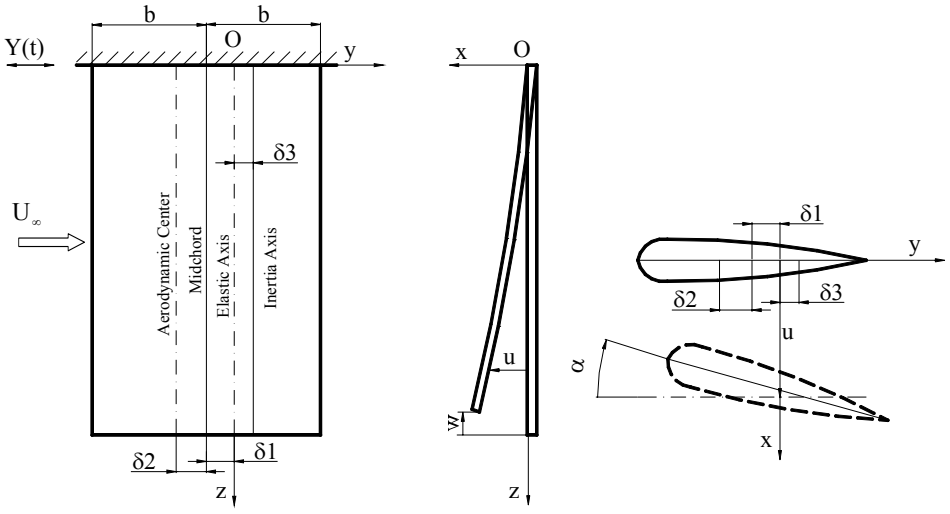


(b) Locations of different axes and deformations in bending, torsion, and longitudinal

Figure 2.1. Schematic diagram of the analytical model, coordinates axes, and deformations

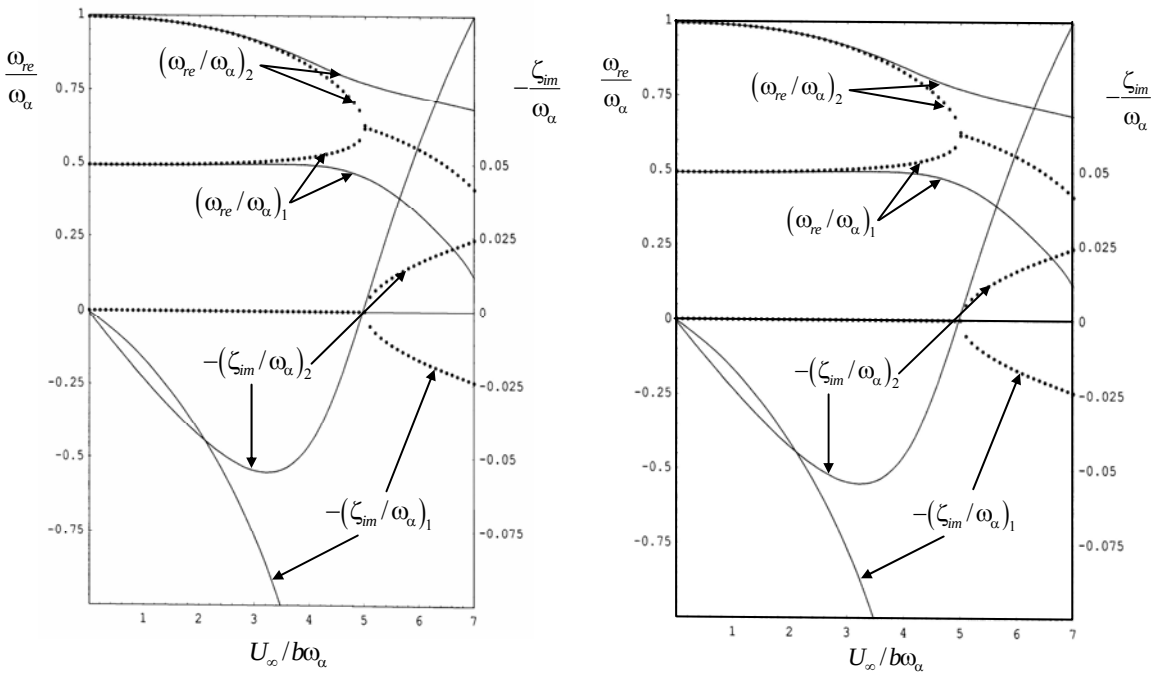


Figure 2.2. Dependence of eigenvalue components on the flow speed parameter showing: (a) the influence of the imaginary component of circulation function, $G \neq 0$ and (b) its absence, $G = 0$.
——— Eigenvalue components in the presence of aerodynamic and structure damping; …….. Eigenvalue components in the absence of aerodynamic and structure damping.

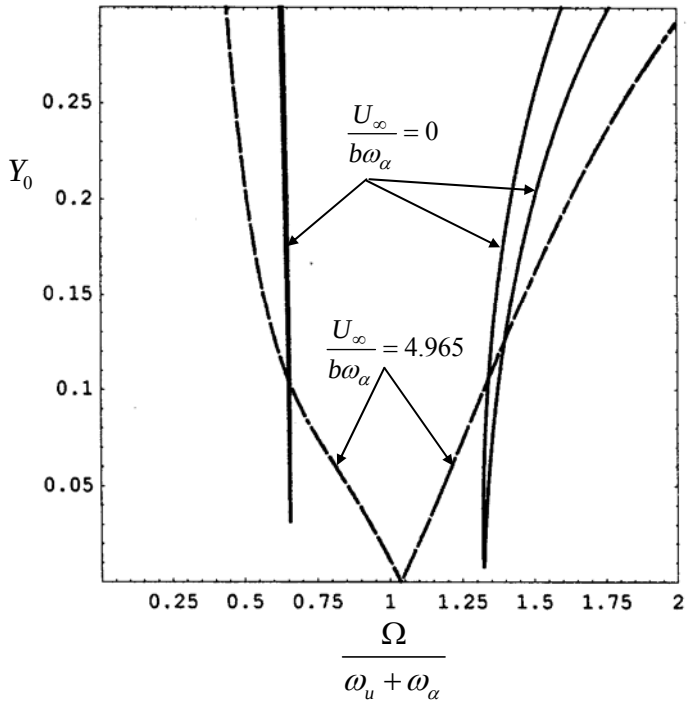


Figure 2.3. Stability boundaries in the neighborhood of parametric combination resonance at zero flow speed and at critical flow speed.

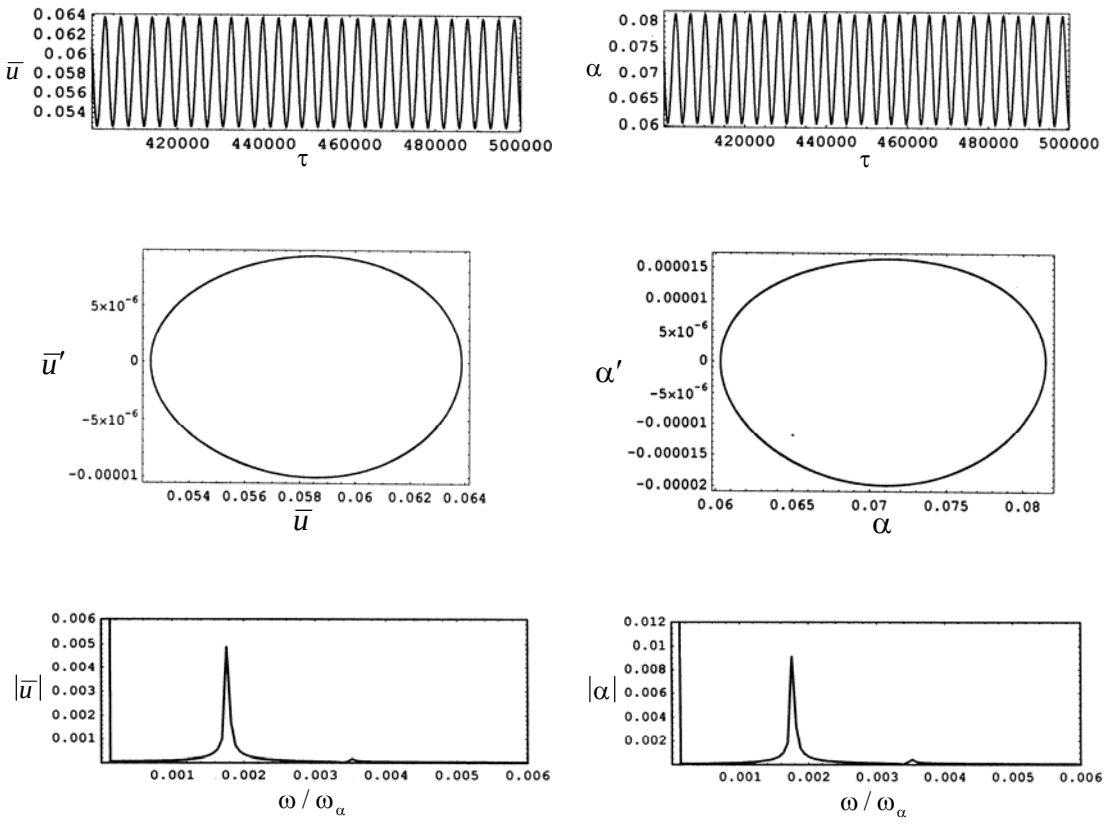


(a) $Y_0 = 0.0015$

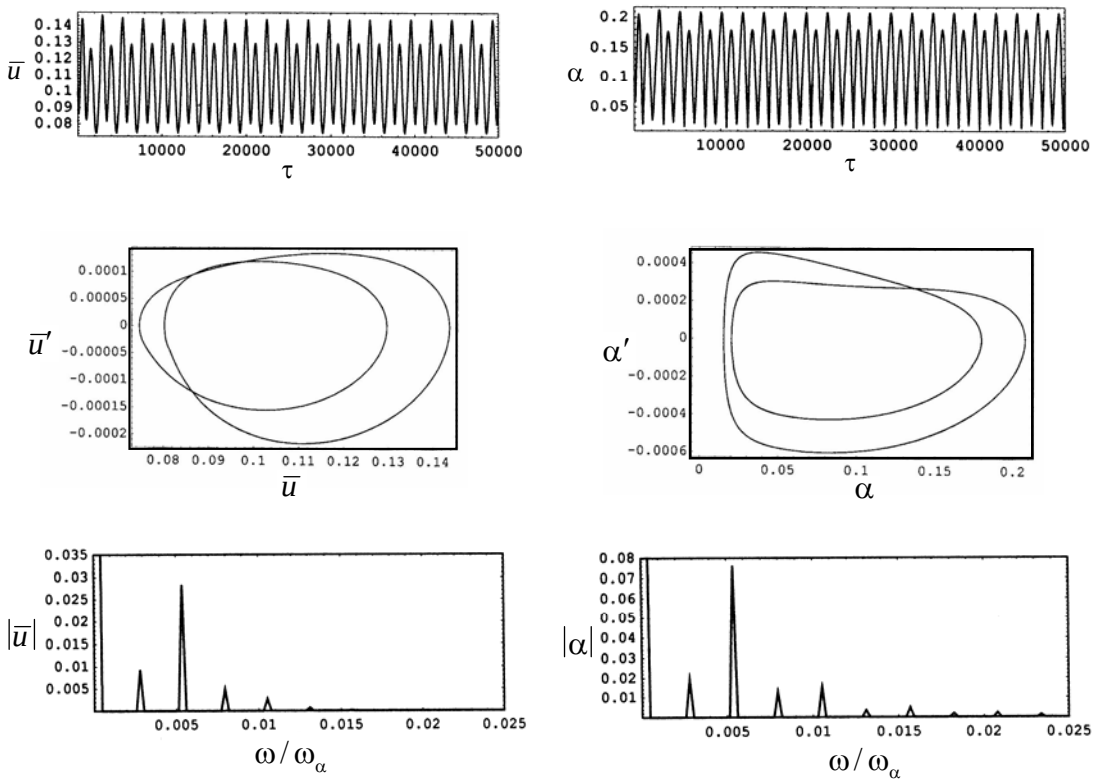


(b) $Y_0 = 0.005$

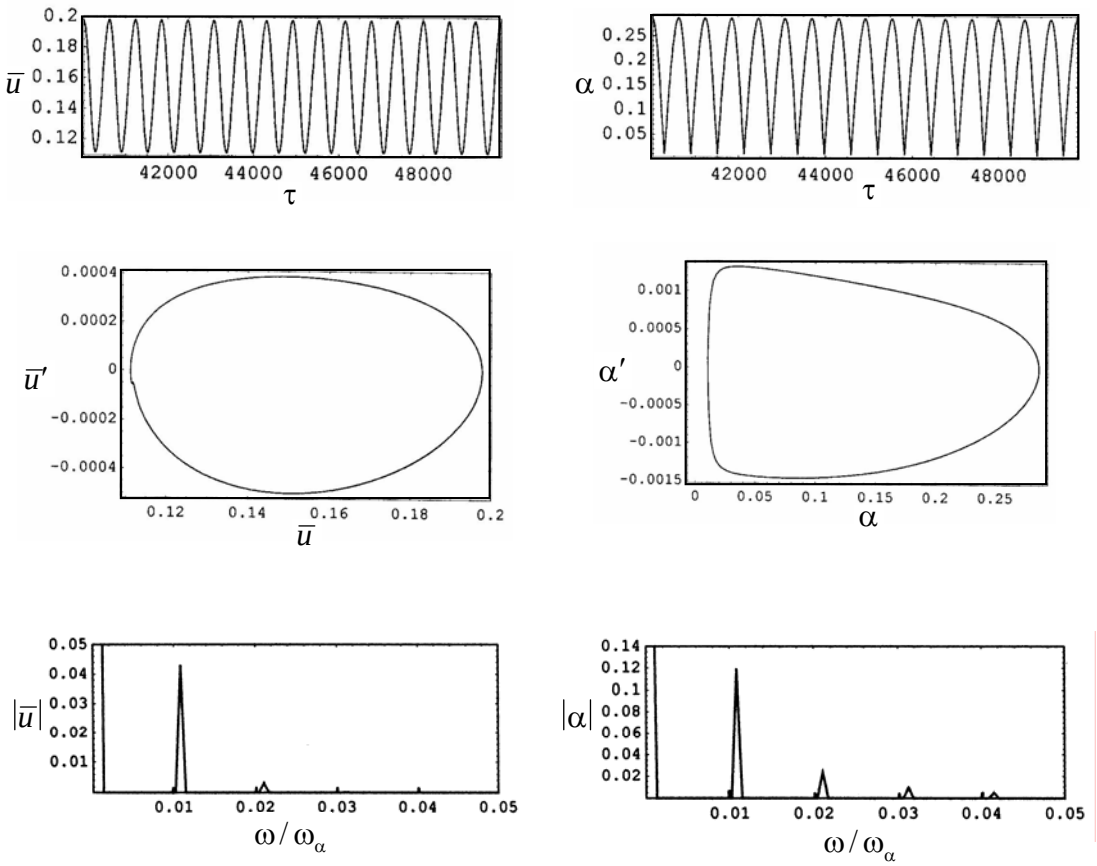


(c) $Y_0 = 0.01$

Figure 2.4. Time histories, phase diagrams, and FFTs at zero flow speed, $\Omega = \omega_1 + \omega_2$, $\omega_1 = 0.5\omega_2$, $\sigma_e = 0$, $\bar{u}(0) = 0.1$, $\alpha(0) = 0.1$, $\bar{u}'(0) = 0$, $\alpha'(0) = 0$

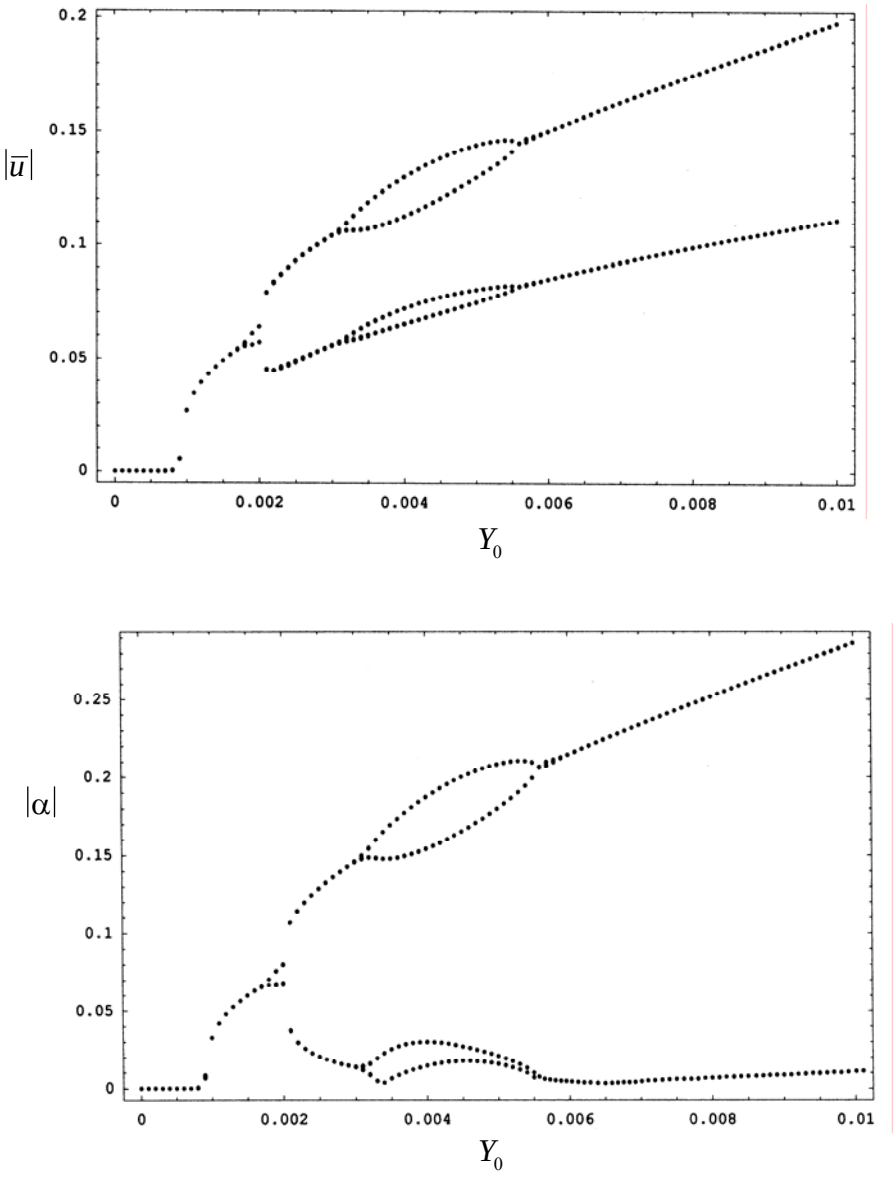


Figure 2.5. Bifurcation diagram at zero flow speed estimated at $\Omega = \omega_1 + \omega_2$, $\omega_1 = 0.5\omega_2$, for $\sigma_e = 0$, $\bar{u}(0) = 0.1$, $\alpha(0) = 0.1$, $\bar{u}'(0) = 0$, $\alpha'(0) = 0$.

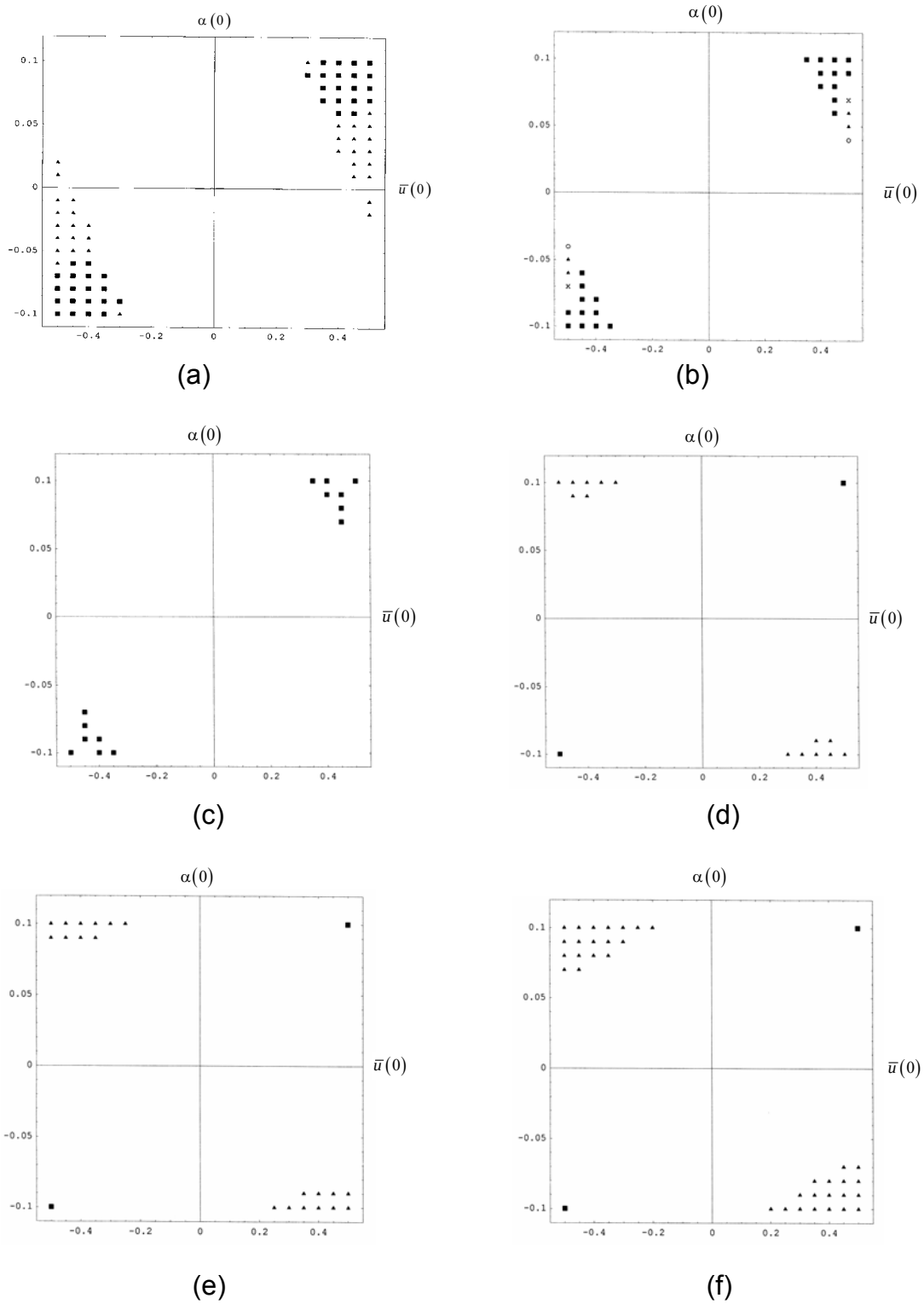


Figure 2.6 Domains of attractions for different values of excitation amplitude. (a) $Y_0 = 0$; (b) $Y_0 = 0.00875$; (c) $Y_0 = 0.01$; (d) $Y_0 = 0.014$; (e) $Y_0 = 0.015$; (f) $Y_0 = 0.017$

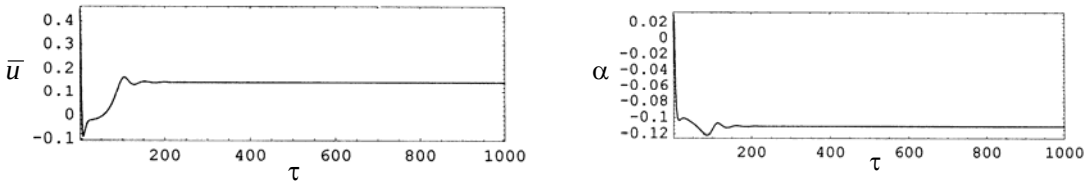


Figure 2.7 Time histories at critical flow speed $U_\infty / b\omega_\alpha = 4.965$, $Y_0 = 0$, $\Omega = \omega_1 + \omega_2$, $\omega_1 = \omega_2$, $\sigma_e = 0$, $\sigma_i = 0.061$, $\bar{u}(0) = 0.45$, $\alpha(0) = 0.01$, $\bar{u}'(0) = 0$, $\alpha'(0) = 0$

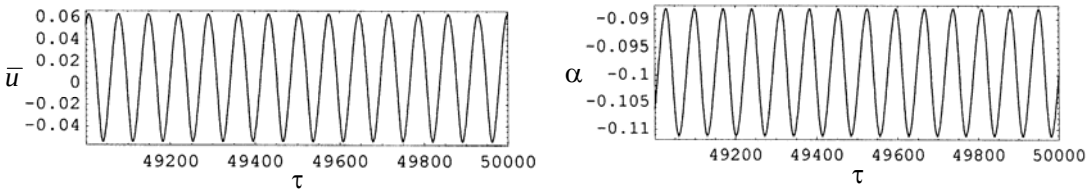


(a) $\bar{u}(0) = 0.5$, $\alpha(0) = 0.04$, $\bar{u}'(0) = 0$, $\alpha'(0) = 0$

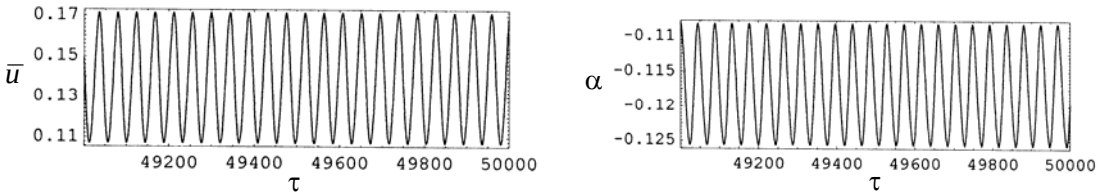


(b) $\bar{u}(0) = 0.5$, $\alpha(0) = 0.05$, $\bar{u}'(0) = 0$, $\alpha'(0) = 0$

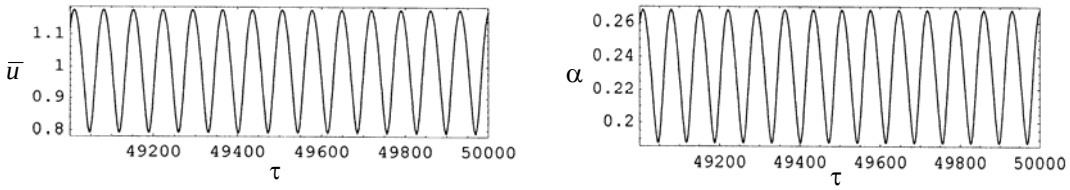


(c) $\bar{u}(0) = 0.5$, $\alpha(0) = 0.07$, $\bar{u}'(0) = 0$, $\alpha'(0) = 0$

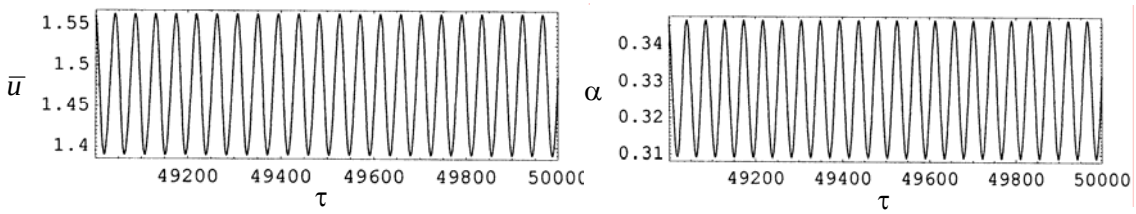


(d) $\bar{u}(0)=0.5$, $\alpha(0)=0.1$, $\bar{u}'(0)=0$, $\alpha'(0)=0$

Figure 2.8 Time histories records at critical flow speed $U_\infty / b\omega_\alpha = 4.965$, $Y_0 = 0.00875$; $\Omega = \omega_1 + \omega_2$, $\omega_1 = \omega_2$, $\sigma_e = 0$, $\sigma_i = 0.061$

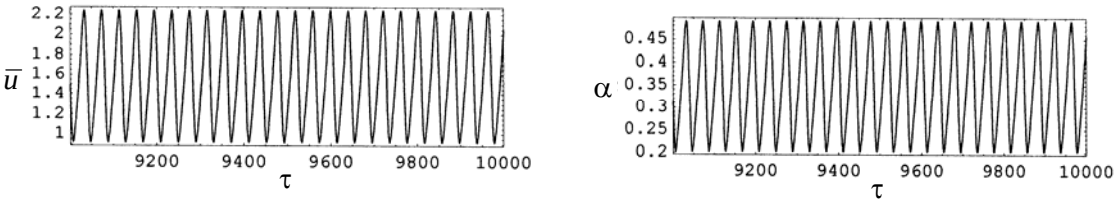


Figure 2.9 Time histories at critical flow speed $U_\infty / b\omega_\alpha = 4.965$, $Y_0 = 0.01$, $\Omega = \omega_1 + \omega_2$, $\omega_1 = \omega_2$, $\sigma_e = 0$, $\sigma_i = 0.061$, $\bar{u}(0)=0.5$, $\alpha(0)=0.1$, $\bar{u}'(0)=0$, $\alpha'(0)=0$

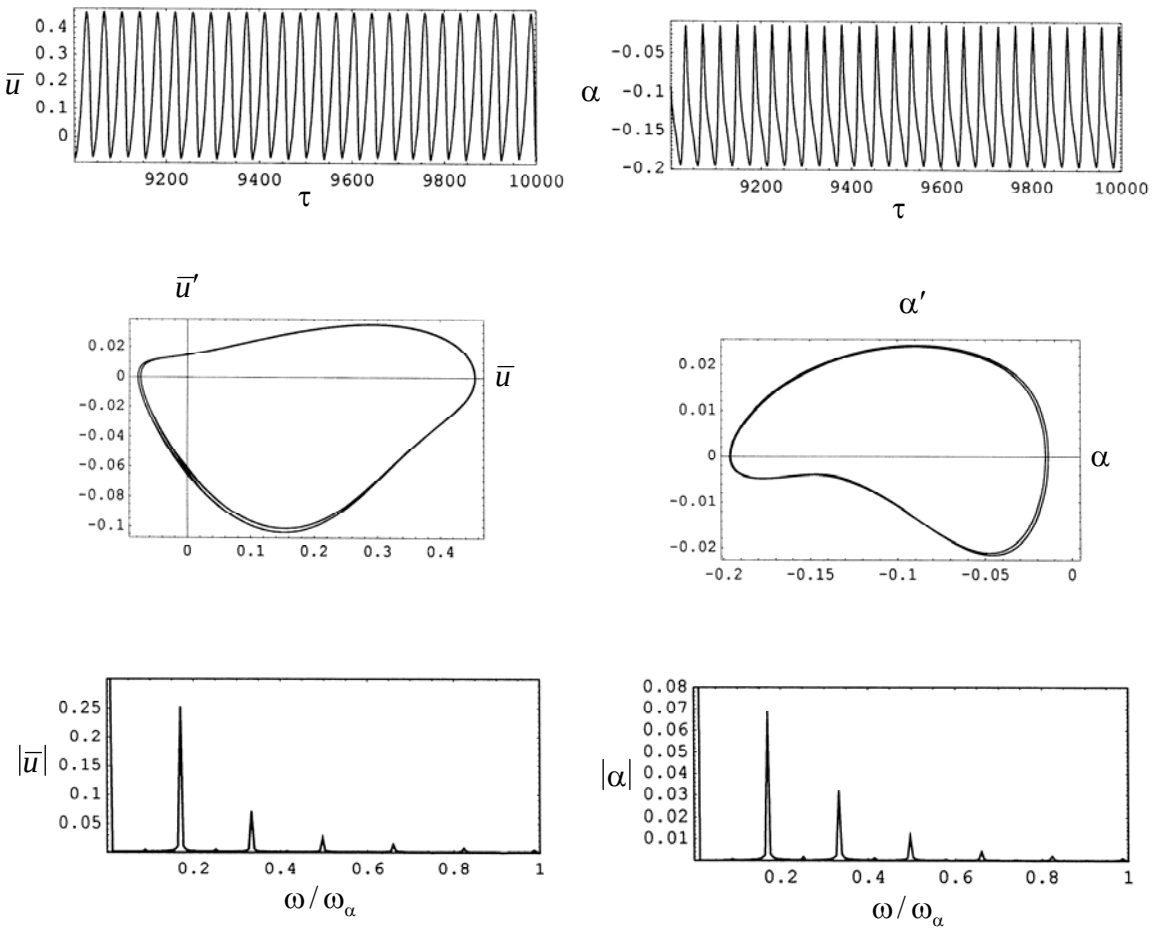


(a) $\bar{u}(0)=0.5,\ \alpha(0)=-0.1,\ \bar{u}'(0)=0,\ \alpha'(0)=0$

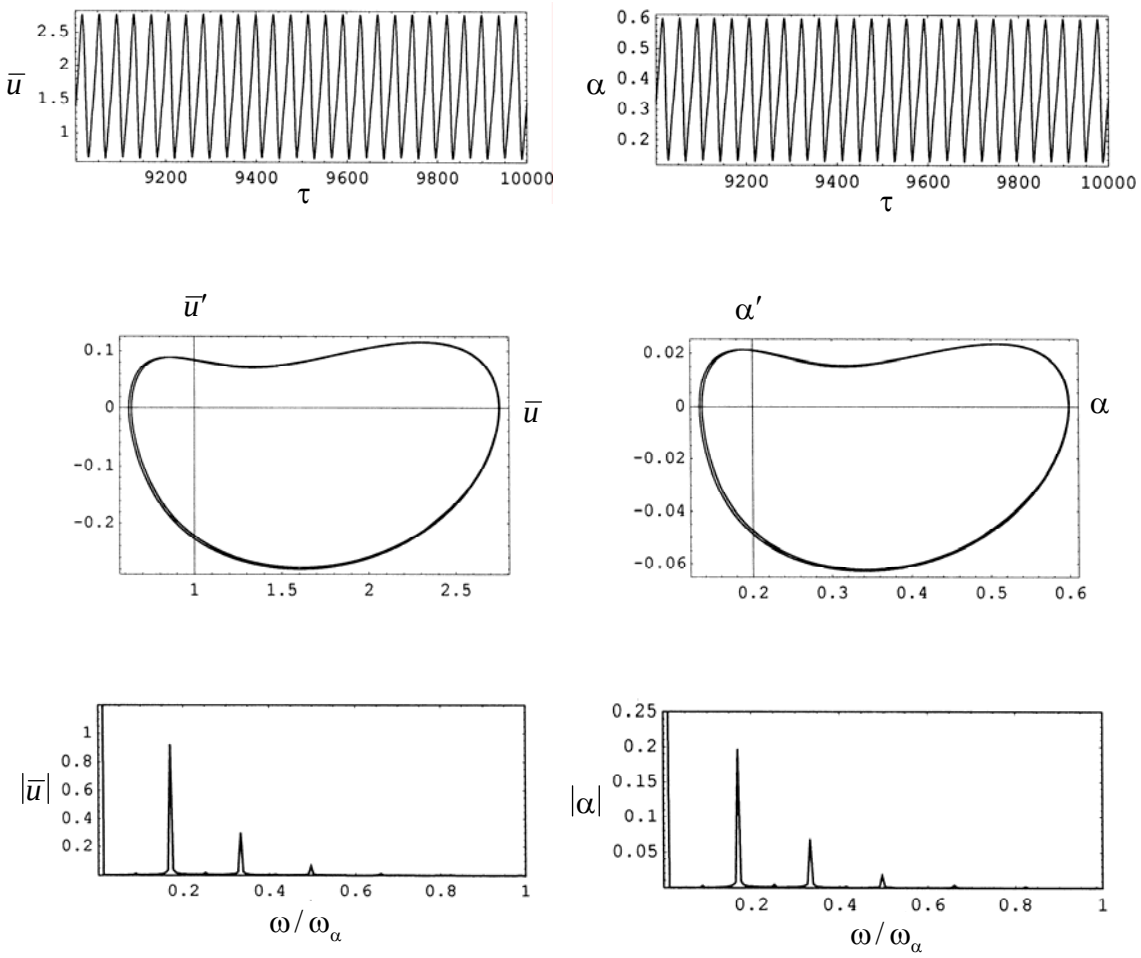


(b) $\bar{u}(0)=0.5$, $\alpha(0)=0.1$, $\bar{u}'(0)=0$, $\alpha'(0)=0$

Figure 2.10 Time histories, phase diagrams, and FFTs at critical flow speed $U_\infty/b\omega_\alpha=4.965$, $Y_0=0.014$; $\Omega=\omega_1+\omega_2$, $\omega_1=\omega_2$, $\sigma_e=0$, $\sigma_i=0.061$,

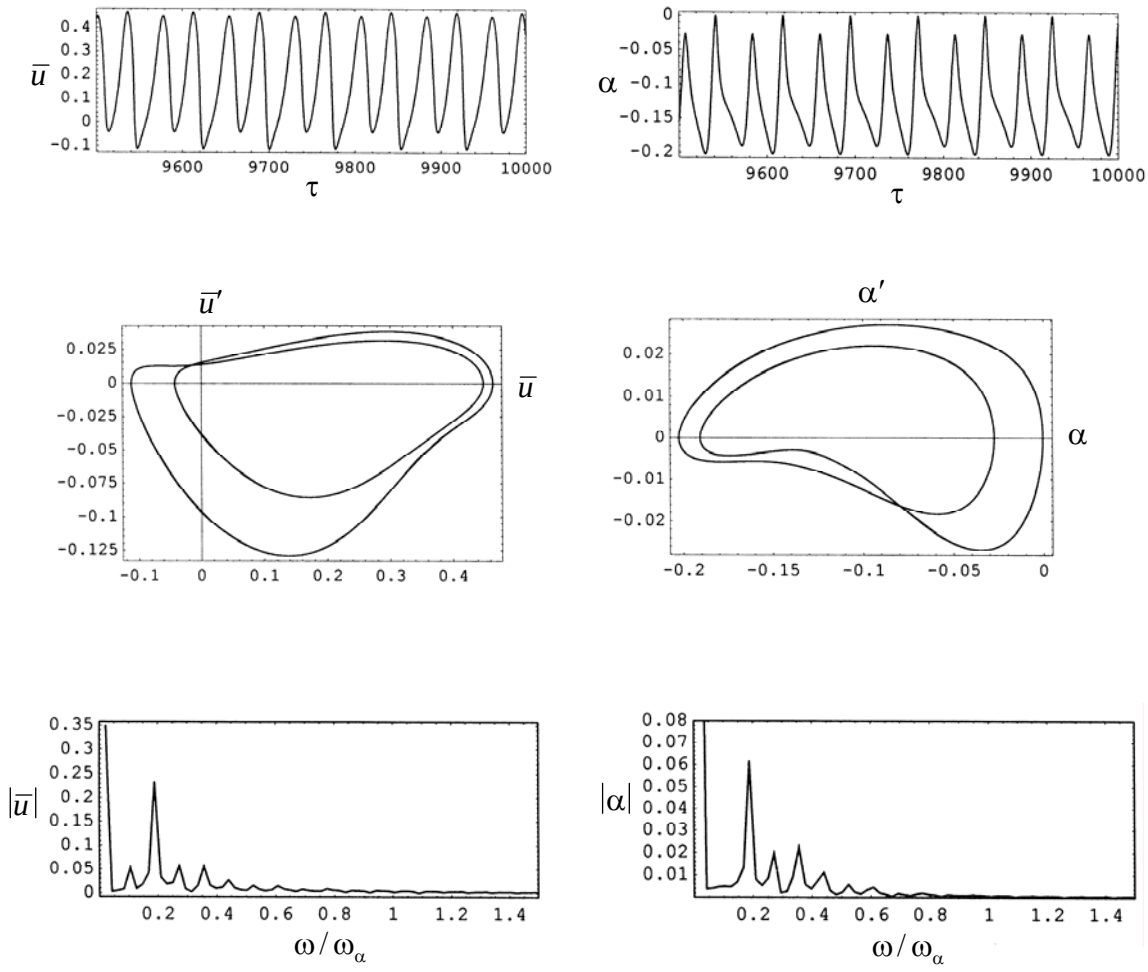


(a) $\bar{u}(0)=0.5,\ \alpha(0)=-0.1,\ \bar{u}'(0)=0,\ \alpha'(0)=0$

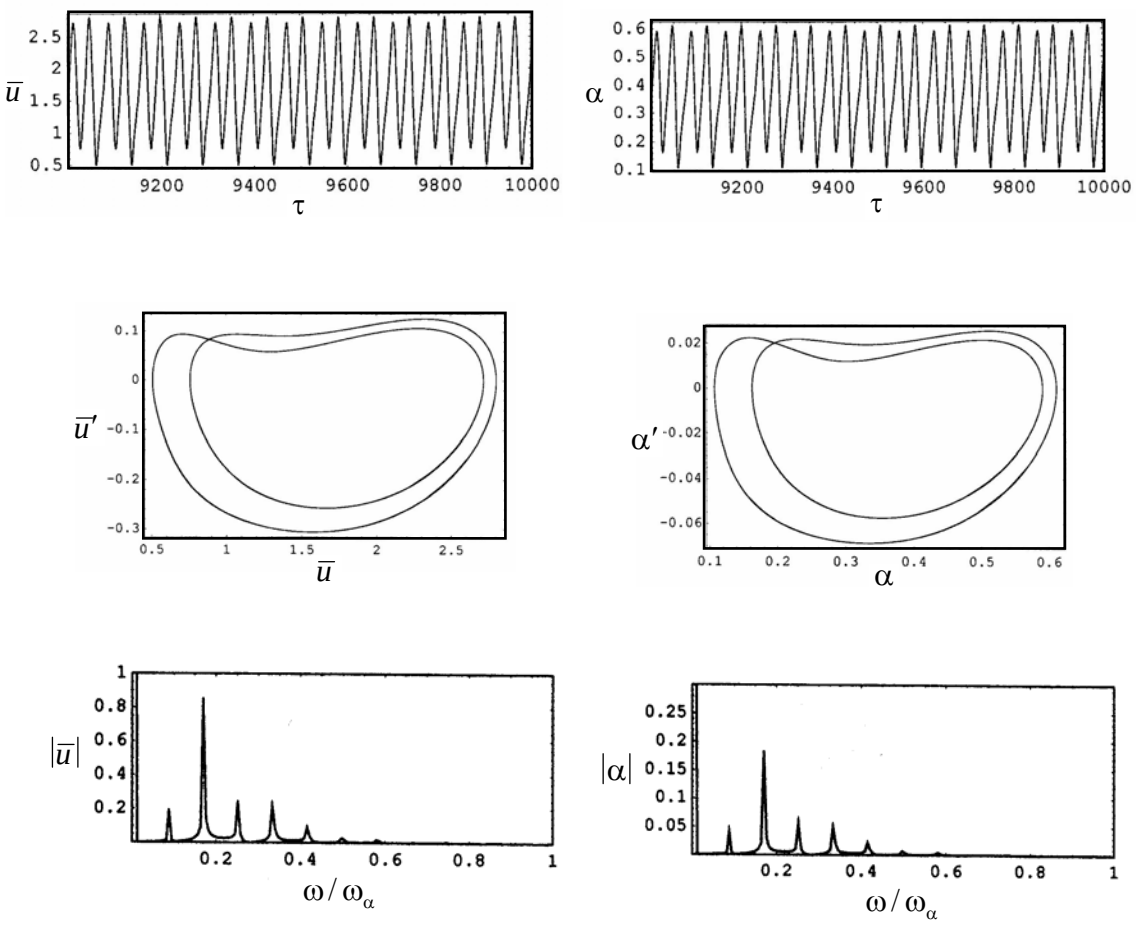


(b) $\bar{u}(0)=0.5$, $\alpha(0)=0.1$, $\bar{u}'(0)=0$, $\alpha'(0)=0$

Figure 2.11 Time histories, phase diagrams, and FFTs at critical flow speed $U_\infty/b\omega_\alpha=4.965$, $Y_0=0.015$; $\Omega=\omega_1+\omega_2$, $\omega_1=\omega_2$, $\sigma_e=0$, $\sigma_i=0.061$,

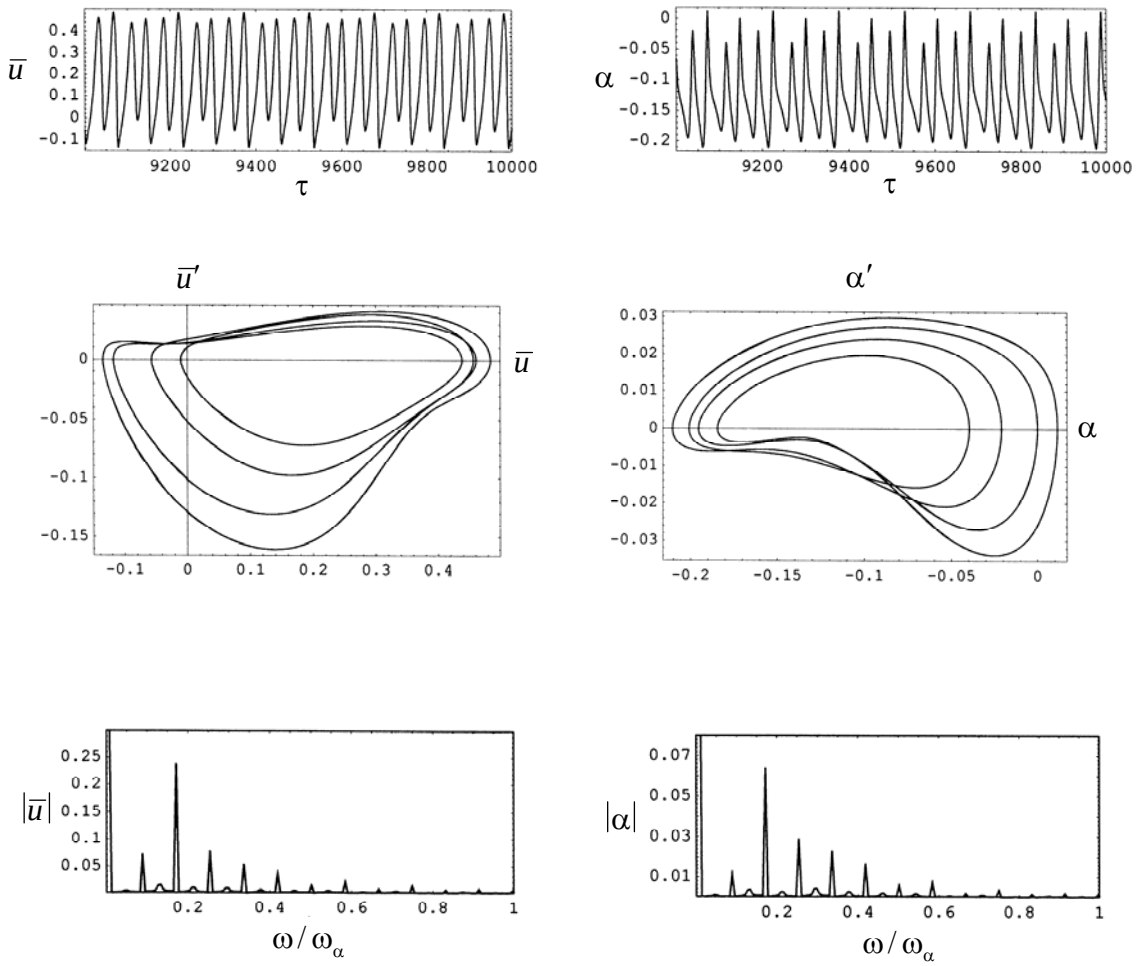


(a) $\bar{u}(0) = 0.5,\ \alpha(0) = -0.1,\ \bar{u}'(0) = 0, \alpha'(0) = 0$

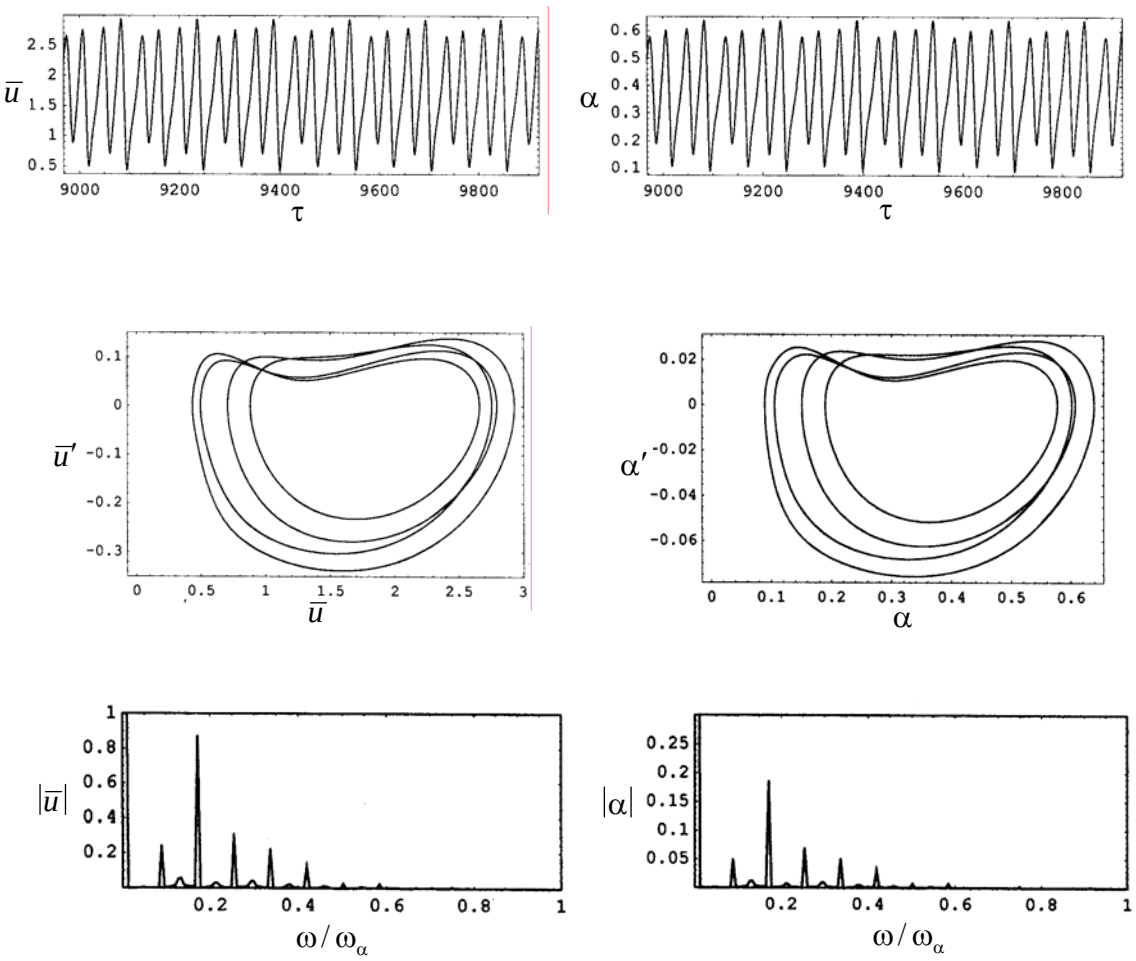


(b) $\bar{u}(0)=0.5$, $\alpha(0)=0.1$, $\bar{u}'(0)=0$, $\alpha'(0)=0$

Figure 2.12 Time histories, phase diagrams, and FFTs at critical flow speed $U_\infty/b\omega_\alpha=4.965$, $Y_0=0.016$; $\Omega=\omega_1+\omega_2$, $\omega_1=\omega_2$, $\sigma_e=0$, $\sigma_i=0.061$

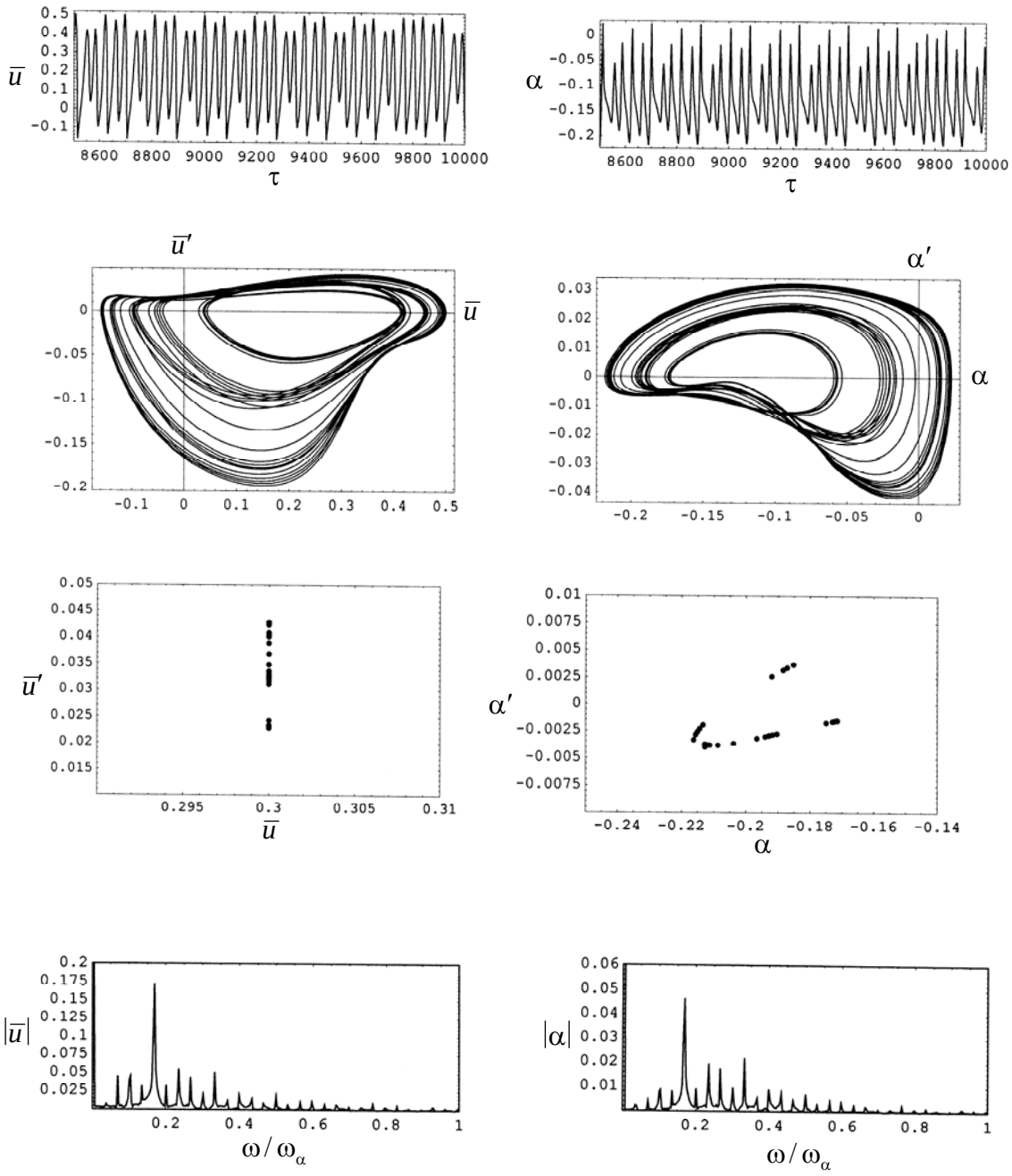


(a) $\bar{u}(0)=0.5,\ \alpha(0)=-0.1,\ \bar{u}'(0)=0, \alpha'(0)=0$

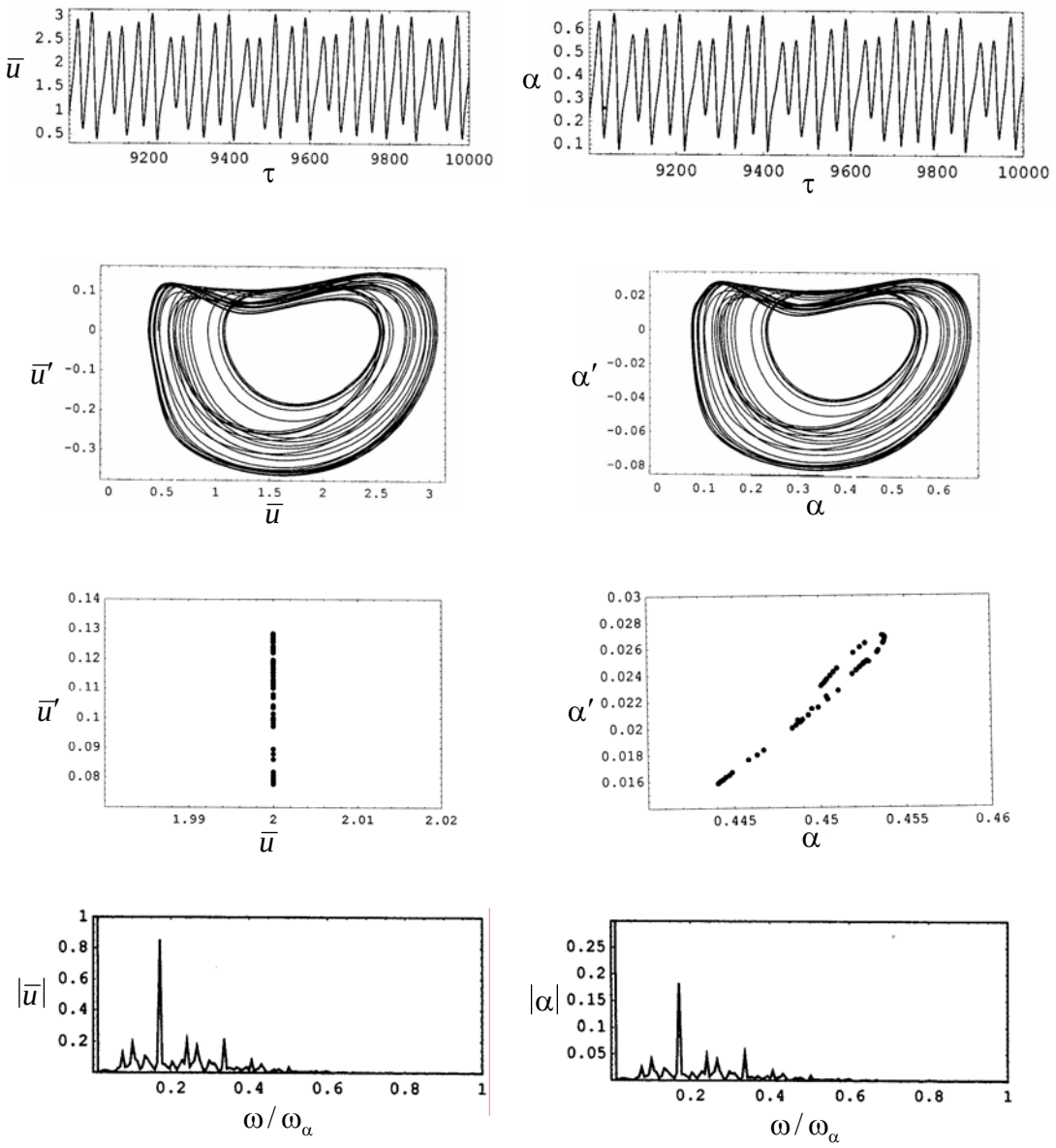


(b) $\bar{u}(0)=0.5$, $\alpha(0)=0.1$, $\bar{u}'(0)=0$, $\alpha'(0)=0$

Figure 2.13 Time histories, Poincare maps, phase diagrams, and FFTs at critical flow speed $U_\infty/b\omega_\alpha=4.965$, $Y_0=0.017$, $\Omega=\omega_1+\omega_2$, $\omega_1=\omega_2$, $\sigma_e=0$, $\sigma_i=0.061$

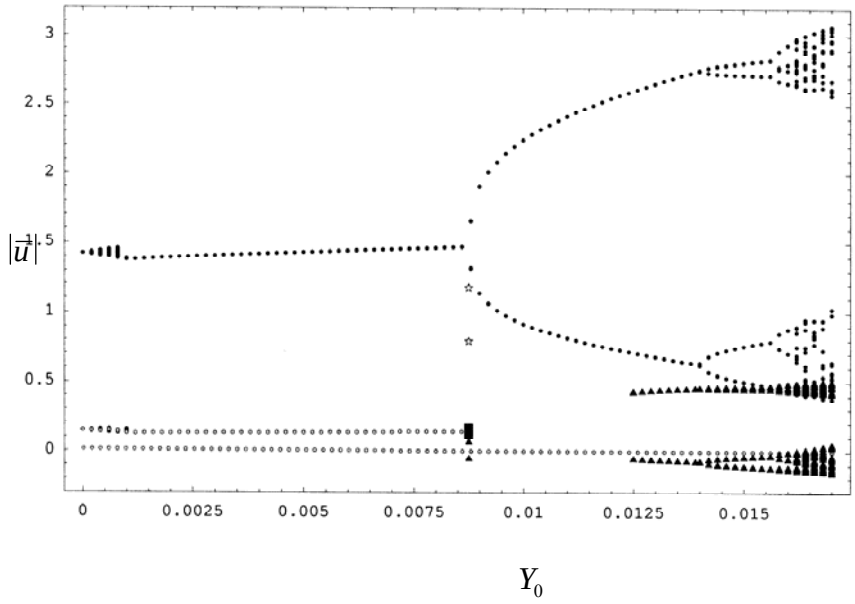


(a) Dependence of bending amplitude on excitation amplitude

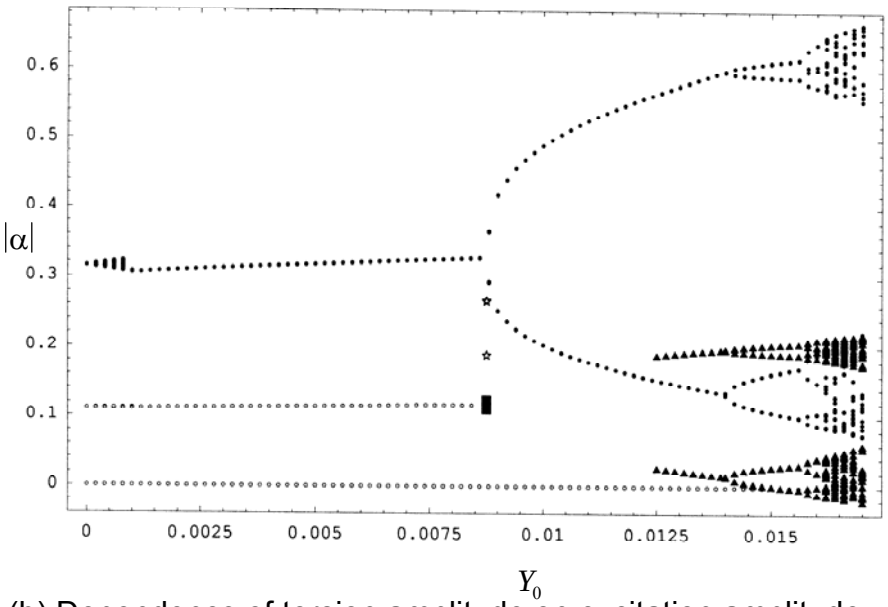


(b) Dependence of torsion amplitude on excitation amplitude

Figure 2.14 Bifurcation diagrams at critical flow speed $U_\infty / b\omega_\alpha = 4.965$, $\Omega = \omega_1 + \omega_2$, $\omega_1 = \omega_2$, $\sigma_e = 0$, $\sigma_i = 0.061$.

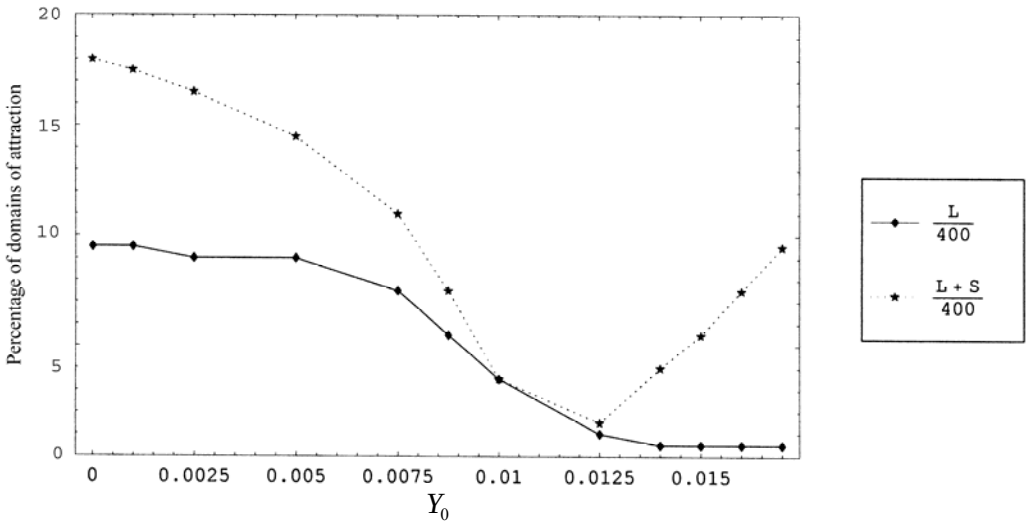


Figure 2.15 Stabilization effect of parametric excitation at critical flow speed $U_\infty / b\omega_\alpha = 4.965$ showing the percentage of domains of attraction for large amplitude response (solid diamond curve) and large plus small amplitude responses (dotted solid circle curve).

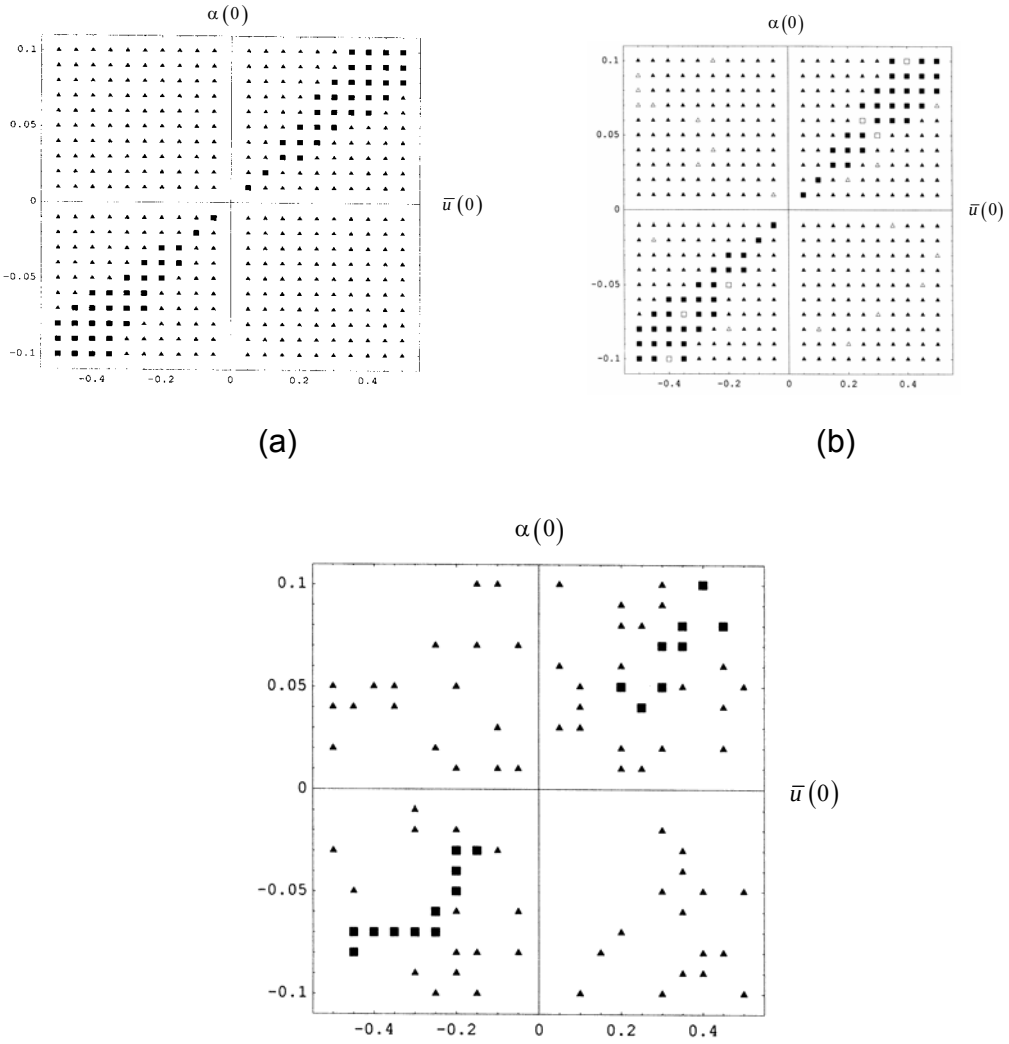


Figure 2.16. Domains of attraction at post-critical flow speed $U_\infty / b\omega_\alpha = 5.02$ for $\Omega = \omega_1 + \omega_2$, $\omega_1 = \omega_2$, $\sigma_e = 0$, $\sigma_i = 0.061$, and different values of excitation amplitude. (a) $Y_0 = 0$; (b) $Y_0 = 0.013$; (c) $Y_0 = 0.014$.

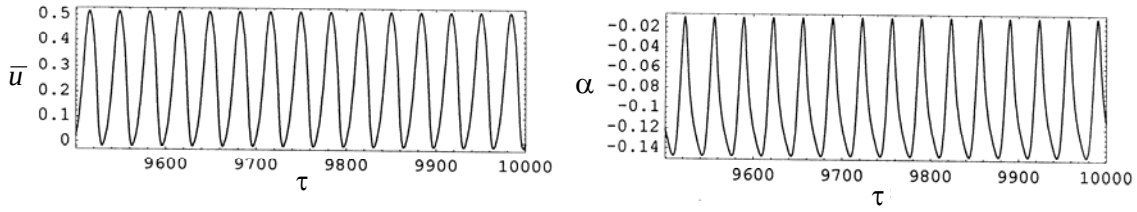


(a) $\bar{u}(0)=0.2$, $\alpha(0)=0.01$, $\bar{u}'(0)=0, \alpha'(0)=0$

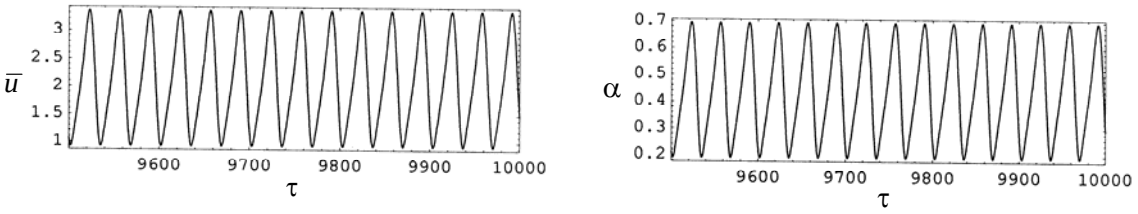


(b) $\bar{u}(0)=0.5$, $\alpha(0)=0.1$, $\bar{u}'(0)=0, \alpha'(0)=0$

Figure 2.17 Time histories at post-critical flow speed $U_\infty / b\omega_\alpha = 5.02$, $Y_0 = 0$; $\Omega = \omega_1 + \omega_2$, $\omega_1 = \omega_2$, $\sigma_e = 0$, $\sigma_i = 0.061$

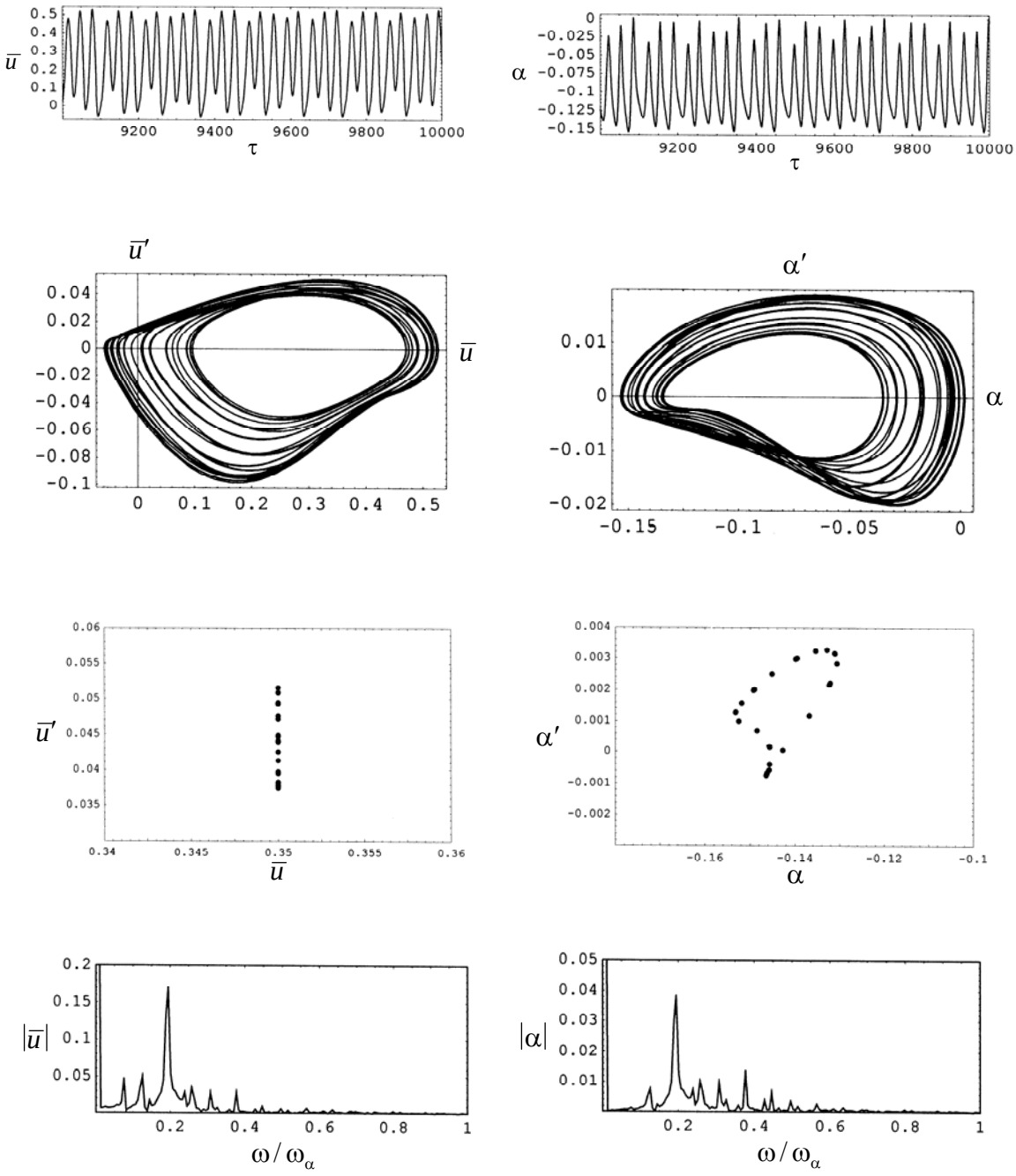


(a) $\bar{u}(0)=0.2$, $\alpha(0)=0.01$, $\bar{u}'(0)=0$, $\alpha'(0)=0$

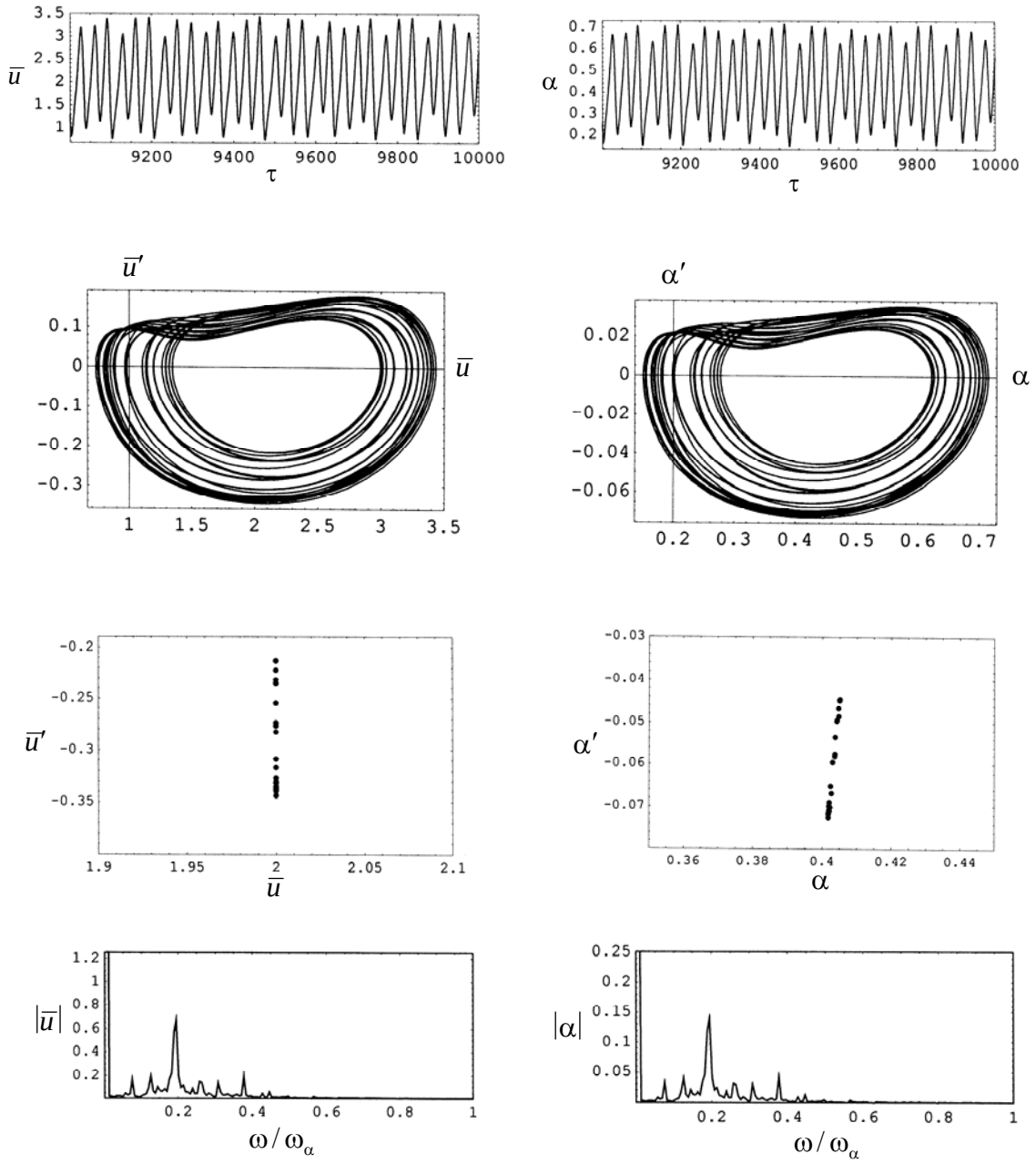


(b) $\bar{u}(0)=0.5$, $\alpha(0)=0.1$, $\bar{u}'(0)=0$, $\alpha'(0)=0$

Figure 2.18 Time histories, Poincare maps, phase diagrams, and FFTs at post-critical flow speed $U_\infty/b\omega_\alpha=5.02$, $Y_0=0.0025$; $\Omega=\omega_1+\omega_2$, $\omega_1=\omega_2$, $\sigma_e=0$, $\sigma_i=0.061$

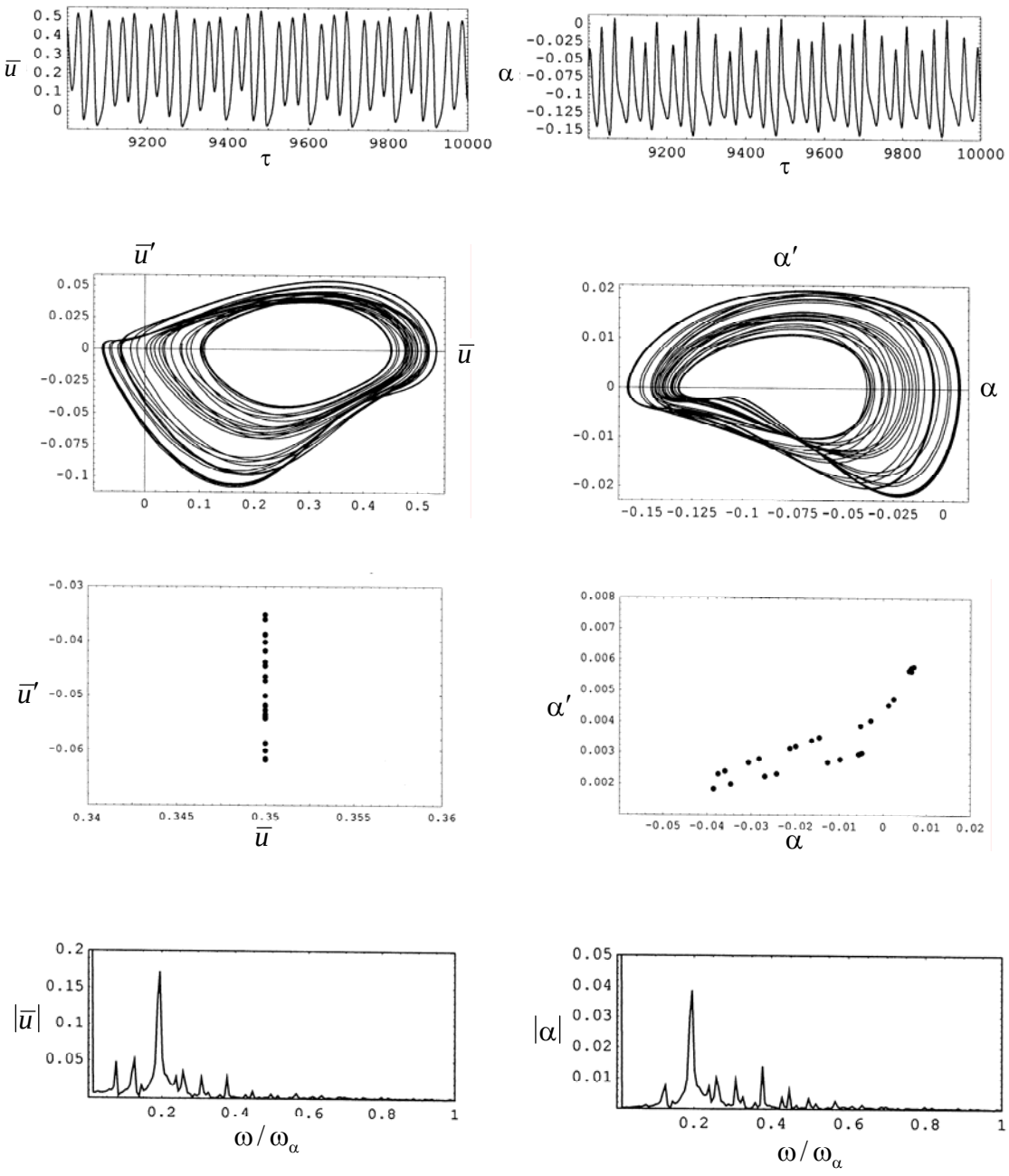


(a) $\bar{u}(0)=0.2,\ \alpha(0)=0.01,\ \bar{u}'(0)=0, \alpha'(0)=0$

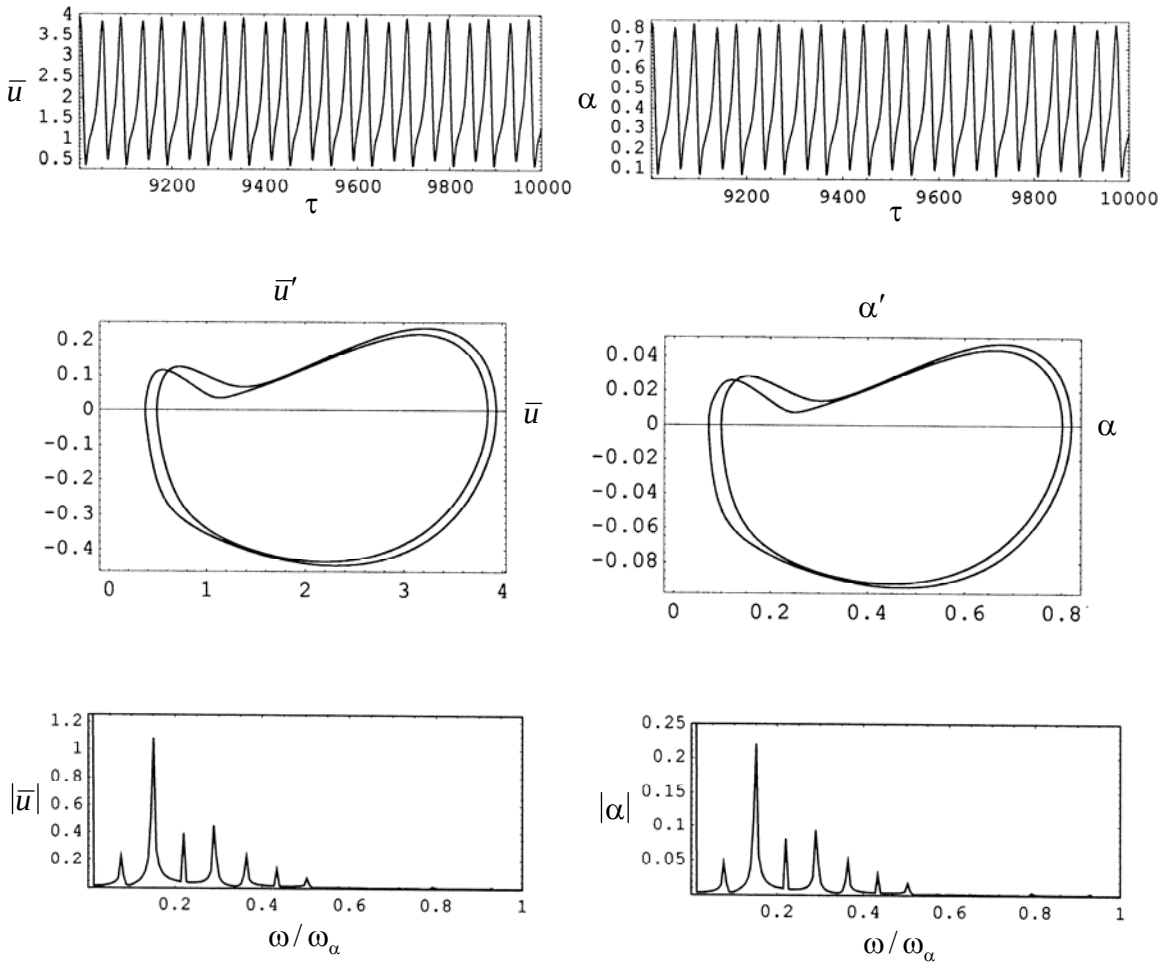


(b) $\bar{u}(0)=0.5$, $\alpha(0)=0.1$, $\bar{u}'(0)=0$, $\alpha'(0)=0$

Figure 2.19 Time histories, Poincare maps, phase diagrams, and FFTs at post-critical flow speed $U_\infty/b\omega_\alpha=5.02$, $Y_0=0.004$, $\Omega=\omega_1+\omega_2$, $\omega_1=\omega_2$, $\sigma_e=0$, $\sigma_i=0.061$

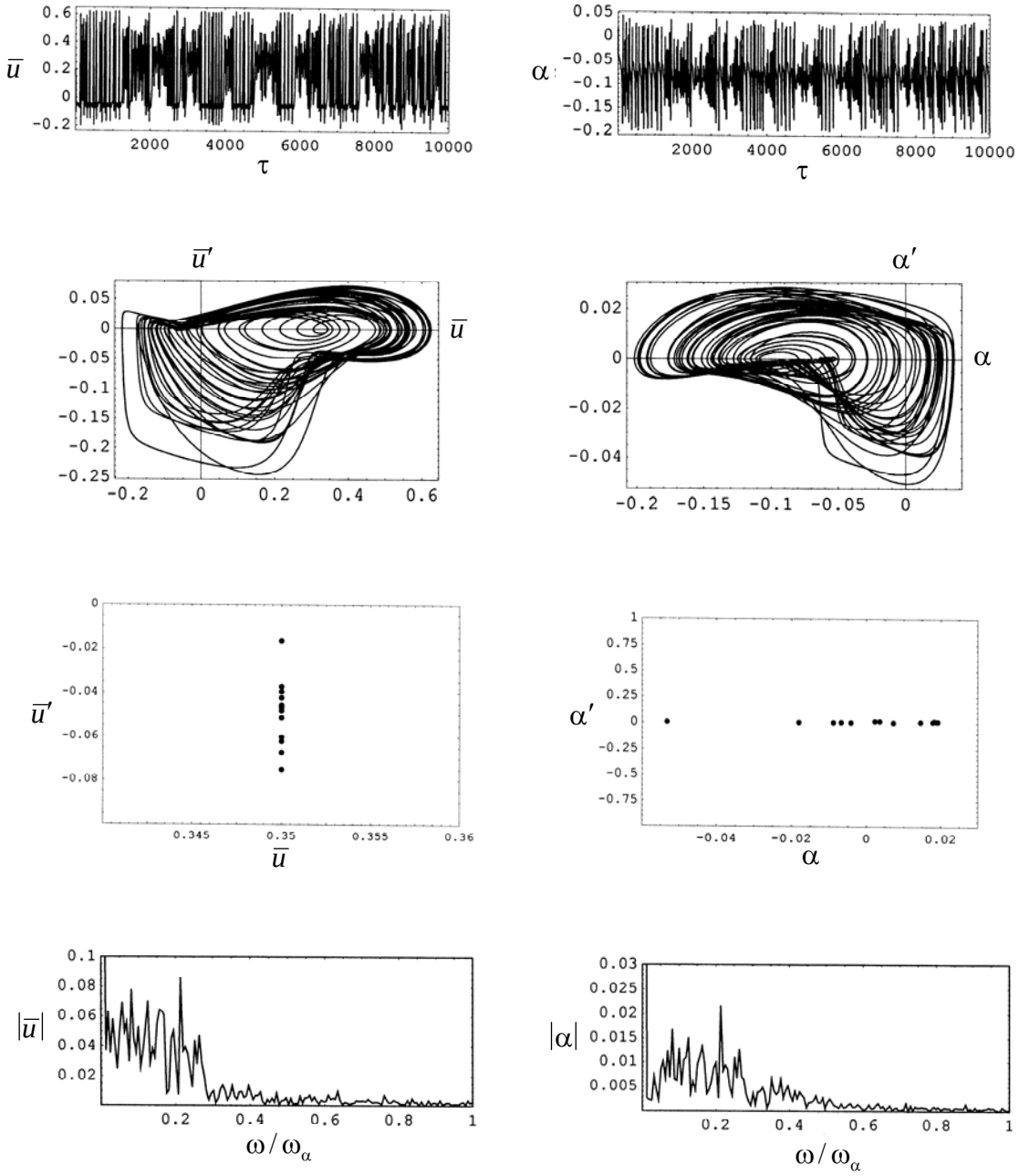


(a) $\bar{u}(0)=0.2,\ \alpha(0)=0.01,\ \bar{u}'(0)=0,\alpha'(0)=0$

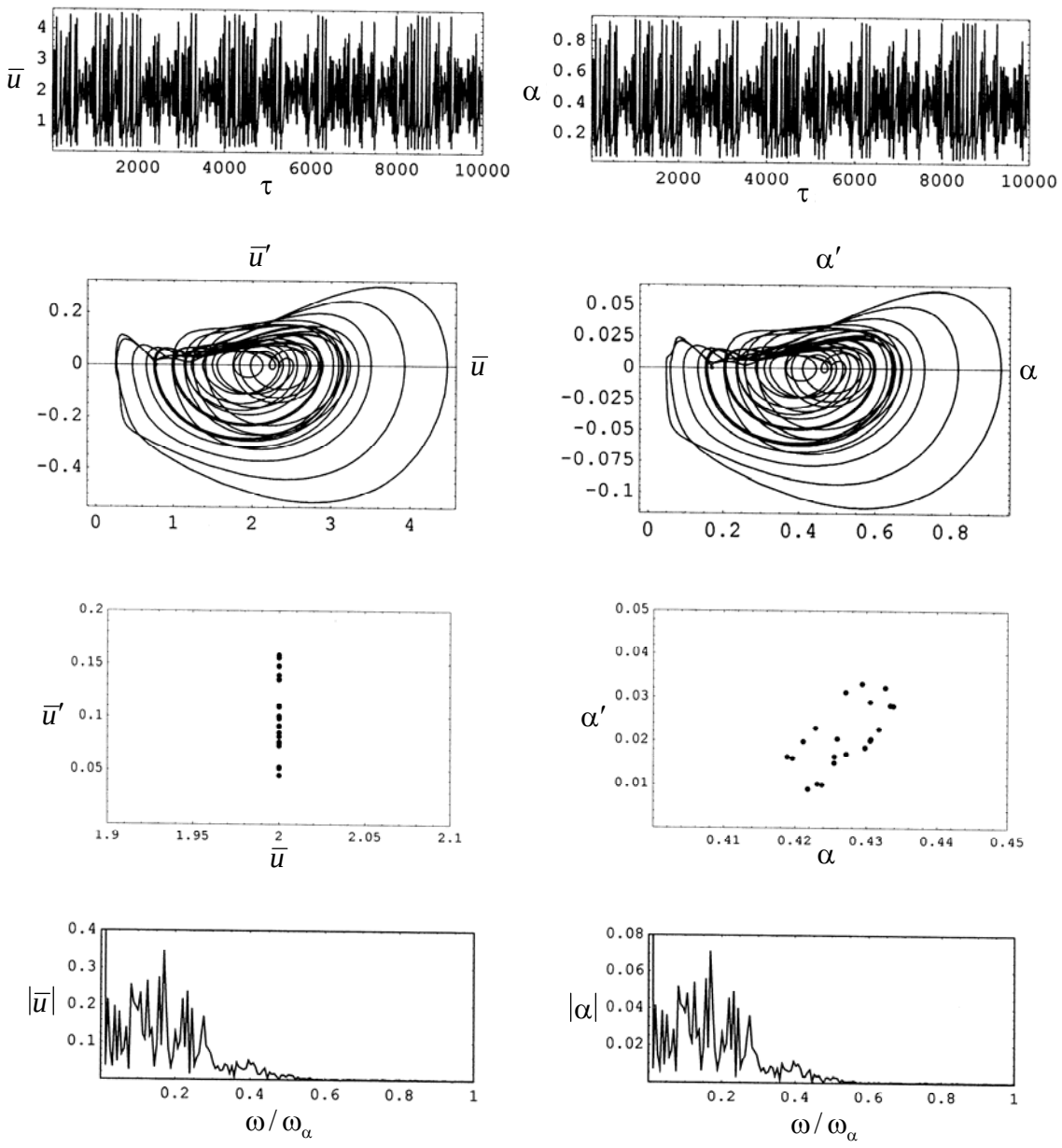


(b) $\bar{u}(0)=0.5$, $\alpha(0)=0.1$, $\bar{u}'(0)=0$, $\alpha'(0)=0$

Figure 2.20 Time histories, Poincare maps, phase diagrams, and FFTs at post-critical flow speed $U_\infty/b\omega_\alpha=5.02$, $Y_0=0.0075$; $\Omega=\omega_1+\omega_2$, $\omega_1=\omega_2$, $\sigma_e=0$, $\sigma_i=0.061$

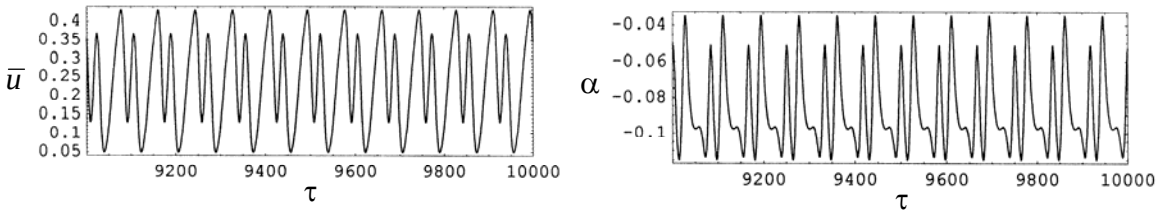


(a) $\bar{u}(0)=0.2$, $\alpha(0)=0.01$, $\bar{u}'(0)=0$, $\alpha'(0)=0$

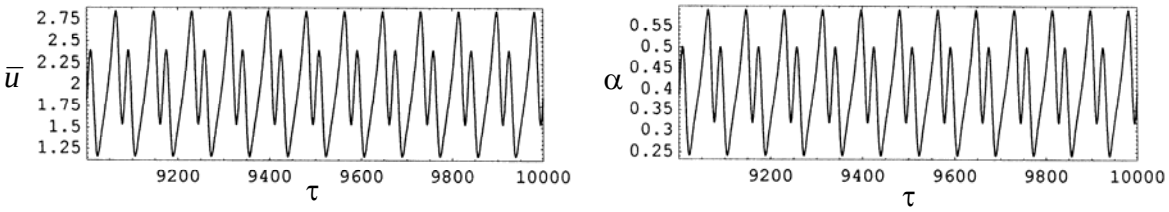


(b) $\bar{u}(0)=0.5$, $\alpha(0)=0.1$, $\bar{u}'(0)=0$, $\alpha'(0)=0$

Figure 2.21 Time histories at post-critical flow speed $U_\infty / b\omega_\alpha = 5.02$, $Y_0 = 0.01$; $\Omega = \omega_1 + \omega_2$, $\omega_1 = \omega_2$, $\sigma_e = 0$, $\sigma_i = 0.061$

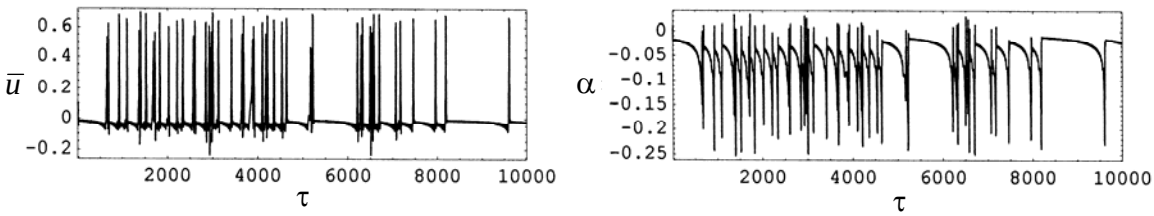


(a) $\bar{u}(0)=0.1,\ \alpha(0)=0.01,\ \bar{u}'(0)=0,\alpha'(0)=0$

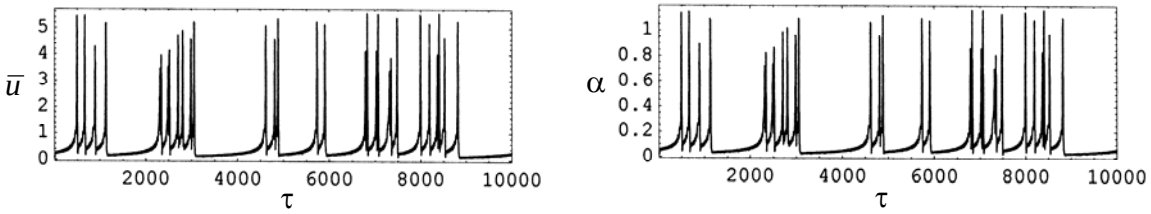


(b) $\bar{u}(0)=0.1,\ \alpha(0)=0.02,\ \bar{u}'(0)=0,\alpha'(0)=0$

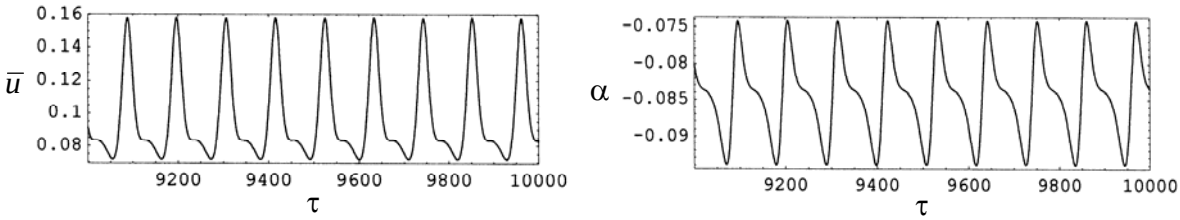


(c) $\bar{u}(0)=0.2,\ \alpha(0)=0.02,\ \bar{u}'(0)=0,\alpha'(0)=0$

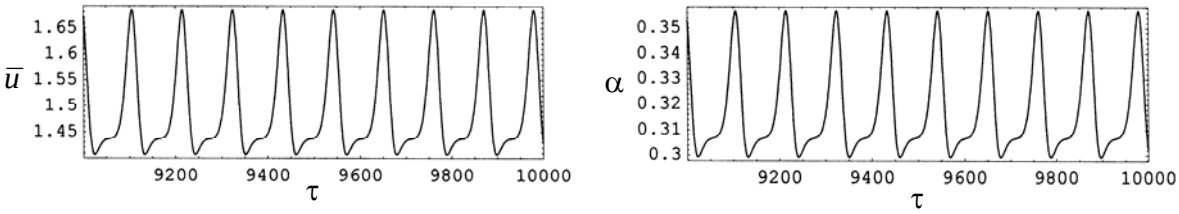


(d) $\bar{u}(0)=0.4,\ \alpha(0)=0.1,\ \bar{u}'(0)=0,\alpha'(0)=0$

Figure 2.22 Time histories at post-critical flow speed $U_\infty / b\omega_\alpha = 5.02$, $Y_0 = 0.013$; $\Omega = \omega_1 + \omega_2$, $\omega_1 = \omega_2$, $\sigma_e = 0$, $\sigma_i = 0.061$

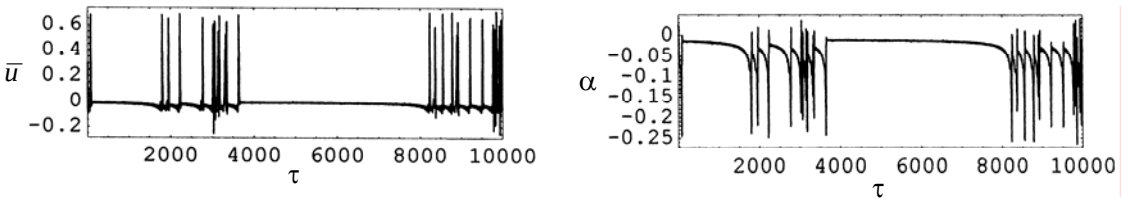


(a) $\bar{u}(0)=0.3$, $\alpha(0)=0.02$, $\bar{u}'(0)=0$, $\alpha'(0)=0$

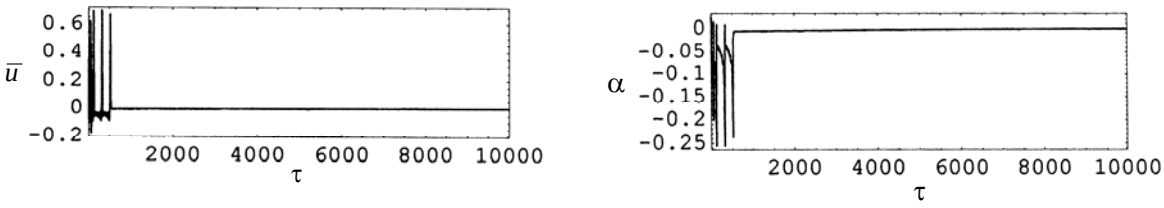


(b) $\bar{u}(0)=0.35$, $\alpha(0)=0.02$, $\bar{u}'(0)=0$, $\alpha'(0)=0$

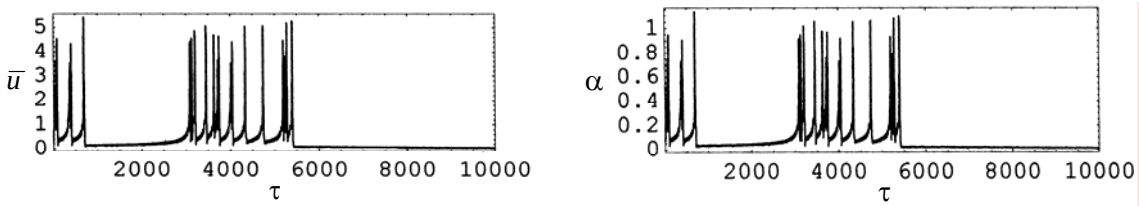


(c) $\bar{u}(0)=0.25$, $\alpha(0)=0.07$, $\bar{u}'(0)=0$, $\alpha'(0)=0$

Figure 2.23 Time histories at post-critical flow speed $U_\infty / b\omega_\alpha = 5.02$, $Y_0 = 0.014$; $\Omega = \omega_1 + \omega_2$, $\omega_1 = \omega_2$, $\sigma_e = 0$, $\sigma_i = 0.061$

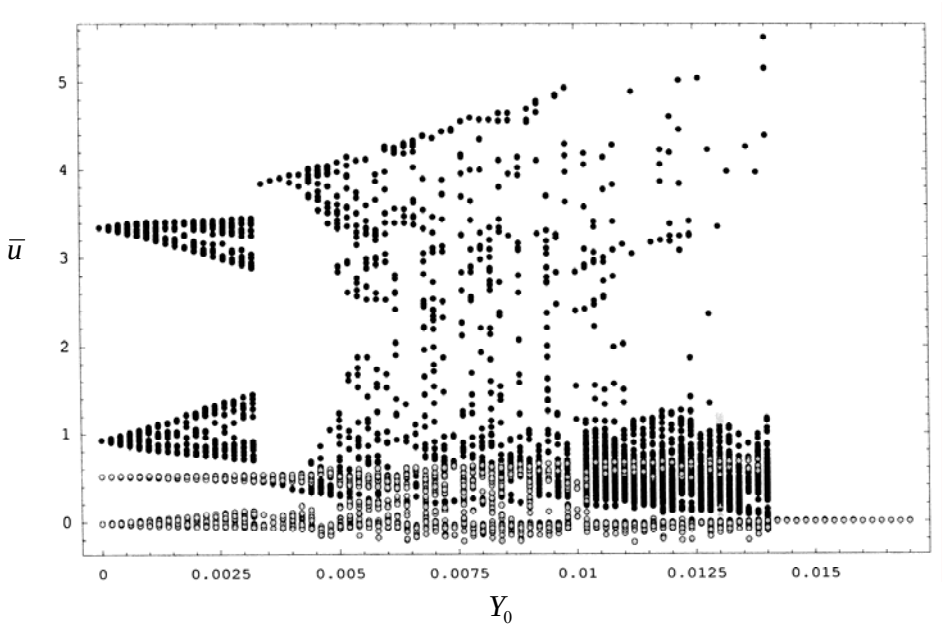


(a) Dependence of bending amplitude on excitation amplitude

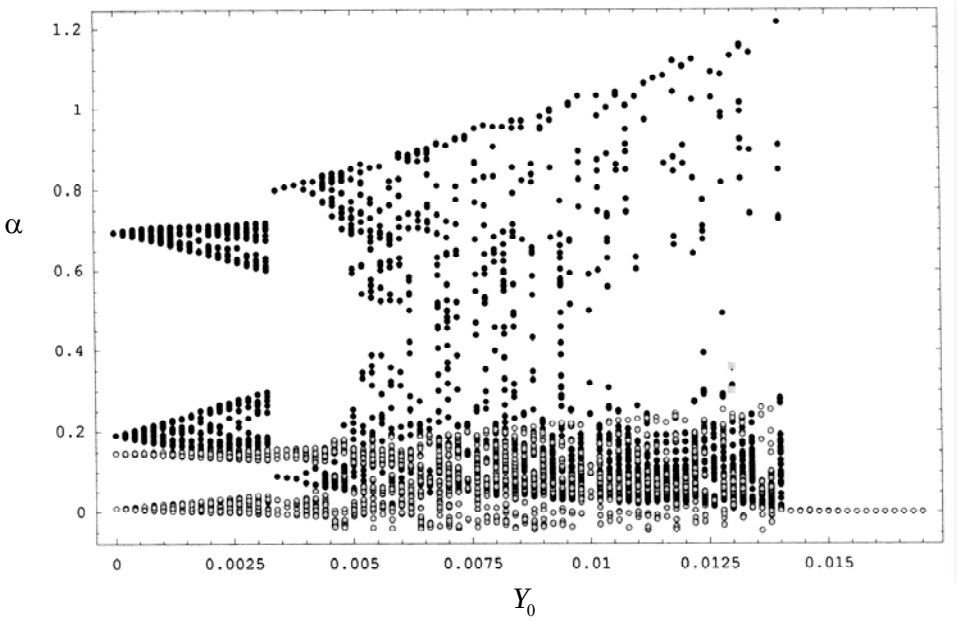


(b) Dependence of torsion amplitude on excitation amplitude

Figure 2.24 Bifurcation diagrams showing different regions of response behavior at post-critical flow speed $U_\infty / b\omega_\alpha = 5.02$, $\Omega = \omega_1 + \omega_2$, $\omega_1 = \omega_2$, $\sigma_e = 0$, $\sigma_i = 0.061$

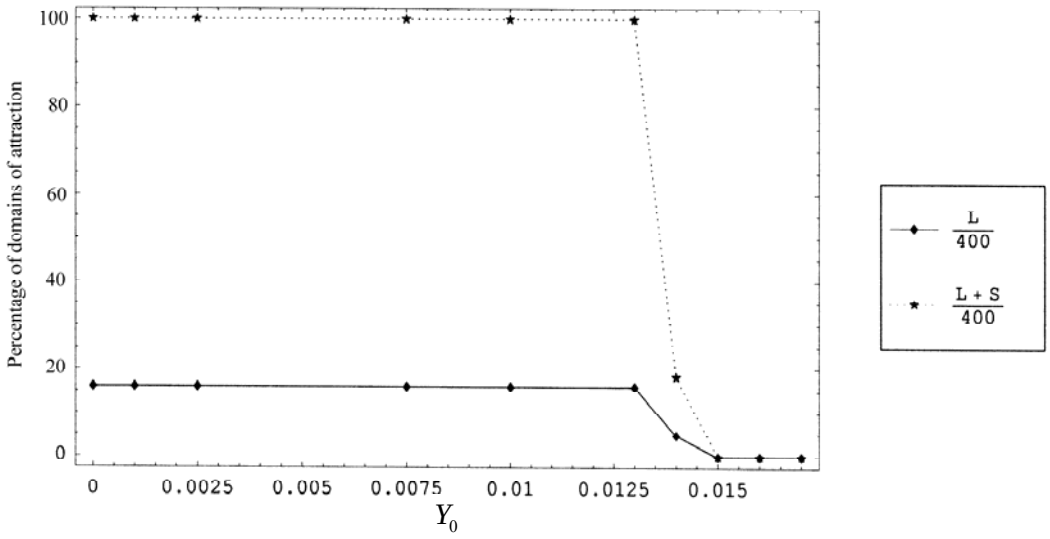


Figure 2.25 Stabilization effect of parametric excitation at post-critical flow speed $U_\infty / b\omega_\alpha = 5.02$ showing the percentage of domains of attraction for large amplitude response (diamond-solid curve) and large plus small amplitude responses (star-dotted curve).

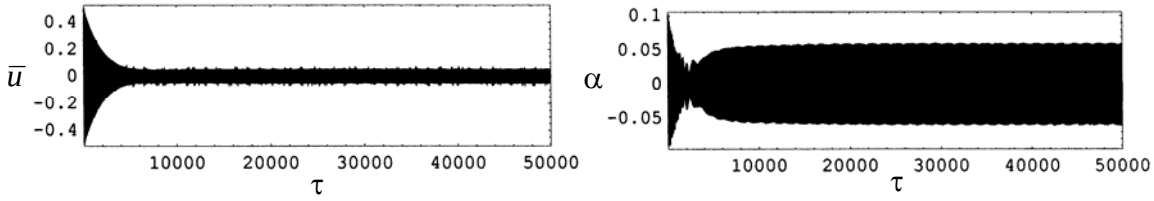


(a) $Y_0 = 0.001$

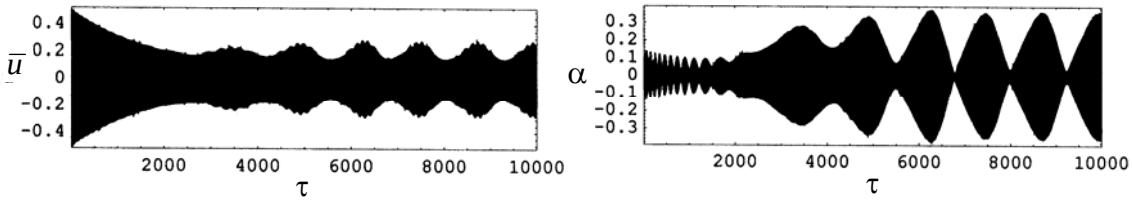


(b) $Y_0 = 0.005$

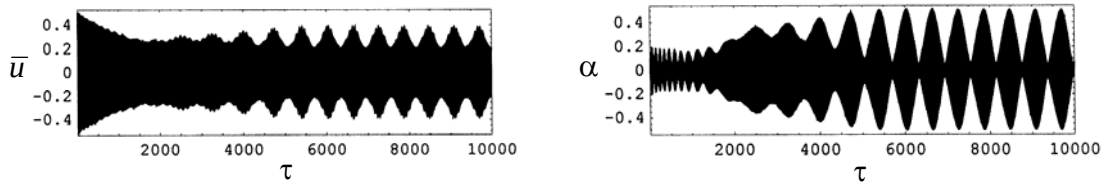


(c) $Y_0 = 0.01$

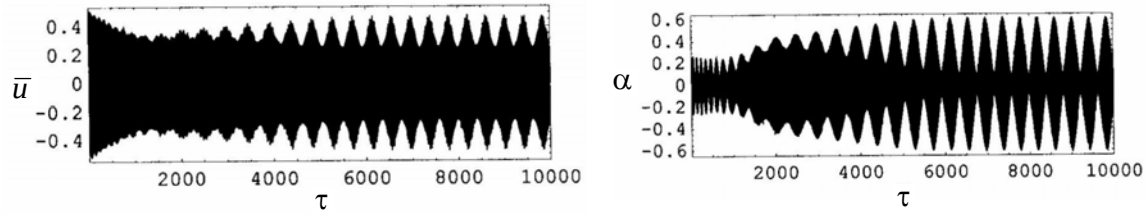


(d) $Y_0 = 0.015$

Figure 2.26 Response time history records according to numerical simulation at zero flow speed for different values of excitation amplitude and for the same initial conditions $\bar{u}(0) = 0.5$, $\alpha(0) = 0.1$, $\bar{u}'(0) = 0$, $\alpha'(0) = 0$.

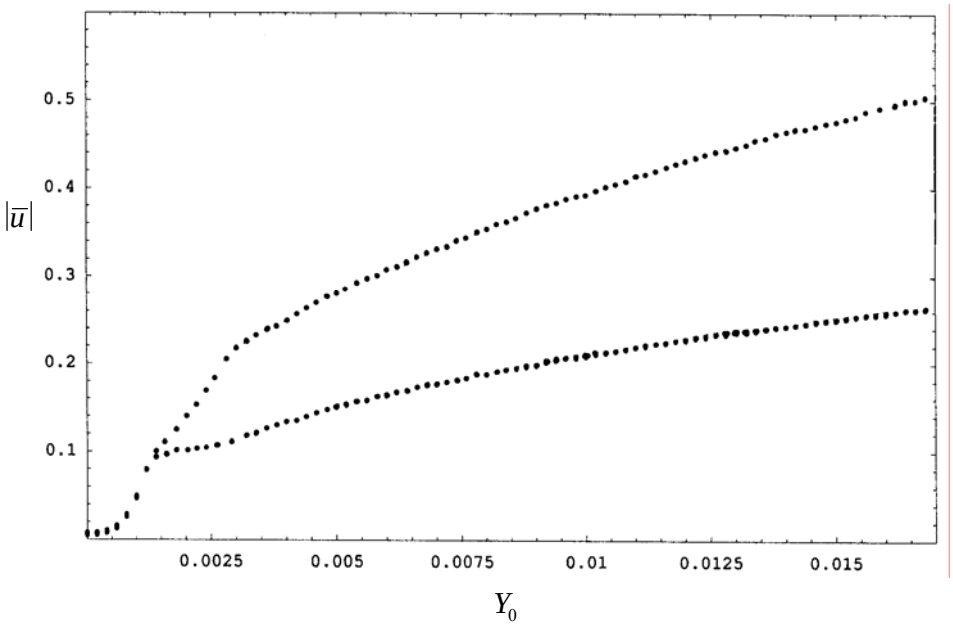


(a) Dependence of bending response amplitude on excitation amplitude

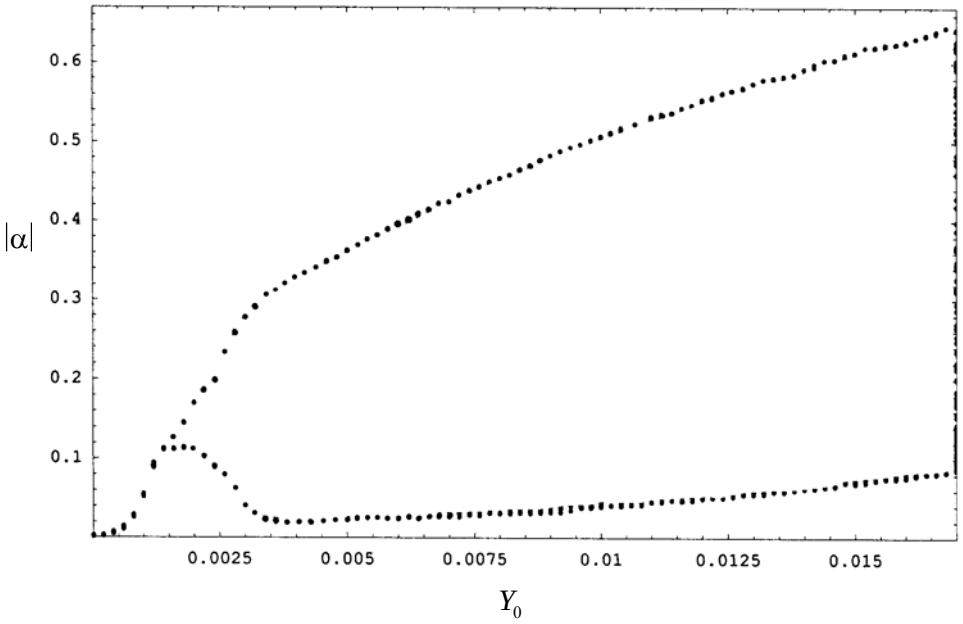


(b) Dependence of torsion response amplitude on excitation amplitude

Figure 2.27 Bifurcation diagram according to the numerical simulation of equations of motion at zero flow speed and $\Omega = \omega_1 + \omega_2$, $\omega_1 = 0.5\omega_2$, $\bar{u}(0) = 0.5$, $\alpha(0) = 0.1$, $\bar{u}'(0) = 0$, $\alpha'(0) = 0$.

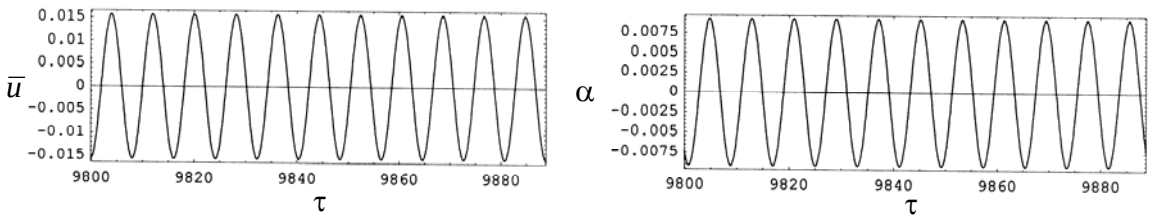


(a) $Y_0 = 0$, $\bar{u}(0) = 0.05$, $\alpha(0) = 0.01$, $\bar{u}'(0) = 0$, $\alpha'(0) = 0$

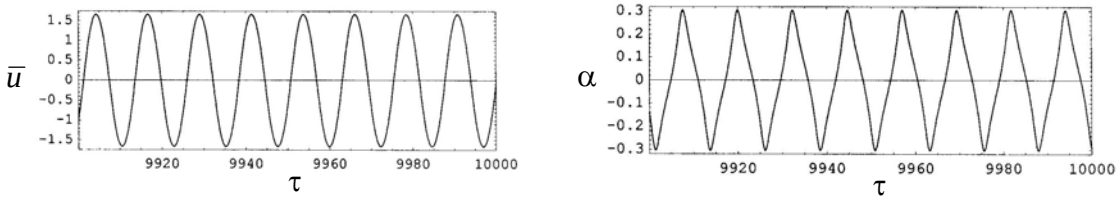


(b) $Y_0 = 0$, $\bar{u}(0) = 0.5$, $\alpha(0) = 0.1$, $\bar{u}'(0) = 0$, $\alpha'(0) = 0$

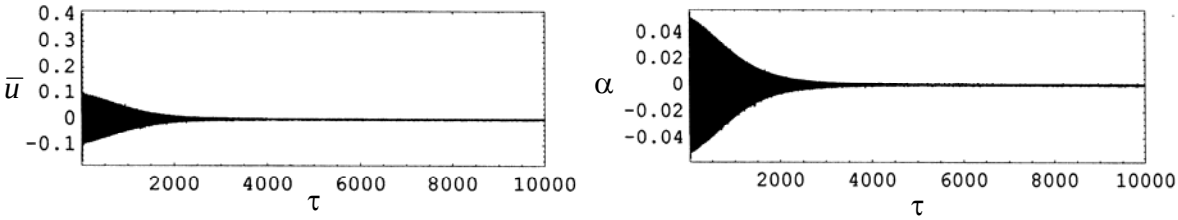


(c) $Y_0 = 0.00875$, $\bar{u}(0) = 0.4$, $\alpha(0) = 0.02$, $\bar{u}'(0) = 0$, $\alpha'(0) = 0$

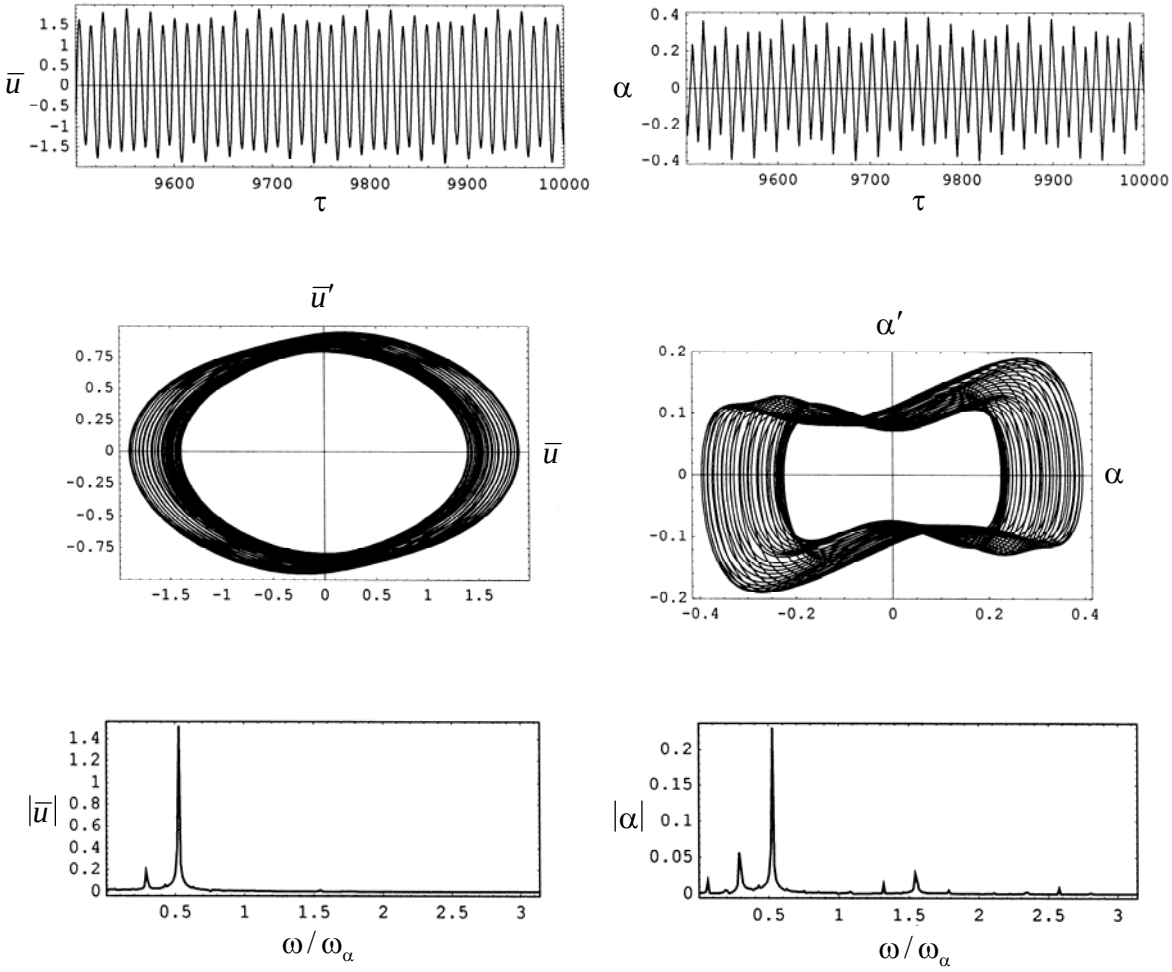


(d) $Y_0 = 0.00875$, $\bar{u}(0) = 0.5$, $\alpha(0) = 0.04$, $\bar{u}'(0) = 0$, $\alpha'(0) = 0$

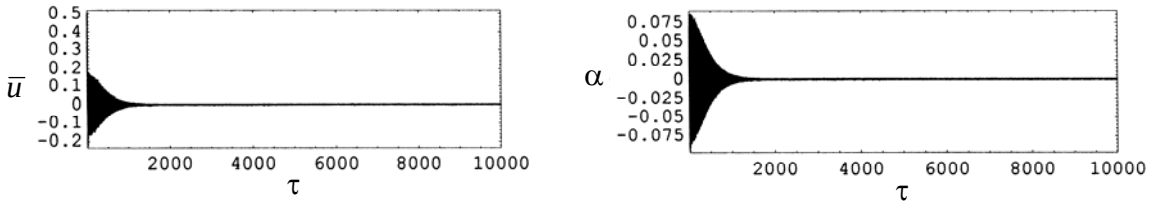


(e) $Y_0 = 0.014$, $\bar{u}(0) = 0.2$, $\alpha(0) = 0.1$, $\bar{u}'(0) = 0$, $\alpha'(0) = 0$

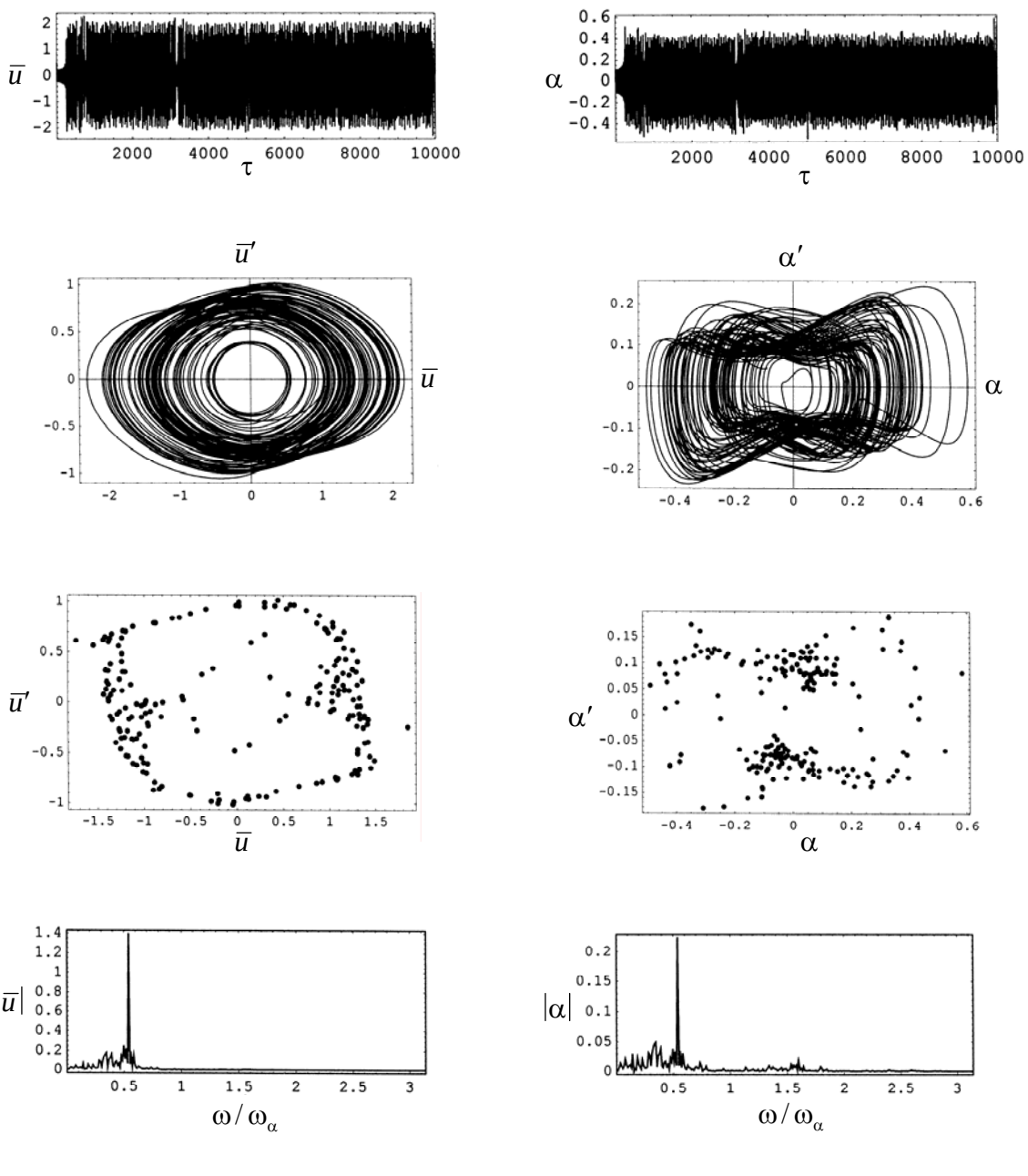


(f) $Y_0 = 0.014$, $\bar{u}(0) = 0.5$, $\alpha(0) = 0.1$, $\bar{u}'(0) = 0$, $\alpha'(0) = 0$

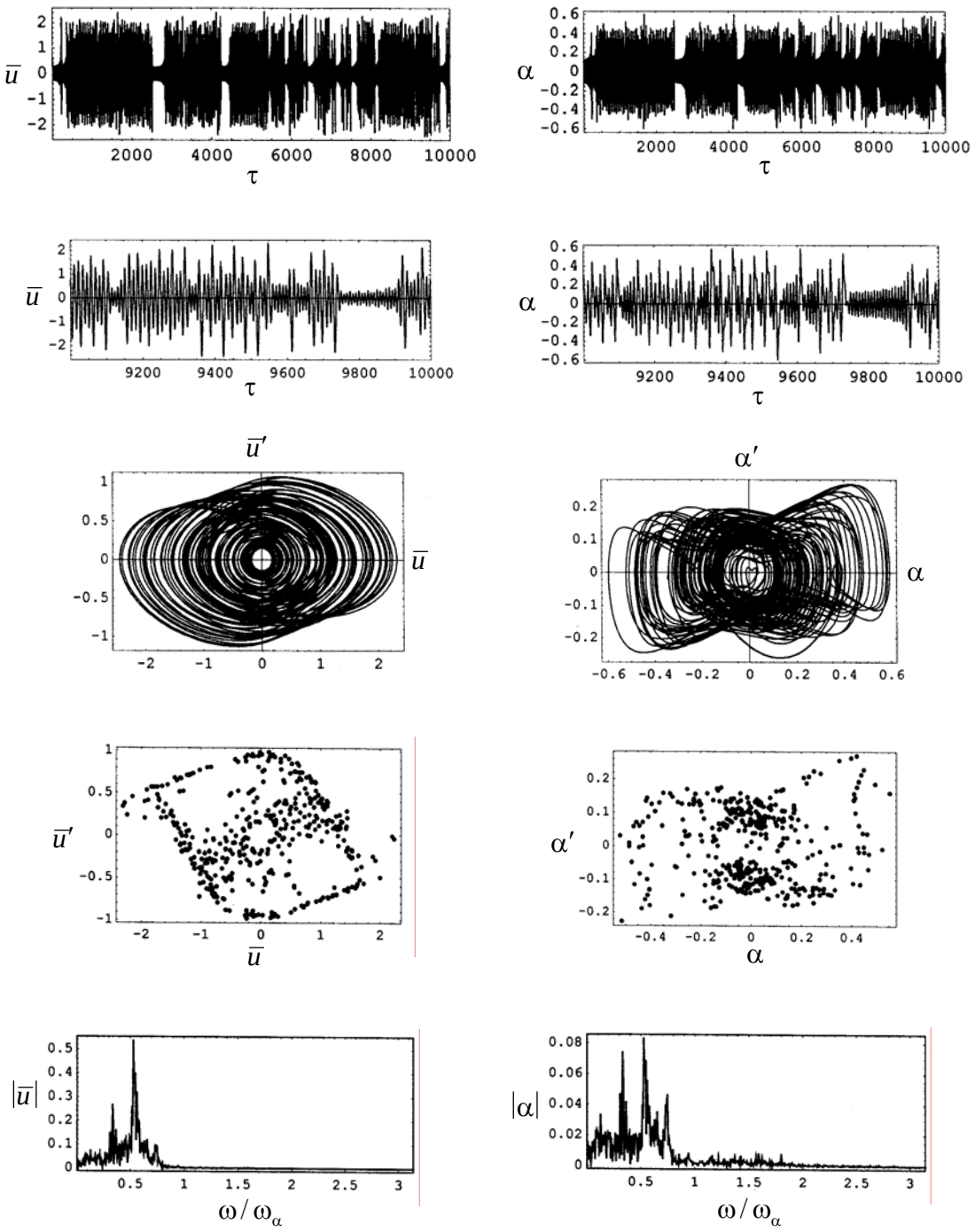


(g) $Y_0 = 0.016$, $\bar{u}(0) = 0.6$, $\alpha(0) = 0.1$, $\bar{u}'(0) = 0$, $\alpha'(0) = 0$

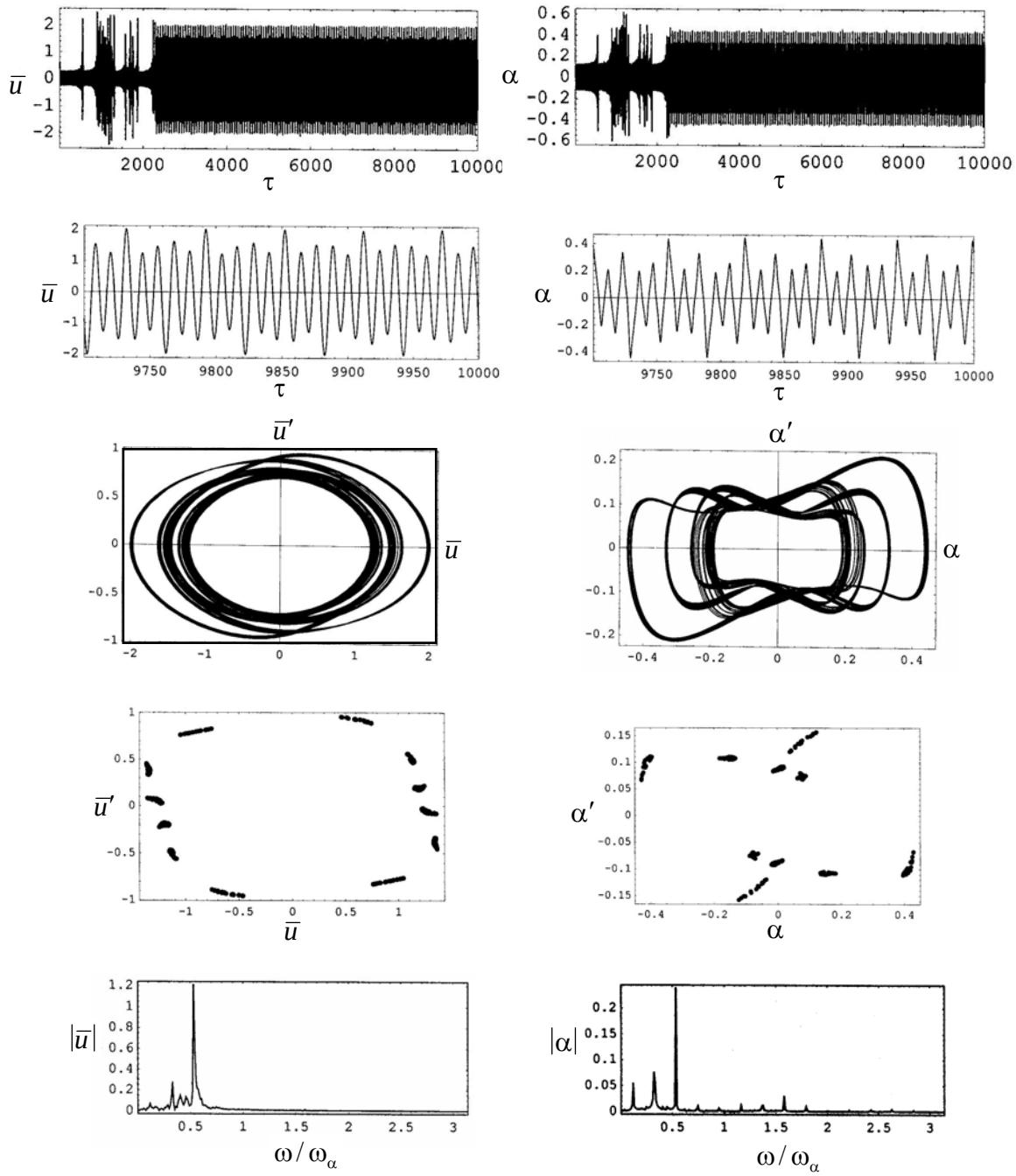


(h) $Y_0 = 0.017$, $\bar{u}(0) = 0.6$, $\alpha(0) = 0.1$, $\bar{u}'(0) = 0$, $\alpha'(0) = 0$

Figure 2.28 Numerical solution time histories, phase diagrams (d, f, g, h), Poincare maps (f, g, h), and FFT (d, f, g, h) at flutter speed $U_\infty / b\omega_\alpha = 4.965$, $\Omega = \omega_1 + \omega_2$, $\omega_2 = \omega_1 + 0.061$

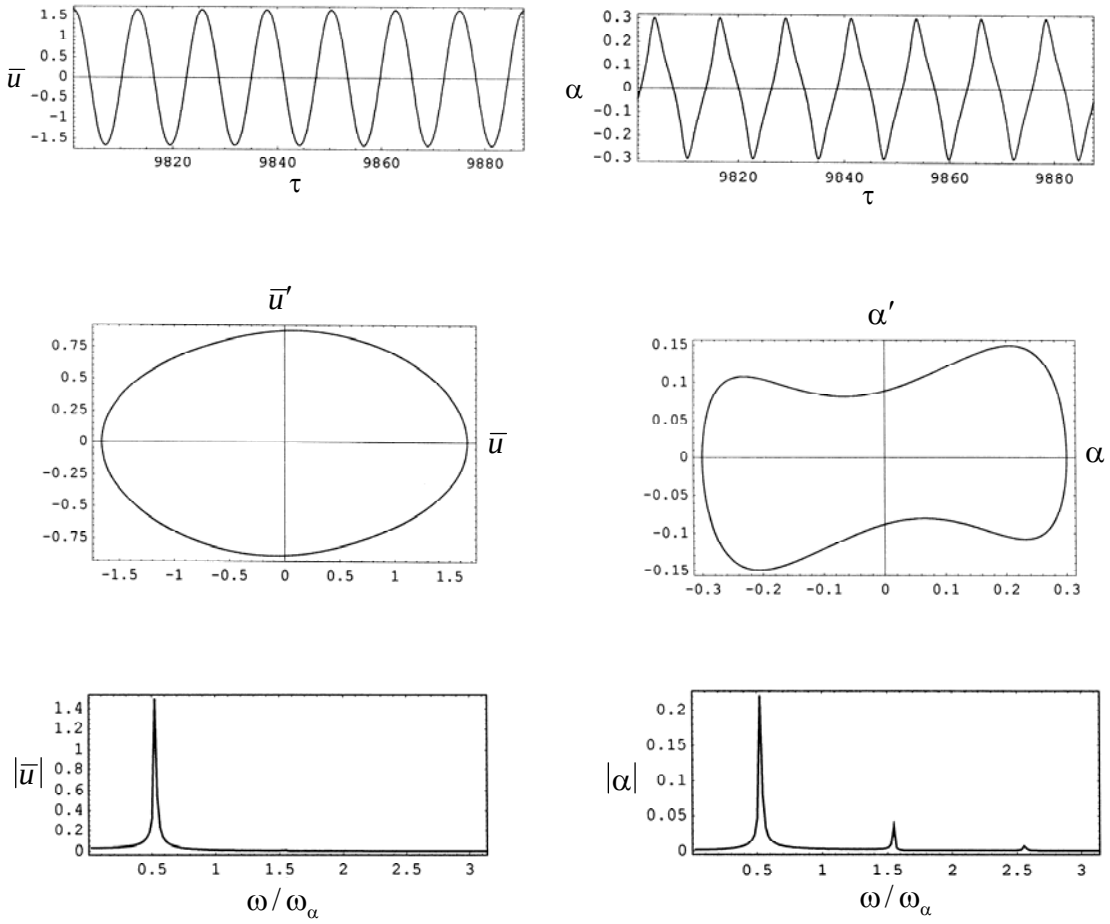


(a) $Y_0 = 0$, $\bar{u}(0) = 0.1$, $\alpha(0) = 0.01$, $\bar{u}'(0) = 0$, $\alpha'(0) = 0$

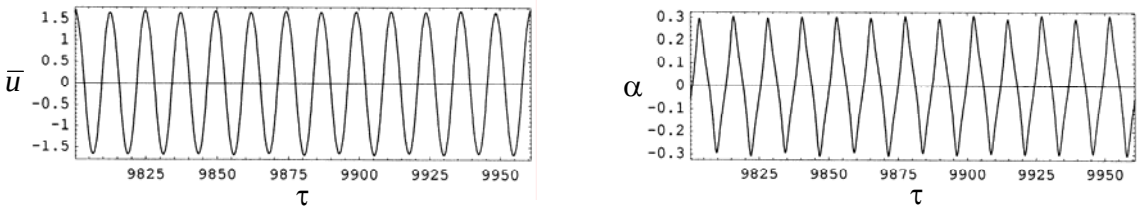


(b) $Y_0 = 0.001,\ \bar{u}(0) = 0.1,\ \alpha(0) = 0.01,\ \bar{u}'(0) = 0,\ \alpha'(0) = 0$

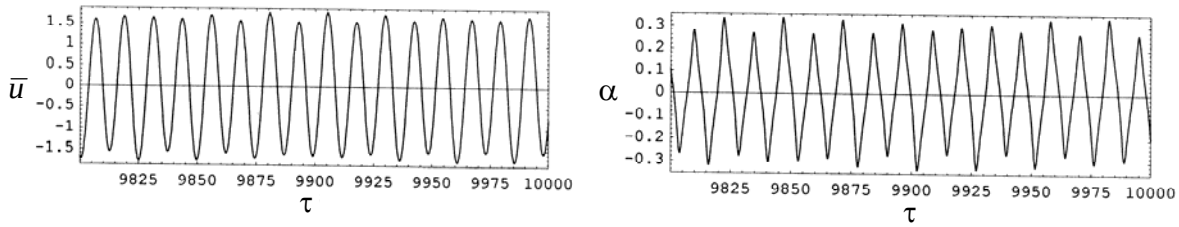


(c) $Y_0 = 0.005,\ \bar{u}(0) = 0.1,\ \alpha(0) = 0.01,\ \bar{u}'(0) = 0,\ \alpha'(0) = 0$

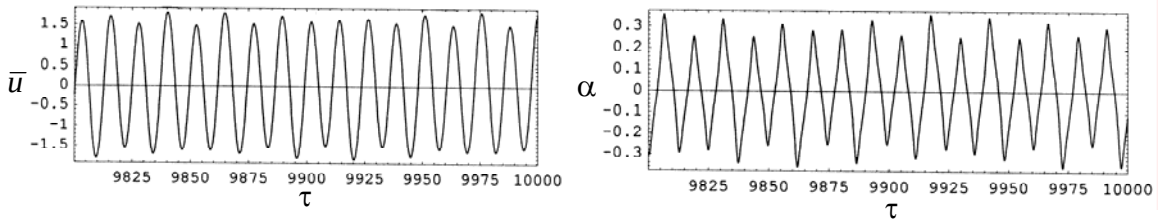


(d) $Y_0 = 0.0075,\ \bar{u}(0) = 0.1,\ \alpha(0) = 0.01,\ \bar{u}'(0) = 0,\ \alpha'(0) = 0$

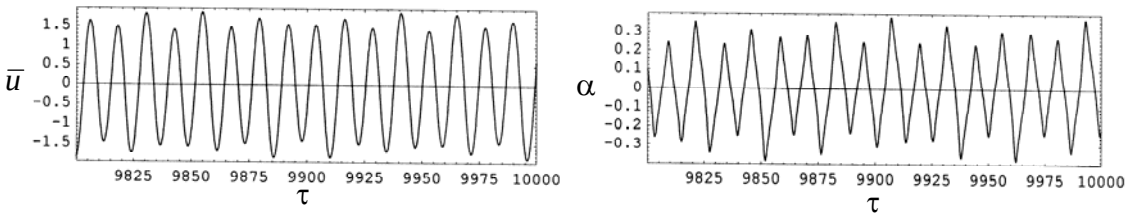


(e) $Y_0 = 0.01,\ \bar{u}(0) = 0.1,\ \alpha(0) = 0.01,\ \bar{u}'(0) = 0,\ \alpha'(0) = 0$

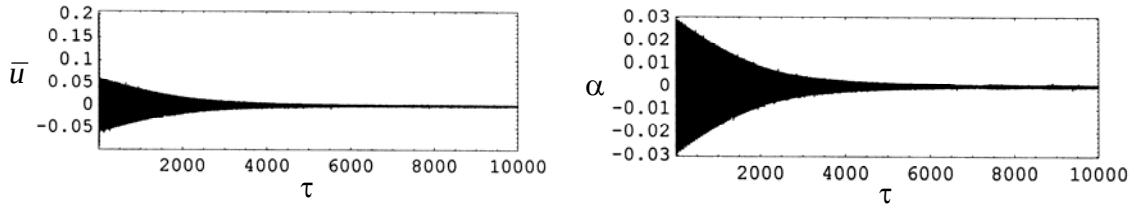


(f) $Y_0 = 0.015$, $\bar{u}(0) = 0.2$, $\alpha(0) = 0.01$, $\bar{u}'(0) = 0$, $\alpha'(0) = 0$

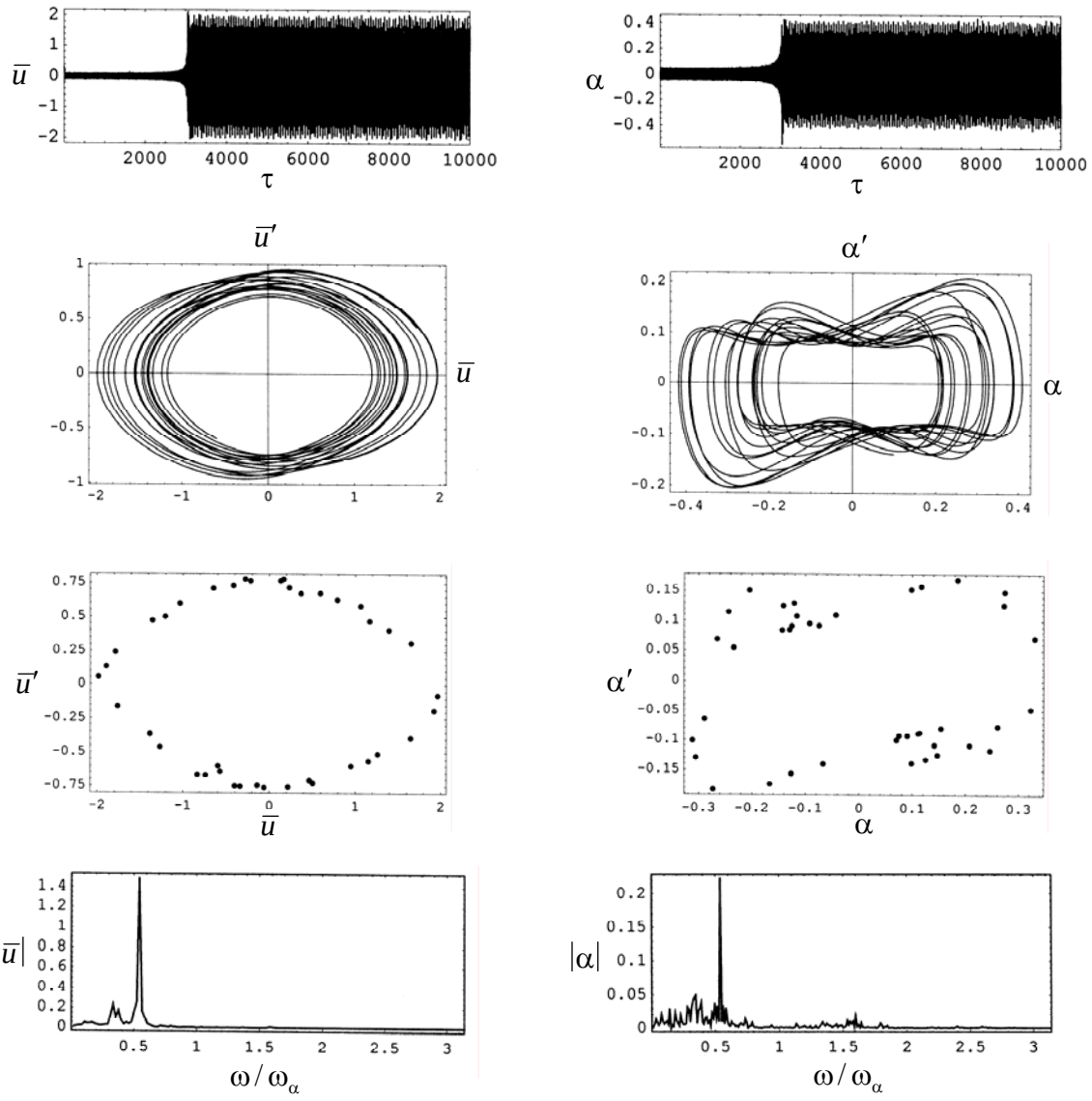


(g) $Y_0 = 0.015$, $\bar{u}(0) = 0.3$, $\alpha(0) = 0.01$, $\bar{u}'(0) = 0$, $\alpha'(0) = 0$

Figure 2.29 Numerical solution time histories, phase diagrams (a, g), and FFTs (a, g) at post critical flow speed $U_\infty / b\omega_\alpha = 5.02$, $\Omega = \omega_1 + \omega_2$, $\omega_2 = \omega_1 + 0.061$

# CHAPTER 3

# INFLUENCE OF PARAMETER UNCERTAINTIES ON THE FLUTTER OF A CANTILEVER WING

## 3.1 Introduction

The present chapter deals with the influence of stiffness uncertainties on the flutter behavior of an aeroelastic wing. The numerical algorithm originally developed by Predikman and Mook [36] will be adopted. This algorithm has been originally developed to simulate unsteady, nonlinear, incompressible flow interacting with linear aeroelastic wing in the absence of uncertainties. In order to implement this algorithm in the presence of uncertainties we introduce a random field that represents bending or torsion stiffness parameters or both as a truncated Karhunen-Love (K-L) expansion [94]. The air flow and wing structure are treated as elements of a single dynamic system. Both perturbation technique and Monte Carlo simulation are used to determine the boundary of stiffness uncertainty level at which the wing exhibits limit cycle oscillation (LCO) and above which the wing experiences dynamic instability. The analysis also includes the limitation of perturbation solution for relatively large level of stiffness uncertainty.

The analytical modeling of aerodynamic loading based on the unsteady vortex lattice method, structural forces interacting with the aerodynamic loading, and stiffness uncertainties based on Karhunen-Loeve expansion are briefly described in sections 3.2 through 3.4, respectively. Section 3.5 establishes the entire system modeling by combining the three models (aerodynamic, structure,

and uncertainty) in the wing governing equations of motion in the finite element discretized form. Sections 3.6 and 3.7 present the perturbation analysis solution and Monte Carlo simulation results, respectively. Part of this work was submitted for possible publication to AIAA Journal.

### 3.2. Aerodynamic Modeling

The aerodynamic modeling requires the estimation of aerodynamic forces and at the same time accounts for the wing elastic deformation. This is achieved by using the unsteady vortex lattice method [24]. The theoretical background which includes the theorems and laws that lead to the unsteady vortex lattice method as well as a detailed description of the method are given in the Appendix D. In the framework of vortex lattice method, the lifting surface is approximated by a set of lattices of short segments of constant circulation. Each segment occupies a portion of the wing surface and is enclosed by a loop of vortex segments. Figure 3.1 shows the discretization of the lifting surface, where the N-frame is the ground fixed coordinate system and B-frame is the coordinate system on the wing body and is moving with the wing. The leading segment of the vortex loop is located at a distance equivalent to quarter of the panel length. The velocities are calculated at a finite number of points named control or collocation points. The control points are located at the lattice center. Figure 3.2 represents the position of an arbitrary control point $P$ on the lattice as a result of the wing structure displacement. Point $P^0$ represents point $P$ before the wing is deformed. The position of $P^0$ is given by the vector $\mathbf{R}_0$ in the N-frame and the

vector $\mathbf{r}_0$ in the B-frame. The position of $P$ is given by the vector $\mathbf{R}$ in the N-frame and the vector $\mathbf{r}$ in the B-frame. The displacement of point $P$ due to the wing deformation is, $\Delta\mathbf{r}_{A_p}$. The position of the B-frame relative to N-frame is $\mathbf{R}_B$. The vectors $\mathbf{R}$ and $\mathbf{r}$ can be represented as functions of the wing displacement, $\Delta\mathbf{r}_{A_p}$, i.e., $\mathbf{R} = \mathbf{R}_0 + \Delta\mathbf{r}_{A_p}$, and $\mathbf{r} = \mathbf{r}_0 + \Delta\mathbf{r}_{A_p}$. In order to estimate the pressure at point P, one can use Bernoulli's equation for unsteady flow:

$$\frac{\partial\Phi(t)}{\partial t} + \frac{1}{2}\mathbf{V}_F(t)\cdot\mathbf{V}_F(t) + \frac{p(t)}{\rho} = H(t) \tag{3.1}$$

where $\Phi$ is the total velocity potential function, $p(t)$ is the pressure at point P, $\rho$ is the fluid density, $H(t)$ is a spatially uniform function of time, and $\mathbf{V}_F$ is the flow absolute velocity given by:

$$\mathbf{V}_F = \mathbf{V}_\infty + \mathbf{V}_B + \mathbf{V}_W \tag{3.2}$$

where $\mathbf{V}_\infty$ is the free stream velocity, $\mathbf{V}_B$ is the velocity due to the bound vortex lattices associated to the boundary layer on the surface of the wing, $\mathbf{V}_W$ is the velocity due to the free vortex lattices representing the wakes (see Figure 3.3(a)). As $|\mathbf{R}| \to \infty$, $\Phi \to \Phi_\infty = \text{constant}$, $\mathbf{V}_F \to \mathbf{V}_\infty$, $\rho \to \rho_\infty$, $p \to p_\infty$, and $H(t) = \frac{1}{2}\mathbf{V}_\infty\cdot\mathbf{V}_\infty + p_\infty/\rho_\infty$. In this case equation (3.1) takes the form:

$$\frac{\partial\Phi}{\partial t} + \frac{1}{2}\mathbf{V}_F\cdot\mathbf{V}_F + \frac{p}{\rho} = \frac{1}{2}\mathbf{V}_\infty\cdot\mathbf{V}_\infty + \frac{p_\infty}{\rho_\infty} \tag{3.3}$$

Alternatively, one may rewrite equation (3.3) in terms of the pressure coefficient $C_p$ as:

$$C_p = \frac{p - p_\infty}{V_\infty^2 \rho / 2} = 1 - \left(\frac{V_F}{V_\infty}\right)^2 - \frac{2}{V_\infty^2}\frac{\partial \Phi}{\partial t} \tag{3.4}$$

Introducing the non-dimensional parameters, $\tau = T_C t$, $\bar{\mathbf{R}} = \mathbf{R} / L_C = (\mathbf{R}_0 / L_C) + (\Delta \mathbf{r}_{A_P} / L_C) = \bar{\mathbf{R}}_0 + \Delta \bar{\mathbf{r}}_{A_P}$, $\bar{\mathbf{V}}_F = \mathbf{V}_F / V_\infty$, and $\bar{\Phi} = \Phi / L_C V_\infty$, where $T_C = L_C / V_\infty$ is a characteristic time, and $L_C$ represents the chord-wise length of one element on the bound lattice. Equation (3.4) takes the form:

$$C_p = 1 - \left(\bar{V}_F\right)^2 - 2\frac{\partial \bar{\Phi}}{\partial \tau} \tag{3.5}$$

The pressure coefficient variation across the lattice surface is:

$$\Delta C_p = \left(C_p\right)_L - \left(C_P\right)_U \tag{3.6}$$

where $\left(C_p\right)_L = 1 - \bar{V}_{FL}^2 - 2\left[\frac{\partial \bar{\Phi}}{\partial \tau}\right]_{\mathbf{R}_L}$ and $\left(C_p\right)_U = 1 - \bar{V}_{FU}^2 - 2\left[\frac{\partial \bar{\Phi}}{\partial \tau}\right]_{\mathbf{R}_U}$ are the pressure coefficients below and above the vortex lattice, respectively. One may write equation (3.6) in the form:

$$\Delta C_p = \bar{V}_{FU}^2 - \bar{V}_{FL}^2 + 2\left(\left[\frac{\partial \bar{\Phi}}{\partial \tau}\right]_{\mathbf{R}_U} - \left[\frac{\partial \bar{\Phi}}{\partial \tau}\right]_{\mathbf{R}_L}\right)$$

$$\approx 2\bar{\mathbf{V}}_{mP}\cdot\Delta\bar{\mathbf{V}}_P + 2\left(\left[\frac{\partial\bar{\Phi}}{\partial\tau}\right]_{\mathbf{R}_U} - \left[\frac{\partial\bar{\Phi}}{\partial\tau}\right]_{\mathbf{R}_L}\right) \tag{3.7}$$

where $\Delta\bar{\mathbf{V}}_P$ is the non-dimensional tangential velocity difference across the vortex lattice and $\bar{\mathbf{V}}_{mP}$ is the "mean" velocity which does not recognize the presence of the local vorticity. $\bar{\mathbf{V}}_{m,P}$ can be considered as the flow velocity at the midpoint of the vortex sheet thickness. For a general element, shown in Figure 3.3(b), the jump in the tangential velocity in dimensional form across the vortex sheet can be expressed as [25]:

$$\Delta\mathbf{V}_P = -\frac{\mathbf{n}\times\boldsymbol{\Gamma}}{A_P} \tag{3.8}$$

where $\mathbf{n}$ is the unit normal vector at the control point, $A_P$ is the area of the element, and $\boldsymbol{\Gamma}$ is a vector given by the expression

$$\boldsymbol{\Gamma} = \frac{\Gamma_1}{2}\mathbf{L}_1 + \frac{\Gamma_2}{2}\mathbf{L}_2 + \frac{\Gamma_3}{2}\mathbf{L}_3 + \frac{\Gamma_4}{2}\mathbf{L}_4 \tag{3.9}$$

$\Gamma_{1,\ldots,4}$ are the circulations of the segments $\mathbf{L}_{1,\ldots,4}$. With reference to Figure 3.3(b), for two adjacent elements with common circulation, say $\Gamma_4$, and whose control points are $P$ and $Q$ possessing circulation loops $G_P$ and $G_Q$ respectively, the value of $\Gamma_4$ is $G_Q - G_P$. The expression for $\left[\frac{\partial\bar{\Phi}}{\partial\tau}\right]_{\mathbf{R}_U} - \left[\frac{\partial\bar{\Phi}}{\partial\tau}\right]_{\mathbf{R}_L}$ can be evaluated at

point $P$ in terms of the non-dimensional velocity increment $\Delta\bar{\mathbf{V}}_P = \Delta\mathbf{V}_P / \mathbf{V}_\infty$, as [25]:

$$\left( \left[ \frac{\partial \bar{\Phi}}{\partial \tau} \right]_{\mathbf{R}_U} - \left[ \frac{\partial \bar{\Phi}}{\partial \tau} \right]_{\mathbf{R}_L} \right)_P = \frac{D}{D\tau} \left[ \bar{G}_P(\tau) \right] - \Delta\bar{\mathbf{V}}_P \cdot \left[ {}^N\bar{\mathbf{v}}^B + {}^B\dot{\bar{\mathbf{r}}}^P + {}^N\bar{\boldsymbol{\omega}}^B \times {}^B\bar{\mathbf{r}}^P \right] \tag{3.10}$$

where $\bar{G}_P$ is the circulation loop in non-dimensional form of the vortex lattice element which encloses the control point $P$, ${}^N\bar{\mathbf{v}}^B$ is the absolute velocity of $O_B$, ${}^B\bar{\mathbf{r}}^P$ and ${}^B\dot{\bar{\mathbf{r}}}^P$ the position and velocity of $P$ relative to the B-frame, respectively, and ${}^N\bar{\boldsymbol{\omega}}^B$ is the angular velocity of the B-frame.

Introducing equation (3.10) into equation (3.7) gives the final expression for the pressure coefficient variation across the lattice surface at point $P$:

$$\Delta C_p = 2\Delta\bar{\mathbf{V}}_P \cdot \left[ \bar{\mathbf{V}}_{mP} - {}^N\bar{\mathbf{v}}^B - {}^B\dot{\bar{\mathbf{r}}}^P - {}^N\bar{\boldsymbol{\omega}}^B \times {}^B\bar{\mathbf{r}}^P \right] + 2\frac{D}{D\tau}\left[ \bar{G}_P \right] \tag{3.11}$$

The non-dimensional aerodynamic load at point $P$ can be computed in terms of $\Delta C_p$:

$$\bar{\mathbf{F}}_{A,P} = \Delta C_p \bar{A}_P \mathbf{n} = 2\left\{ \Delta\bar{\mathbf{V}}_P \cdot \left[ \bar{\mathbf{V}}_{mP} - {}^N\bar{\mathbf{v}}^B - {}^B\dot{\bar{\mathbf{r}}}^P - \bar{\boldsymbol{\omega}}^B \times {}^B\bar{\mathbf{r}}^P \right] + \frac{D}{D\tau}\left[ \bar{G}_P \right] \right\} \bar{A}_P \mathbf{n} \tag{3.12}$$

where $\bar{A}_P = A_P / L_C^2$ is the non-dimensional area of the element $P$. The expression for the aerodynamic load at point $P$ in dimensional form is:

$$\mathbf{F}_{A,P}(t) = \left[ \left( \rho_\infty V_\infty^2 / 2 \right) L_C^2 \right] \bar{\mathbf{F}}_{A,P}(\tau) \tag{3.13}$$

This aerodynamic force is interacting with the elastic and inertia forces of the wing structure and their modeling is given in the next section. Note that this aerodynamic force is acting at the center of each lattice as shown in Figure 3.4.

### 3.3. Structural Modeling

Figure 3.5 shows a cantilever wing with a straight elastic axis at distance $\delta_3$ from the inertia axis. The wing is modeled as an Euler-Bernoulli beam. The coordinate system coincides with B-frame coordinate system from the aerodynamic modeling. The governing equations of motion are obtained using Lagrange's equation. The kinetic energy of the wing is:

$$KE = \frac{1}{2}\int_0^L m\left[\left(\frac{\partial \tilde{u}(y,t)}{\partial t}\right)^2 + \left(\frac{\partial \tilde{v}(y,t)}{\partial t}\right)^2 + \left(\frac{\partial \tilde{w}(y,t)}{\partial t} + \delta_3 \frac{\partial \tilde{\alpha}(y,t)}{\partial t}\right)^2\right] dy$$

$$+ \frac{1}{2}\int_0^L I_0 \left(\frac{\partial \tilde{\alpha}(y,t)}{\partial t}\right)^2 dy \qquad (3.14)$$

where $\tilde{u}(y,t)$, $\tilde{v}(y,t)$, and $\tilde{w}(y,t)$ are the displacements along $x$-, $y$-, $z$-directions, respectively, $\tilde{\alpha}(y,t)$ is the torsion angle, $m$ is mass per unit length, $I_0$ is mass moment of inertia (about inertia axis) per unit length, and $L$ is the wing length.

The strain energy is:

$$PE = \frac{1}{2} EI_x \int_0^L \left\{\frac{\partial^2 \tilde{w}(y,t)}{\partial y^2}\right\}^2 dy + \frac{1}{2} EI_z \int_0^L \left\{\frac{\partial^2 \tilde{u}(y,t)}{\partial y^2}\right\}^2 dy$$

$$+\frac{1}{2}AE\int_0^L\left\{\frac{\partial\tilde{\mathrm{v}}}{\partial y}\right\}^2 dy+\frac{1}{2}cGJ\int_0^L\left(\frac{\partial\tilde{\alpha}(y,t)}{\partial y}\right)^2 dy \tag{3.15}$$

where $A$ is the wing cross-sectional area, $E$ is Young's modulus, $I_x$ is the area moment of inertia of the wing cross-section about $x$ axis, $I_z$ is the area moment of inertia of the wing cross-section about $z$ axis, $J$ is the polar moment of inertia of the wing cross-section about $z$ axis, $G$ is the modulus of rigidity, and $c$ is a factor accounting for the non-circular geometry of the wing cross-section.

The work done by external forces and moments:

$$W=\int_0^L F_u\tilde{u}(y,t)\,dy+\int_0^L F_{\mathrm{v}}\tilde{\mathrm{v}}(y,t)\,dy+\int_0^L F_w\tilde{w}(y,t)\,dy+\int_0^L M_\alpha\tilde{\alpha}(y,t)\,dy \tag{3.16}$$

where $F_u$, $F_{\mathrm{v}}$, and $F_w$ are the external forces acting along x-, y-, and z-directions, respectively, and $M_\alpha$ is the external moment about the inertia axis.

The wing is divided into elements as shown in Figure 3.6(a), where a single element with two nodes is shown in Figure 3.6(b). The displacements of each element, $\tilde{u}(y,t)$, $\tilde{\mathrm{v}}(y,t)$, and $\tilde{w}(y,t)$, are expressed in terms of the nodal displacements $u_i$, $\mathrm{v}_i$, $w_i$ in $x$, $y$, and $z$ directions, respectively, and nodal rotations $\beta_i$, $\alpha_i$, $\gamma_i$ about $x$, $y$, and $z$ axes, respectively. The relationships between the element and nodal displacements are

$$\tilde{u}(y,t)=\mathbf{Y}_u^T(y)\mathbf{u}_e(t),\quad \tilde{\mathrm{v}}(y,t)=\mathbf{Y}_{\mathrm{v}}^T(y)\mathbf{v}_e(t) \tag{3.17}$$

$$\tilde{w}(y,t) = \mathbf{Y}_w^T(y)\mathbf{w}_e(t), \quad \tilde{\alpha}(y,t) = \mathbf{Y}_\alpha^T(y)\boldsymbol{\alpha}_e(t)$$

where $\mathbf{Y}_u^T(y) = \mathbf{Y}_w^T(y) = \{Y_3 \quad Y_5 \quad Y_4 \quad Y_6\}$, $\mathbf{Y}_v^T(y) = \mathbf{Y}_\alpha^T(y) = \{Y_1 \quad Y_2\}$,

$$\mathbf{u}_e = \begin{Bmatrix} u_i \\ \gamma_i \\ u_{i+1} \\ \gamma_{i+1} \end{Bmatrix}, \quad \mathbf{v}_e = \begin{Bmatrix} v_i \\ v_{i+1} \end{Bmatrix}, \quad \mathbf{w}_e(t) = \begin{Bmatrix} w_i \\ \beta_i \\ w_{i+1} \\ \beta_{i+1} \end{Bmatrix}, \quad \boldsymbol{\alpha}_e(t) = \begin{Bmatrix} \alpha_i \\ \alpha_{i+1} \end{Bmatrix}$$

$Y_j, \quad j = 1,2,...,6$ are the shape functions given by the expressions [192]

$$Y_1 = \frac{y_{i+1} - y}{y_{i+1} - y_i}, \; Y_2 = \frac{y - y_i}{y_{i+1} - y_i}, \; Y_3 = 1 - 3\left(\frac{y - y_i}{y_{i+1} - y_i}\right)^2 + 2\left(\frac{y - y_i}{y_{i+1} - y_i}\right)^3, Y_4 = 3\left(\frac{y - y_i}{y_{i+1} - y_i}\right)^2$$

$$-2\left(\frac{y - y_i}{y_{i+1} - y_i}\right)^3, \; Y_5 = (y - y_i) - \frac{2}{y_{i+1} - y_i}(y - y_i)^2 + \frac{1}{(y_{i+1} - y_i)^2}(y - y_i)^3,$$

$$Y_6 = -\frac{1}{y_{i+1} - y_i}(y - y_i)^2 + \frac{1}{(y_{i+1} - y_i)^2}(y - y_i)^3, \qquad y_i \le y \le y_{i+1}. \quad (3.18)$$

Introducing equation (3.17) into equations (3.14-3.16), and applying Lagrange's equation to each coordinate, gives the following set of equations of motion:

$$m\left(\int_{y_i}^{y_{i+1}} \mathbf{Y}_u(y)\mathbf{Y}_u(y)^T dy\right)\ddot{\mathbf{u}}_e(t) + \left(\int_{y_i}^{y_{i+1}} EI_z \mathbf{Y}_u(y)''\left(\mathbf{Y}_u(y)''\right)^T dy\right)\mathbf{u}_e(t) = \left(\int_{y_i}^{y_{i+1}} F_u \mathbf{Y}_u(y)\, dy\right)$$

(3.19a)

$$m\left(\int_{y_i}^{y_{i+1}} \mathbf{Y}_v(y)\mathbf{Y}_v(y)^T dy\right)\ddot{\mathbf{v}}_e(t) + \left(\int_{y_i}^{y_{i+1}} AE\mathbf{Y}_v(y)'\left(\mathbf{Y}_v(y)'\right)^T dy\right)\mathbf{v}_e(t) = \left(\int_{y_i}^{y_{i+1}} F_v \mathbf{Y}_v(y)\, dy\right)$$

(3.19b)

$$m\left(\int_{y_i}^{y_{i+1}} \mathbf{Y}_w(y)\mathbf{Y}_w(y)^T dy\right)\ddot{\mathbf{w}}_e(t) + m\delta_3\left(\int_{y_i}^{y_{i+1}} \mathbf{Y}_w(y)\mathbf{Y}_\alpha(y)^T dy\right)\ddot{\boldsymbol{\alpha}}_e(t)$$
$$+\left(\int_{y_i}^{y_{i+1}} EI_x\mathbf{Y}_w(y)''\left(\mathbf{Y}_w(y)''\right)^T dy\right)\mathbf{w}_e(t) = \left(\int_{y_i}^{y_{i+1}} F_w\mathbf{Y}_w(y)\,dy\right) \quad (3.19c)$$

$$\left(\int_{y_i}^{y_{i+1}} I_\alpha\mathbf{Y}_\alpha(y)\mathbf{Y}_\alpha(y)^T dy\right)\ddot{\boldsymbol{\alpha}}_e(t) + m\delta_3\left(\int_{y_i}^{y_{i+1}} \mathbf{Y}_\alpha(y)\mathbf{Y}_w(y)^T dy\right)\ddot{\mathbf{w}}_e(t)$$
$$+\left(\int_{y_i}^{y_{i+1}} cGJ\mathbf{Y}_\alpha(y)'\left(\mathbf{Y}_\alpha(y)'\right)^T dy\right)\boldsymbol{\alpha}_e(t) = \left(\int_{y_i}^{y_{i+1}} M_\alpha\mathbf{Y}_\alpha(y)\,dy\right) \quad (3.19d)$$

where a prime denotes a derivative with respect to spatial variable, $y$. Equations (3.19) may be written in the matrix form:

$$\mathbf{M}^e\ddot{\mathbf{U}}^e + \mathbf{K}^e\mathbf{U}^e = \mathbf{F}^e \quad (3.20)$$

where

$$\mathbf{M}^e = m\left(\int_{y_i}^{y_{i+1}} \mathbf{Y}_u(y)\mathbf{Y}_u(y)^T dy\right) + m\left(\int_{y_i}^{y_{i+1}} \mathbf{Y}_v(y)\mathbf{Y}_v(y)^T dy\right) + m\left(\int_{y_i}^{y_{i+1}} \mathbf{Y}_w(y)\mathbf{Y}_w(y)^T dy\right) +$$
$$m\delta_3\left(\int_{y_i}^{y_{i+1}} \mathbf{Y}_w(y)\mathbf{Y}_\alpha(y)^T dy\right) + \left(\int_{y_i}^{y_{i+1}} I_\alpha\mathbf{Y}_\alpha(y)\mathbf{Y}_\alpha(y)^T dy\right) + m\delta_3\left(\int_{y_i}^{y_{i+1}} \mathbf{Y}_\alpha(y)\mathbf{Y}_w(y)^T dy\right) \quad (3.21a)$$

$$\mathbf{K}^e = \left(\int_{y_i}^{y_{i+1}} EI_z\mathbf{Y}_u(y)''\left(\mathbf{Y}_u(y)''\right)^T dy\right) + \left(\int_{y_i}^{y_{i+1}} AE\mathbf{Y}_v(y)'\left(\mathbf{Y}_v(y)'\right)^T dy\right) +$$
$$\left(\int_{y_i}^{y_{i+1}} EI_x\mathbf{Y}_w(y)''\left(\mathbf{Y}_w(y)''\right)^T dy\right) + \left(\int_{y_i}^{y_{i+1}} cGJ\mathbf{Y}_\alpha(y)'\left(\mathbf{Y}_\alpha(y)'\right)^T dy\right) \quad (3.21b)$$

$$\mathbf{F}_s^e = \left( \int_{y_i}^{y_{i+1}} F_u \mathbf{Y}_u(y) dy \right) + \left( \int_{y_i}^{y_{i+1}} F_v \mathbf{Y}_v(y) dy \right) + \left( \int_{y_i}^{y_{i+1}} F_w \mathbf{Y}_w(y) dy \right) + \left( \int_{y_i}^{y_{i+1}} M_\alpha \mathbf{Y}_\alpha(y) dy \right) \quad (3.21c)$$

$$\mathbf{U}^e = \{ u_i \quad v_i \quad w_i \quad \beta_i \quad \alpha_i \quad \gamma_i \quad u_{i+1} \quad v_{i+1} \quad w_{i+1} \quad \beta_{i+1} \quad \alpha_{i+1} \quad \gamma_{i+1} \}^T \quad (3.21d)$$

Equation (3.20) constitutes the governing equations of motion for a single element without uncertainties. The inclusion of material uncertainties will be considered in the next section.

### 3.4. Modeling of Material Uncertainties

Material uncertainty is considered for bending and torsion stiffness parameters. Let the bending and torsion stiffness parameters be represented in the form,

$$EI_x(y) = \overline{EI}_x + \widetilde{EI}_x(y), \qquad GJ(y) = \overline{GJ} + \widetilde{GJ}(y) \quad (3.22a)$$

The mean values $\overline{EI}_x >> 0$, and $\overline{GJ} >> 0$ are assumed to be much larger than the root-mean-square of the random field variability represented by $\widetilde{EI}_x(y)$ and $\widetilde{GJ}(y)$. Both $\widetilde{EI}_x(y)$ and $\widetilde{GJ}(y)$ are assumed to be Gaussian distributed with zero mean and their standard deviations $\sigma_{EI_x}$, and $\sigma_{GJ}$ are much smaller than the corresponding mean value, i.e., $\sigma_{EI_x} / \overline{EI}_x \ll 1$, and $\sigma_{GJ} / \overline{GJ} \ll 1$. This implies that the stiffness parameters $EI_x(y)$ and $GJ(y)$ form positive-valued random fields. Let the stiffness parameters be represented by the random

function $\chi(y,\theta)$, where $\theta$ is a parameter that belongs to the space of random events and $y \in [-L/2, L/2]$. The random field $\chi(y,\theta)$ can be expressed by the truncated Karhunen-Loeve (K-L) expansion [94]:

$$\chi(y,\theta) = \overline{\chi}(y) + \sum_{n=1}^{N} \xi_n(\theta)\sqrt{\lambda_n}\, f_n(y) \tag{3.22b}$$

where $\overline{\chi}(y)$ is the mean value of $\chi(y,\theta)$, $\lambda_n$ is some constant, $f_n(y)$ is a set of deterministic functions, and $\xi_n(\theta)$ is the set of random variables with zero mean and $E[\xi_n(\theta)\xi_m(\theta)] = \delta_{nm}$, $\delta_{nm}$ is the Kronecker delta. $\lambda_n$ and $f_n(y)$ are given by the solution of the integral equation

$$\int_{-L/2}^{L/2} C(y, y_1) f_n(y_1) dy_1 = \lambda_n f_n(y) \tag{3.23}$$

where $C(y, y_1)$ is the covariance kernel of the random field $\chi(y,\theta)$.

Expansion (3.22b) is mathematically well founded and is guaranteed to converge. In addition, it is optimum in the sense that it minimizes the mean square error resulting from truncating the series at a finite number of terms. The bending and torsion stiffness parameters will be modeled by one-dimensional Gaussian random field models with bounded mean squares. Ghanem and Spanos [94] and Loeve [111] showed that for a Gaussian process the K-L expansion is convergent. The covariance kernel of the random field $\chi(y,\theta)$ may be assumed in the form:

$$C(y, y_1) = \sigma_\chi^2 e^{-|y-y_1|/l_{cor}} \tag{3.24}$$

where $\sigma_\chi^2$ is the variance of the random field $\chi$, such that $\sigma_\chi \ll \overline{\chi}(y)$ implying that $\chi(y,\theta)$ will always be positive, $l_{cor}$ is correlation length such that $l_{cor} \to L$. For one-dimensional Gaussian process, the eigenvalue problem (3.23) possesses the closed form analytical solution [94]

$$f_n(y) = \frac{\cos(\omega_n y)}{\sqrt{\frac{L}{2} + \frac{\sin(2\omega_n L/2)}{2\omega_n}}}, \qquad \lambda_n = \frac{2\sigma_\chi^2 / l_{cor}}{\omega_n^2 + 1/l_{cor}^2} \tag{3.25a,b}$$

where $\omega_n$ are the eigenvalues of the characteristic equation:

$$\left[\frac{1}{l_{cor}} - \omega\tan\left(\omega\frac{L}{2}\right)\right]\left[\omega + \frac{1}{l_{cor}}\tan\left(\omega\frac{L}{2}\right)\right] = 0 \tag{3.26}$$

Introducing the expressions (3.25) into (3.22) the random field takes the form:

$$\chi(y,\theta) = \overline{\chi}(y) + \sum_{n=1}^{N} 2\xi_n(\theta)\sigma_\chi \sqrt{\frac{\omega_n / l_{cor}}{\left(\omega_n^2 + 1/l_{cor}^2\right)\left[L\omega_n + \sin(2\omega_n L/2)\right]}}\cos(\omega_n y) \tag{3.27}$$

For bending stiffness, the random field $\chi$ is denoted by $EI_x$ with mean value $\overline{EI}_x$ and variance $\sigma_{EI_x}^2$ and for torsion stiffness the random field $\chi$ is denoted by $cGJ$ with mean value $\overline{cGJ}$ and variance $\sigma_{GJ}^2$. Introducing equation (3.27) into elemental stiffness expression $\mathbf{K}^e$ given by equation (3.21b), the following expression is obtained:

$$\mathbf{K}^e(\theta) = \mathbf{K}_0^e + \sum_{n=1}^{N} \mathbf{K}_{b,n}^e \xi_n(\theta) + \sum_{n=1}^{N} \mathbf{K}_{t,n}^e \xi_n(\theta) \tag{3.28}$$

where

$$\mathbf{K}_0^e = EI_z \left( \int_{y_i}^{y_{i+1}} \left( \mathbf{Y}_u'' \right)^T \mathbf{Y}_u'' \, dy \right) + AE \left( \int_{y_i}^{y_{i+1}} \left( \mathbf{Y}_v' \right)^T \mathbf{Y}_v' dy \right) + \overline{EI}_x \left( \int_{y_i}^{y_{i+1}} \left( \mathbf{Y}_w'' \right)^T \mathbf{Y}_w'' \, dy \right) + \overline{cGJ} \left( \int_{y_i}^{y_{i+1}} \left( \mathbf{Y}_\alpha' \right)^T \mathbf{Y}_\alpha' dy \right) \tag{3.29a}$$

$$\mathbf{K}_{b,n}^e = \int_{y_i}^{y_{i+1}} 2\xi_n(\theta) \sigma_{EI_x} \sqrt{\frac{\omega_n / l_{cor}}{\left(\omega_n^2 + 1/l_{cor}^2\right)\left[L\omega_n + \sin\left(2\omega_n L/2\right)\right]}} \cos(\omega_n y) \mathbf{Y}_w''(y)^T \mathbf{Y}_w''(y) dy \tag{3.29b}$$

$$\mathbf{K}_{t,n}^e = \int_{y_i}^{y_{i+1}} 2\xi_n(\theta) \sigma_{GJ} \sqrt{\frac{\omega_n / l_{cor}}{\left(\omega_n^2 + 1/l_{cor}^2\right)\left[L\omega_n + \sin\left(2\omega_n L/2\right)\right]}} \cos(\omega_n y) \mathbf{Y}_\alpha'(y)^T \mathbf{Y}_\alpha'(y) dy \tag{3.29c}$$

Assembling the elemental matrices gives

$$\mathbf{M}\ddot{\mathbf{U}}(t,\theta) + \mathbf{K}_0 \mathbf{U}(t,\theta) + \left( \sum_{n=1}^{N} \mathbf{K}_{b,n} \xi_n(\theta) \right) \mathbf{U}(t,\theta) + \left( \sum_{n=1}^{N} \mathbf{K}_{t,n} \xi_n(\theta) \right) \mathbf{U}(t,\theta) = \mathbf{F}_s(\mathbf{U}, t, \theta) \tag{3.30}$$

where $\mathbf{M}$ is a $(6n_S \times 6n_S)$ mass matrix representing the assembled elemental mass matrix $\mathbf{M}^e$, $n_S$ is the number of points in the structural grid, $\mathbf{K}_0$ is a $(6n_S \times 6n_S)$ matrix representing the assembled elemental mean value of the stiffness matrix $\mathbf{K}_0^e$. $\mathbf{K}_{b,n}$ and $\mathbf{K}_{t,n}$ are $(6n_S \times 6n_S)$ matrices representing the

assembled elemental bending $\mathbf{K}_{b,n}^{e}$ and torsion $\mathbf{K}_{t,n}^{e}$ random stiffness matrices, respectively. $\mathbf{F}_s(\mathbf{U},t,\theta)$ is a $(6n_S \times 1)$ vector representing the assembled elemental force vector $\mathbf{F}_s^e$, and $\mathbf{U}(t,\theta)$ is a $(6n_S \times 1)$ vector of the displacements of the points in the structural grid and represents the assembled elemental displacement vector $\mathbf{U}^e$. In the numerical analysis the wing structure will be discretized into 9 elements so the number of points in the structural grid will be $n_s = 9+1=10$ nodes. The number of equations in the expression (3.30) will be $6n_S = 60$.

Note that the left-hand side of equation (3.30) constitutes a set of stochastic second-order differential equations with random variable coefficients with Gaussian distribution. In the absence of aerodynamic forces, these equations are always stable, since the stiffness matrices are real positive definite. This is guaranteed by the fact that the uncertain components of the stiffness parameters are very small compared with their mean values as stated in the beginning of this section. In the next section the aerodynamic nodes will be connected to the structural finite element mesh and the aerodynamic forces will be transferred to the structural grid.

In the next section the aerodynamic nodes will be connected to the structural finite element mesh and the aerodynamic forces will be transferred to the structural grid.

### 3.5. System Modeling

Figure 3.7(a) shows the structural grid superimposed to the aerodynamic grid. The relationship between the displacements of the aerodynamic grid points and displacements of the structural grid points is given by the following relationship:

$$\Delta\underline{\Re}_A = \begin{Bmatrix} \Delta\mathbf{r}_1 \\ \Delta\mathbf{r}_2 \\ \vdots \\ \Delta\mathbf{r}_{n_A} \end{Bmatrix} = \mathbf{G}_{AS}\mathbf{U} \tag{3.31}$$

where $\Delta\underline{\Re}_A$ is a $(3n_A \times 1)$ vector representing the displacements of the control points in the aerodynamic grid, $n_A$ is the number of control points in the aerodynamic grid, $\mathbf{G}_{AS}$ is an $3n_A \times 6n_S$ interpolation matrix that connects the displacements of the nodal points in the aerodynamic grid to the displacements of the nodal points in the structural grid [25].

Figure 3.7(b) exemplifies how an aerodynamic point is connected to an internal structural grid point, where an aerodynamic point $P_A$ is connected to a point $P_S$ on the elastic axis between two successive structural nodes. For the example showed in the Figure 3.7(b), the structural nodes are labeled by the index $i$, where $i = 1,2,...,8(=n_S)$ while the aerodynamic points are labeled by the index $j$, where $j = 1,2,...,18(=n_A)$. The points $P_S$ and $P_A$ are in the same plane, which is perpendicular to the elastic axis. The relative position between $P_A$ and $P_S$ is given by the vector $\mathbf{r}_j^{AS} = (x_j, y_j, z_j)$. The displacement of the point $P_A$ is

given by $\Delta\mathbf{r}_j^A = \left\{\Delta r_1^A, \Delta r_2^A, \Delta r_3^A\right\}^T$ and the displacement of the point $P_S$ is given by $\mathbf{U}_i = \left\{u_i^s, \mathrm{v}_i^s, w_i^s, \beta_i^s, \alpha_i^s, \gamma_i^s\right\}^T$. The relationship between the points $P_A$ and $P_S$ is given by [25]:

$$\Delta\mathbf{r}_{j_A} = \tilde{\mathbf{G}}_{ji}\mathbf{U}_{i_S}, \qquad \tilde{\mathbf{G}}_{ji} = \begin{bmatrix} 1 & 0 & 0 & 0 & z_j & 0 \\ 0 & 1 & 0 & -z_j & 0 & x_j \\ 0 & 0 & 1 & 0 & -x_j & 0 \end{bmatrix} \tag{3.32}$$

The displacement vector $\mathbf{U}_{P_S}$ is obtained by finite element interpolation as a function of displacements on nodes $i$ and $i+1$ as follows:

$$\mathbf{U}_{P_S} = \begin{bmatrix} \mathbf{Y}_{11} & \mathbf{Y}_{12} & \mathbf{Y}_{13} & \mathbf{Y}_{14} \\ \mathbf{Y}_{21} & \mathbf{Y}_{22} & \mathbf{Y}_{23} & \mathbf{Y}_{24} \end{bmatrix}\mathbf{U}_{i,i+1} = \tilde{\mathbf{Y}}\mathbf{U}_{i,i+1} \tag{3.33}$$

where $\mathbf{U}_{i,i+1} = \left\{u_i \quad \mathrm{v}_i \quad w_i \quad \beta_i \quad \alpha_i \quad \gamma_i \quad u_{i+1} \quad \mathrm{v}_{i+1} \quad w_{i+1} \quad \beta_{i+1} \quad \alpha_{i+1} \quad \gamma_{i+1}\right\}^T$, and the detailed structures of $\mathbf{Y}_{ij}$ are given in the Appendix E. Introducing equation (3.33) into equation (3.32) gives:

$$\Delta\mathbf{r}_{j_A} = \left[\tilde{\mathbf{G}}_{ji}\tilde{\mathbf{Y}}\right]\begin{Bmatrix}\mathbf{U}_i \\ \mathbf{U}_{i+1}\end{Bmatrix} = \begin{bmatrix}\mathbf{G}_{j,i} & \mathbf{G}_{j,i+1}\end{bmatrix}\begin{Bmatrix}\mathbf{U}_i \\ \mathbf{U}_{i+1}\end{Bmatrix} \tag{3.34}$$

Next, the matrix $\mathbf{G}_{j,i}$ will be assembled into the global matrix, $\mathbf{G}_{AS}$, which is introduced into equation (3.31). In order to obtain the relationship between the aerodynamic forces $\mathbf{F}_A$ and structural forces $\mathbf{F}_S$, the two force systems must have the same work for any virtual displacement, i.e.,

$$\delta\left(\Delta\underline{\mathfrak{R}}_A\right)^T \mathbf{F}_A = \delta\mathbf{U}_{St}^T \left\{\left(\mathbf{G}_{AS}\right)^T \mathbf{F}_A\right\} = \delta\mathbf{U}_{St}^T \mathbf{F}_S \tag{3.35}$$

where $\delta\left(\Delta\underline{\mathfrak{R}}_A\right)$ and $\delta\mathbf{U}_{St}^T$ are virtual displacements of control points of the aerodynamic grid and of structural nodes, respectively. $\mathbf{G}_{AS}$ is the global matrix which connects the control points of the aerodynamic grid to the structural grid points, $\mathbf{F}_A$ is the matrix of aerodynamic force, which is located at the aerodynamic control point, and $\mathbf{F}_S$ is the matrix of the structural load, which is located at the structural grid points. For the present study the detailed forms of the matrices $\mathbf{G}_{AS}$, $\mathbf{F}_A$, and $\mathbf{F}_S$ are given in the Appendix E. Equation (3.35) yields the relationship between structural forces and the aerodynamic forces,

$$\mathbf{F}_S = \left(\mathbf{G}_{AS}\right)^T \mathbf{F}_A = \mathbf{G}_{SA}\mathbf{F}_A \tag{3.36}$$

where $\left(\mathbf{G}_{AS}\right)^T = \mathbf{G}_{SA}$. Introducing equation (3.36) into the equation (3.30), the equations of motion of the system is:

$$\mathbf{M}\ddot{\mathbf{U}}(\theta) + \left[\mathbf{K}_0 + \left(\sum_{n=1}^{N}\mathbf{K}_{b,n}\xi_n(\theta)\right) + \left(\sum_{n=1}^{N}\mathbf{K}_{t,n}\xi_n(\theta)\right)\right]\mathbf{U}(\theta) = \mathbf{G}_{SA}\mathbf{F}_A(\theta) \tag{3.37}$$

Equation (3.37) constitutes the equations of motion of a wing involving stiffness uncertainties. A modal analysis of equation (3.37) is performed and gives:

$$\mathbf{K}_0\tilde{\mathbf{\Psi}} = \mathbf{M}\tilde{\mathbf{\Psi}}\tilde{\mathbf{\Lambda}} \tag{3.38}$$

where $\tilde{\mathbf{\Psi}}$ is an $\mathbb{N}\times\mathbb{N}$ eigenvector matrix where $\mathbb{N}$ is the number of degrees of freedom of the finite element model, and $\tilde{\mathbf{\Lambda}}$ is a $\mathbb{N}\times\mathbb{N}$ diagonal matrix of

eigenvalues. Equation (3.37) will be solved using perturbation analysis in the next section.

### 3.6. Perturbation Analysis

The stochastic finite element method based on perturbation techniques has been developed in the literature by several researchers [103-105, 113]. The following coordinate transformation will be used to approximate the deformation of the beam:

$$\mathbf{U}(t,\theta) \cong \sum_{k=1}^{\tilde{N}} \Psi_k q_k = \mathbf{\Psi q}\,; \tag{3.39a}$$

where $\mathbf{\Psi}$ is a truncated form of $\tilde{\mathbf{\Psi}}$. For the present application, the method requires displacement vector be expanded into the truncated Taylor series:

$$\mathbf{U}(t,\theta) = \mathbf{\Psi}\left[\mathbf{q}_0(t) + \sum_{n=1}^{N} \frac{\partial \mathbf{q}}{\partial \xi_n}|_{\xi=0}\, \xi_n(\theta) + \frac{1}{2}\sum_{n=1}^{N}\sum_{m=1}^{N} \frac{\partial^2 \mathbf{q}}{\partial \xi_n \partial \xi_m}|_{\xi=0}\, \xi_n(\theta)\xi_m(\theta) + \ldots\right] \tag{3.39b}$$

Note that $\mathbf{\Psi}$ is an $\mathbb{N}\times\tilde{N}$ matrix that includes first $\tilde{N}$ mode shape vector, $\mathbf{q}$ is an $\tilde{N}\times 1$ generalized coordinates vector, and $\mathbf{q}_0$ is the mean value of $\mathbf{q}$. Substituting equation (3.39b) into equation (3.37), pre-multiplying both sides by $\mathbf{M}^{-1}\mathbf{\Psi}^{\mathrm{T}}$ and collecting terms of the same power of $\xi$ yields a set of perturbational equations of zero-order, first-order, second-order, and so on. For simplification sake we restrict the analysis up to the first-order and the following perturbational equations are obtained:

- Zero-order equation (coefficients of $\xi_n^0$):

$$\ddot{\mathbf{q}}_0 + \left[\boldsymbol{\Psi}^T \mathbf{K}_0 \boldsymbol{\Psi}\right] \mathbf{q}_0 = \left[\mathbf{M}^{-1} \boldsymbol{\Psi}^{\mathrm{T}} \mathbf{G}_{SA}\right] \mathbf{F}_{A,0} \tag{3.40a}$$

- First-order equation (coefficients of $\xi_n^1$):

$$\ddot{\mathbf{q}}_{1,n} + \left[\boldsymbol{\Psi}^T \mathbf{K}_0 \boldsymbol{\Psi}\right] \mathbf{q}_{1,n} = -\left[\boldsymbol{\Psi}^{\mathrm{T}} \mathbf{K}_{b,n} \boldsymbol{\Psi} + \boldsymbol{\Psi}^{\mathrm{T}} \mathbf{K}_{t,n} \boldsymbol{\Psi}\right] \mathbf{q}_0 + \left[\mathbf{M}^{-1} \boldsymbol{\Psi}^{\mathrm{T}} \mathbf{G}_{SA}\right] \frac{\partial \mathbf{F}_A}{\partial \xi_n} \tag{3.40b}$$

where $n = 1 \ldots N$, $\mathbf{q}_{1,n} = \dfrac{\partial \mathbf{q}}{\partial \xi_n}$, and $\left[\boldsymbol{\Psi}^T \mathbf{K}_0 \boldsymbol{\Psi}\right]$ is am $\tilde{N} \times \tilde{N}$ diagonal matrix of first $\tilde{N}$ eigenvectors. Alternatively, using the non-dimensional variables from the aerodynamic modeling, the perturbation equations in non-dimensional form are obtained:

$$\ddot{\mathbf{q}}_0 + T_{Cc}^2 \left[\boldsymbol{\Psi}^T \mathbf{K}_0 \boldsymbol{\Psi}\right] \mathbf{q}_0 = \bar{\mathbf{G}}_{MA} \bar{\mathbf{F}}_A \tag{3.41a}$$

$$\ddot{\mathbf{q}}_{1,n} + T_{Cc}^2 \left[\boldsymbol{\Psi}^T \mathbf{K}_0 \boldsymbol{\Psi}\right] \mathbf{q}_{1,n} = -\left[\hat{\mathbf{K}}_{b,n} + \hat{\mathbf{K}}_{t,n}\right] \mathbf{q}_0 + \bar{\mathbf{G}}_{MA} \frac{\partial \bar{\mathbf{F}}_A}{\partial \xi_n} \tag{3.41b}$$

where $\bar{\mathbf{G}}_{MA} = \left(\dfrac{1}{2} \rho_C L_C^4\right) \mathbf{M}^{-1} \boldsymbol{\Psi}^{\mathrm{T}} \mathbf{G}_{SA}$, $\hat{\mathbf{K}}_b^n = T_C^2 \boldsymbol{\Psi}^{\mathrm{T}} \mathbf{K}_{b,n} \boldsymbol{\Psi}$, $\hat{\mathbf{K}}_t^n = T_C^2 \boldsymbol{\Psi}^{\mathrm{T}} \mathbf{K}_{t,n} \boldsymbol{\Psi}$.

Equations (3.41) are numerically integrated once using an adapted Hamming's fourth order predictor-corrector method [36]. The numerical solutions are performed using the following values of the wing [38]: $\overline{EI}_x = 10^6 \, Nm^2$; $EI_z = 50 \times 10^6 \, Nm^2$; $\overline{GJ} = 1.5 \times 10^6 \, Nm^2$; $EA = 20 \times 10^6 \, N$; $m = \ 10 \, kg/m$; $I_0 = 15 kg \, m$; $\delta_3 = 0.15 \, m$; wing length $L = 3m$; wing chord $C = 1m$; angle of attack $\alpha_a = 5°$; $L_C = 0.16667m$.

In order to obtain realistic results the wing will be discretized using 9 elements for the wing structure and $6\times10$ elements for the lattice. The response will be obtained from perturbation method at various flow speeds and various bending and torsion stiffness uncertainty levels, i.e.,

$$q_{ben}(\tau,\theta)=q_{0,ben}(\tau)+\sum_{n=1}^{N}q_{1,ben}(\tau)\xi_n(\theta),\qquad q_{tor}(\tau,\theta)=q_{0,tor}(\tau)+\sum_{n=1}^{N}q_{1,tor}(\tau)\xi_n(\theta) \tag{3.42a,b}$$

where $N=2$, $q_{0,ben}$ and $q_{0,tor}$ are obtained from the equation (3.41a), $q_{1,ben}$ and $q_{1,tor}$ from the equation (3.41b). The analysis is carried out for $N=2$ since for $N>2$ the results converge as shown in Figure 3.8. The temporal component of the variance of the response along the ensemble is given by:

$$s^2_{ben}(t,\theta)=\left(q_{ben}(t,\theta)-E\left[q_{ben}(t,\theta)\right]\right)^2,\qquad s^2_{tor}(t,\theta)=\left(q_{tor}(t,\theta)-E\left[q_{tor}(t,\theta)\right]\right)^2 \tag{3.43a,b}$$

Four cases are studied and the results are shown below: (1) in the absence of uncertainties; (2) the influence of bending stiffness uncertainty; (3) the influence of torsion stiffness uncertainty; (4) the influence of combination bending-torsion stiffness uncertainty.

### 3.6.1 RESULTS IN THE ABSENCE OF UNCERTAINTIES

The purpose of the system analysis in the absence of uncertainties is to find the wing critical flutter speed. Figures 3.9, 3.10, 3.11, and 3.12 show the time history records and their corresponding variances for the airflow speeds 120 m/s, 140 m/s, 143 m/s, and 145 m/s respectively. These plots and the subsequent plots are obtained at angle of attack $\alpha = 5^o$ and initial conditions $q_{ben}(0) = -0.05$, $\dot{q}_{ben}(0) = 0.0$, $q_{tor}(0) = 0.01$, and $\dot{q}_{tor}(0) = 0.0$.

It is observed that the system is stable up to the flow speed 143 m/s when limit cycle oscillations (LCOs) appear. A slightly increase in the flow speed, let say 145 m/s, the system become unstable with growing amplitude. Next sections will show the influence of uncertainties on the stability of the system.

### 3.6.2 THE INFLUENCE OF BENDING STIFFNESS UNCERTAINTY

Under bending stiffness uncertainty, the results are obtained for airflow speeds of 120 m/s, 125 m/s, 130 m/s, 135 m/s, and 140 m/s.

- Figures 3.13 and 3.14 show the results for the airflow speed 120m/s. In the presence of small level of bending stiffness uncertainty up to $\sigma_{EI_x} / \overline{EI}_x = 0.09$, the wing remains stable and both time history records and their variances decay with time (see Figure 3.13). When the bending stiffness uncertainty reaches the critical value $\sigma_{EI_x} / \overline{EI}_x = 0.1$ the wing experiences limit cycle oscillations as shown in Figure 3.14. Above that level of bending stiffness uncertainty the wing oscillations grow without limit.

- For the airflow speed 125 m/s the time histories and their corresponding variances are shown in the Figures 3.15 – 3.17 for bending stiffness uncertainty levels of $\sigma_{EI_x} / \overline{EI}_x = 0.07$, $\sigma_{EI_x} / \overline{EI}_x = 0.08$, and $\sigma_{EI_x} / \overline{EI}_x = 0.09$, respectively. As we observe from the figures, LCOs are obtained at $\sigma_{EI_x} / \overline{EI}_x = 0.08$. Below this value the system is stable and above it is unstable.
- For the airflow speed 130 m/s the time histories and their corresponding variances are shown in the Figures 3.18 – 3.20 for bending stiffness uncertainty levels of $\sigma_{EI_x} / \overline{EI}_x = 0.05$, $\sigma_{EI_x} / \overline{EI}_x = 0.06$, and $\sigma_{EI_x} / \overline{EI}_x = 0.07$, respectively. The LCOs are obtained at $\sigma_{EI_x} / \overline{EI}_x = 0.06$. Below this value the system is stable and above it is unstable.
- For the airflow speed 135 m/s the time histories and their corresponding variances are shown in the Figures 3.21 – 3.23 for bending stiffness uncertainty levels of $\sigma_{EI_x} / \overline{EI}_x = 0.03$, $\sigma_{EI_x} / \overline{EI}_x = 0.04$, and $\sigma_{EI_x} / \overline{EI}_x = 0.05$, respectively. The LCOs are obtained at $\sigma_{EI_x} / \overline{EI}_x = 0.04$. Below this value the system is stable and above it is unstable.
- For the airflow speed 140 m/s the time histories and their corresponding variances are shown in Figures 3.24 – 3.26 for bending stiffness uncertainty levels of $\sigma_{EI_x} / \overline{EI}_x = 0.01$, $\sigma_{EI_x} / \overline{EI}_x = 0.015$, and $\sigma_{EI_x} / \overline{EI}_x = 0.02$, respectively. The LCOs are obtained at $\sigma_{EI_x} / \overline{EI}_x = 0.015$. Below this value the system is stable and above it is unstable.

All the above results are summarized in Figure 3.27 which shows the stability bifurcation diagram $V_\infty$- $\sigma_{EI_x} / \overline{EI}_x$, where the region occupied by small empty circles, "○", designates stable wing response, and the region covered by small empty triangles, "Δ", is belonging to unstable wing. The line separating the two regions signals the occurrence of LCO and it is designated by empty squares "□". From the stability diagram we may conclude that the unstable region increases with the flow speed.

### 3.6.3 THE INFLUENCE OF TORSION STIFFNESS UNCERTAINTY

This section examines the influence of torsion stiffness uncertainty on the stability of the wing in the absence of bending stiffness uncertainty. The analysis is done in the range of airflow speed 120-140m/s as follows. For the airflow speed 120 m/s the time histories and their corresponding variances are shown in the Figures 3.28 – 3.30 in absence of bending stiffness uncertainty and in the presence of torsion stiffness uncertainty levels of $\sigma_{GJ} / \overline{GJ} = 0.03$, $\sigma_{GJ} / \overline{GJ} = 0.035$, and $\sigma_{GJ} / \overline{GJ} = 0.04$, respectively. The LCOs are obtained at $\sigma_{GJ} / \overline{GJ} = 0.035$. Below this value the system is stable and above it is unstable.

Figures 3.31 – 3.33 show the appearance of LCOs at airflow speeds $V_\infty = 130\text{m/s}$, $V_\infty = 135\text{m/s}$, and $V_\infty = 140\text{m/s}$ and torsion uncertainty levels of $\sigma_{GJ} / \overline{GJ} = 0.03$, $\sigma_{GJ} / \overline{GJ} = 0.02$, $\sigma_{GJ} / \overline{GJ} = 0.01$, respectively. Below the uncertainty level where the LCOs appear, the system is stable while above it is unstable.

Figure 3.34 shows the stability bifurcation diagram $V_\infty$ - $\sigma_{GJ}/\overline{GJ}$. It is seen that the stable region in the presence of torsion stiffness uncertainty is smaller than the stable region in the presence of bending stiffness uncertainty. This demonstrates the significant influence of torsion stiffness uncertainty on the stability of the wing.

### 3.6.4 THE INFLUENCE OF COMBINATION BENDING – TORSION STIFFNESS UNCERTAINTY

The influence of combined bending-torsion stiffness uncertainty is shown in the Figures 3.35 – 3.46. The Figures show only the appearance of LCO which corresponds to the boundary between stable and unstable region.

- Figures 3.35 – 3.39 show the time history records and their corresponding variances for the flow speed $V_\infty = 120\text{m/s}$ and the following uncertainty levels: ($\sigma_{EI_x}/\overline{EI}_x = 0.01$, $\sigma_{GJ}/\overline{GJ} = 0.0325$), ($\sigma_{EI_x}/\overline{EI}_x = 0.03$, $\sigma_{GJ}/\overline{GJ} = 0.025$), ($\sigma_{EI_x}/\overline{EI}_x = 0.05$, $\sigma_{GJ}/\overline{GJ} = 0.02$), ($\sigma_{EI_x}/\overline{EI}_x = 0.07$, $\sigma_{GJ}/\overline{GJ} = 0.015$), and ($\sigma_{EI_x}/\overline{EI}_x = 0.09$, $\sigma_{GJ}/\overline{GJ} = 0.01$), respectively.
- Figures 3.40 – 3.44 show the time history records and their corresponding variances for the flow speed $V_\infty = 130\text{m/s}$ and the following uncertainty levels: ($\sigma_{EI_x}/\overline{EI}_x = 0.01$, $\sigma_{GJ}/\overline{GJ} = 0.025$), ($\sigma_{EI_x}/\overline{EI}_x = 0.02$, $\sigma_{GJ}/\overline{GJ} = 0.021$), ($\sigma_{EI_x}/\overline{EI}_x = 0.03$, $\sigma_{GJ}/\overline{GJ} = 0.015$), ($\sigma_{EI_x}/\overline{EI}_x = 0.04$, $\sigma_{GJ}/\overline{GJ} = 0.01$), and ($\sigma_{EI_x}/\overline{EI}_x = 0.05$, $\sigma_{GJ}/\overline{GJ} = 0.075$), respectively.

- Figure 3.45 shows the time history records and their corresponding variances for the flow speed $V_\infty = 140\text{m/s}$ and the uncertainty levels ($\sigma_{EI_x} / \overline{EI}_x = 0.01$, $\sigma_{GJ} / \overline{GJ} = 0.005$).

The above results are summarized in the Figure 3.46 which shows the influence of both bending and torsion uncertainties on the stability of the wing. Figure 3.46(a) reveals the stability boundaries for the bending-torsion combination uncertainties ($\sigma_{EI_x} / \overline{EI}_x$ - $\sigma_{GJ} / \overline{GJ}$) at different flow speeds and Figure 3.46(b) is a 3-dimensional representation of Figure 3.46(a) with airflow speed represented by the third axis.

### 3.7. Monte Carlo Simulation

In order to define the limitation of the perturbation method, the Monte Carlo simulation will be performed. First consider the deterministic equations of motion for one element as given by equation (3.20). Uncertainties will be introduced in bending stiffness, which is described by equation (3.22a). Introducing equation (322a) into equation (3.21b) the expression for the elemental stiffness takes the form:

$$\mathbf{K}^e = EI_z \left( \int_{y_i}^{y_{i+1}} \left( \mathbf{Y}_u(y)'' \right)^T \mathbf{Y}_u(y)'' \, dy \right) + AE \left( \int_{y_i}^{y_{i+1}} \left( \mathbf{Y}_v(y)' \right)^T \mathbf{Y}_v(y)' \, dy \right) +$$

$$\left( \int_{y_i}^{y_{i+1}} \left( \overline{EI}_x + \widetilde{EI}_x \right) \left( \mathbf{Y}_w(y)'' \right)^T \mathbf{Y}_w(y)'' \, dy \right) + c \left( \int_{y_i}^{y_{i+1}} \left( \overline{GJ} + \widetilde{GJ} \right) \left( \mathbf{Y}_\alpha(y)' \right)^T \mathbf{Y}_\alpha(y)' \, dy \right) \tag{3.44}$$

Assembling the elemental matrices given in the equation (3.20), having the elemental stiffness given by equation (3.44), and introducing the aerodynamic loads given by expression (3.36) gives the system equation:

$$\mathbf{M}\ddot{\mathbf{U}} + \mathbf{K}\mathbf{U} = \mathbf{G}_{SA}^{CP}\mathbf{F}_A \tag{3.45}$$

Using the coordinate transformation given by equation (3.39a), equation (3.45) takes the form

$$\ddot{\mathbf{q}} + \mathbf{\Lambda}\mathbf{q} = \mathbf{M}^{-1}\mathbf{\Psi}^{\mathrm{T}}\mathbf{G}_{SA}^{CP}\mathbf{F}_A \tag{3.46}$$

The number of equations in the expression (3.46) is 7. Equation (3.46) will be integrated numerically once based on the assumption that the response is ergodic.

Time history records together with their corresponding variances obtained from Monte Carlo method as well as a comparison with perturbation method results are shown in Figures 3.47 – 3.51 in the presence of bending uncertainty.

- Figure 3.47 reveals the results obtained for airflow speed $V_\infty = 120\mathrm{m/s}$ and bending uncertainty level $\sigma_{EI_x} / \overline{EI}_x = 0.1$;
- Figure 3.48 reveals the results obtained for airflow speed $V_\infty = 125\mathrm{m/s}$ and bending uncertainty level $\sigma_{EI_x} / \overline{EI}_x = 0.08$;
- Figure 3.49 reveals the results obtained for airflow speed $V_\infty = 130\mathrm{m/s}$ and bending uncertainty level $\sigma_{EI_x} / \overline{EI}_x = 0.06$;

- Figure 3.50 reveals the results obtained for airflow speed $V_\infty = 135\text{m/s}$ and bending uncertainty level $\sigma_{EI_x} / \overline{EI}_x = 0.04$;
- Figure 3.51 reveals the results obtained for airflow speed $V_\infty = 140\text{m/s}$ and bending uncertainty level $\sigma_{EI_x} / \overline{EI}_x = 0.01$.

From the comparisons between the two methods shown in the Figures 3.47(c), 3.48(c), 3.49(c), 3.50(c), 3.51(c), we may conclude by increasing the airflow speed and decreasing the uncertainty level, the accuracy of the perturbation method increases. The Monte Carlo simulation confirms the perturbation results in predicting the LCO for low values of bending stiffness variance.

The bifurcation diagram shown in Figure 3.52 obtained from Monte Carlo simulation is identical with the one shown in Figure 3.27 estimated by perturbation method. This demonstrates that the perturbation method is very accurate in predicting LCOs and the establishment of stability boundaries in the presence of bending uncertainties. The dependence of bending and torsion variances on bending uncertainties is shown in Figure 3.53 for different values of airflow speed.

Figures 3.54 – 3.56 show the Monte Carlo simulation time history responses for three values of airflow speed, 120m/s, 130m/s and 140m/s, and three different levels of torsion stiffness uncertainty, $\sigma_{GJ} / \overline{GJ} = 0.05$, $0.03$ and $0.01$, respectively. The comparison shown in Figure 3.54(c) reveals a poor approximation of the perturbation method as compared with the Monte Carlo

simulation for flow speed 120 m/s and $\sigma_{EI_x} / \overline{EI}_x = 0$, $\sigma_{GJ} / \overline{GJ} = 0.05$. Note that the Monte Carlo simulation yields LCO while the perturbation method gives unstable response. Better correlation between the two methods is obtained at higher speeds but lower uncertainty levels as demonstrated in Figure 3.56(c) for flow speed 140 m/s, $\sigma_{EI_x} / \overline{EI}_x = 0$, $\sigma_{GJ} / \overline{GJ} = 0.01$. The stability bifurcation diagram $V_\infty$- $\sigma_{GJ} / \overline{GJ}$ obtained from Monte Carlo simulation is shown in Figure 3.57. Comparing the bifurcation diagrams from Figures 3.34 and 3.57, one observes a good correlation in the prediction of LCOs up to flow speed 130 m/s and $\sigma_{GJ} / \overline{GJ} = 0.03$. As the airflow speed decreases and torsion stiffness uncertainty level increases, the perturbation method loses the ability to predict LCOs. For example at flow speed 120 m/s, LCO is obtained form Monte Carlo simulation at $\sigma_{GJ} / \overline{GJ} = 0.05$, while from perturbation method at $\sigma_{GJ} / \overline{GJ} = 0.035$. Figure 3.58(a) and 3.58(b) shows the dependence of bending and torsion variances on the torsion stiffness uncertainty level for different values of airflow speed indicated on each curve. Both diagrams confirm the limitation of perturbation method for low level of stiffness uncertainty.

### 3.8. Closing Remarks

The influence of uncertainties on the flutter behavior of an aeroelastic wing is examined. The uncertainties are modeled using a modified first order stochastic perturbation method together with a truncated Karhunen-Loeve expansion instead of Taylor series. However, the Taylor series is used for

displacement vector expansion. The results of the perturbation approach are compared with those predicted by Monte Carlo simulation and the comparison revealed good correlation for low values of stiffness uncertainty levels. As the uncertainty level increases, the perturbation method loses accuracy. For the prediction of LCO, the perturbation method is very accurate for all levels of bending stiffness uncertainty examined, but the method loses its accuracy at upper levels of torsion stiffness uncertainty. The stability boundary in the flow speed versus stiffness uncertainty reveals the appearance of LCOs below the flutter speed. Further increase of uncertainty level produces instability. The uncertainties in torsion stiffness induce a greater disturbance in the system. A smaller level of torsion stiffness uncertainty induces instability in the system.

One last remark pertaining to the CPU time in generating the results of the two approaches. The CPU, on a PC of 3.2 GHz, for a single Monte Carlo simulation (based on assuming ergodicty of the response) requires 8 hours which is the CPU time required for perturbation analysis. Even though for Monte Carlo simulation, 7 equations are necessary to be solved and for the perturbation method 21 equations, the computational time is approximately the same. In the case of Monte Carlo simulation the equations must be solved for each value of airflow speed and each value of uncertainty level. In the case of perturbation method, the $\xi_n^0$ order equations (3.41a) are necessary to be solved only once for each value of air-flow speed regardless of level of uncertainty. For the same airflow speed and different levels of uncertainty, only equations (3.41b) need to be solved. The equations (3.41b), if they are solved simultaneously, will take less

computational time than a single Monte Carlo simulation. The next chapter will provide the final conclusions and recommendations pertaining to the entire work presented here as well as the proposal for the future work.

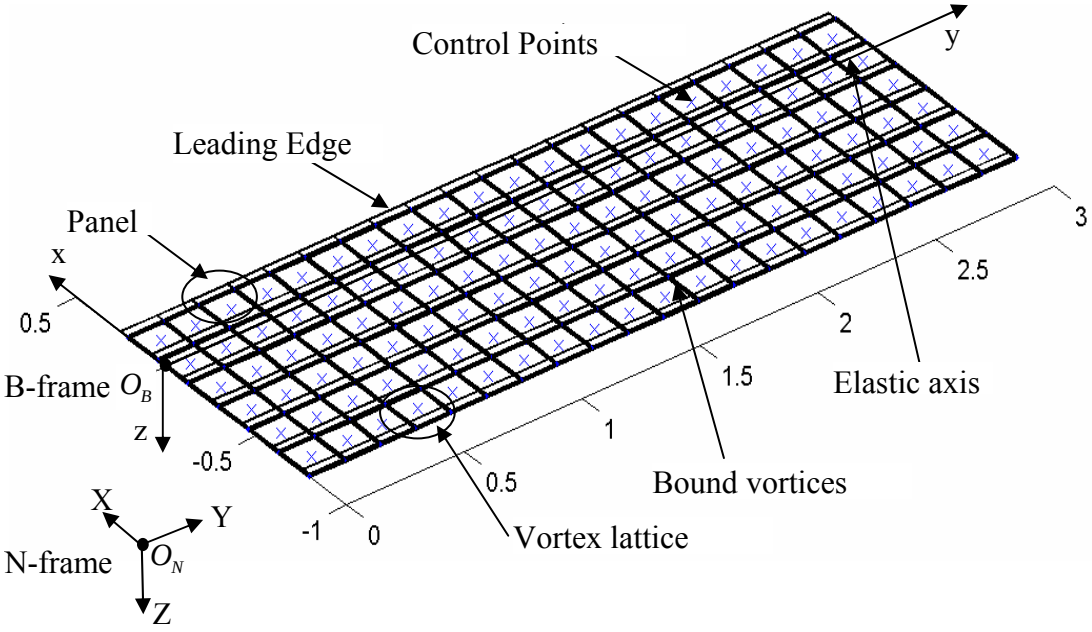


Figure 3.1. Lifting Surface Discretization

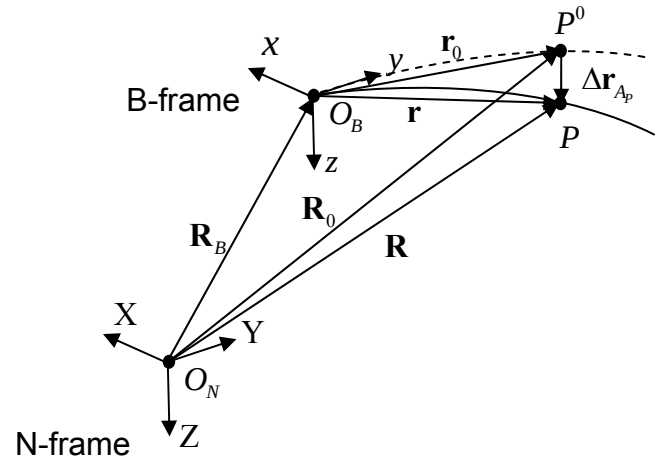


Figure 3.2. The position of an arbitrary point $P$ on the lifting surface caused by the wing structure deformation

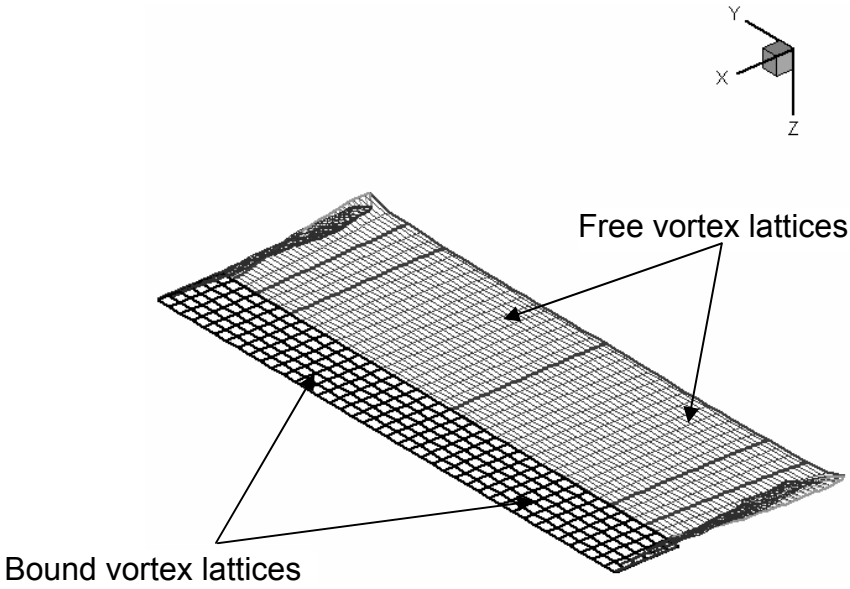


Figure 3.3(a). Bound and free vortex lattices

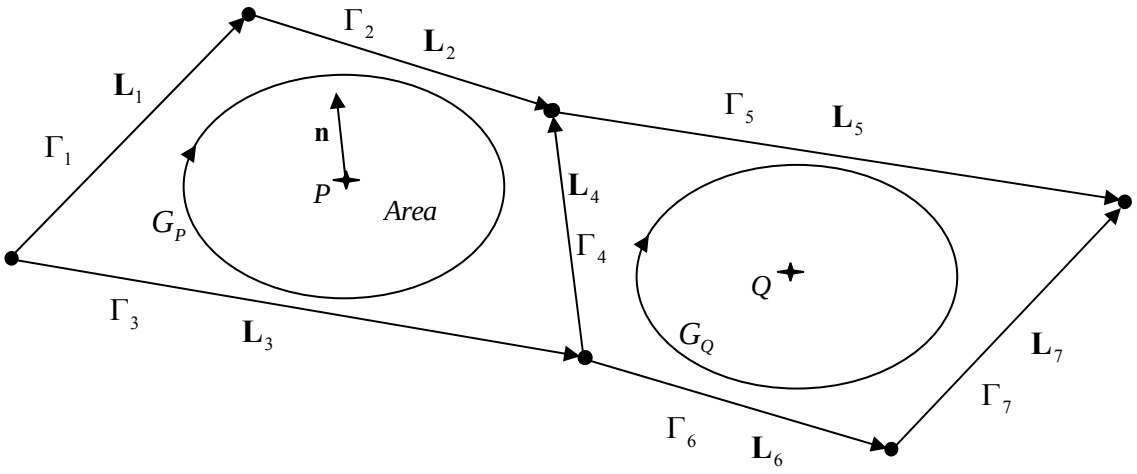


Figure 3.3(b). Representation of a general bound lattice element

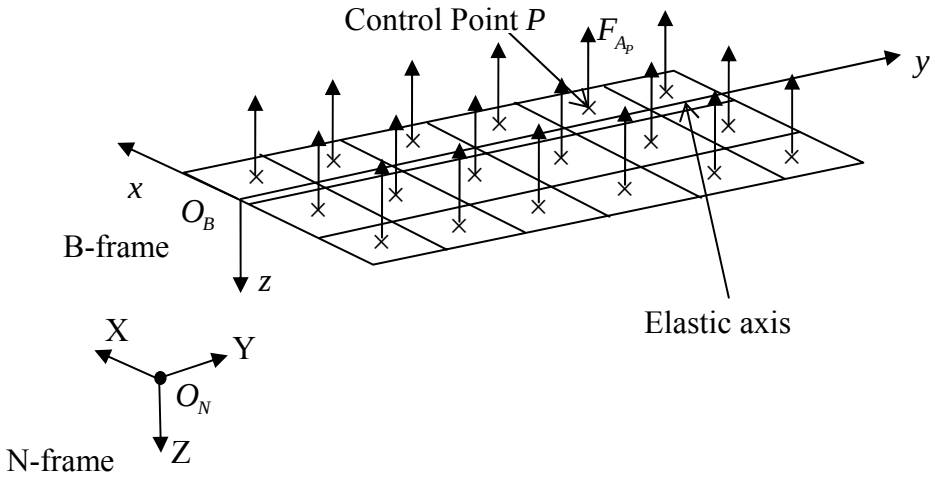


Figure 3.4 A portion of the lattice with representation of the aerodynamic loads

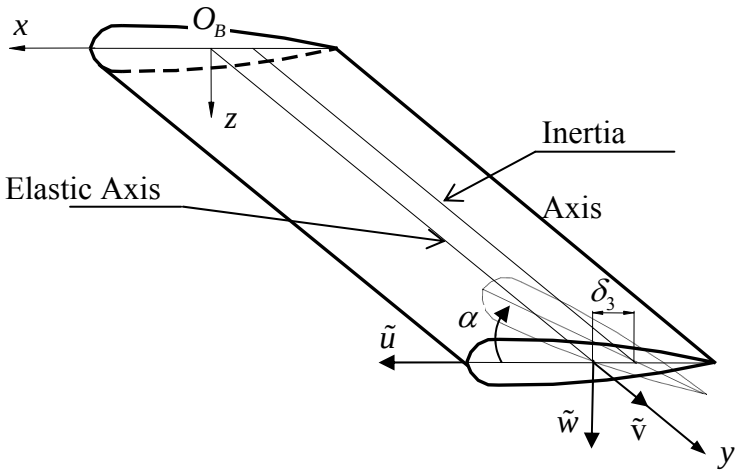


Figure 3.5. Wing structure model

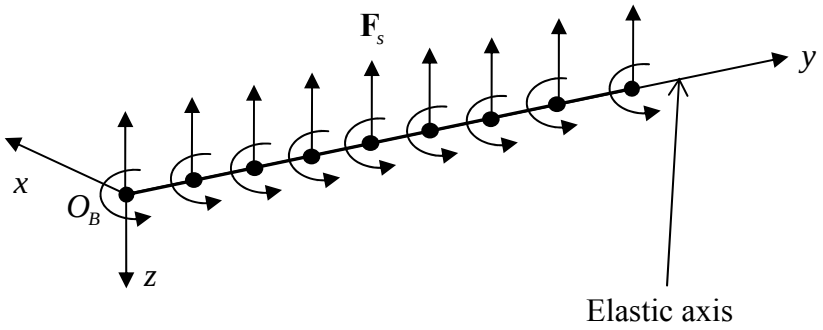


Figure 3.6(a). Finite elements discretization

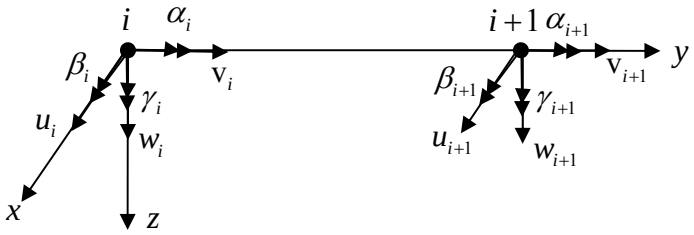


Figure 3.6(b). A finite element representation

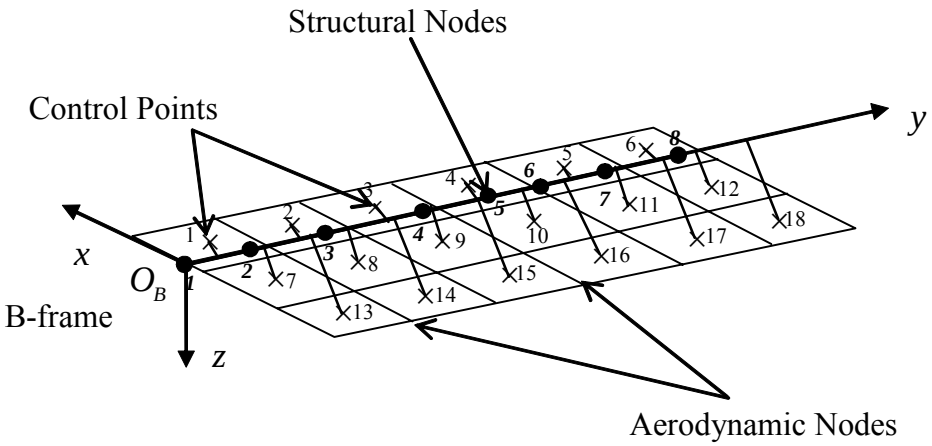


Structure nodes: $i = 1, 2, ..., 8$, Aerodynamic control points: $j = 1, 2, ..., 18$

Figure 3.7(a). Structural grid superimposed to the aerodynamic grid

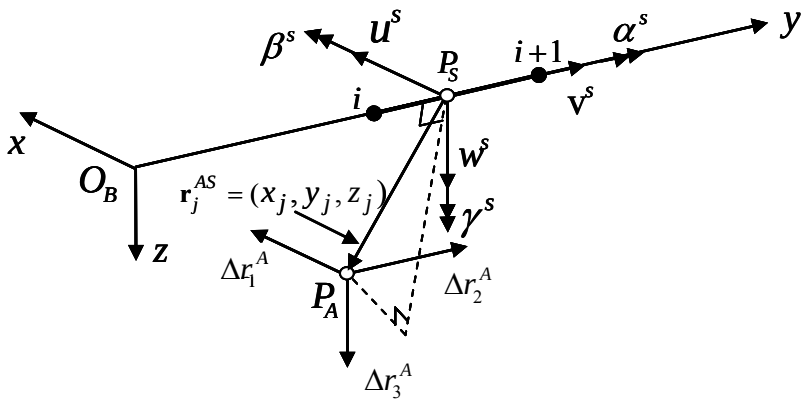


Figure 3.7(b). Connection of an aerodynamic grid point to an internal point of the structural grid point

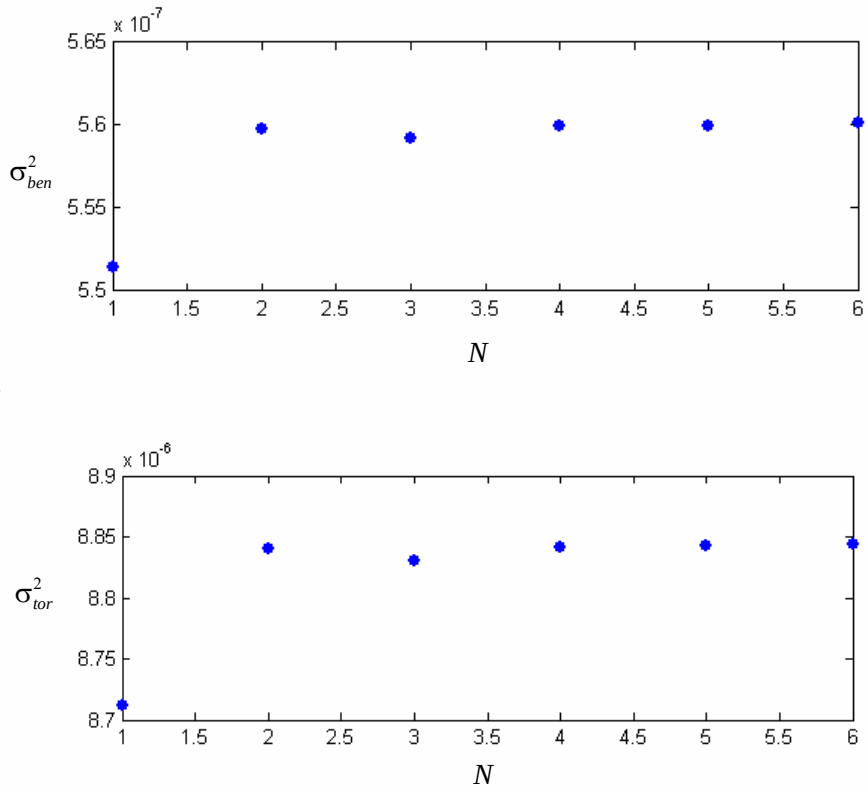


Figure 3.8. Dependence of wing response variances on the number of terms *N* in the Karhunen-Loeve expansion showing the convergence is achieved for $N \geq 2$.

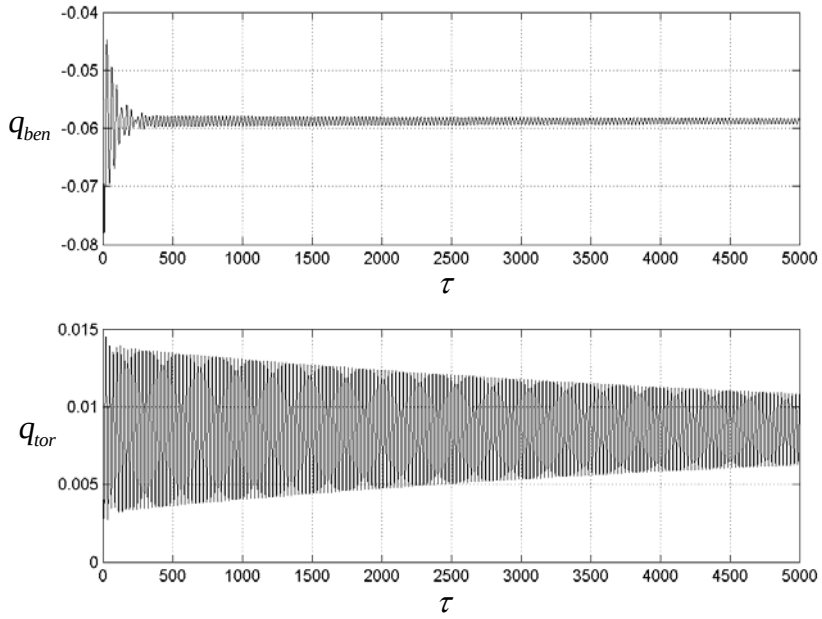


(a) Time history response of bending and torsion at the wing tip

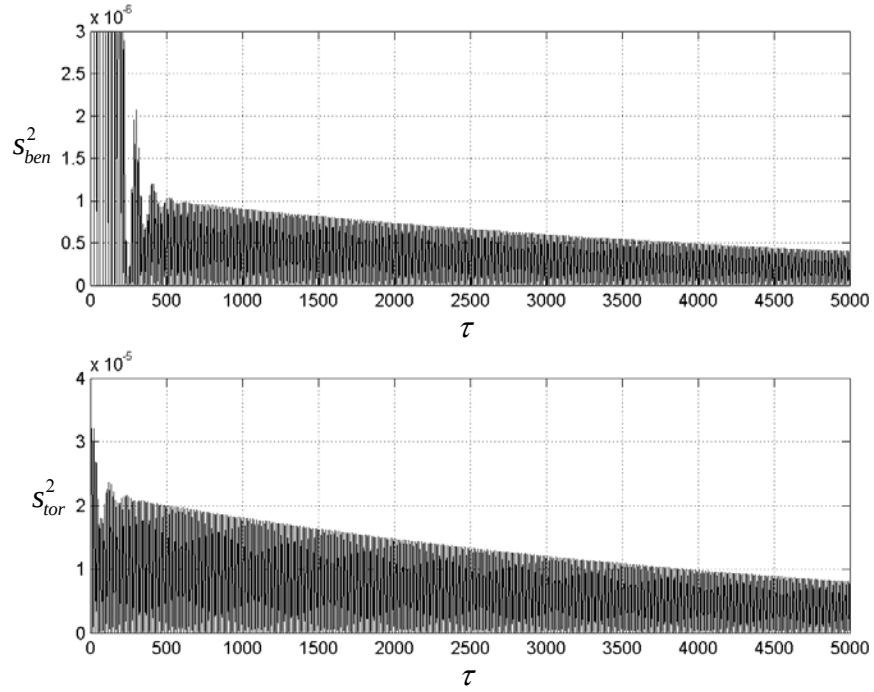


(b) Bending and torsion variances time history plots

Figure 3.9. Time history records of bending and torsion responses and their variances for $V_\infty = 120m/s$, $\sigma_{EI_x}/\overline{EI}_x = 0$, $\sigma_{GJ}/\overline{GJ} = 0$, $\alpha_a = 5°$, $q_{ben}(0) = -0.05$, $\dot{q}_{ben}(0) = 0$, $q_{tor}(0) = 0.01$, $\dot{q}_{tor}(0) = 0$

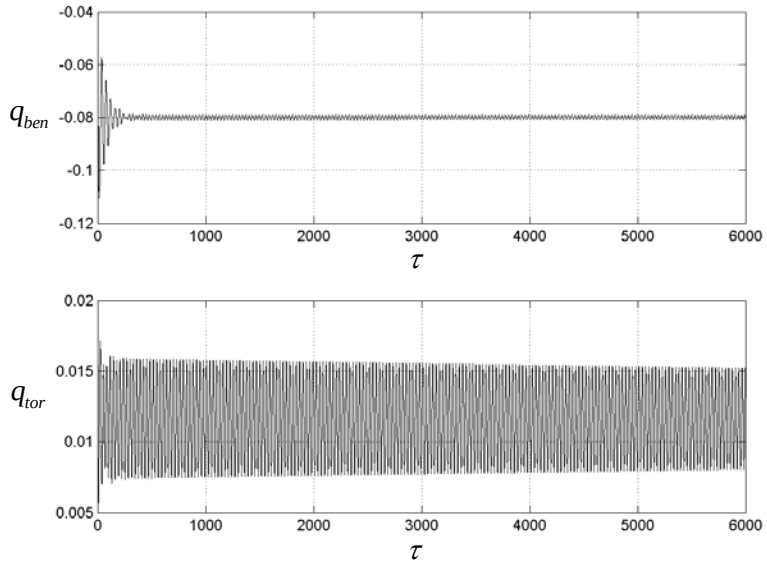


(a) Time history response of bending and torsion at the wing tip

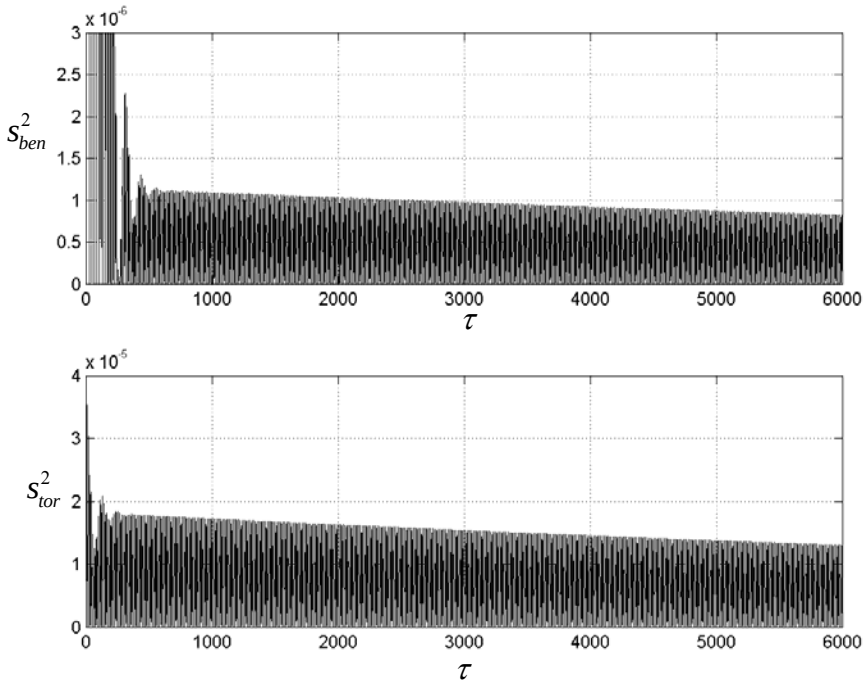


(b) Bending and torsion variances time history plots

Figure 3.10. Time history records of bending and torsion responses and their variances for $V_\infty = 140 m/s$, $\sigma_{EI_x} / \overline{EI}_x = 0$, $\sigma_{GJ} / \overline{GJ} = 0$, $\alpha_a = 5°$, $q_{ben}(0) = -0.05$, $\dot{q}_{ben}(0) = 0$, $q_{tor}(0) = 0.01$, $\dot{q}_{tor}(0) = 0$

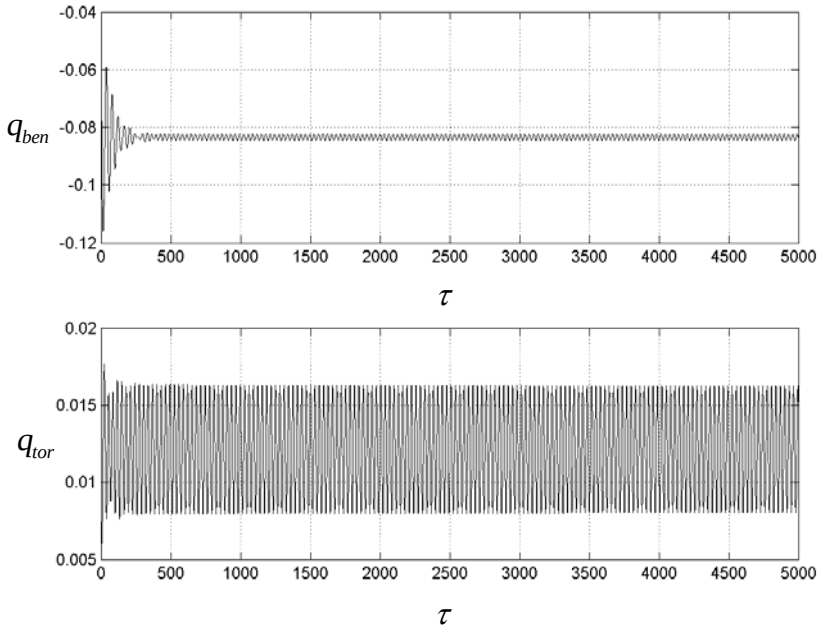


(a) Time history response of bending and torsion at the wing tip

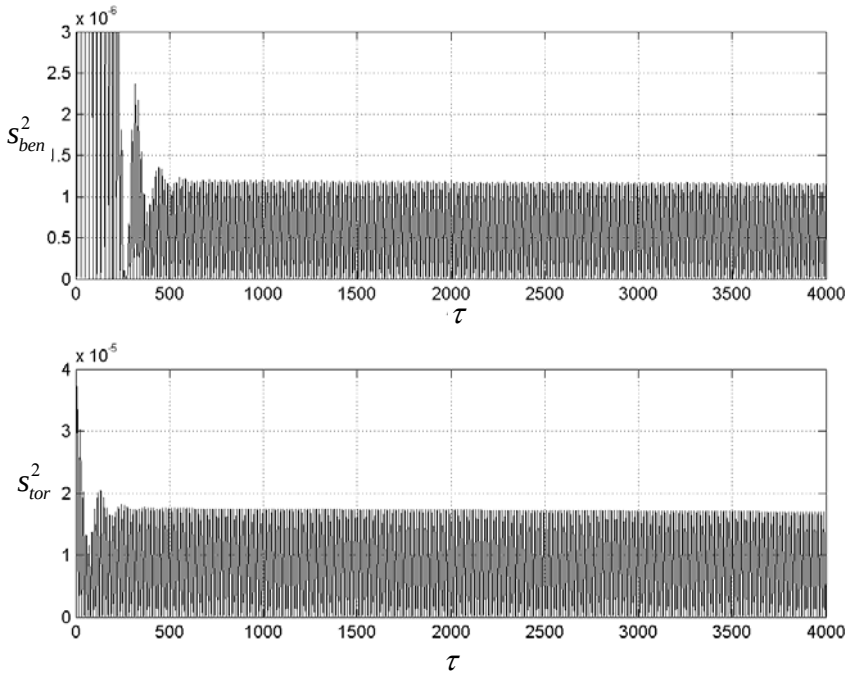


(b) Bending and torsion variances time history plots

Figure 3.11. Time history records of bending and torsion responses and their variances for flutter speed $V_\infty = 143m/s$, $\sigma_{EI_x}/\overline{EI}_x = 0$, $\sigma_{GJ}/\overline{GJ} = 0$, $\alpha_a = 5°$, $q_{ben}(0) = -0.05$, $\dot{q}_{ben}(0) = 0$, $q_{tor}(0) = 0.01$, $\dot{q}_{tor}(0) = 0$

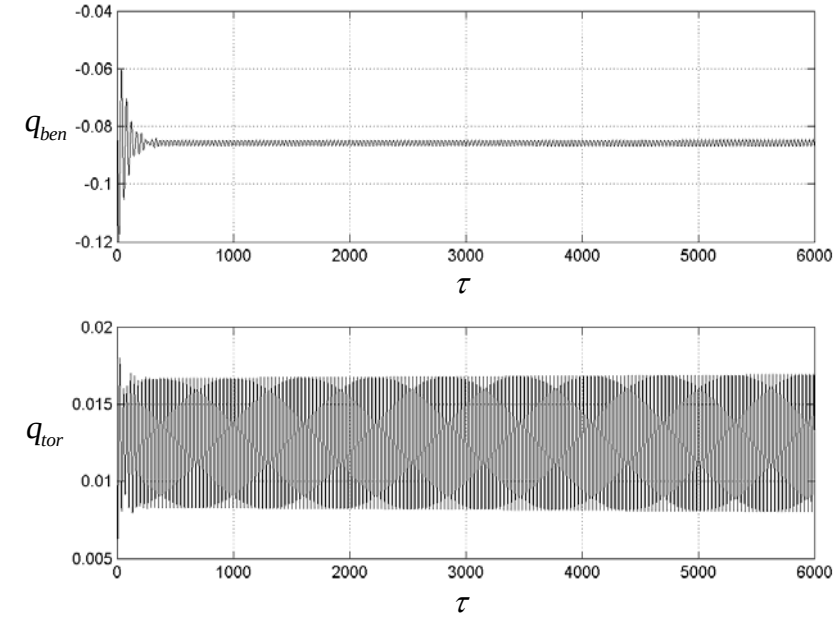


(a) Time history response of bending and torsion at the wing tip

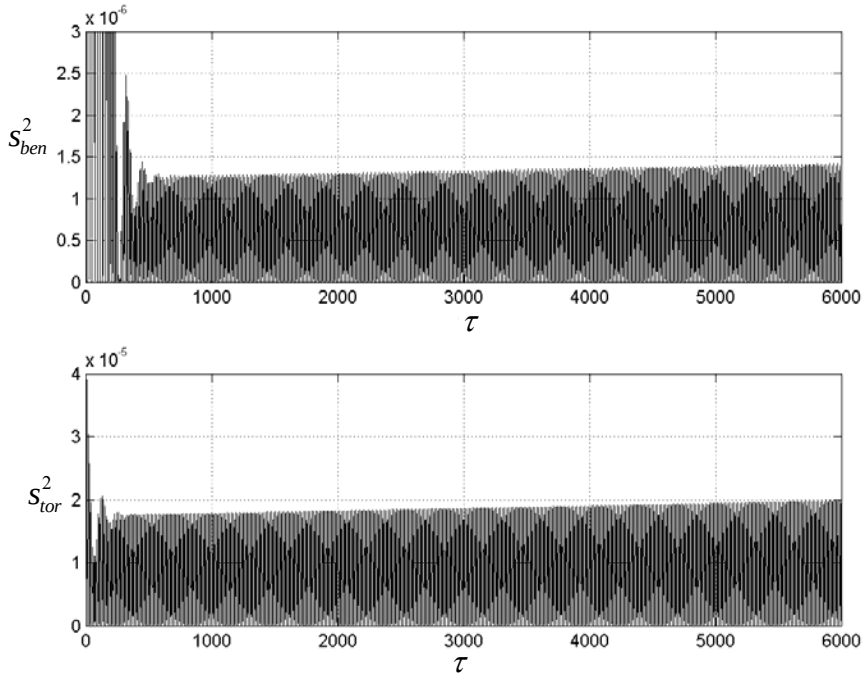


(b) Bending and torsion variances time history plots

Figure 3.12. Time history records of bending and torsion responses and their variances for $V_\infty = 145 m/s$, $\sigma_{EI_x} / \overline{EI}_x = 0$, $\sigma_{GJ} / \overline{GJ} = 0$, $\alpha_a = 5°$, $q_{ben}(0) = -0.05$, $\dot{q}_{ben}(0) = 0$, $q_{tor}(0) = 0.01$, $\dot{q}_{tor}(0) = 0$

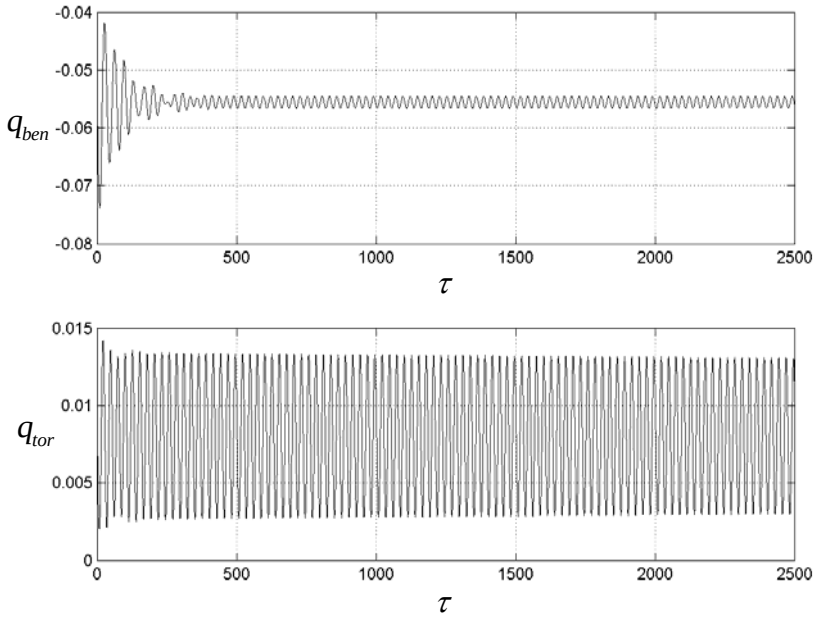


(a) Time history response of bending and torsion at the wing tip

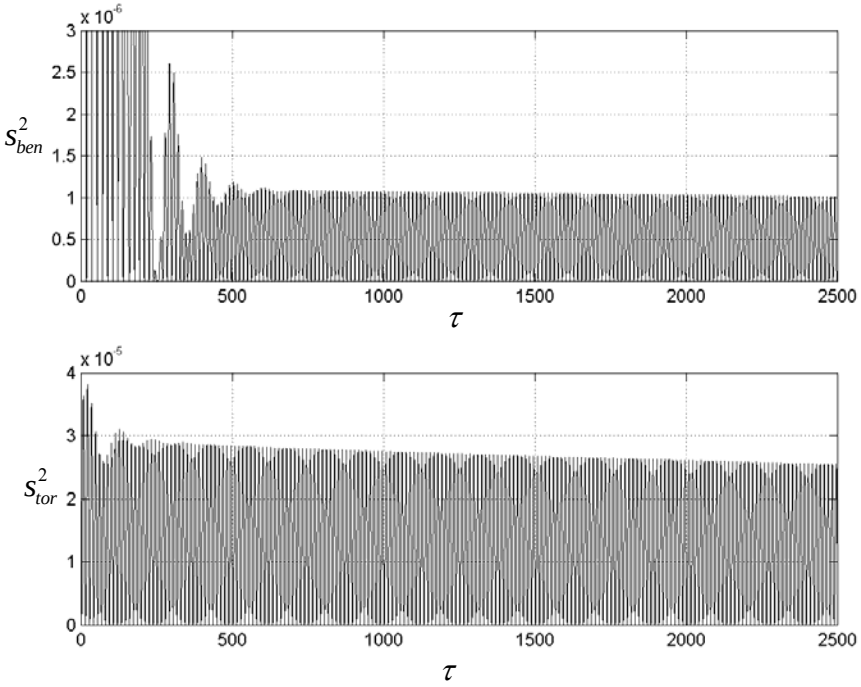


(b) Bending and torsion variances time history plots

Figure 3.13. Time history records of bending and torsion responses and their variances for $V_\infty = 120m/s$, $\sigma_{EI_x}/\overline{EI}_x = 0.09$, $\sigma_{GJ}/\overline{GJ} = 0$, $\alpha_a = 5°$, $q_{ben}(0) = -0.05$, $\dot{q}_{ben}(0) = 0$, $q_{tor}(0) = 0.01$, $\dot{q}_{tor}(0) = 0$

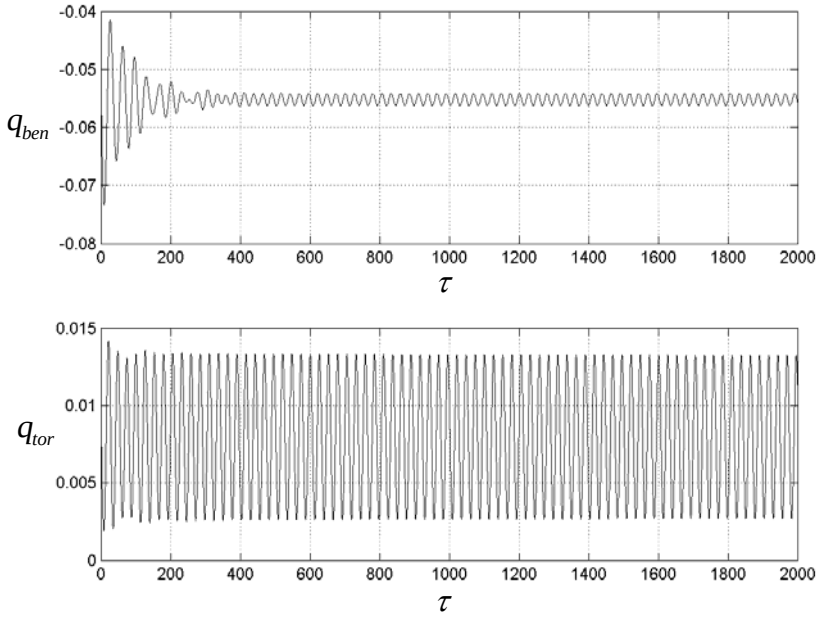


(a) Time history response of bending and torsion at the wing tip

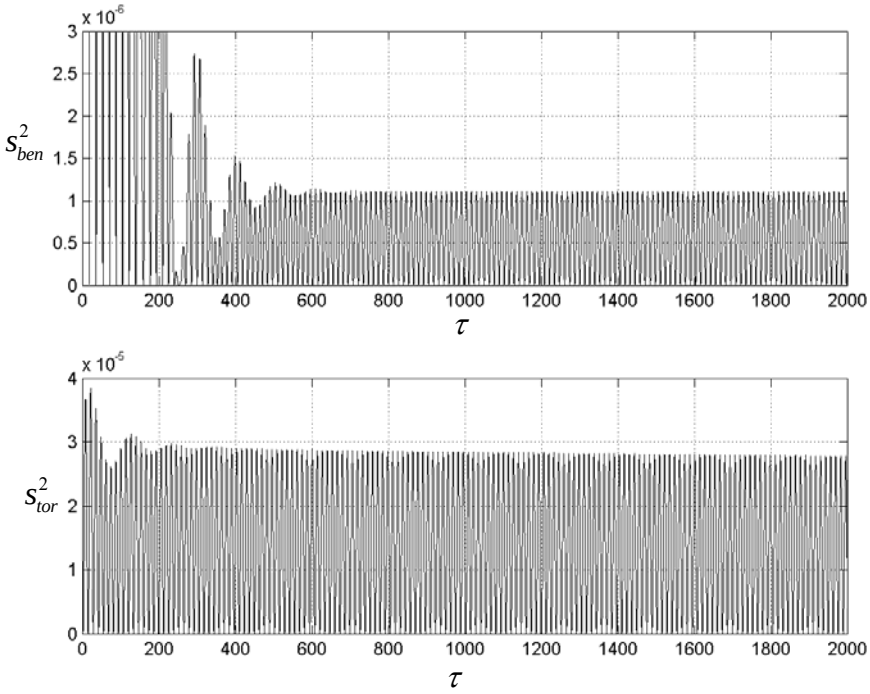


(b) Bending and torsion variances time history plots

Figure 3.14. Time history records of bending and torsion responses and their variances for $V_\infty = 120m/s$, $\sigma_{EI_x}/\overline{EI}_x = 0.1$, $\sigma_{GJ}/\overline{GJ} = 0$, $\alpha_a = 5°$, $q_{ben}(0) = -0.05$, $\dot{q}_{ben}(0) = 0$, $q_{tor}(0) = 0.01$, $\dot{q}_{tor}(0) = 0$

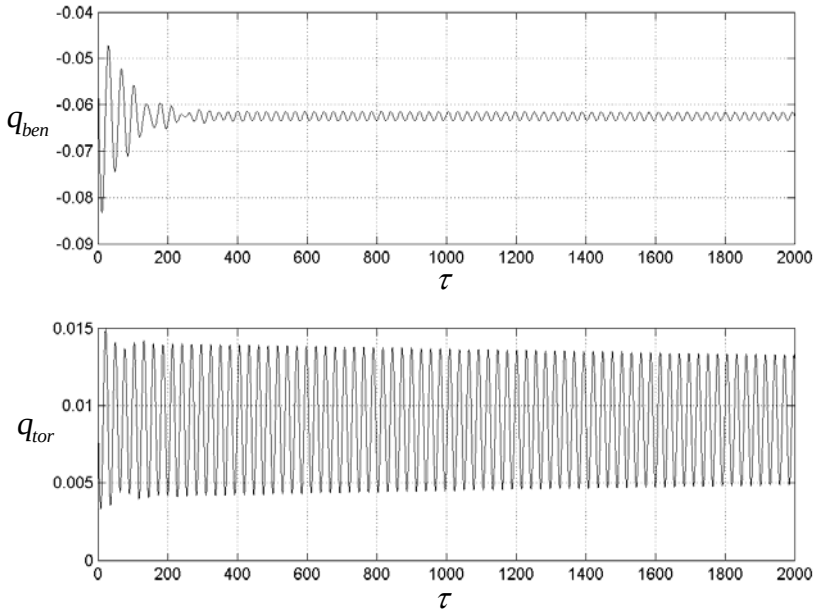


(a) Time history response of bending and torsion at the wing tip

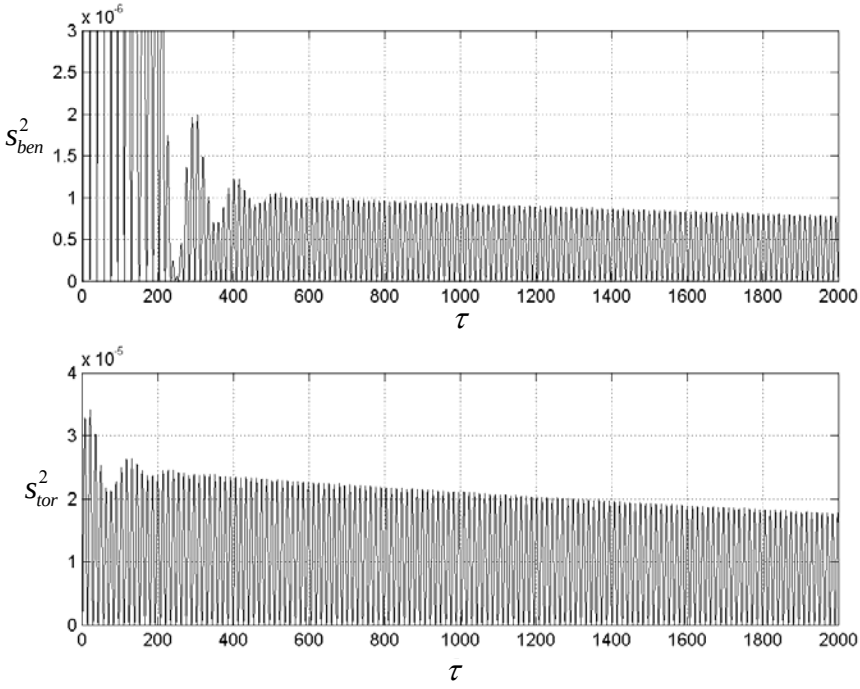


(b) Bending and torsion variances time history plots

Figure 3.15. Time history records of bending and torsion responses and their variances for $V_\infty = 125m/s$, $\sigma_{EI_x}/\overline{EI}_x = 0.07$, $\sigma_{GJ}/\overline{GJ} = 0$, $\alpha_a = 5°$, $q_{ben}(0) = -0.05$, $\dot{q}_{ben}(0) = 0$, $q_{tor}(0) = 0.01$, $\dot{q}_{tor}(0) = 0$

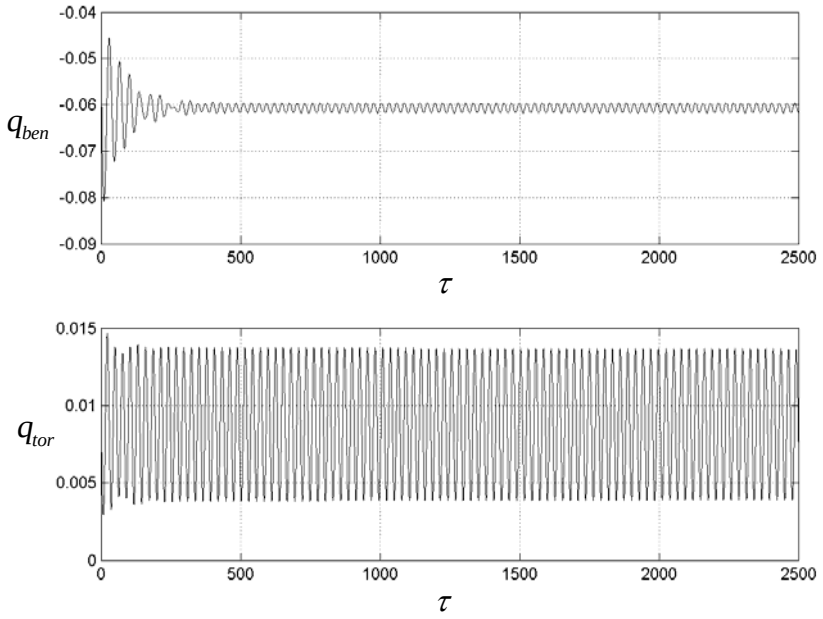


(a) Time history response of bending and torsion at the wing tip

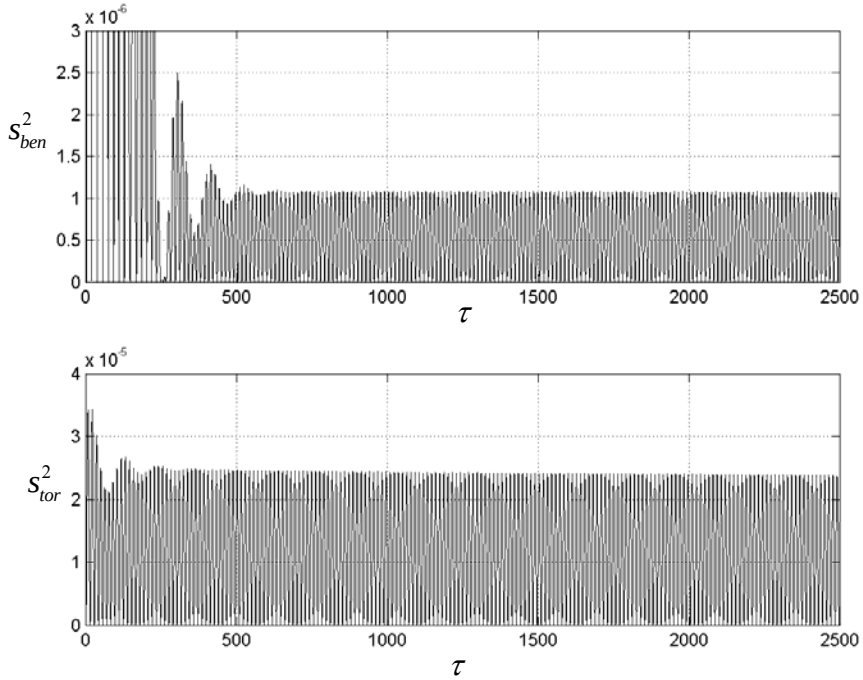


(b) Bending and torsion variances time history plots

Figure 3.16. Time history records of bending and torsion responses and their variances for $V_\infty = 125m/s$, $\sigma_{EI_x}/\overline{EI}_x = 0.08$, $\sigma_{GJ}/\overline{GJ} = 0$, $\alpha_a = 5°$, $q_{ben}(0) = -0.05$, $\dot{q}_{ben}(0) = 0$, $q_{tor}(0) = 0.01$, $\dot{q}_{tor}(0) = 0$

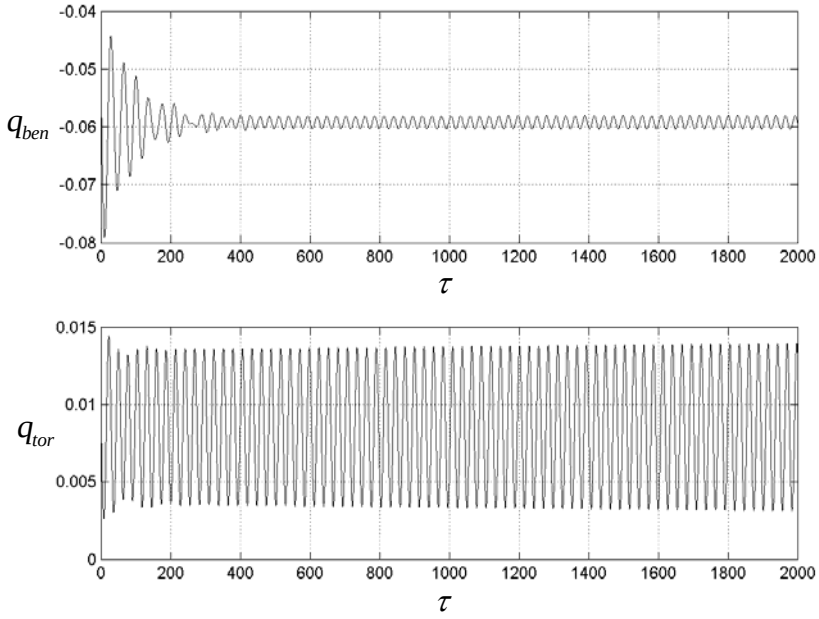


(a) Time history response of bending and torsion at the wing tip

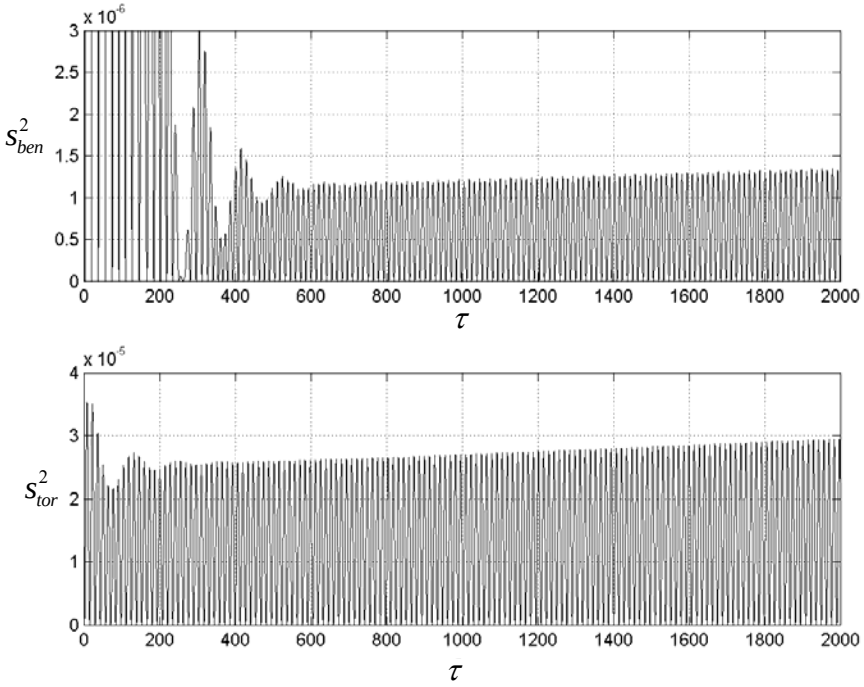


(b) Bending and torsion variances time history plots

Figure 3.17. Time history records of bending and torsion responses and their variances for $V_\infty = 125m/s$, $\sigma_{EI_x}/\overline{EI}_x = 0.09$, $\sigma_{GJ}/\overline{GJ} = 0$, $\alpha_a = 5°$, $q_{ben}(0) = -0.05$, $\dot{q}_{ben}(0) = 0$, $q_{tor}(0) = 0.01$, $\dot{q}_{tor}(0) = 0$

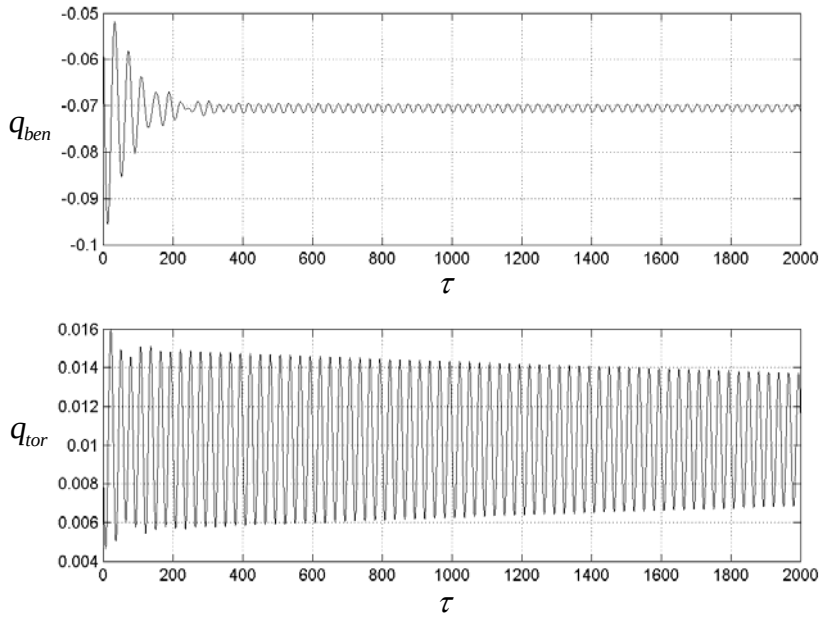


(a) Time history response of bending and torsion at the wing tip

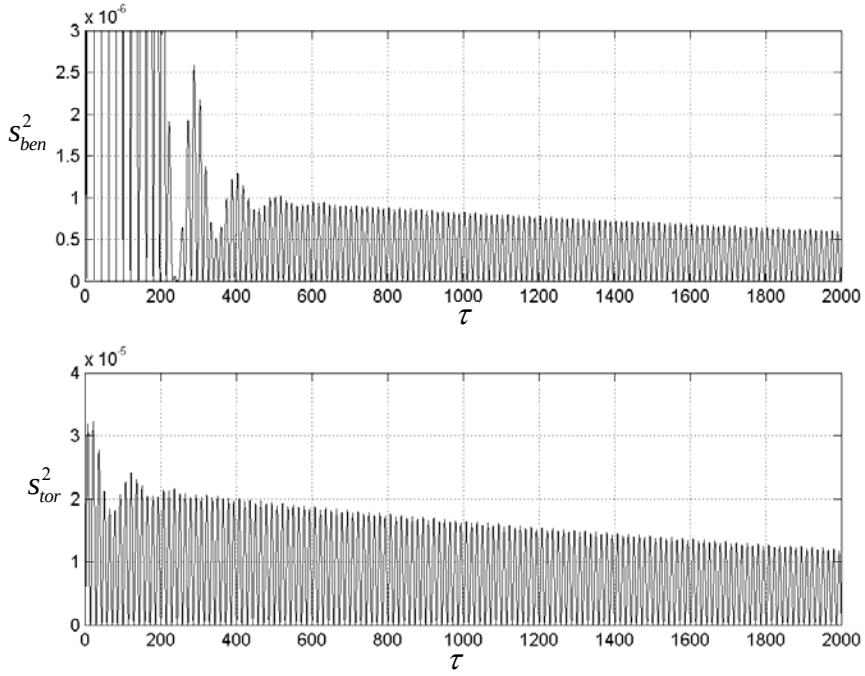


(b) Bending and torsion variances time history plots

Figure 3.18. Time history records of bending and torsion responses and their variances for $V_\infty = 130m/s$, $\sigma_{EI_x}/\overline{EI}_x = 0.05$, $\sigma_{GJ}/\overline{GJ} = 0$, $\alpha_a = 5°$, $q_{ben}(0) = -0.05$, $\dot{q}_{ben}(0) = 0$, $q_{tor}(0) = 0.01$, $\dot{q}_{tor}(0) = 0$

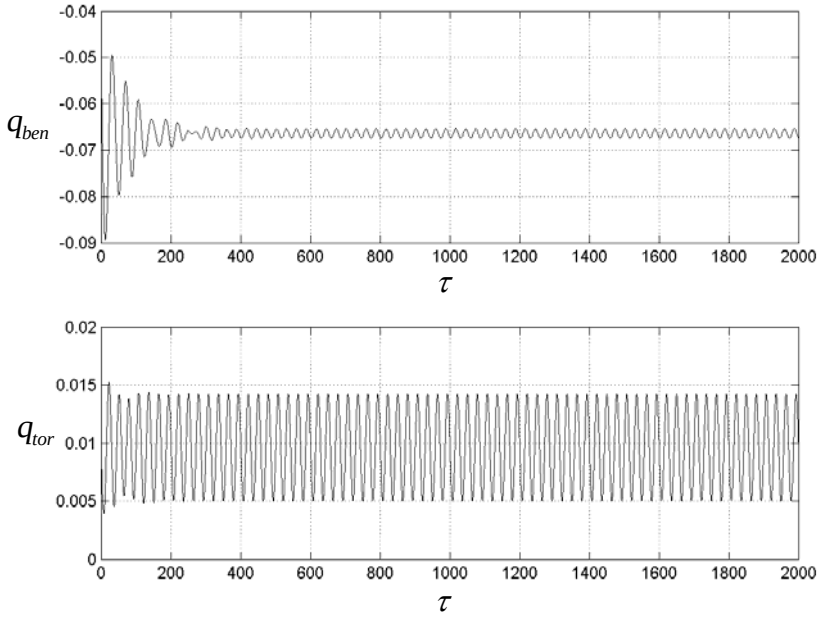


(a) Time history response of bending and torsion at the wing tip

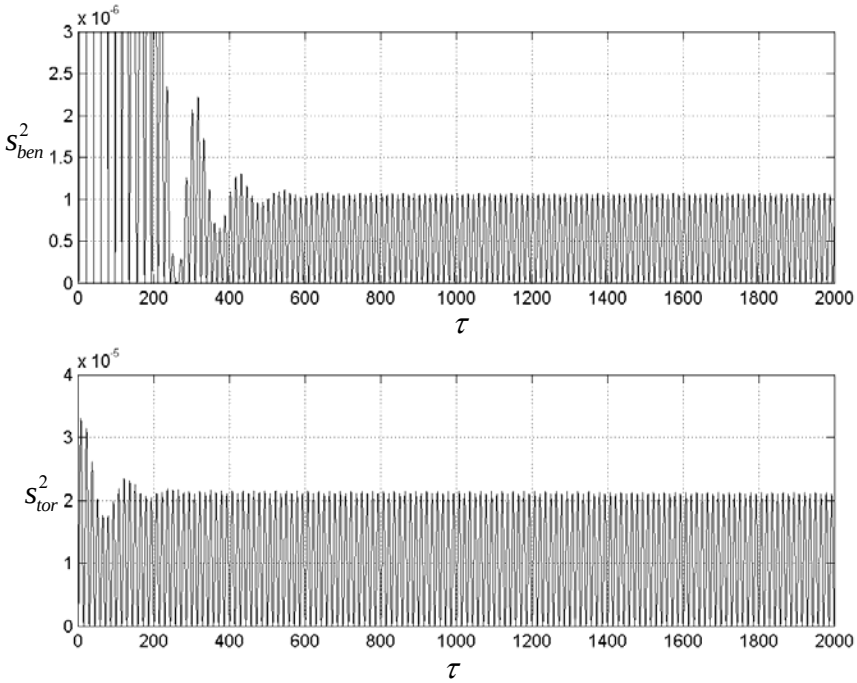


(b) Bending and torsion variances time history plots

Figure 3.19. Time history records of bending and torsion responses and their variances for $V_\infty = 130m/s$, $\sigma_{EI_x}/\overline{EI}_x = 0.06$, $\sigma_{GJ}/\overline{GJ} = 0$, $\alpha_a = 5°$, $q_{ben}(0) = -0.05$, $\dot{q}_{ben}(0) = 0$, $q_{tor}(0) = 0.01$, $\dot{q}_{tor}(0) = 0$

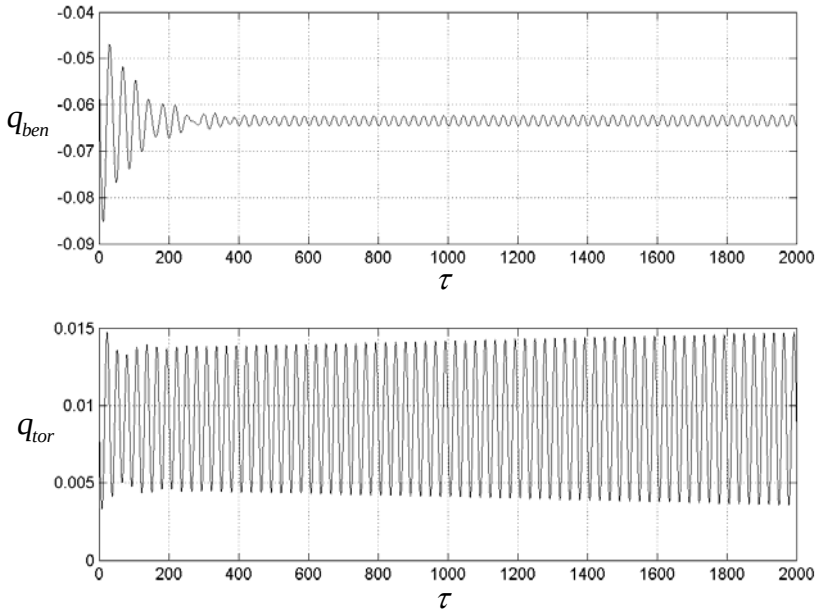


(a) Time history response of bending and torsion at the wing tip

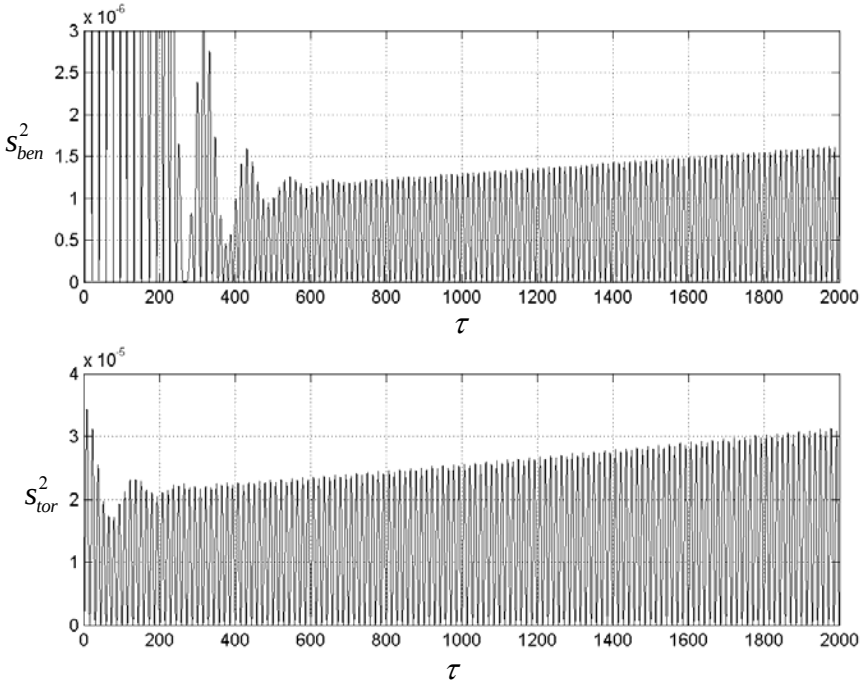


(b) Bending and torsion variances time history plots

Figure 3.20. Time history records of bending and torsion responses and their variances for $V_\infty = 130m/s$, $\sigma_{EI_x}/\overline{EI}_x = 0.07$, $\sigma_{GJ}/\overline{GJ} = 0$, $\alpha_a = 5°$, $q_{ben}(0) = -0.05$, $\dot{q}_{ben}(0) = 0$, $q_{tor}(0) = 0.01$, $\dot{q}_{tor}(0) = 0$

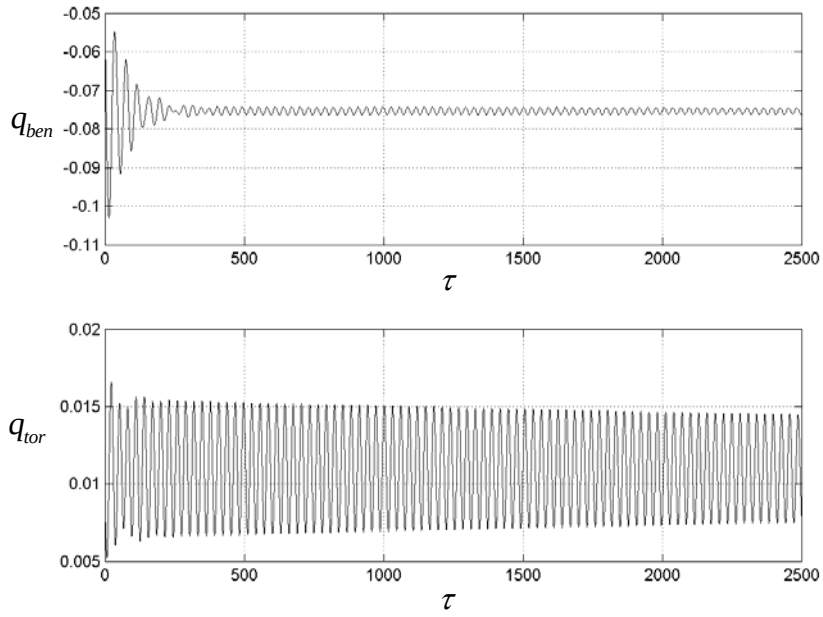


(a) Time history response of bending and torsion at the wing tip

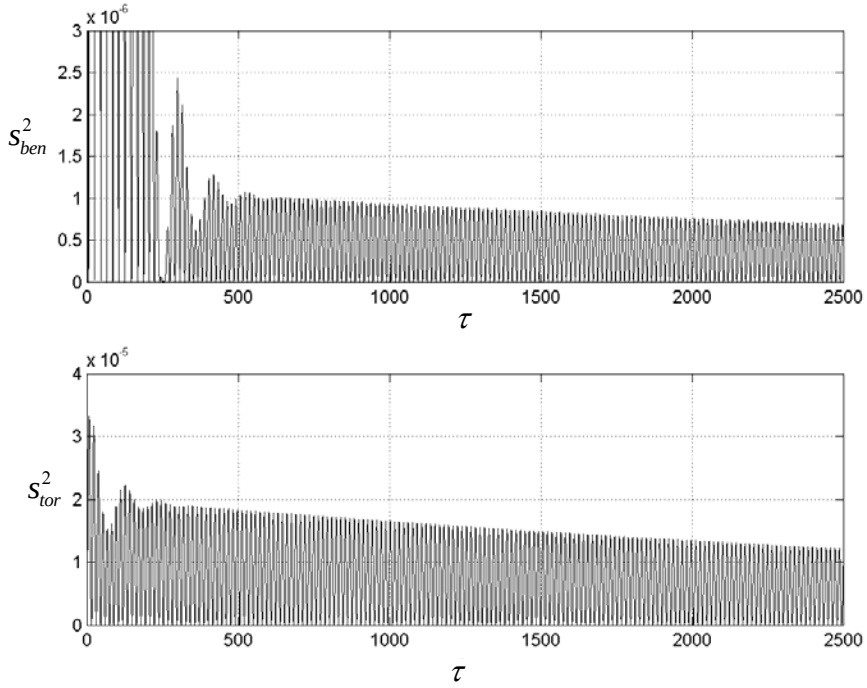


(b) Bending and torsion variances time history plots

Figure 3.21. Time history records of bending and torsion responses and their variances for $V_\infty = 135m/s$, $\sigma_{EI_x}/\overline{EI}_x = 0.03$, $\sigma_{GJ}/\overline{GJ} = 0$, $\alpha_a = 5°$, $q_{ben}(0) = -0.05$, $\dot{q}_{ben}(0) = 0$, $q_{tor}(0) = 0.01$, $\dot{q}_{tor}(0) = 0$

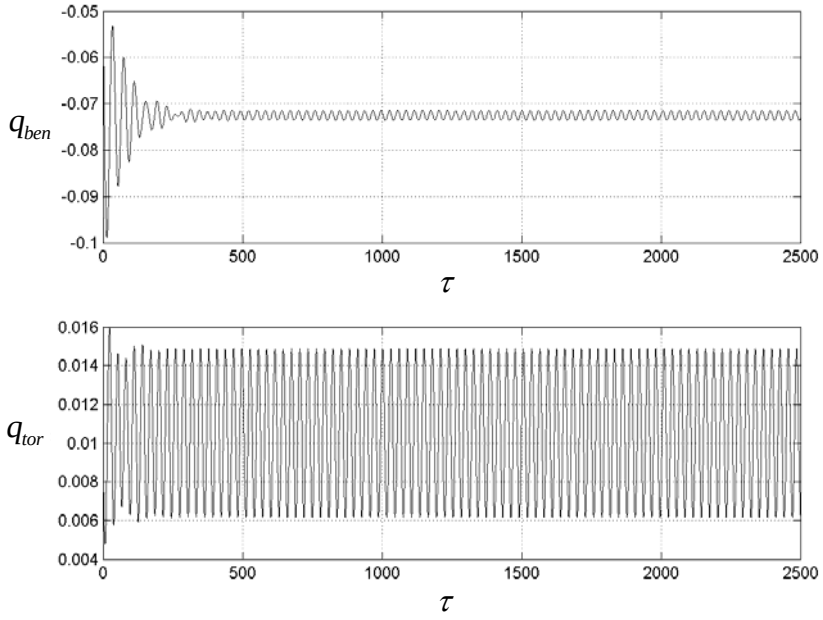


(a) Time history response of bending and torsion at the wing tip

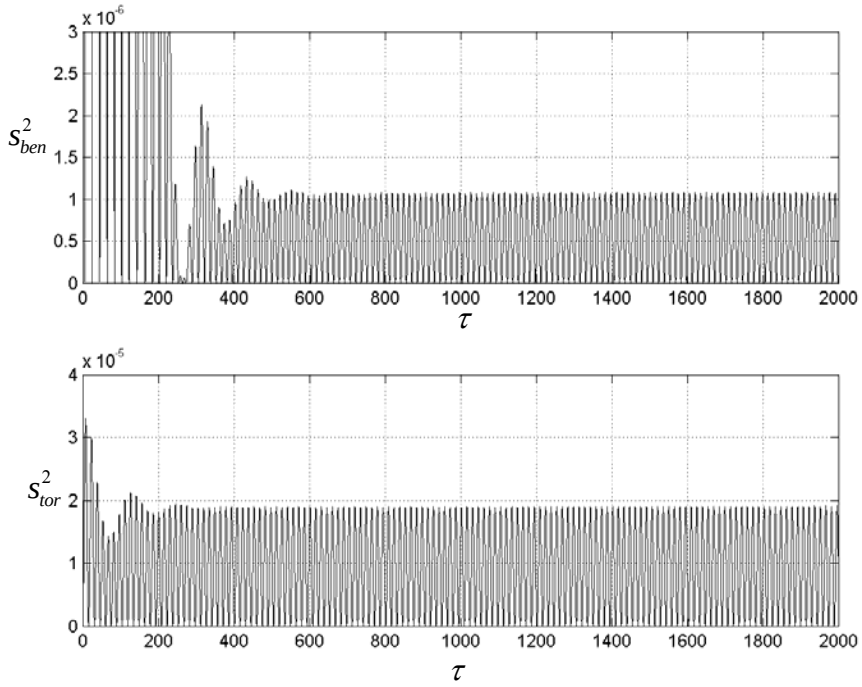


(b) Bending and torsion variances time history plots

Figure 3.22. Time history records of bending and torsion responses and their variances for $V_\infty = 135m/s$, $\sigma_{EI_x}/\overline{EI}_x = 0.04$, $\sigma_{GJ}/\overline{GJ} = 0$, $\alpha_a = 5°$, $q_{ben}(0) = -0.05$, $\dot{q}_{ben}(0) = 0$, $q_{tor}(0) = 0.01$, $\dot{q}_{tor}(0) = 0$

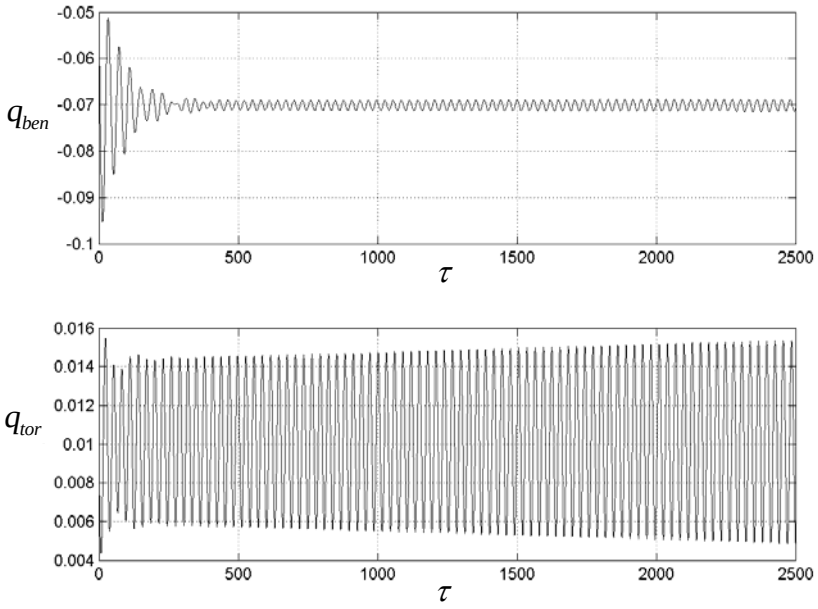


(a) Time history response of bending and torsion at the wing tip

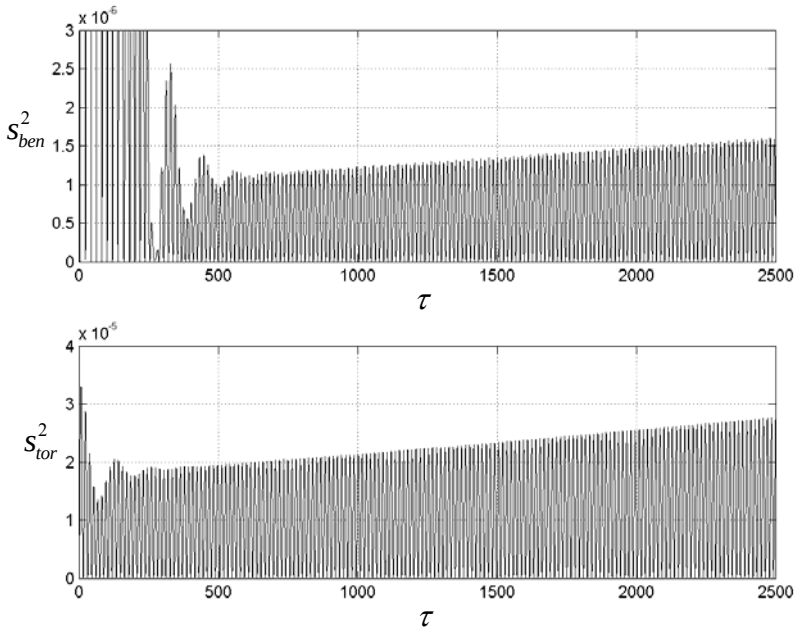


(b) Bending and torsion variances time history plots

Figure 3.23. Time history records of bending and torsion responses and their variances for $V_\infty = 135m/s$, $\sigma_{EI_x}/\overline{EI}_x = 0.05$, $\sigma_{GJ}/\overline{GJ} = 0$, $\alpha_a = 5°$, $q_{ben}(0) = -0.05$, $\dot{q}_{ben}(0) = 0$, $q_{tor}(0) = 0.01$, $\dot{q}_{tor}(0) = 0$

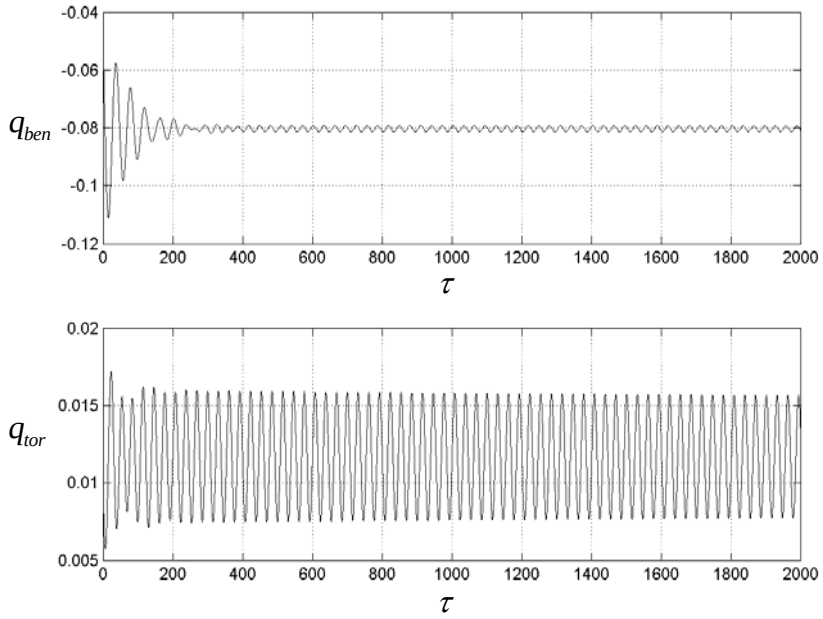


(a) Time history response of bending and torsion at the wing tip

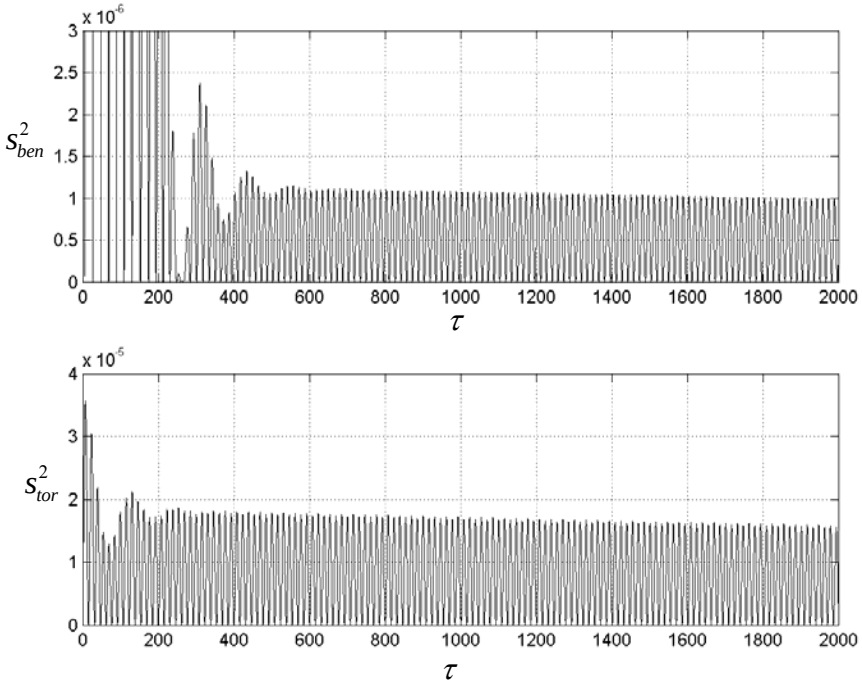


(b) Bending and torsion variances time history plots

Figure 3.24. Time history records of bending and torsion responses and their variances for $V_\infty = 140m/s$, $\sigma_{EI_x}/\overline{EI}_x = 0.01$, $\sigma_{GJ}/\overline{GJ} = 0$, $\alpha_a = 5°$, $q_{ben}(0) = -0.05$, $\dot{q}_{ben}(0) = 0$, $q_{tor}(0) = 0.01$, $\dot{q}_{tor}(0) = 0$

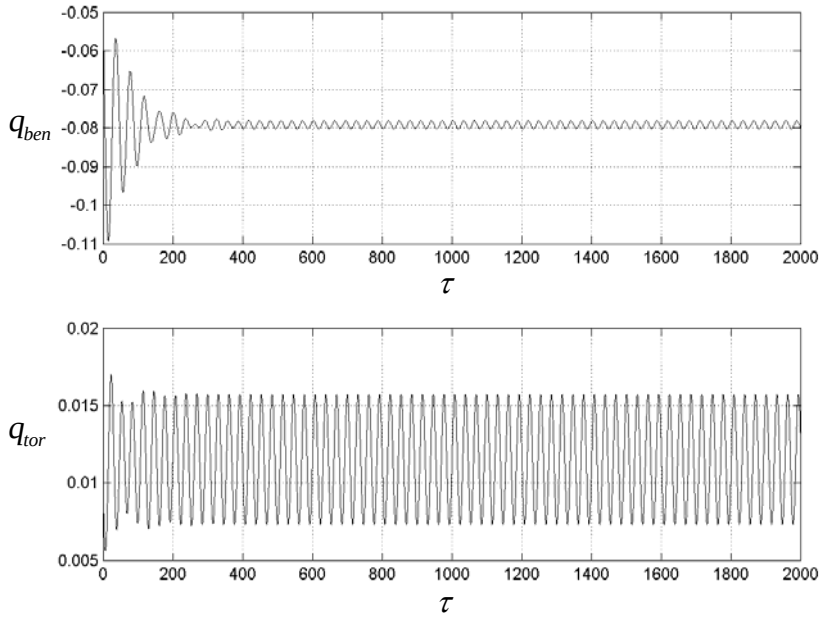


(a) Time history response of bending and torsion at the wing tip

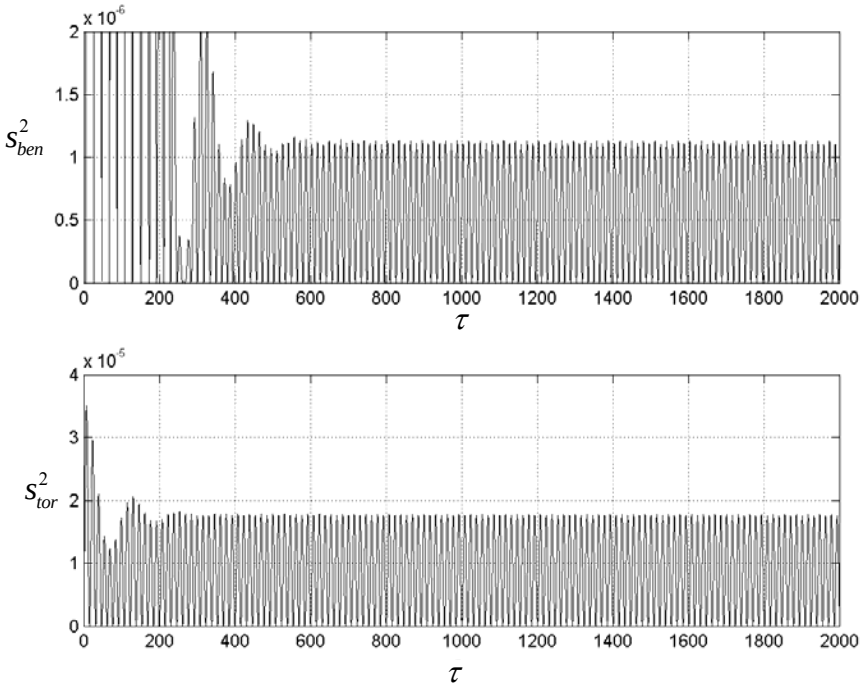


(b) Bending and torsion variances time history plots

Figure 3.25. Time history records of bending and torsion responses and their variances for $V_\infty = 140m/s$, $\sigma_{EI_x}/\overline{EI}_x = 0.015$, $\sigma_{GJ}/\overline{GJ} = 0$, $\alpha_a = 5°$, $q_{ben}(0) = -0.05$, $\dot{q}_{ben}(0) = 0$, $q_{tor}(0) = 0.01$, $\dot{q}_{tor}(0) = 0$

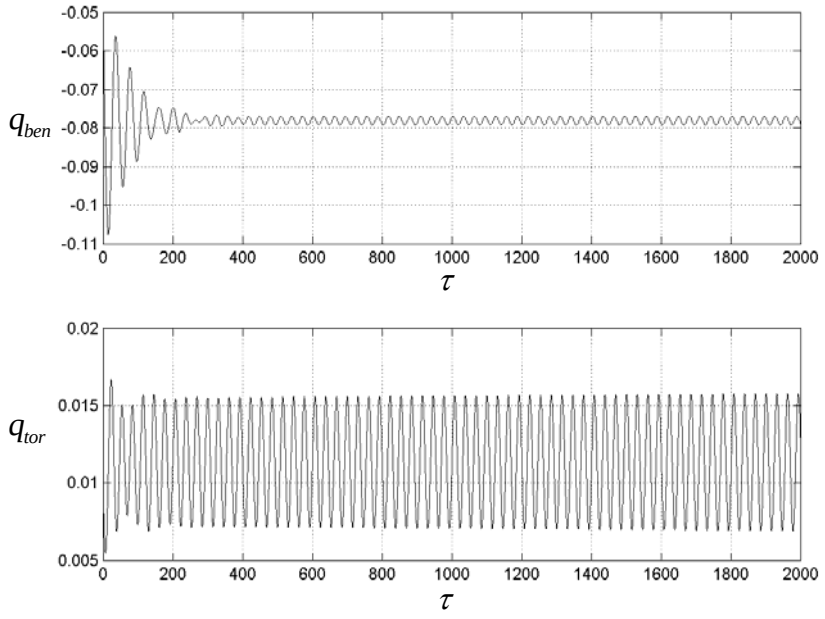


(a) Time history response of bending and torsion at the wing tip

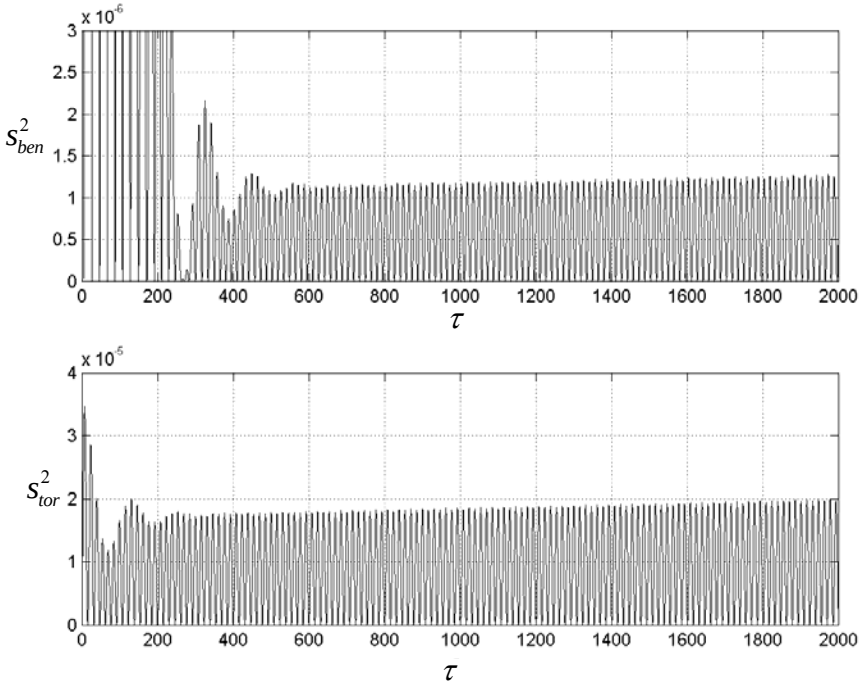


(b) Bending and torsion variances time history plots

Figure 3.26. Time history records of bending and torsion responses and their variances for $V_\infty = 140 m/s$, $\sigma_{EI_x} / \overline{EI}_x = 0.02$, $\sigma_{GJ} / \overline{GJ} = 0$, $\alpha_a = 5°$, $q_{ben}(0) = -0.05$, $\dot{q}_{ben}(0) = 0$, $q_{tor}(0) = 0.01$, $\dot{q}_{tor}(0) = 0$

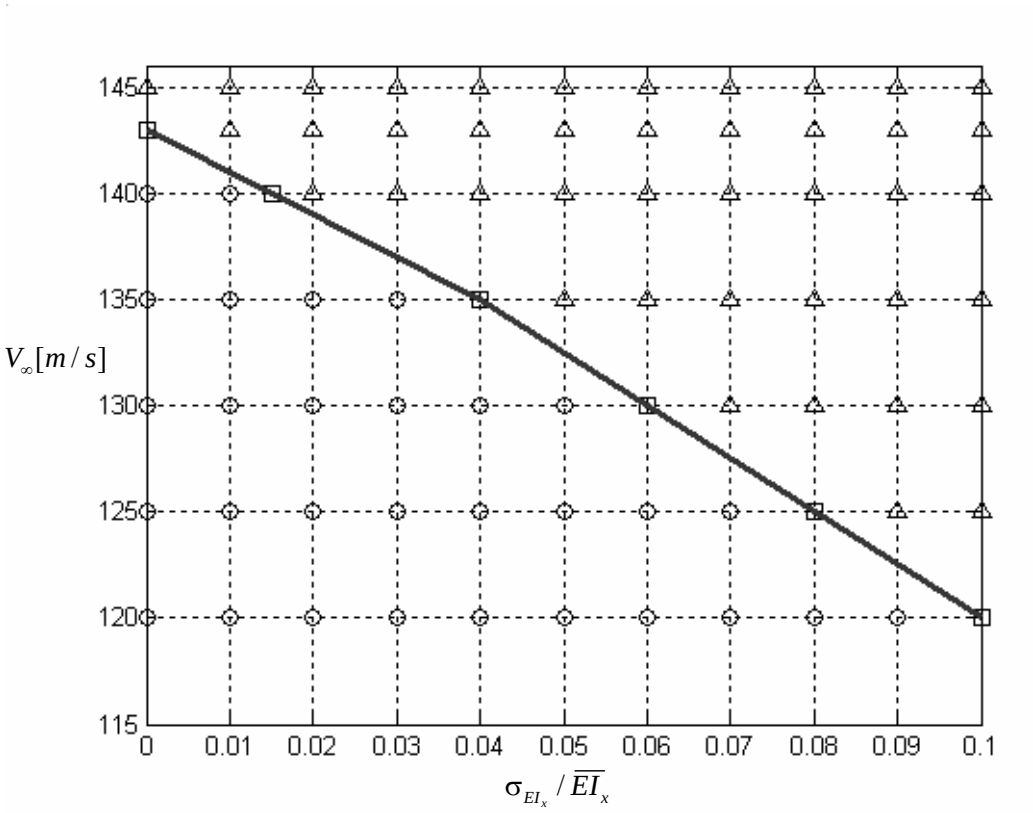


Figure 3.27. Stability bifurcation diagram $V_\infty$ vs. $\sigma_{EI_x} / \overline{EI}_x$

○ Stable, □ LCO, △ Unstable

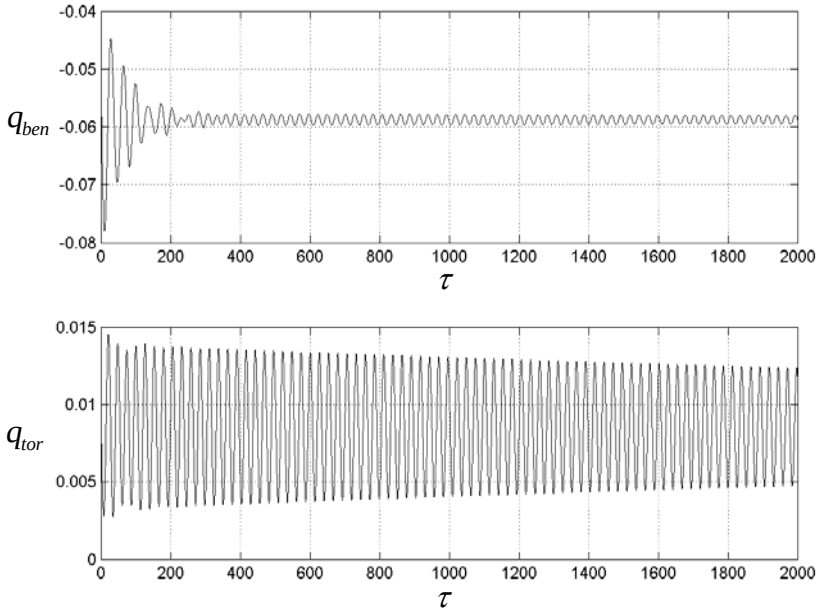


(a) Time history response of bending and torsion at the wing tip

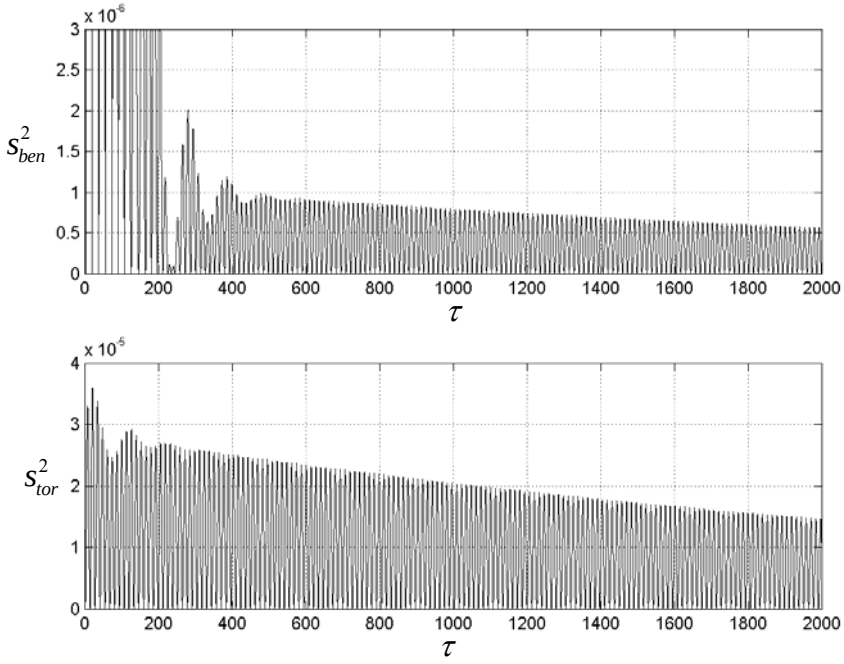


(b) Bending and torsion variances time history plots

Figure 3.28. Time history records of bending and torsion responses and their variances for $V_\infty = 120m/s$, $\sigma_{EI_x}/\overline{EI}_x = 0$, $\sigma_{GJ}/\overline{GJ} = 0.03$, $\alpha_a = 5°$, $q_{0,ben}(0) = -0.05$, $\dot{q}_{0,ben}(0) = 0$, $q_{0,tor}(0) = 0.01$, $\dot{q}_{0,tor}(0) = 0$

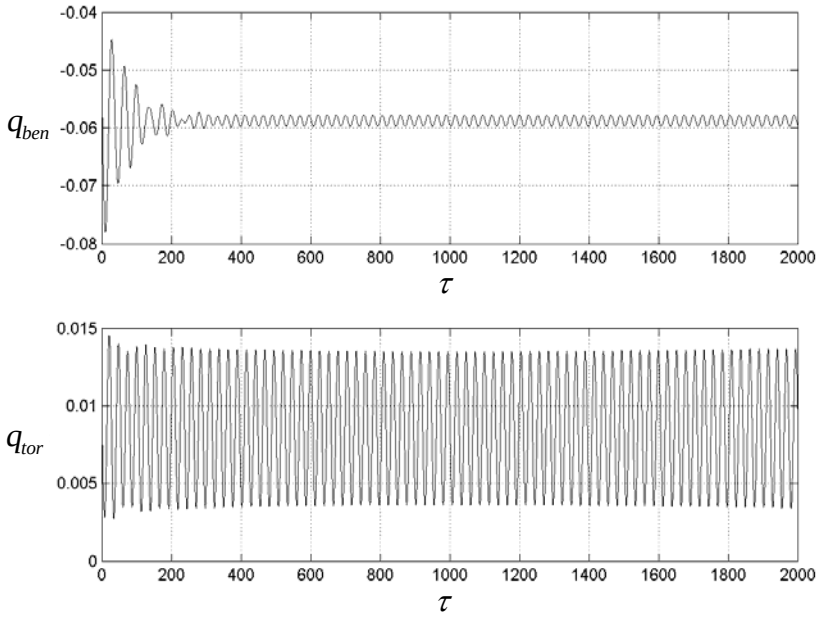


(a) Time history response of bending and torsion at the wing tip

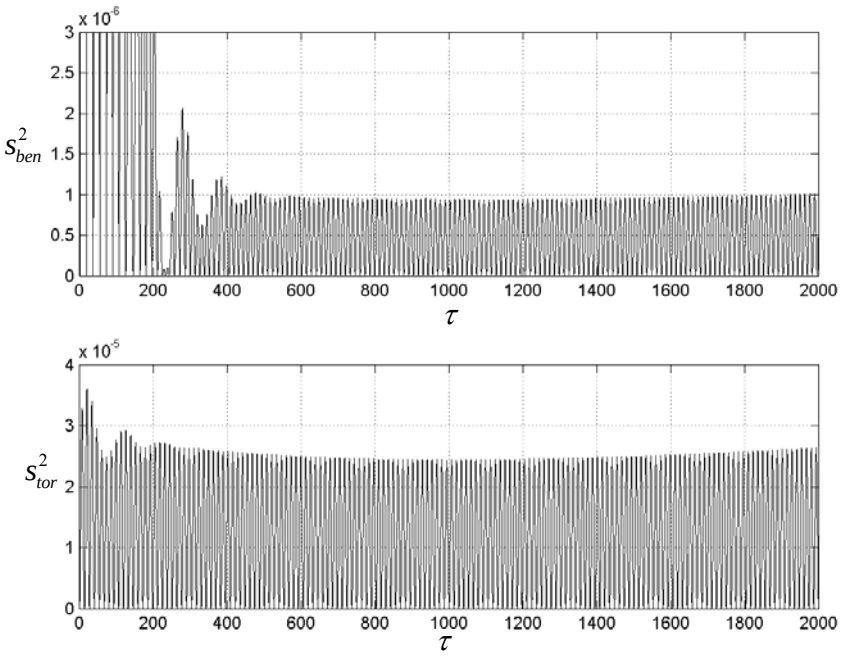


(b) Bending and torsion variances time history plots

Figure 3.29. Time history records of bending and torsion responses and their variances for $V_\infty = 120m/s$, $\sigma_{EI_x}/\overline{EI}_x = 0$, $\sigma_{GJ}/\overline{GJ} = 0.035$, $\alpha_a = 5°$, $q_{0,ben}(0) = -0.05$, $\dot{q}_{0,ben}(0) = 0$, $q_{0,tor}(0) = 0.01$, $\dot{q}_{0,tor}(0) = 0$

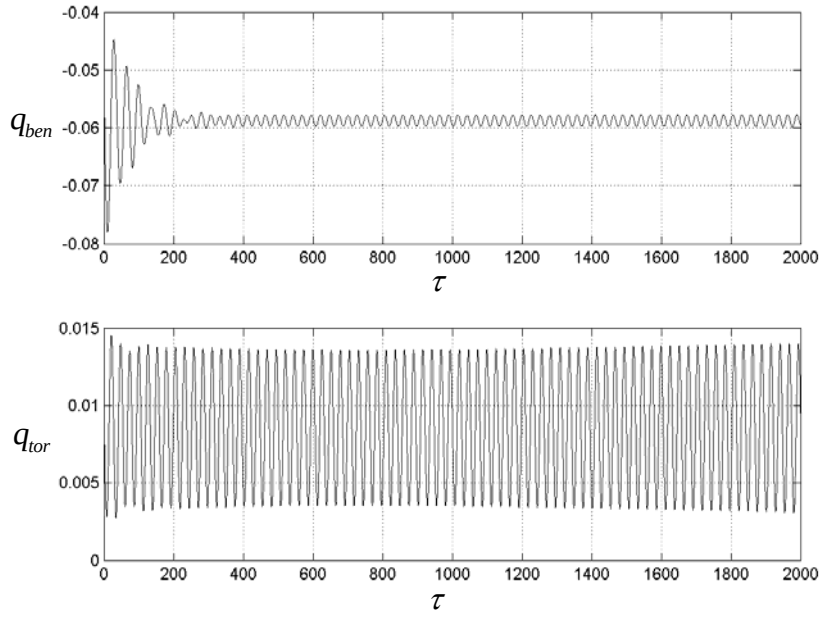


(a) Time history response of bending and torsion at the wing tip

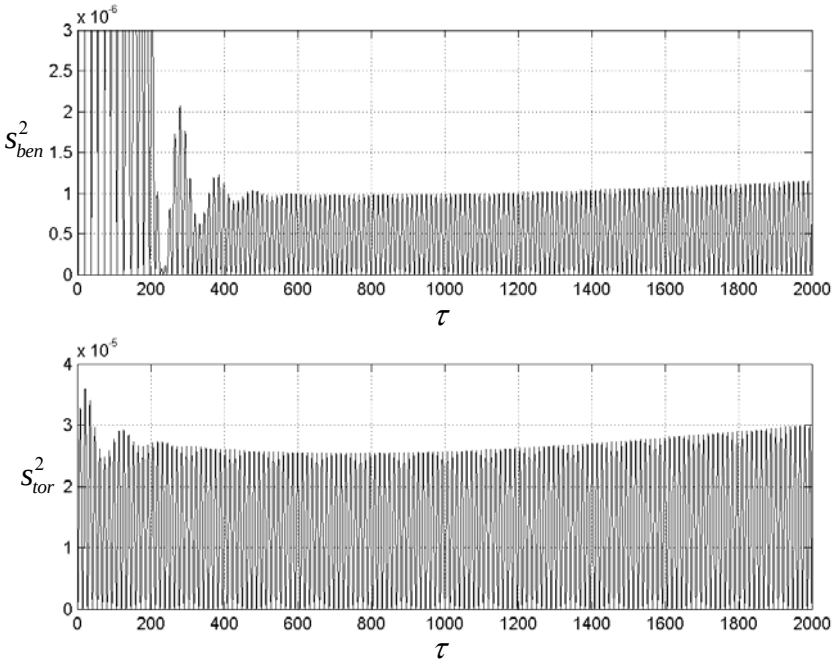


(b) Bending and torsion variances time history plots

Figure 3.30. Time history records of bending and torsion responses and their variances for $V_\infty = 120m/s$, $\sigma_{EI_x}/\overline{EI}_x = 0$, $\sigma_{GJ}/\overline{GJ} = 0.04$, $\alpha_a = 5°$, $q_{0,ben}(0) = -0.05$, $\dot{q}_{0,ben}(0) = 0$, $q_{0,tor}(0) = 0.01$, $\dot{q}_{0,tor}(0) = 0$

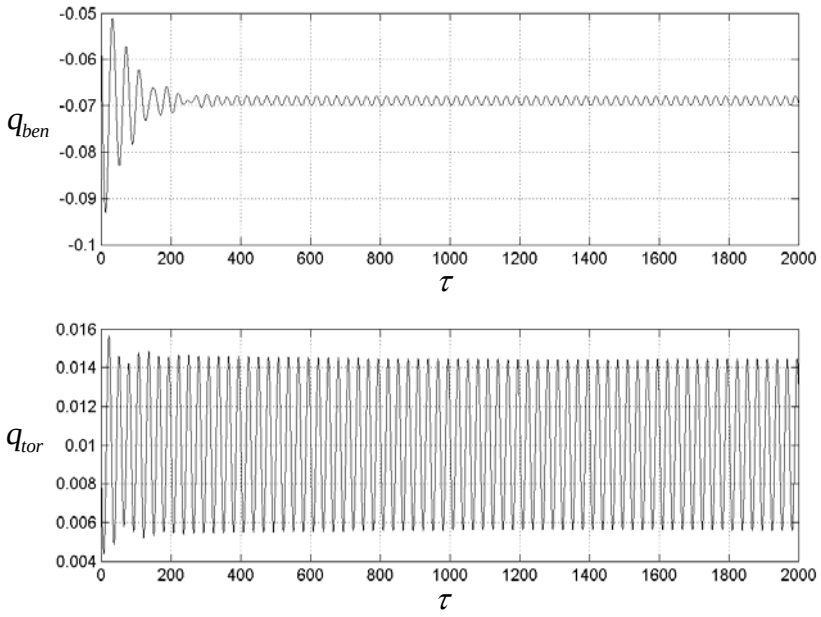


(a) Time history response of bending and torsion at the wing tip

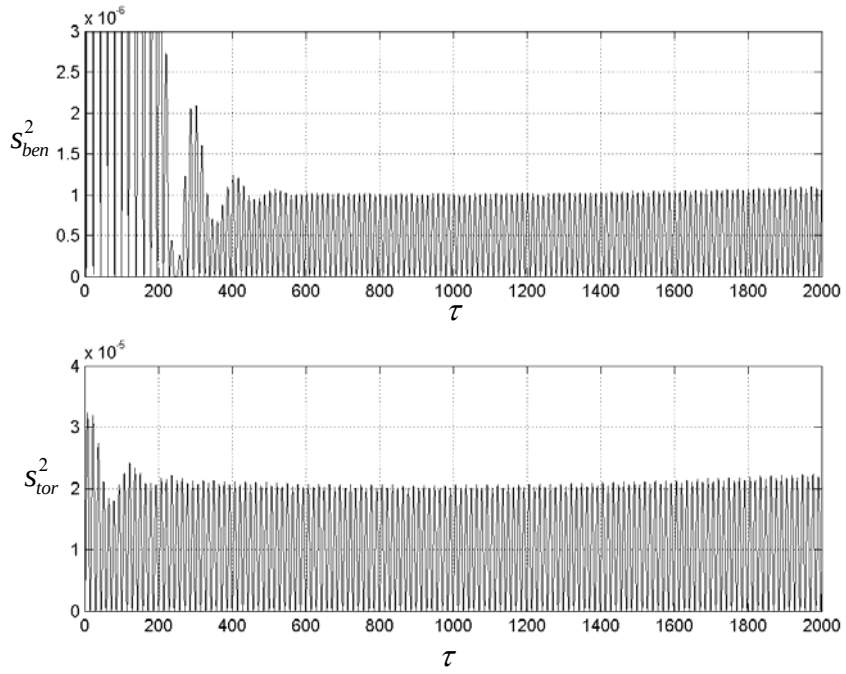


(b) Bending and torsion variances time history plots

Figure 3.31. Time history records of bending and torsion responses and their variances for $V_\infty = 130 m/s$, $\sigma_{EI_x} / \overline{EI}_x = 0$, $\sigma_{GJ} / \overline{GJ} = 0.03$, $\alpha_a = 5°$, $q_{0,ben}(0) = -0.05$, $\dot{q}_{0,ben}(0) = 0$, $q_{0,tor}(0) = 0.01$, $\dot{q}_{0,tor}(0) = 0$

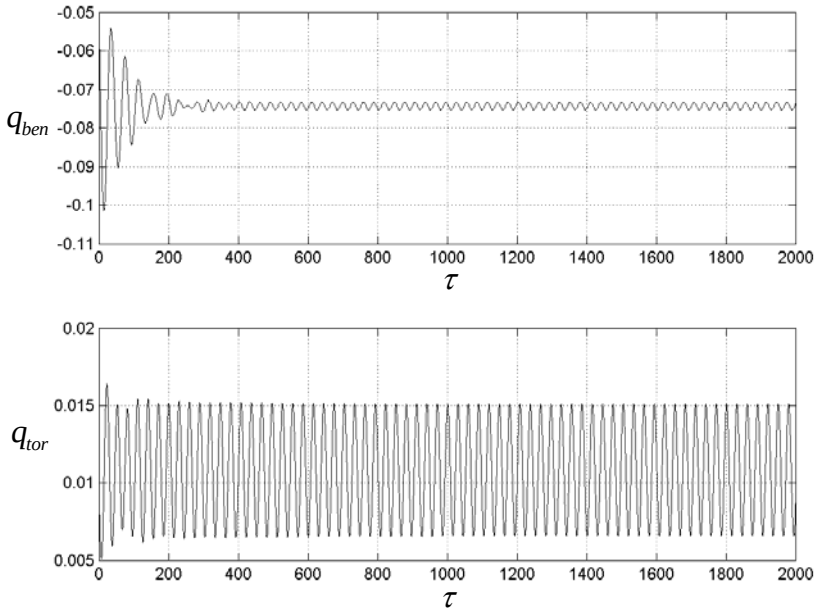


(a) Time history response of bending and torsion at the wing tip

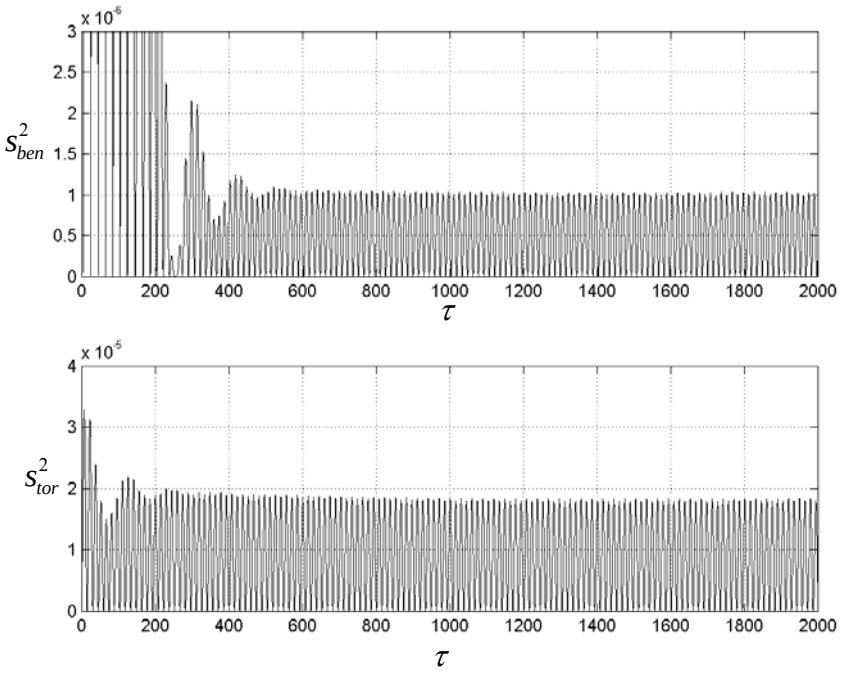


(b) Bending and torsion variances time history plots

Figure 3.32. Time history records of bending and torsion responses and their variances for $V_\infty = 135m/s$, $\sigma_{EI_x}/\overline{EI}_x = 0$, $\sigma_{GJ}/\overline{GJ} = 0.02$, $\alpha_a = 5°$, $q_{0,ben}(0) = -0.05$, $\dot{q}_{0,ben}(0) = 0$, $q_{0,tor}(0) = 0.01$, $\dot{q}_{0,tor}(0) = 0$

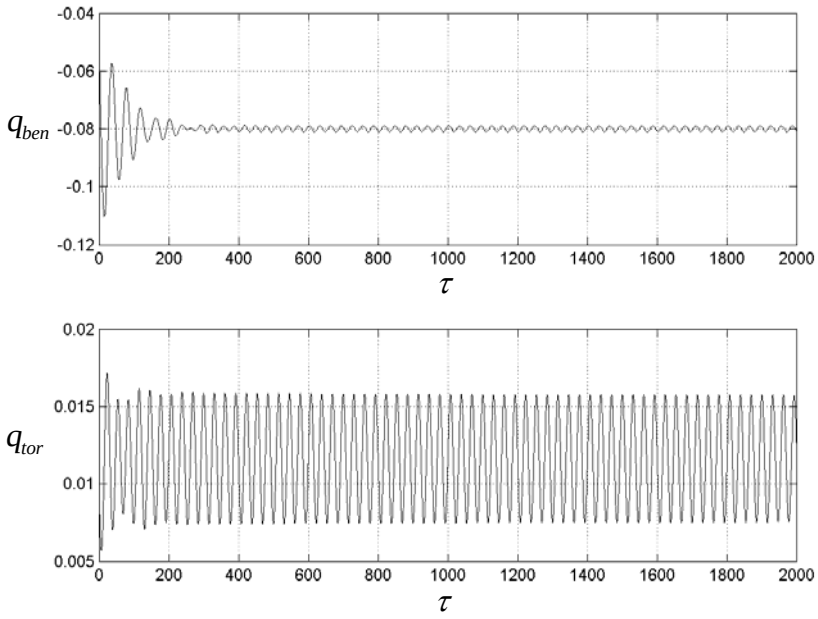


(a) Time history response of bending and torsion at the wing tip

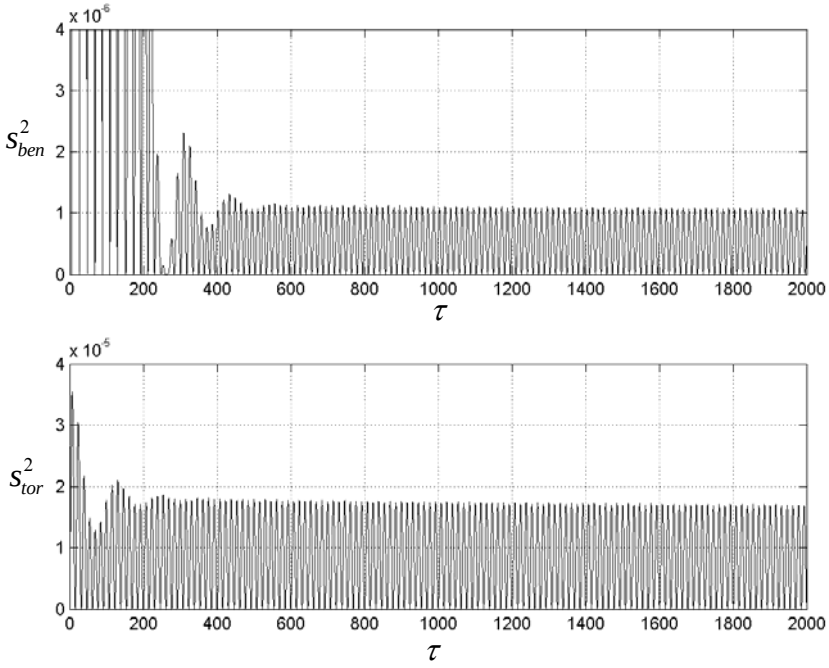


(b) Bending and torsion variances time history plots

Figure 3.33. Time history records of bending and torsion responses and their variances for $V_\infty = 140m/s$, $\sigma_{EI_x}/\overline{EI}_x = 0$, $\sigma_{GJ}/\overline{GJ} = 0.01$, $\alpha_a = 5°$, $q_{0,ben}(0) = -0.05$, $\dot{q}_{0,ben}(0) = 0$, $q_{0,tor}(0) = 0.01$, $\dot{q}_{0,tor}(0) = 0$

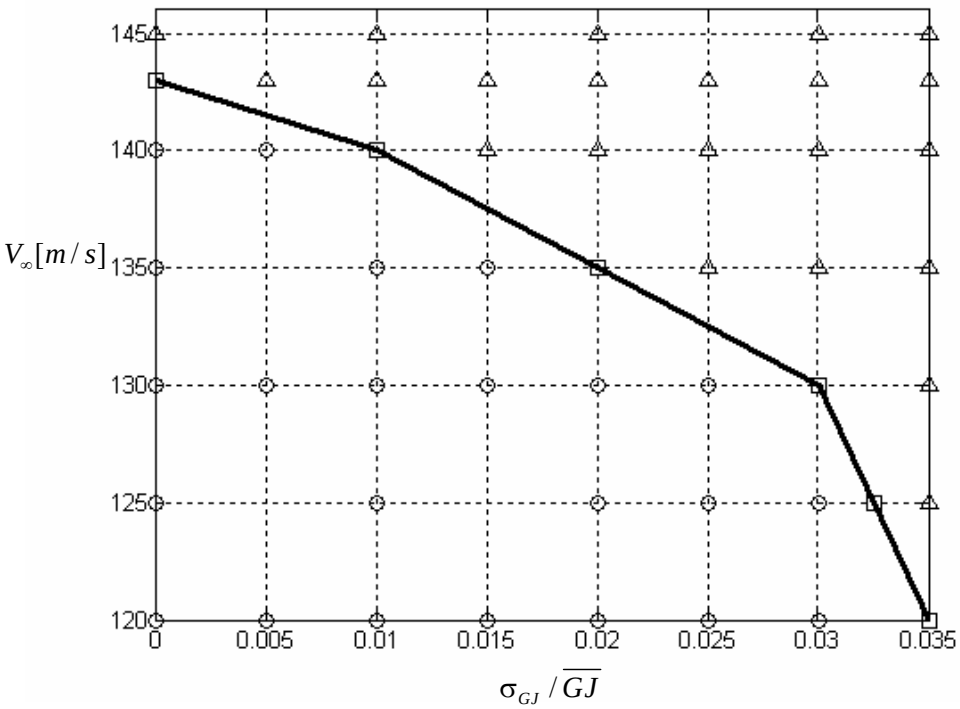


Figure 3.34. Stability bifurcation diagram $V_\infty$ vs. $\sigma_{GJ}/\overline{GJ}$
○ Stable, □ LCO, △ Unstable

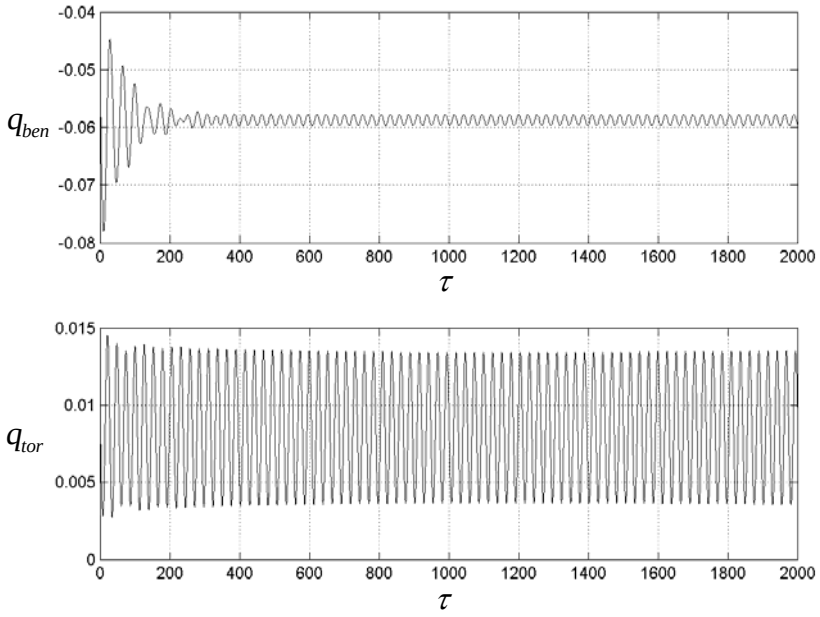


(a) Time history response of bending and torsion at the wing tip

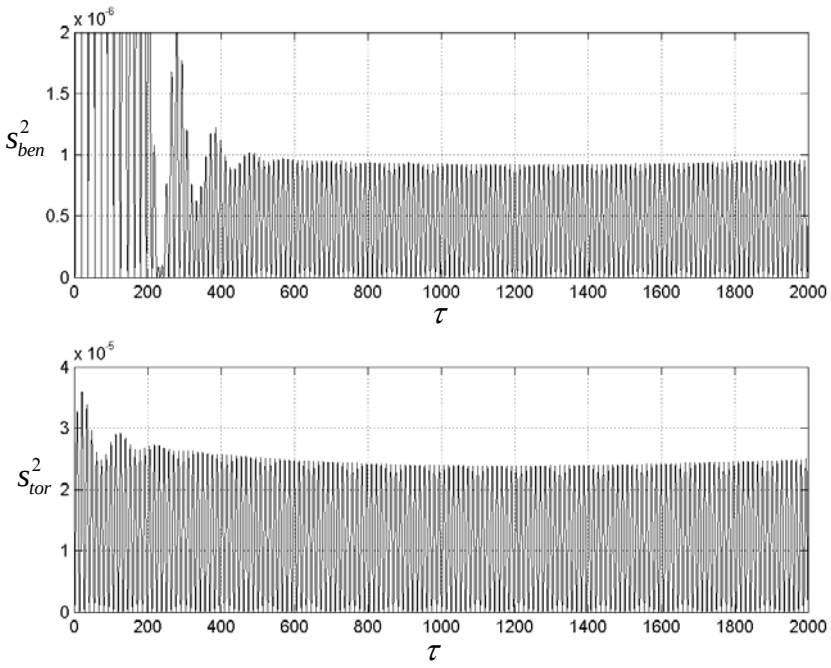


(b) Bending and torsion variances time history plots

Figure 3.35. Time history records of bending and torsion responses and their variances for $V_\infty = 120m/s$, $\sigma_{EI_x}/\overline{EI}_x = 0.01$, $\sigma_{GJ}/\overline{GJ} = 0.0325$, $\alpha_a = 5°$, $q_{0,ben}(0) = -0.05$, $\dot{q}_{0,ben}(0) = 0$, $q_{0,tor}(0) = 0.01$, $\dot{q}_{0,tor}(0) = 0$

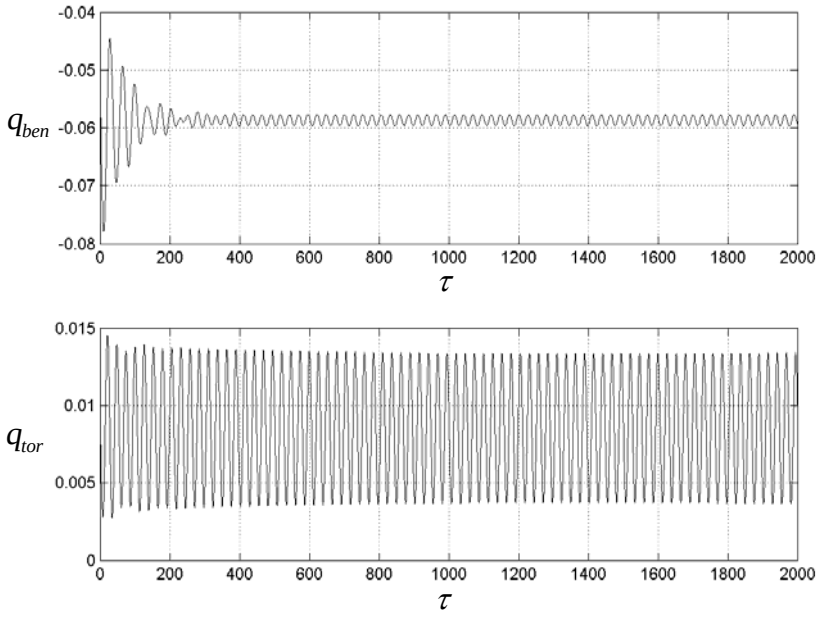


(a) Time history response of bending and torsion at the wing tip

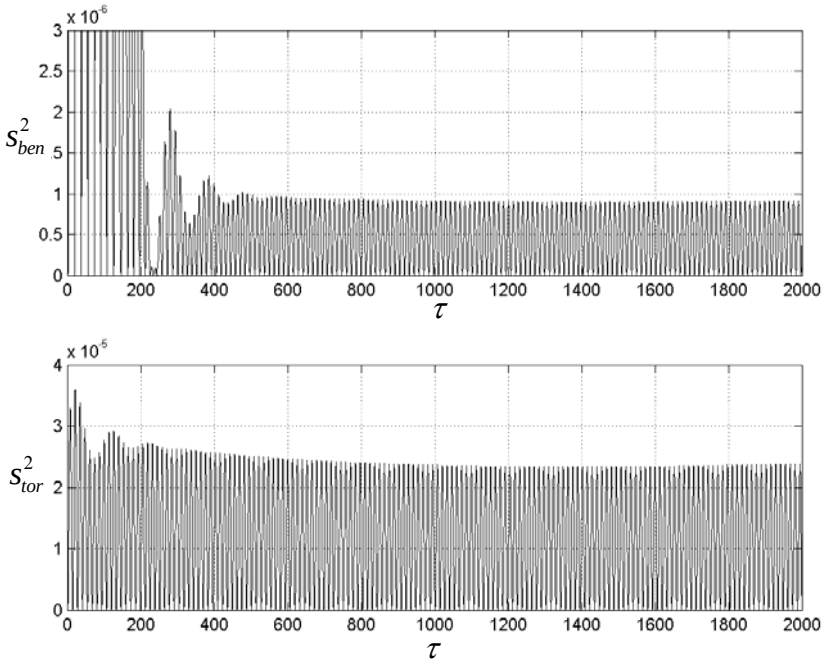


(b) Bending and torsion variances time history plots

Figure 3.36. Time history records of bending and torsion responses and their variances for $V_\infty = 120m/s$, $\sigma_{EI_x} / \overline{EI}_x = 0.03$, $\sigma_{GJ} / \overline{GJ} = 0.025$, $\alpha_a = 5°$, $q_{0,ben}(0) = -0.05$, $\dot{q}_{0,ben}(0) = 0$, $q_{0,tor}(0) = 0.01$, $\dot{q}_{0,tor}(0) = 0$

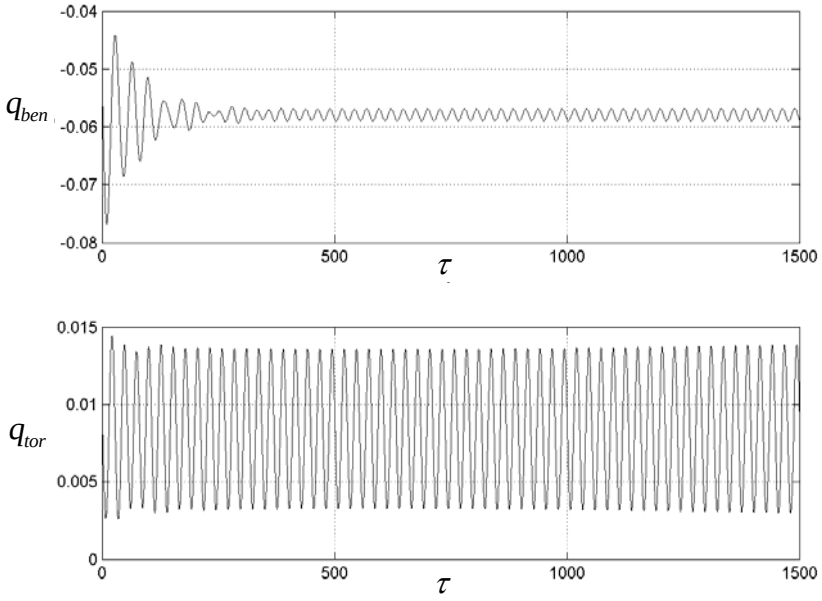


(a) Time history response of bending and torsion at the wing tip

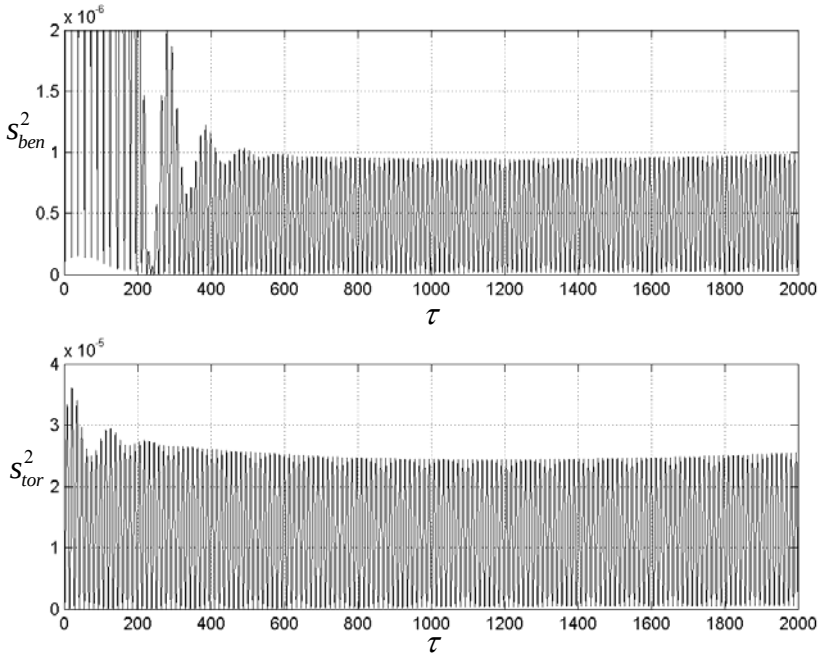


(b) Bending and torsion variances time history plots

Figure 3.37. Time history records of bending and torsion responses and their variances for $V_\infty = 120m/s$, $\sigma_{EI_x}/\overline{EI}_x = 0.05$, $\sigma_{GJ}/\overline{GJ} = 0.02$, $\alpha_a = 5°$, $q_{0,ben}(0) = -0.05$, $\dot{q}_{0,ben}(0) = 0$, $q_{0,tor}(0) = 0.01$, $\dot{q}_{0,tor}(0) = 0$

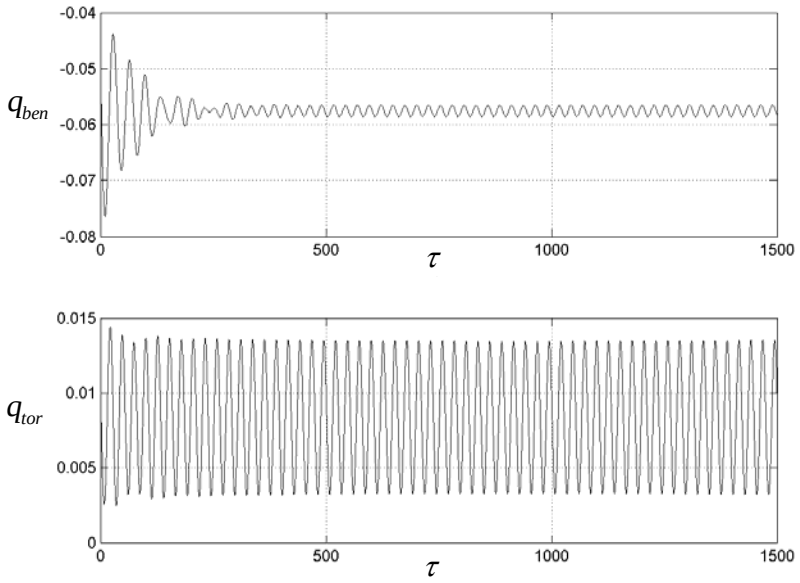


(a) Time history response of bending and torsion at the wing tip

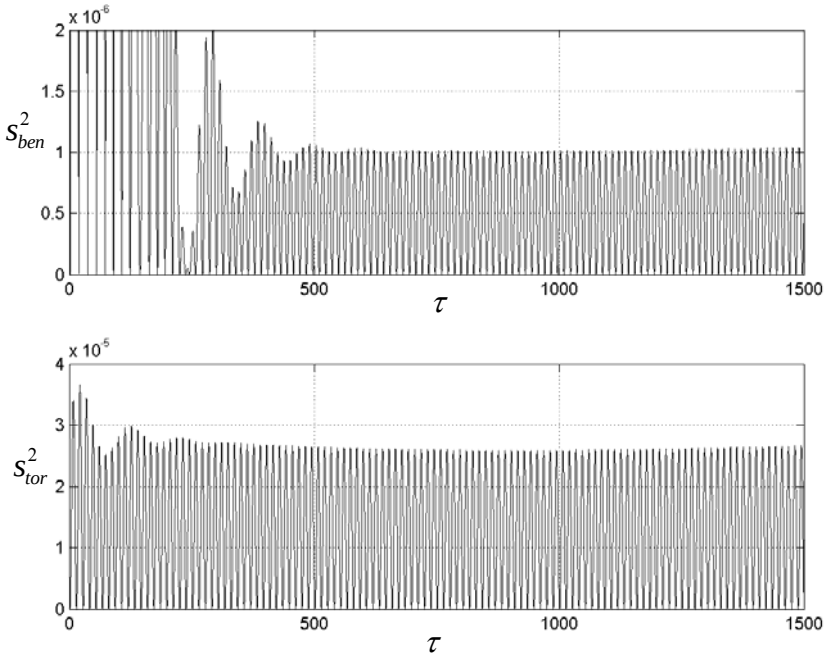


(b) Bending and torsion variances time history plots

Figure 3.38. Time history records of bending and torsion responses and their variances for $V_\infty = 120m/s$, $\sigma_{EI_x}/\overline{EI}_x = 0.07$, $\sigma_{GJ}/\overline{GJ} = 0.015$, $\alpha_a = 5°$, $q_{0,ben}(0) = -0.05$, $\dot{q}_{0,ben}(0) = 0$, $q_{0,tor}(0) = 0.01$, $\dot{q}_{0,tor}(0) = 0$

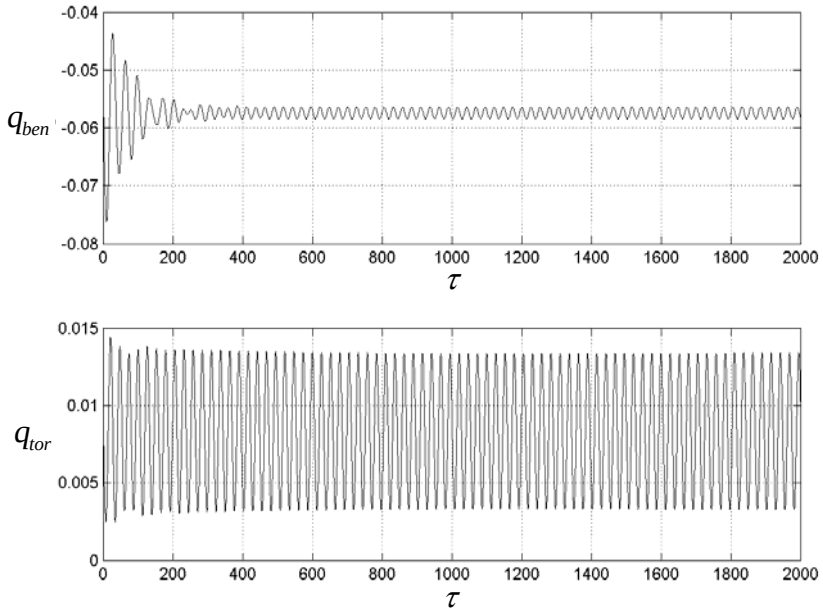


(a) Time history response of bending and torsion at the wing tip

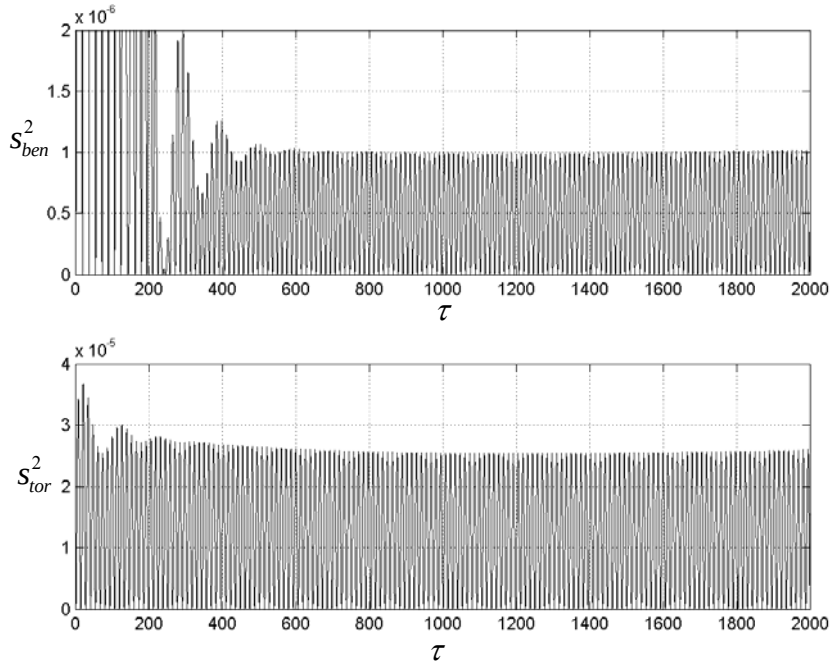


(b) Bending and torsion variances time history plots

Figure 3.39. Time history records of bending and torsion responses and their variances for $V_\infty = 120m/s$, $\sigma_{EI_x}/\overline{EI}_x = 0.09$, $\sigma_{GJ}/\overline{GJ} = 0.01$, $\alpha_a = 5°$, $q_{0,ben}(0) = -0.05$, $\dot{q}_{0,ben}(0) = 0$, $q_{0,tor}(0) = 0.01$, $\dot{q}_{0,tor}(0) = 0$

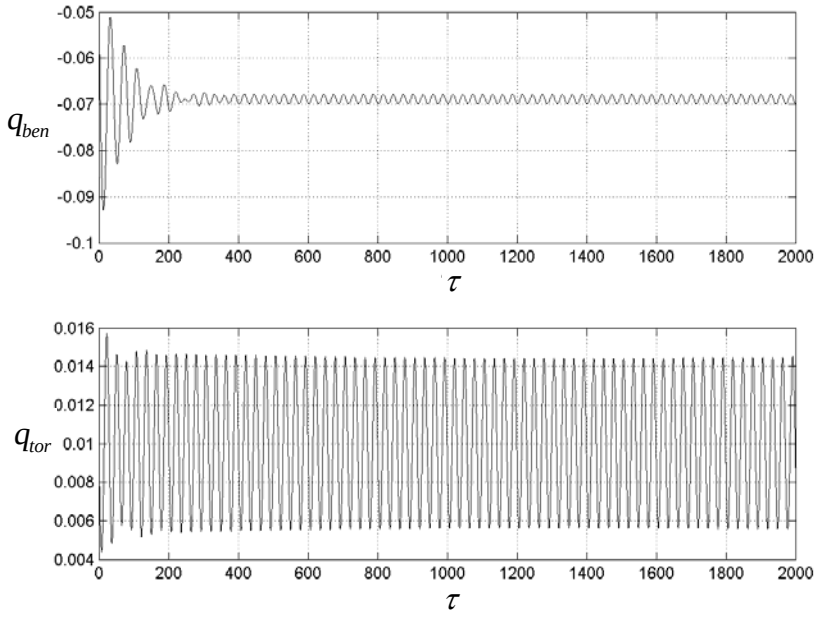


(a) Time history response of bending and torsion at the wing tip

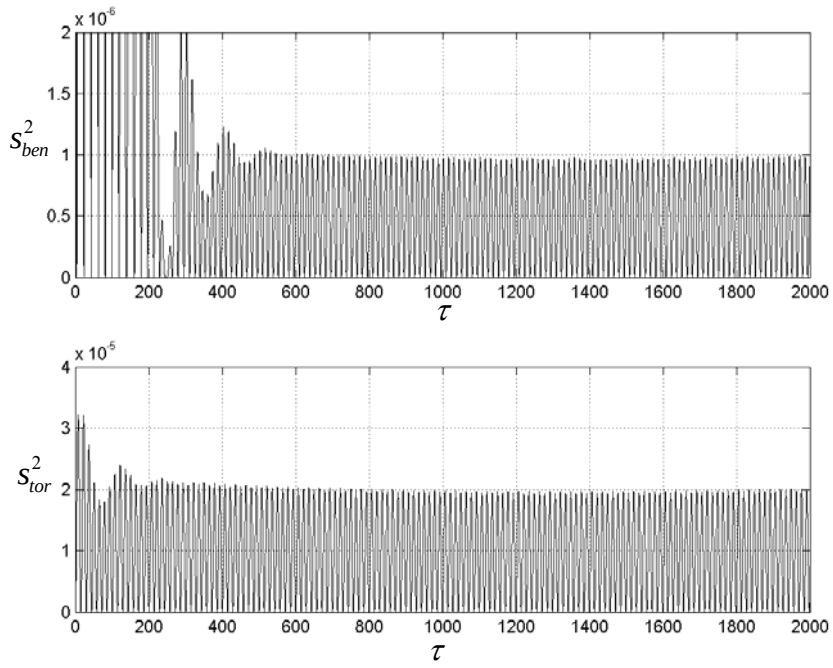


(b) Bending and torsion variances time history plots

Figure 3.40. Time history records of bending and torsion responses and their variances for $V_\infty = 130m/s$, $\sigma_{EI_x} / \overline{EI}_x = 0.01$, $\sigma_{GJ} / \overline{GJ} = 0.025$, $\alpha_a = 5°$, $q_{0,ben}(0) = -0.05$, $\dot{q}_{0,ben}(0) = 0$, $q_{0,tor}(0) = 0.01$, $\dot{q}_{0,tor}(0) = 0$

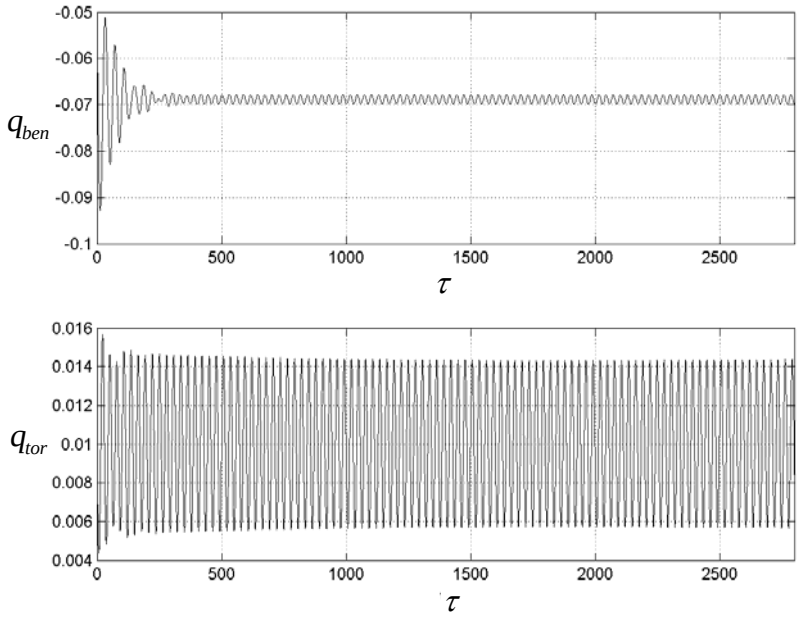


(a) Time history response of bending and torsion at the wing tip

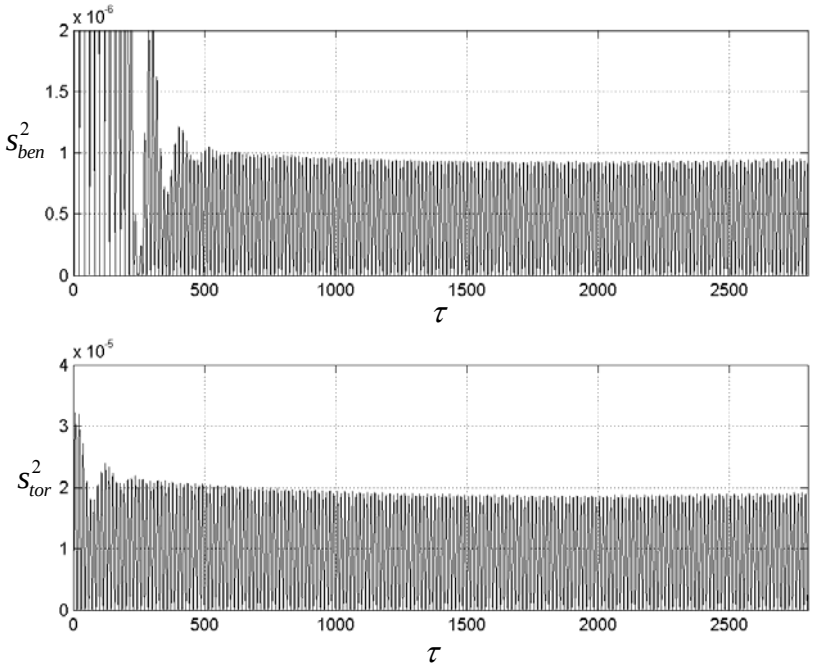


(b) Bending and torsion variances time history plots

Figure 3.41. Time history records of bending and torsion responses and their variances for $V_\infty = 130m/s$, $\sigma_{EI_x}/\overline{EI}_x = 0.02$, $\sigma_{GJ}/\overline{GJ} = 0.021$, $\alpha_a = 5°$, $q_{0,ben}(0) = -0.05$, $\dot{q}_{0,ben}(0) = 0$, $q_{0,tor}(0) = 0.01$, $\dot{q}_{0,tor}(0) = 0$

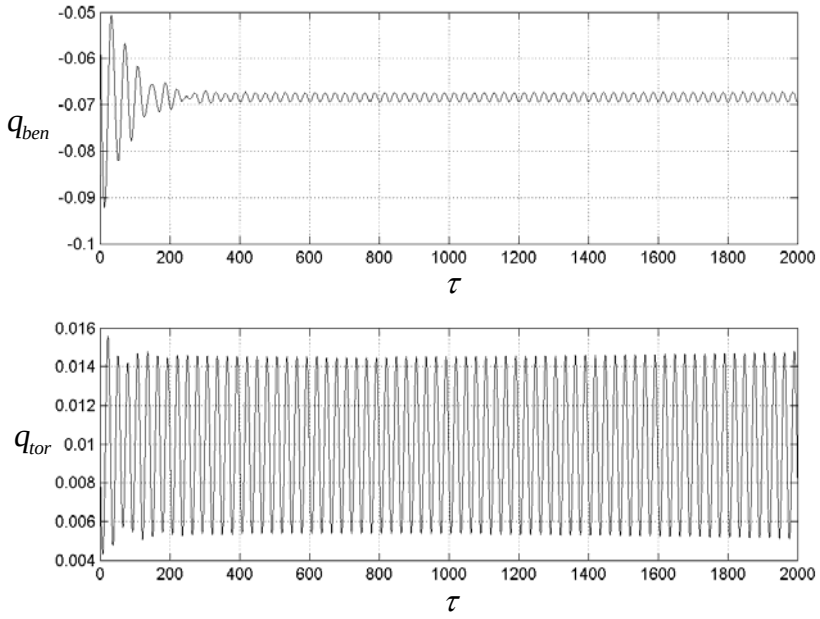


(a) Time history response of bending and torsion at the wing tip

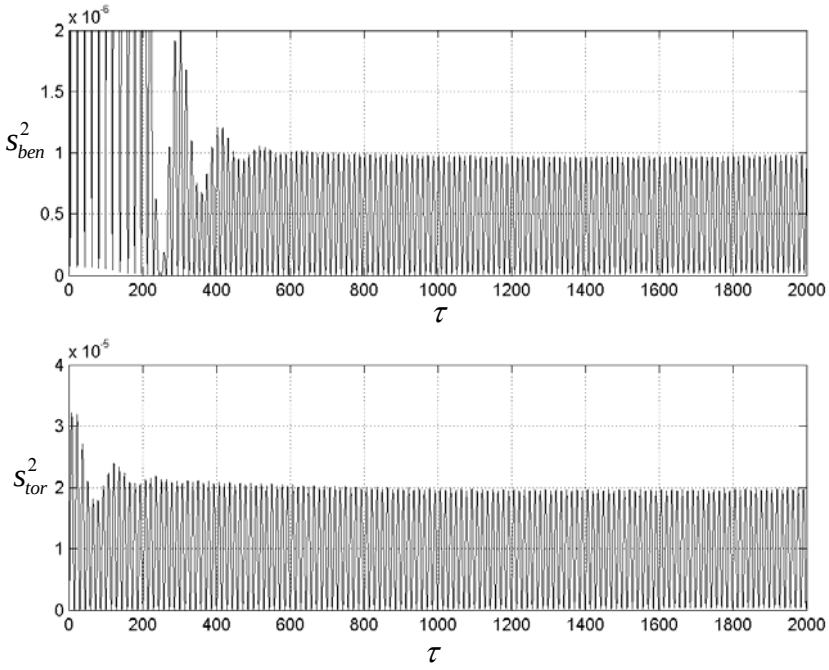


(b) Bending and torsion variances time history plots

Figure 3.42. Time history records of bending and torsion responses and their variances for $V_\infty = 130m/s$, $\sigma_{EI_x}/\overline{EI}_x = 0.03$, $\sigma_{GJ}/\overline{GJ} = 0.015$, $\alpha_a = 5°$, $q_{0,ben}(0) = -0.05$, $\dot{q}_{0,ben}(0) = 0$, $q_{0,tor}(0) = 0.01$, $\dot{q}_{0,tor}(0) = 0$

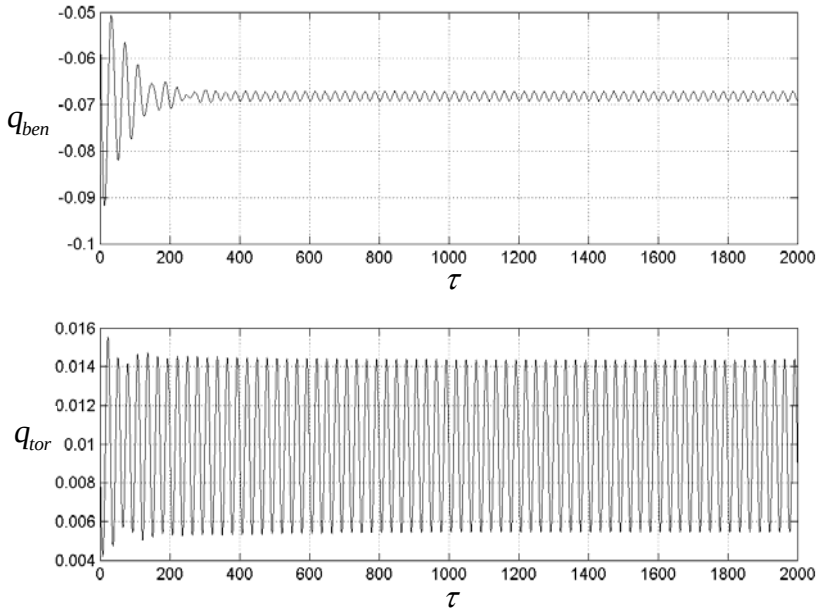


(a) Time history response of bending and torsion at the wing tip

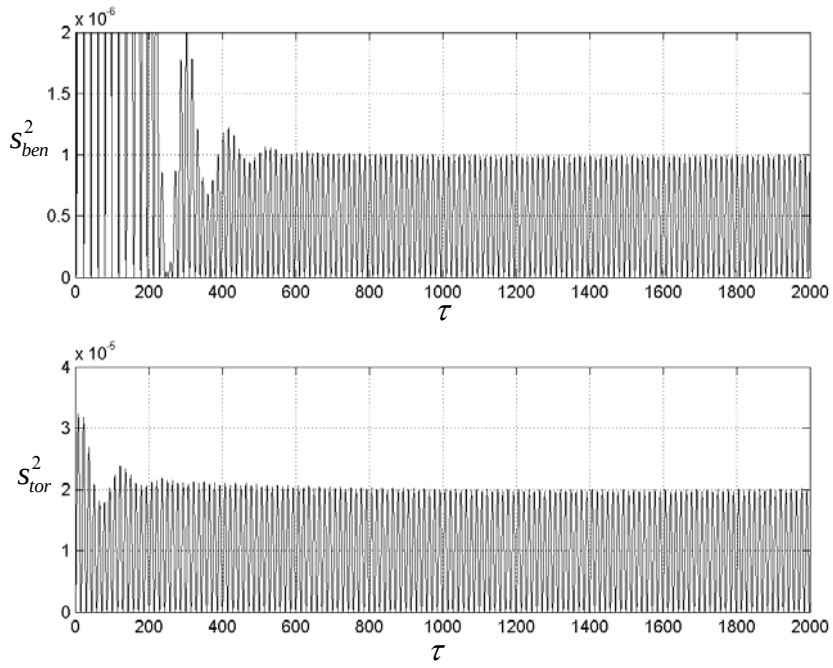


(b) Bending and torsion variances time history plots

Figure 3.43. Time history records of bending and torsion responses and their variances for $V_\infty = 130m/s$, $\sigma_{EI_x}/\overline{EI}_x = 0.04$, $\sigma_{GJ}/\overline{GJ} = 0.01$, $\alpha_a = 5°$, $q_{0,ben}(0) = -0.05$, $\dot{q}_{0,ben}(0) = 0$, $q_{0,tor}(0) = 0.01$, $\dot{q}_{0,tor}(0) = 0$

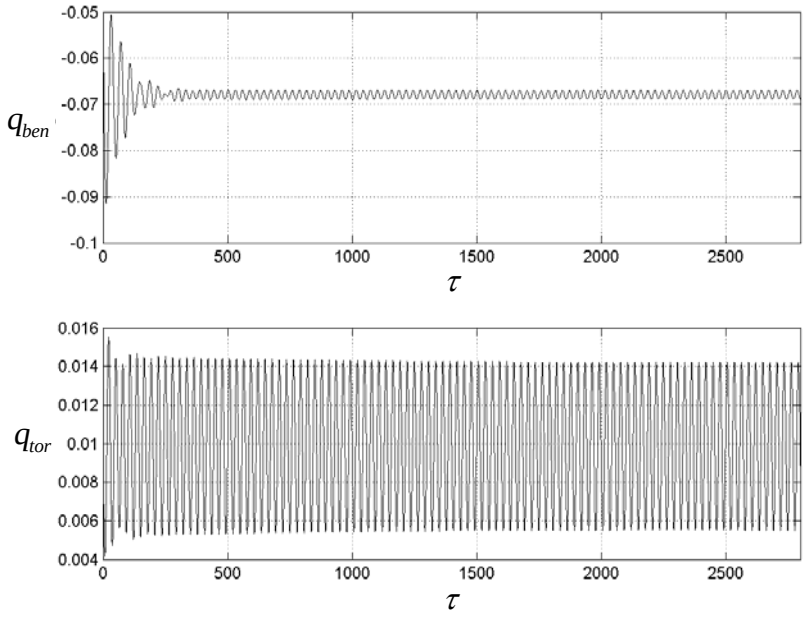


(a) Time history response of bending and torsion at the wing tip

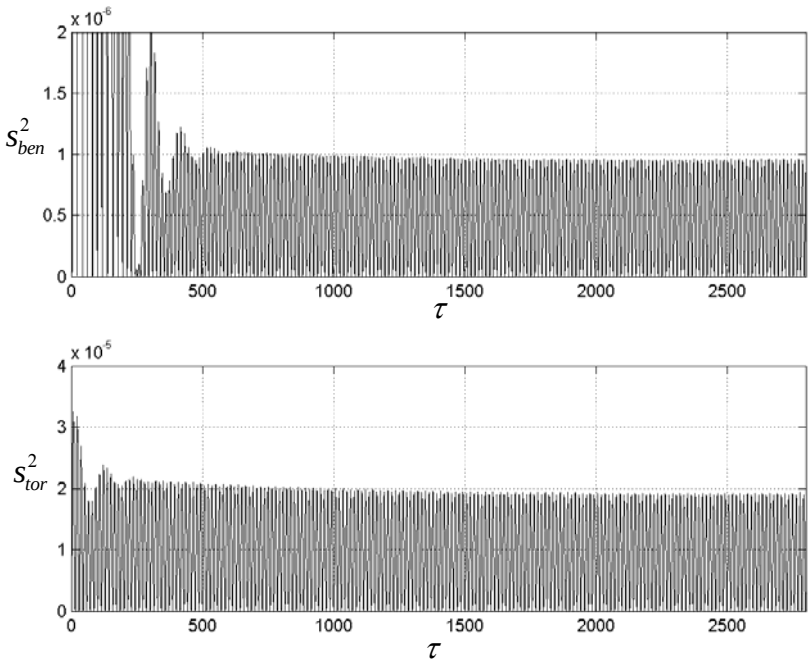


(b) Bending and torsion variances time history plots

Figure 3.44. Time history records of bending and torsion responses and their variances for $V_\infty = 130m/s$, $\sigma_{EI_x}/\overline{EI}_x = 0.05$, $\sigma_{GJ}/\overline{GJ} = 0.0075$, $\alpha_a = 5°$, $q_{0,ben}(0) = -0.05$, $\dot{q}_{0,ben}(0) = 0$, $q_{0,tor}(0) = 0.01$, $\dot{q}_{0,tor}(0) = 0$

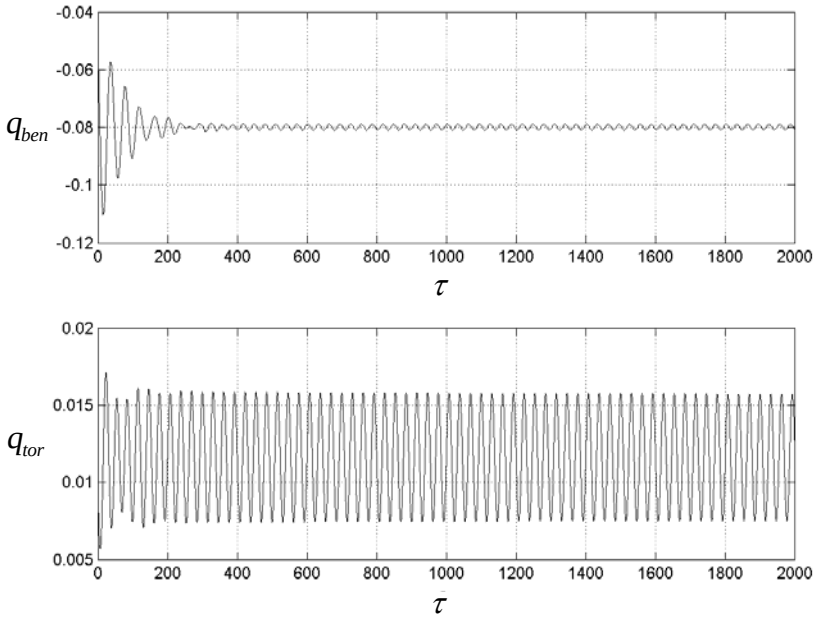


(a) Time history response of bending and torsion at the wing tip

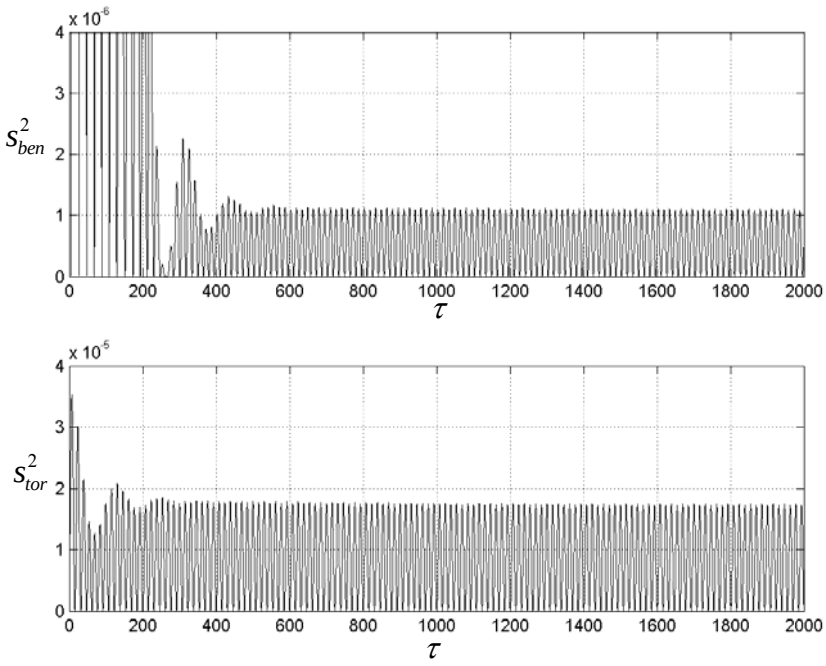


(b) Bending and torsion variances time history plots

Figure 3.45. Time history records of bending and torsion responses and their variances for $V_\infty = 140m/s$, $\sigma_{EI_x}/\overline{EI}_x = 0.01$, $\sigma_{GJ}/\overline{GJ} = 0.005$, $\alpha_a = 5°$, $q_{0,ben}(0) = -0.05$, $\dot{q}_{0,ben}(0) = 0$, $q_{0,tor}(0) = 0.01$, $\dot{q}_{0,tor}(0) = 0$

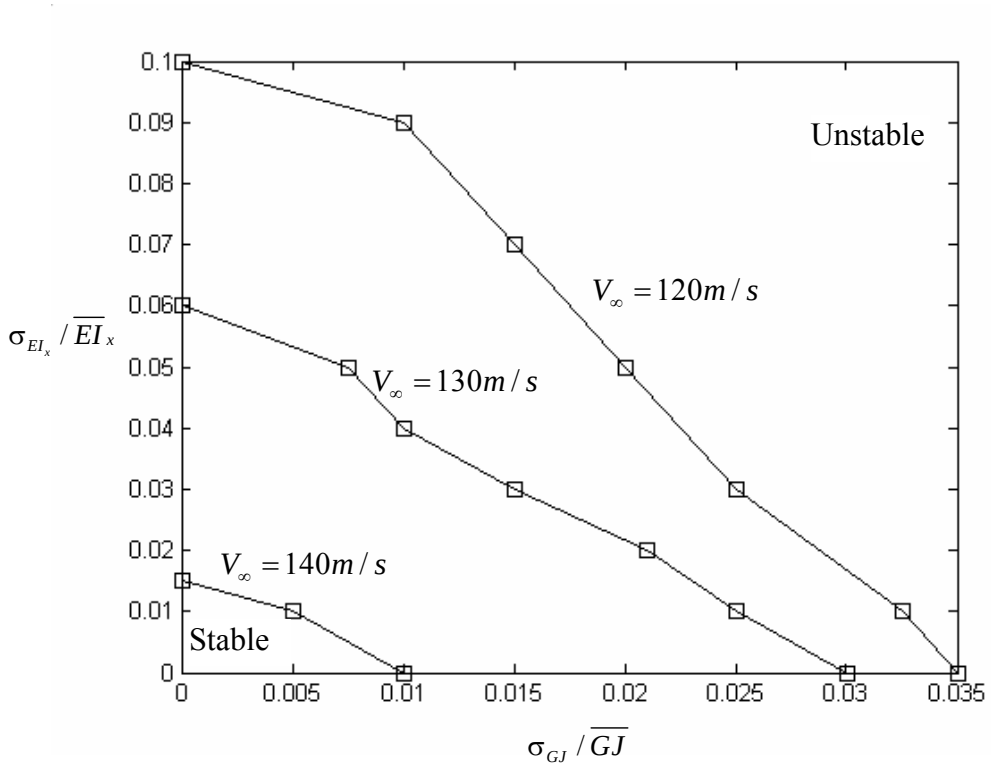


(a)

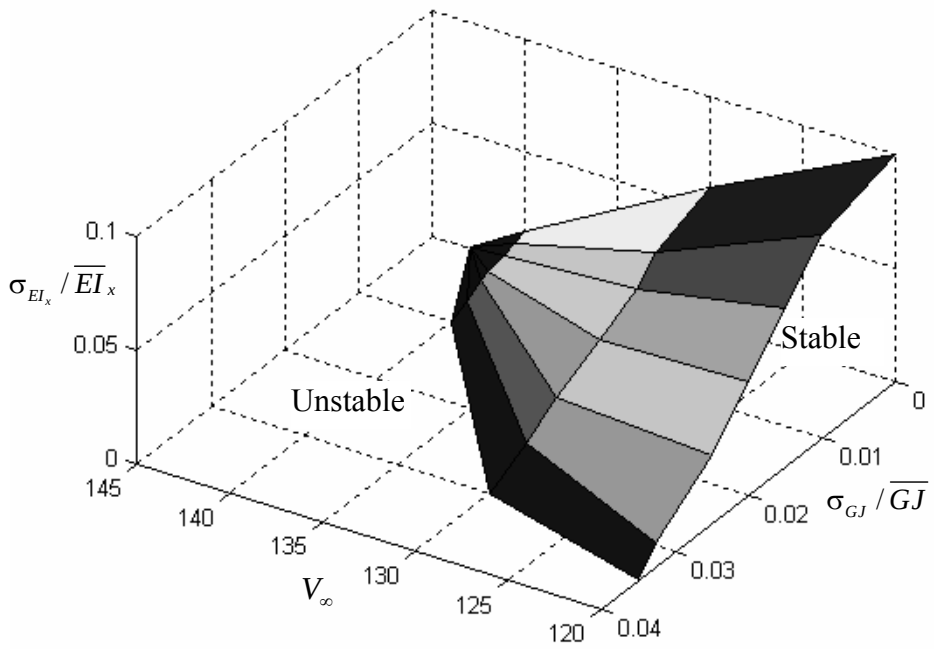


(b)

Figure 3.46. Stability boundaries $\sigma_{EI_x} / \overline{EI}_x$ vs. $\sigma_{GJ} / \overline{GJ}$ at different flow speeds (a) 2D representation and (b) 3D representation

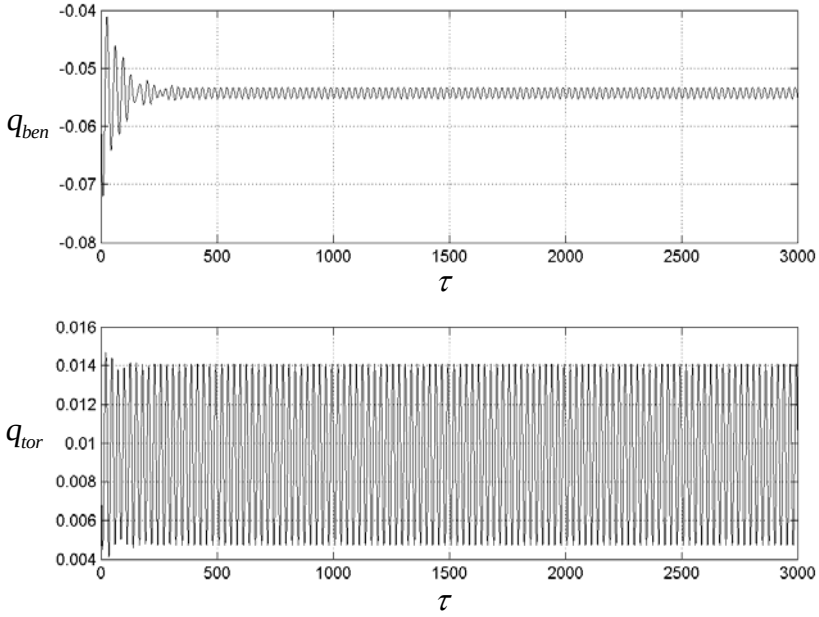


(a) Time history response of bending and torsion at the wing tip

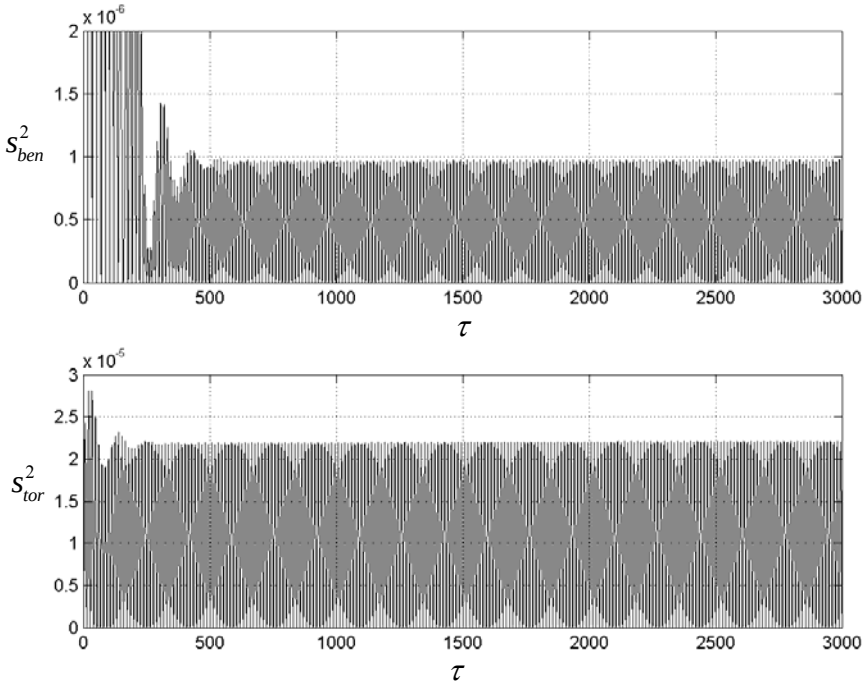


(b) Bending and torsion variances time history plots

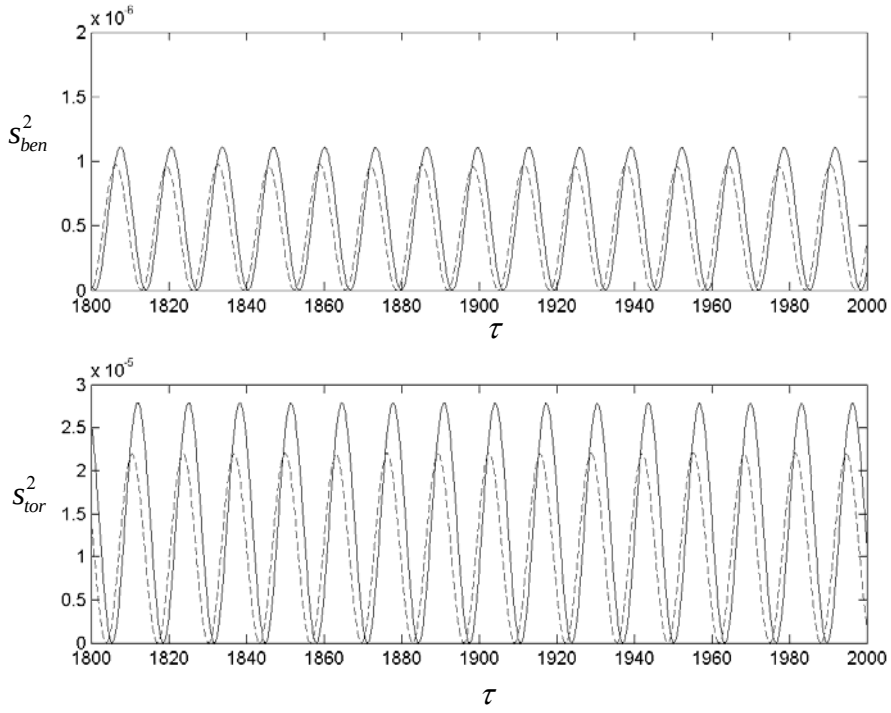


(c) Bending and torsion variances time history comparison plots
——— Perturbation method; -------- Monte Carlo Simulation

Figure 3.47. Time history records of bending and torsion responses and their variances from Monte Carlo Simulation; $V_\infty = 120m/s$, $\sigma_{EI_x}/\overline{EI}_x = 0.1$, $\sigma_{GJ}/\overline{GJ} = 0$, $\alpha_a = 5°$, $q_{ben}(0) = -0.05$, $\dot{q}_{ben}(0) = 0$, $q_{tor}(0) = 0.01$, $\dot{q}_{tor}(0) = 0$

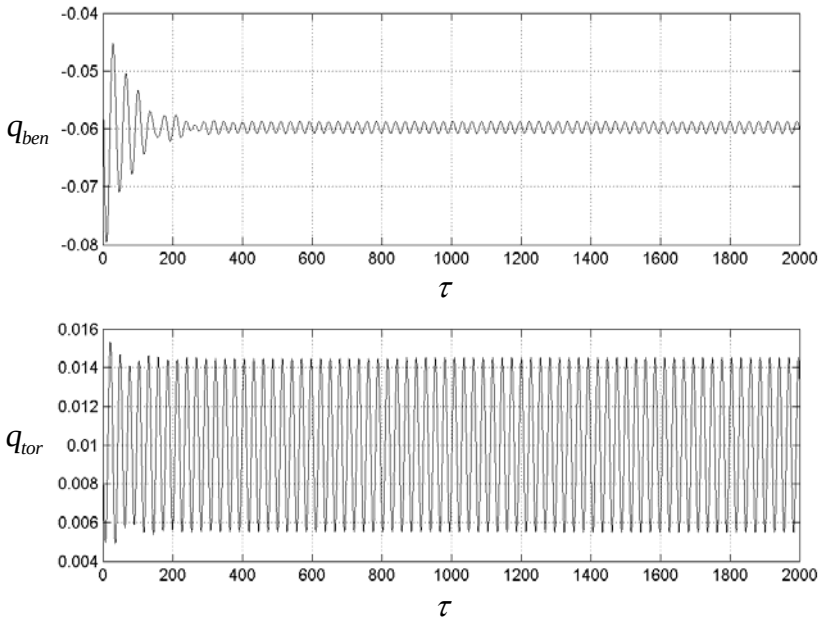


(a) Time history response of bending and torsion at the wing tip

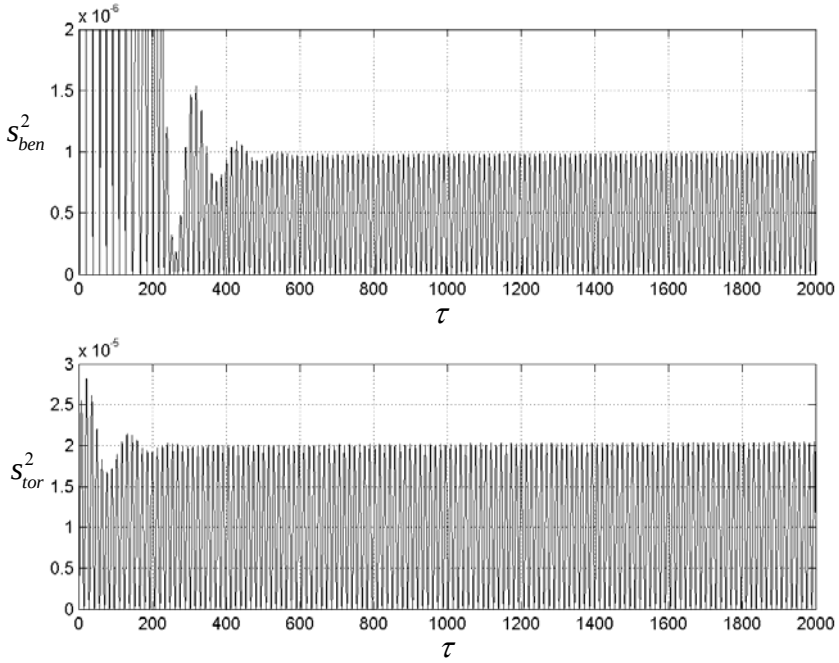


(b) Bending and torsion variances time history plots

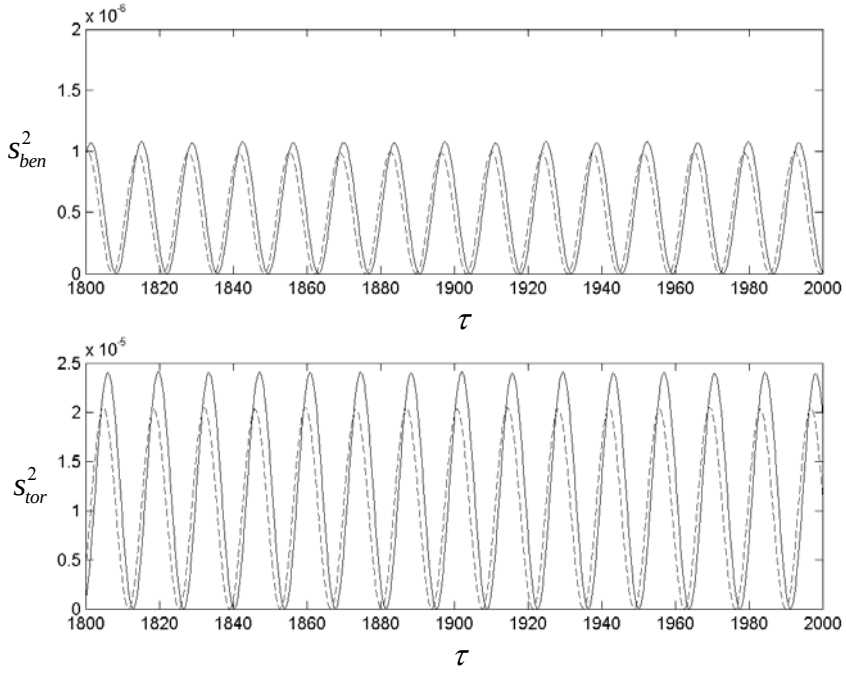


(c) Bending and torsion variances time history comparison plots
——— Perturbation method; -------- Monte Carlo Simulation

Figure 3.48. Time history records of bending and torsion responses and their variances from Monte Carlo Simulation; $V_\infty = 125m/s$, $\sigma_{EI_x}/\overline{EI}_x = 0.08$, $\sigma_{GJ}/\overline{GJ} = 0$, $\alpha_a = 5°$, $q_{ben}(0) = -0.05$, $\dot{q}_{ben}(0) = 0$, $q_{tor}(0) = 0.01$, $\dot{q}_{tor}(0) = 0$

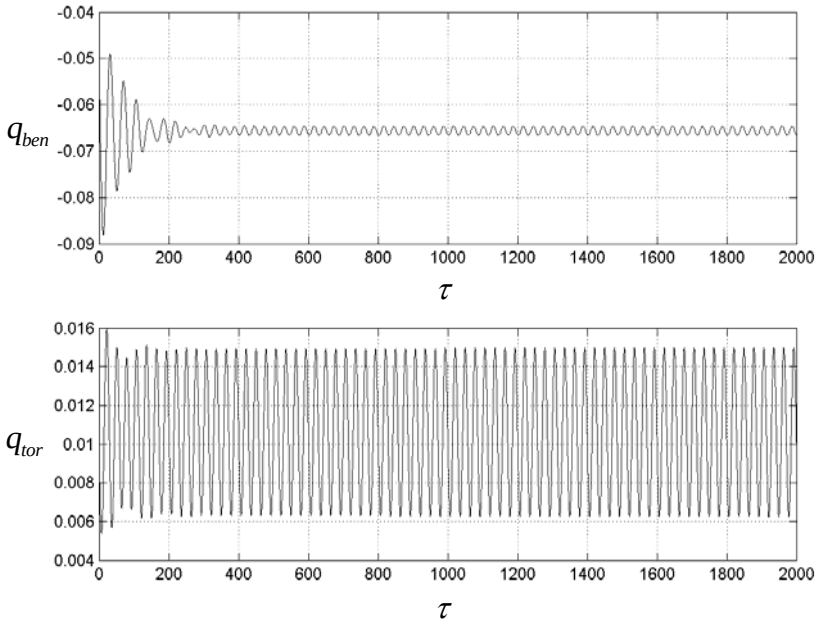


(a) Time history response of bending and torsion at the wing tip

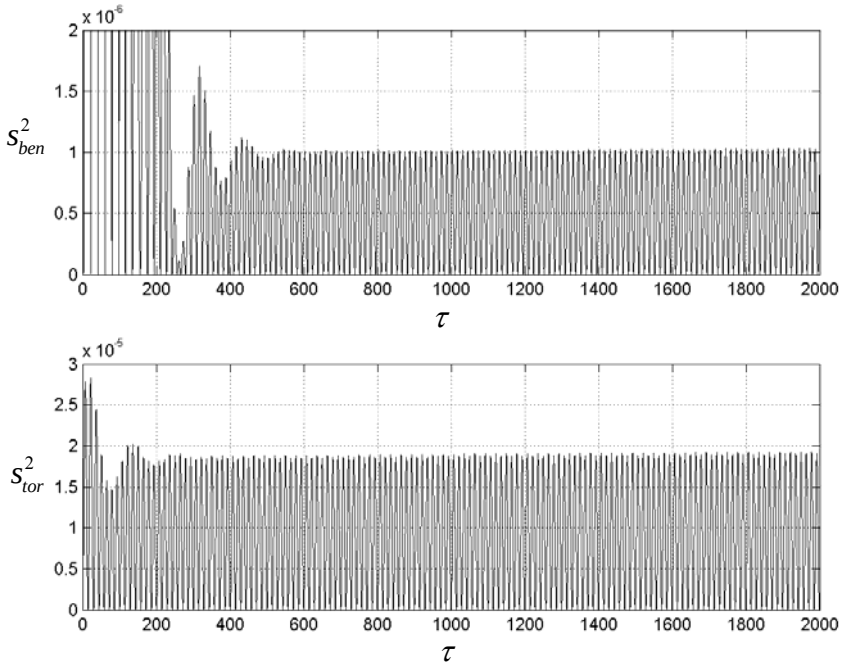


(b) Bending and torsion variances time history plots

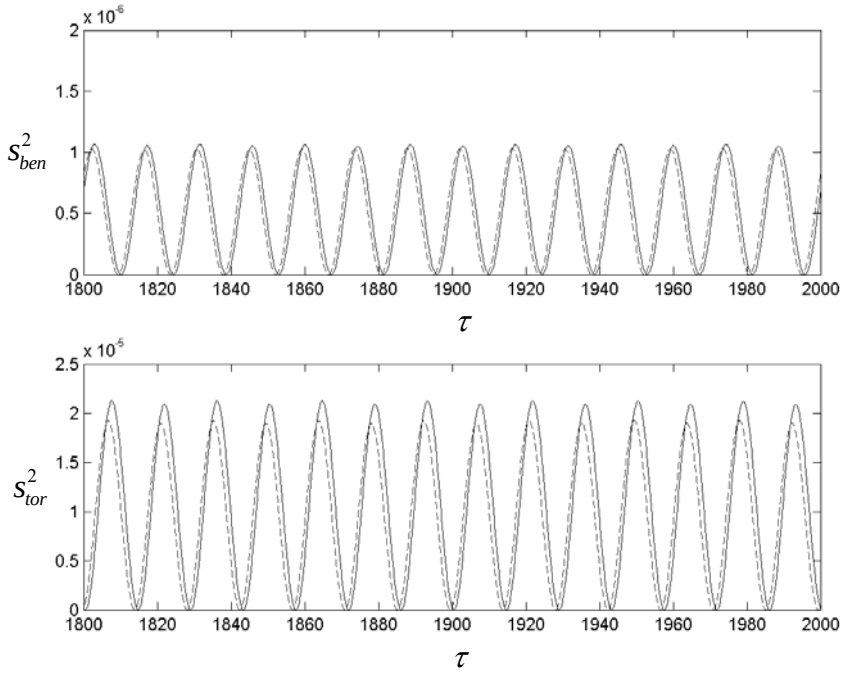


(c) Bending and torsion variances time history comparison plots
——— Perturbation method; -------- Monte Carlo Simulation

Figure 3.49. Time history records of bending and torsion responses and their variances from Monte Carlo Simulation; $V_\infty = 130m/s$, $\sigma_{EI_x}/\overline{EI}_x = 0.06$, $\sigma_{GJ}/\overline{GJ} = 0$, $\alpha_a = 5°$, $q_{ben}(0) = -0.05$, $\dot{q}_{ben}(0) = 0$, $q_{tor}(0) = 0.01$, $\dot{q}_{tor}(0) = 0$

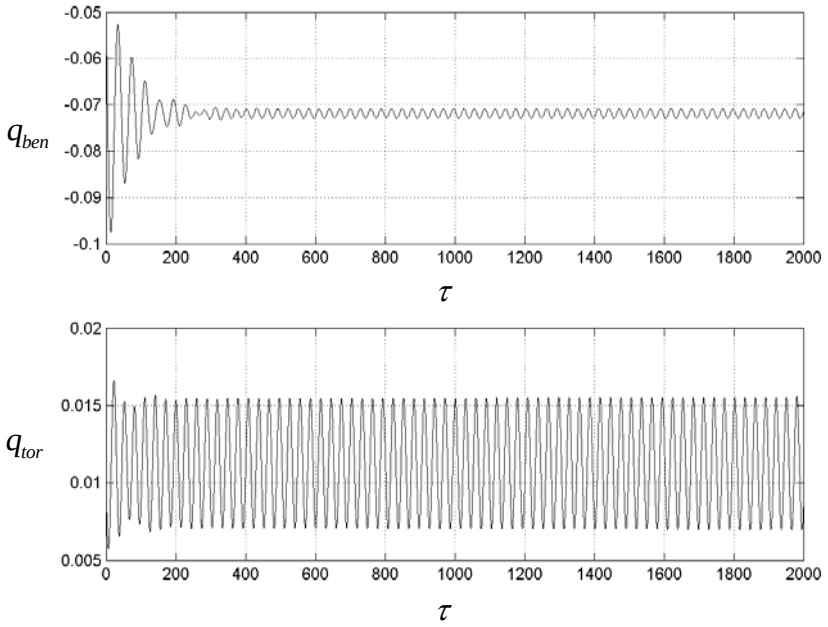


(a) Time history response of bending and torsion at the wing tip

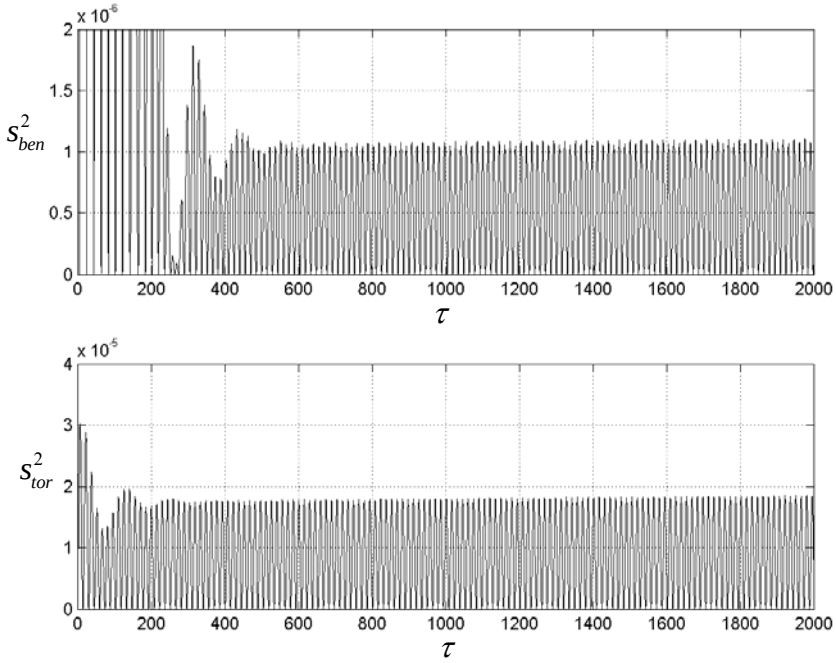


(b) Bending and torsion variances time history plots

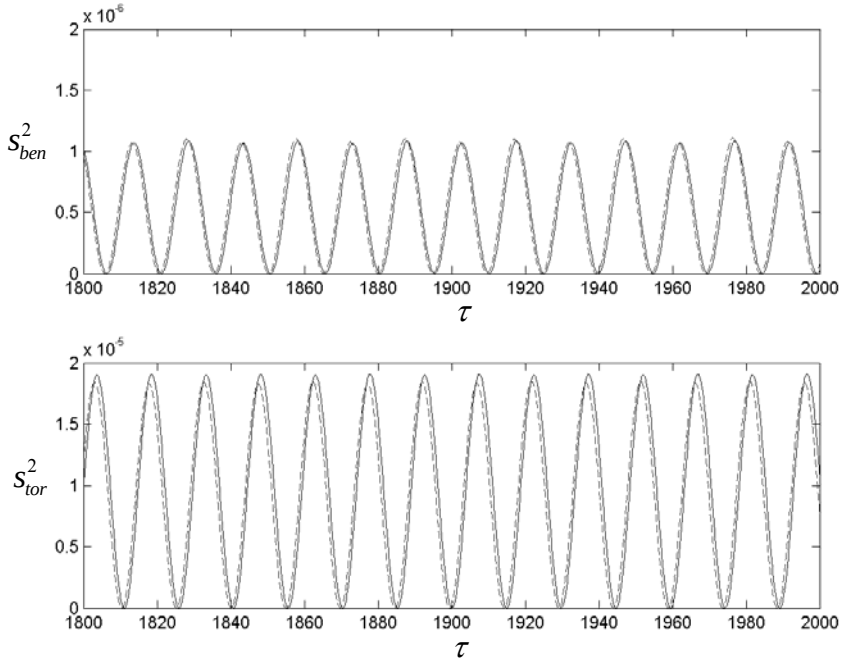


(c) Bending and torsion variances time history comparison plots
——— Perturbation method; -------- Monte Carlo Simulation

Figure 3.50. Time history records of bending and torsion responses and their variances from Monte Carlo Simulation; $V_\infty = 135m/s$, $\sigma_{EI_x}/\overline{EI}_x = 0.04$, $\sigma_{GJ}/\overline{GJ} = 0$, $\alpha_a = 5°$, $q_{ben}(0) = -0.05$, $\dot{q}_{ben}(0) = 0$, $q_{tor}(0) = 0.01$, $\dot{q}_{tor}(0) = 0$

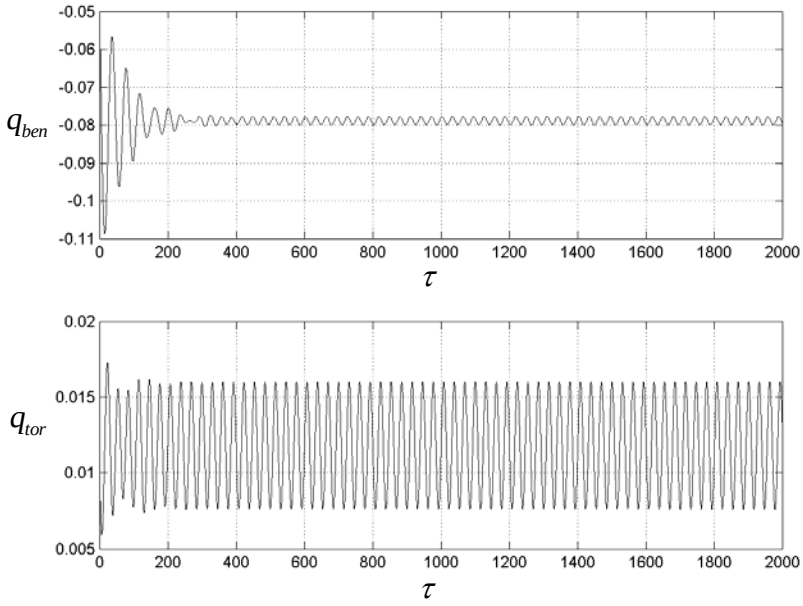


(a) Time history response of bending and torsion at the wing tip

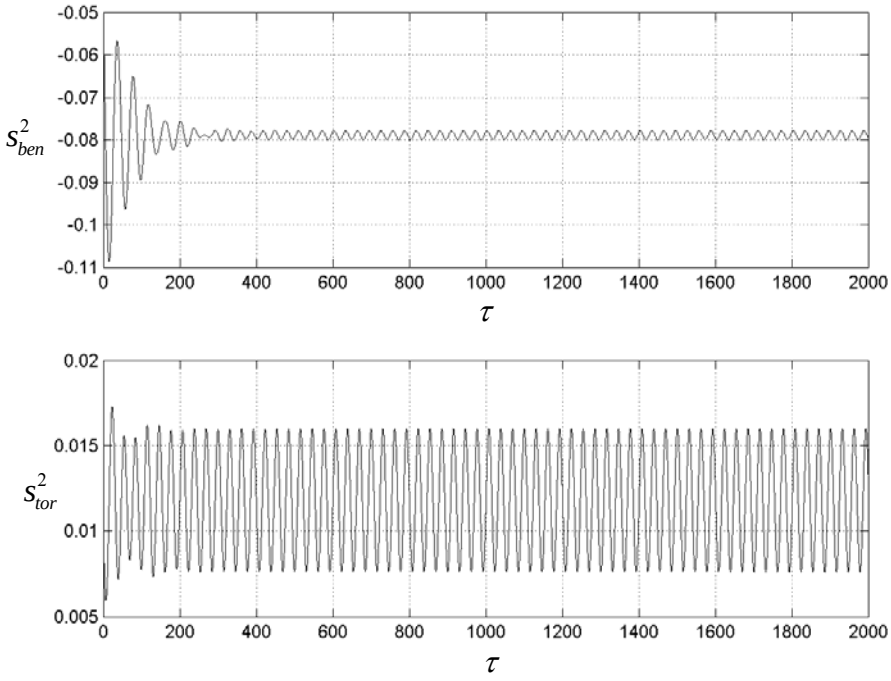


(b) Bending and torsion variances time history plots

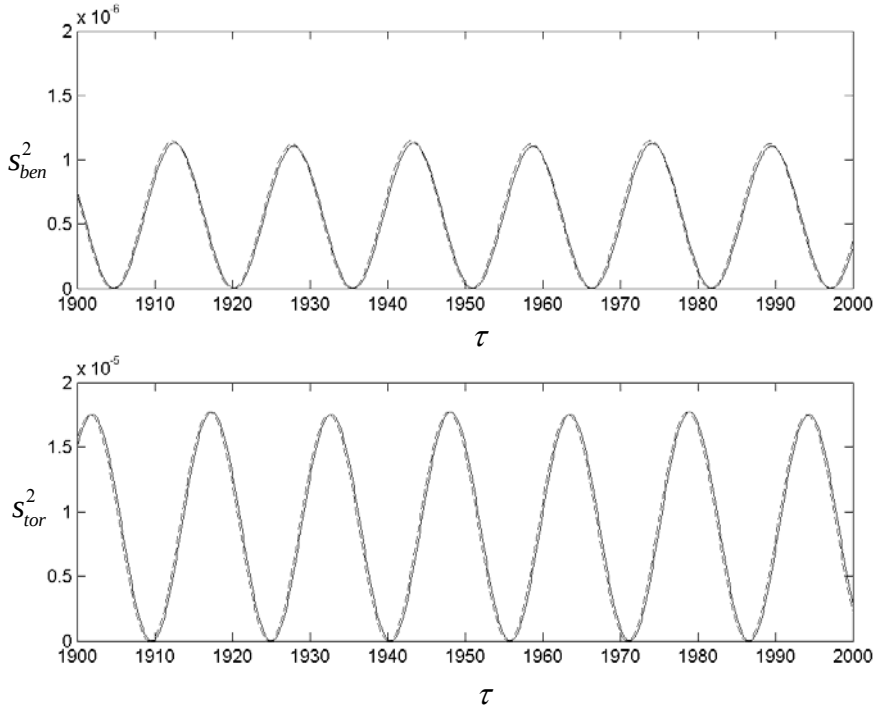


(c) Bending and torsion variances time history comparison plots
——— Perturbation method; -------- Monte Carlo Simulation

Figure 3.51. Time history records of bending and torsion responses and their variances from Monte Carlo Simulation; $V_\infty = 140m/s$, $\sigma_{EI_x} / \overline{EI}_x = 0.015$, $\alpha_a = 5°$, $q_{ben}(0) = -0.05$, $\dot{q}_{ben}(0) = 0$, $q_{tor}(0) = 0.01$, $\dot{q}_{tor}(0) = 0$

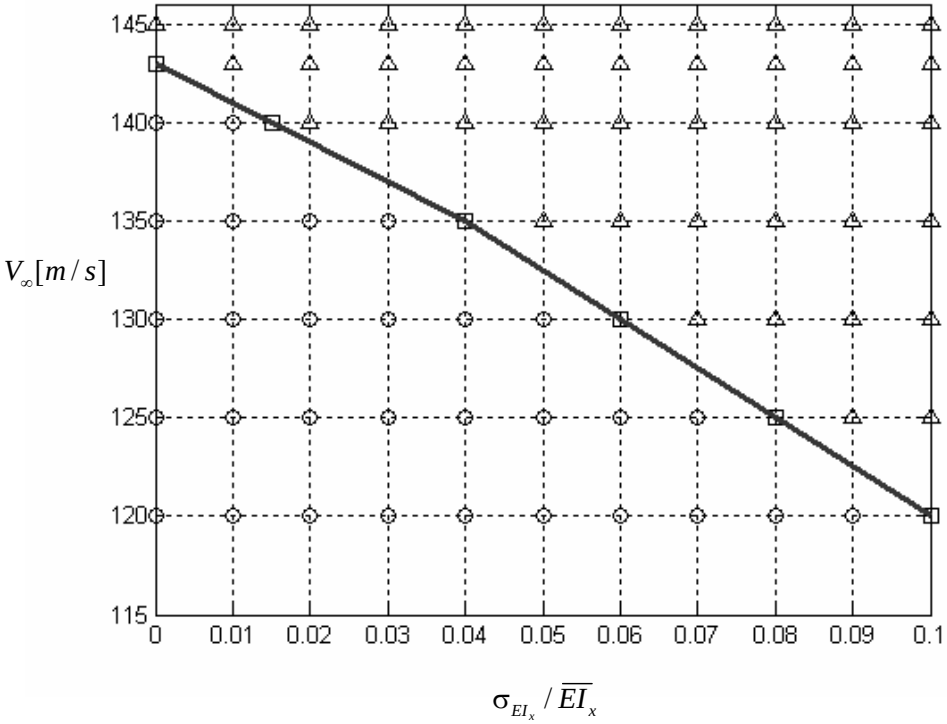


Figure 3.52. Stability bifurcation diagram $V_\infty$ vs. $\sigma_{EI_x} / \overline{EI}_x$ for Monte Carlo Simulation

○ Stable, □ LCO, △ Unstable

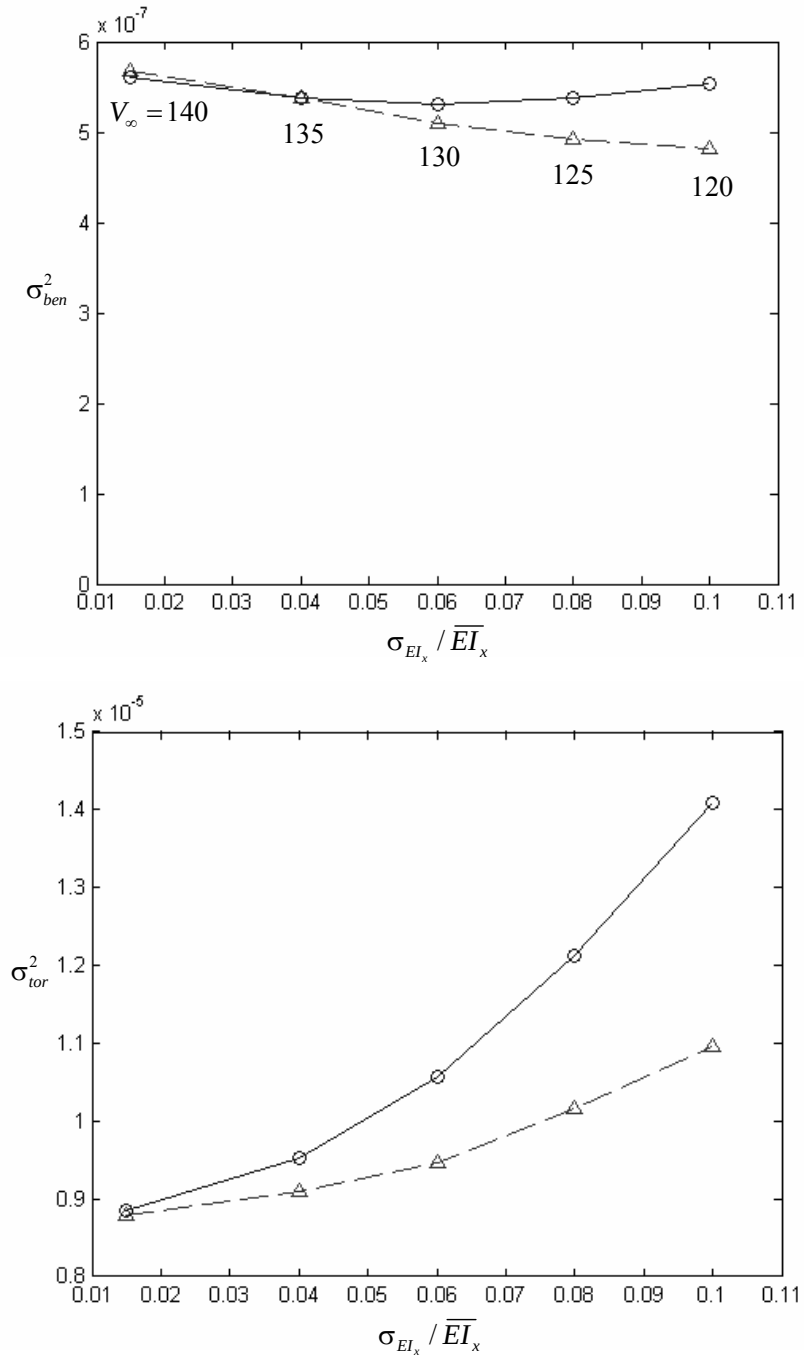


Figure 3.53. Perturbation method convergence

Perturbation Method; Monte Carlo Simulation

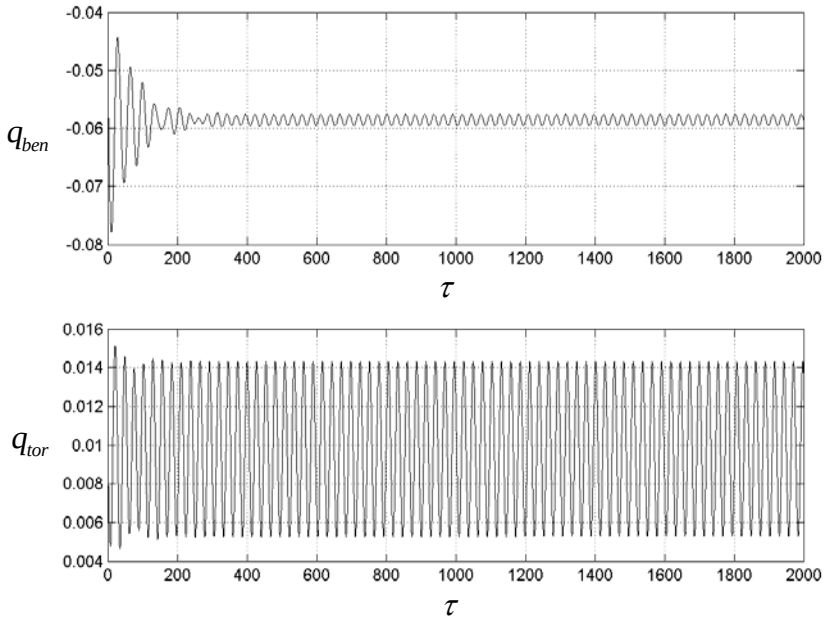


(a) Time history response of bending and torsion at the wing tip

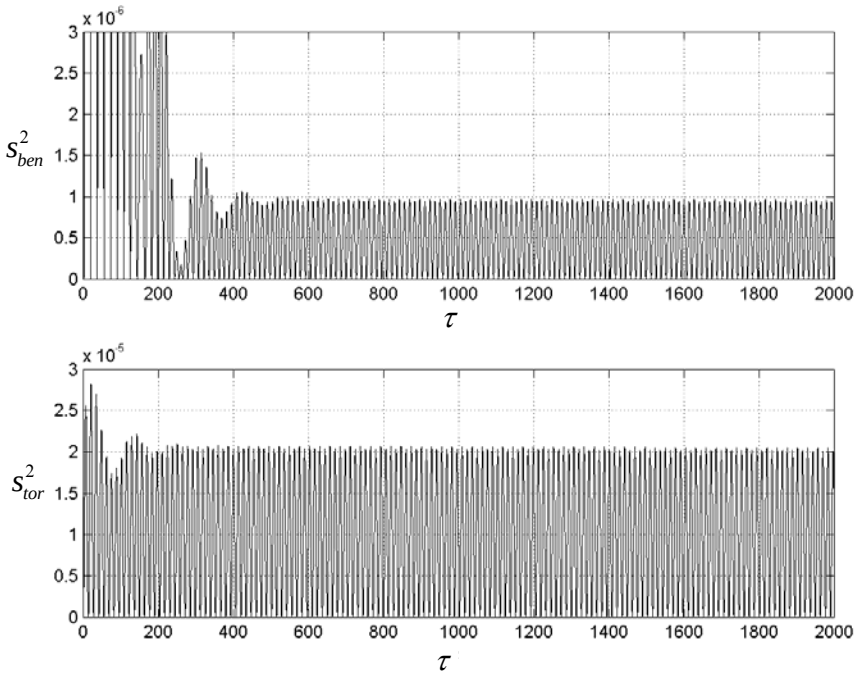


(b) Bending and torsion variances time history plots

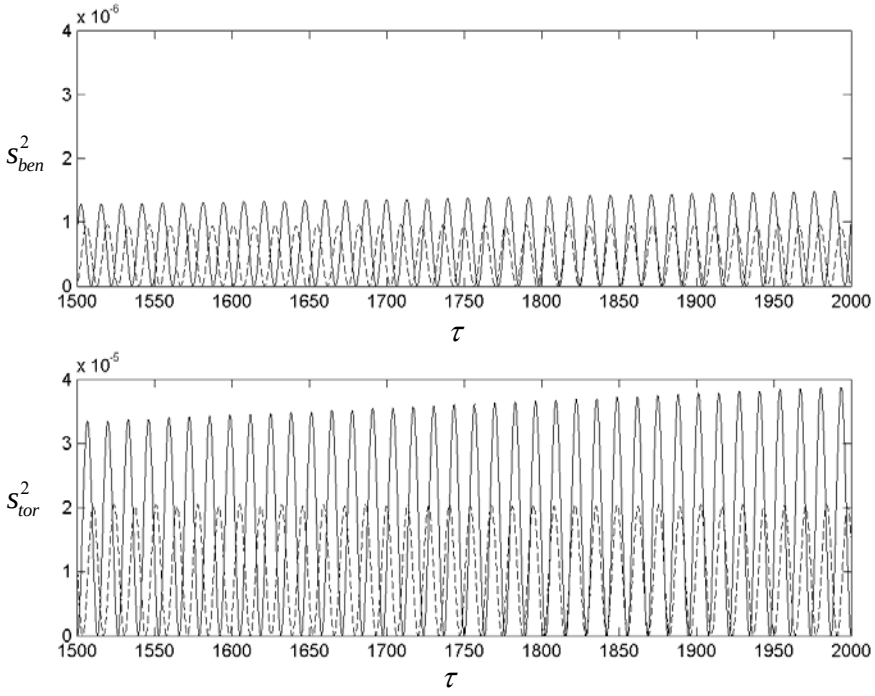


(c) Bending and torsion variances time history comparison plots
——— Perturbation method; -------- Monte Carlo Simulation

Figure 3.54. Time history records of bending and torsion responses and their variances from Monte Carlo Simulation; $V_\infty = 120m/s$, $\sigma_{EI_x}/\overline{EI}_x = 0$, $\sigma_{GJ}/\overline{GJ} = 0.05$, $\alpha_a = 5°$, $q_{ben}(0) = -0.05$, $\dot{q}_{ben}(0) = 0$, $q_{tor}(0) = 0.01$, $\dot{q}_{tor}(0) = 0$

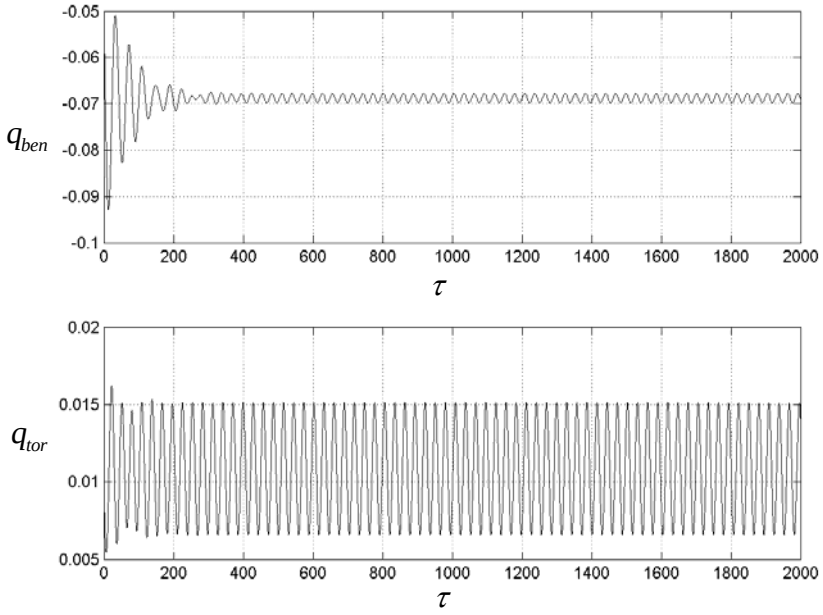


(a) Time history response of bending and torsion at the wing tip

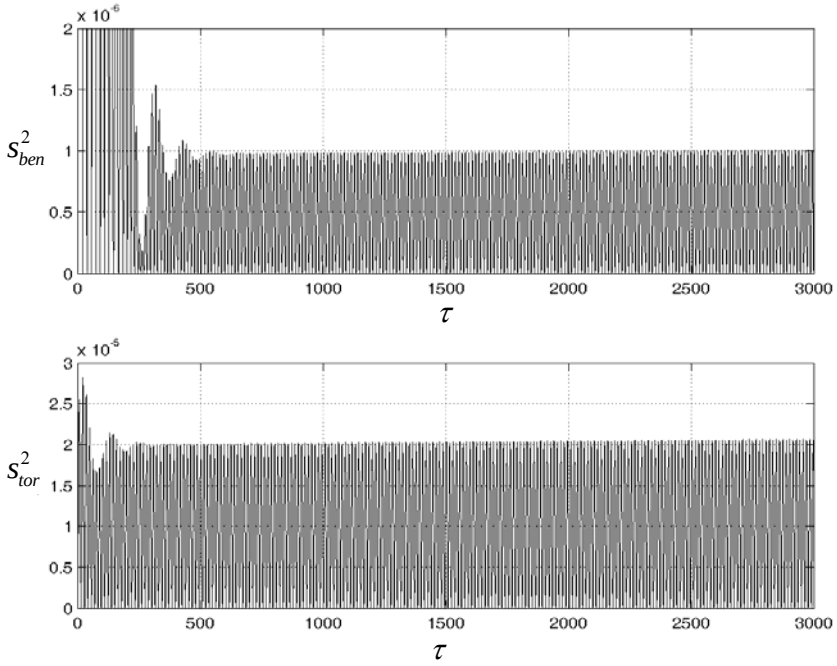


(b) Bending and torsion variances time history plots

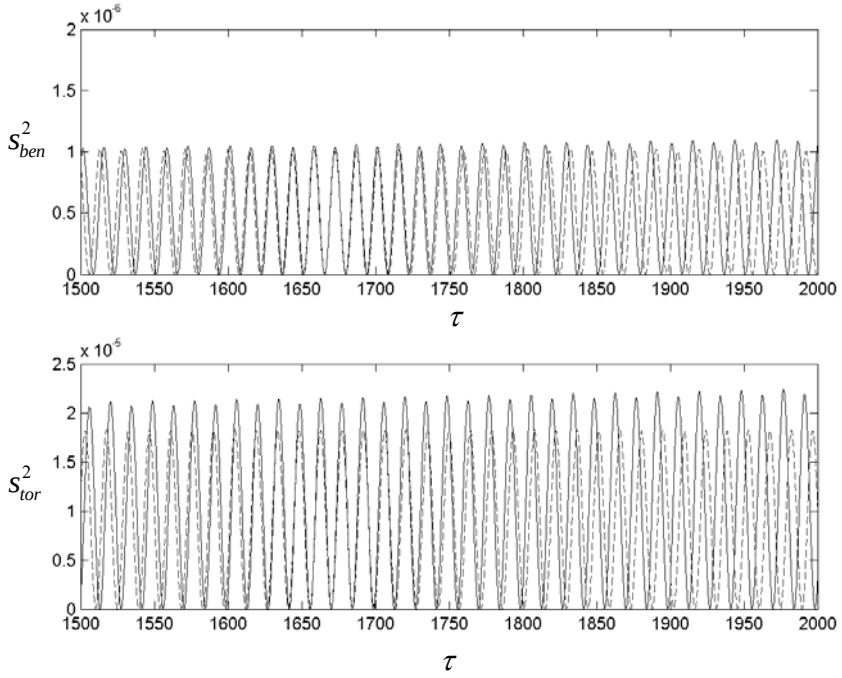


(c) Bending and torsion variances time history comparison plots
——— Perturbation method; -------- Monte Carlo Simulation

Figure 3.55. Time history records of bending and torsion responses and their variances from Monte Carlo Simulation; $V_\infty = 130 m/s$, $\sigma_{EI_x} / \overline{EI}_x = 0$, $\sigma_{GJ} / \overline{GJ} = 0.03$, $\alpha_a = 5°$, $q_{ben}(0) = -0.05$, $\dot{q}_{ben}(0) = 0$, $q_{tor}(0) = 0.01$, $\dot{q}_{tor}(0) = 0$

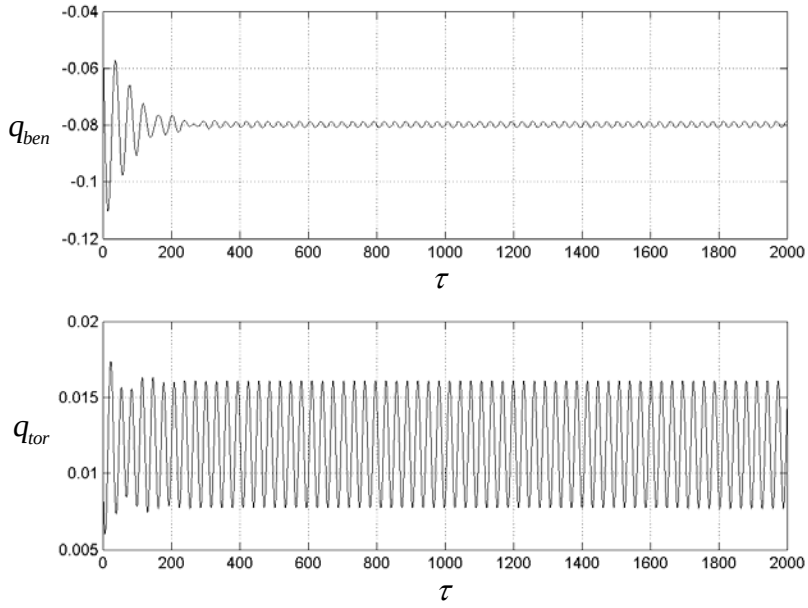


(a) Time history response of bending and torsion at the wing tip

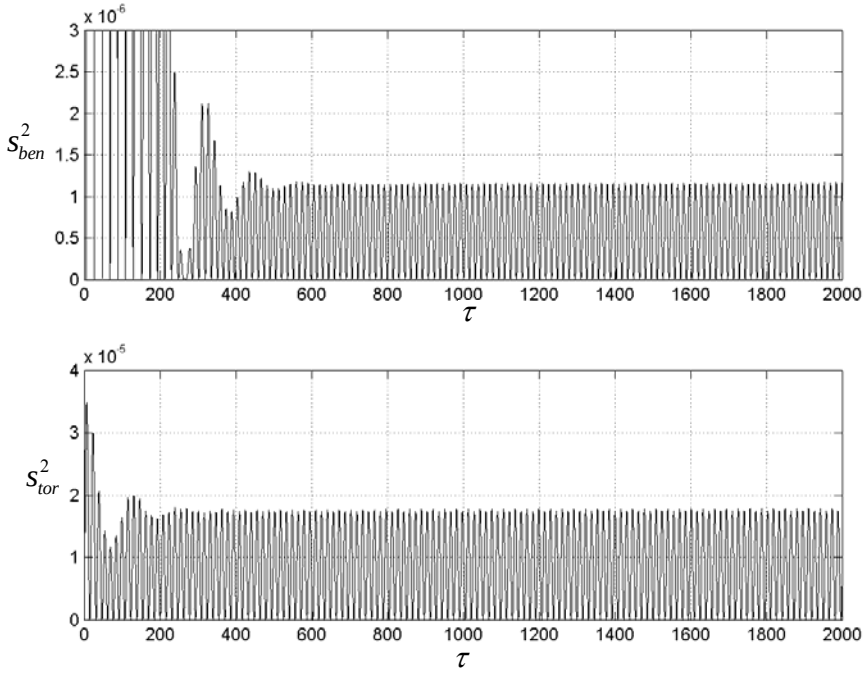


(b) Bending and torsion variances time history plots

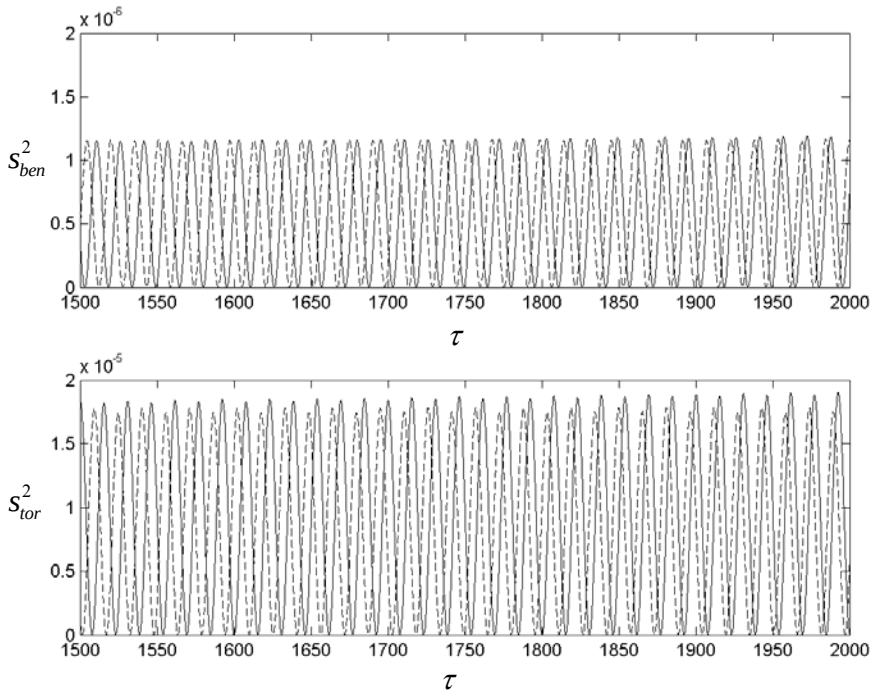


(c) Bending and torsion variances time history comparison plots
——— Perturbation method; -------- Monte Carlo Simulation

Figure 3.56. Time history records of bending and torsion responses and their variances from Monte Carlo Simulation; $V_\infty = 140 m/s$, $\sigma_{EI_x} / \overline{EI}_x = 0$, $\sigma_{GJ} / \overline{GJ} = 0.01$, $\alpha_a = 5°$, $q_{ben}(0) = -0.05$, $\dot{q}_{ben}(0) = 0$, $q_{tor}(0) = 0.01$, $\dot{q}_{tor}(0) = 0$

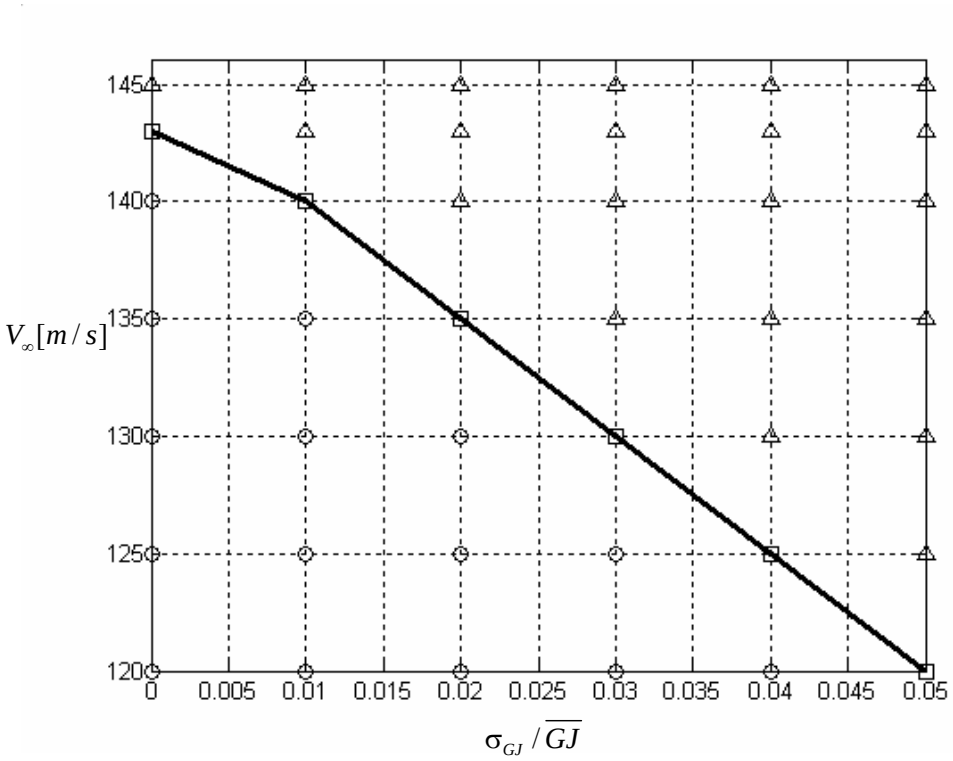


Figure 3.57. Stability bifurcation diagram $V_\infty$ vs. $\sigma_{GJ}/\overline{GJ}$ for Monte Carlo Simulation

○ Stable, □ LCO, △ Unstable

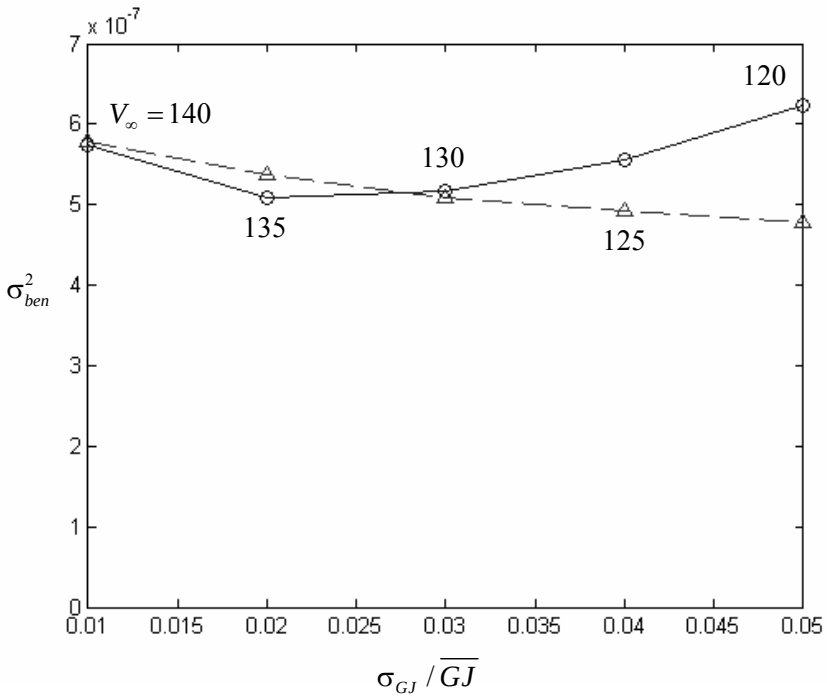


(a)

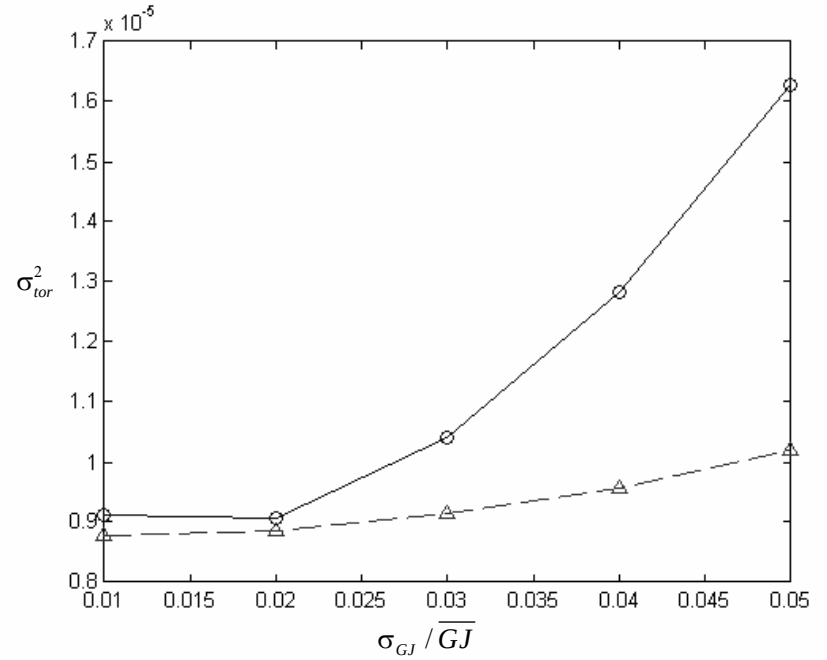


(b)

Figure 3.58. Perturbation method convergence

Perturbation Method; Monte Carlo Simulation

# CHAPTER 4

# CONCLUSIONS AND RECOMMENDATIONS

Two related problems were analyzed in this dissertation. The first problem is related to the suppression of flutter via parametric excitation. In order to accomplish that, a two-dimensional nonlinear cantilever wing model was proposed. The wing is excited at the clamped end in the plane of largest rigidity such that the bending and torsion modes are cross-coupled through the excitation. The Theodorsen's theory was adopted for the modeling of aerodynamic lift and moment. The nonlinearities arise from small in-plane displacement and nonlinear curvature. The equations of motion are then derived using Hamilton's principle.

For the linearized system, an eigenvalue problem was solved to find the critical flutter speed. Two cases were analyzed: one considering complex circulation function, the other one considering real circulation function. It was found that the error between the two flutter speeds obtained in both cases is very small, so in the subsequent analyzes the circulation function was adopted real. Also, in the presence of parametric excitation, the regions of parametric instability were obtained for different values of flow speed. At the critical flutter speed the bottom of instability region touches the frequency axis. Below and above the critical speed the instability regions move away from the frequency axis.

The method of multiple scales was used to analyze the nonlinear system. The system was studied in the neighborhood of combination parametric resonance at the critical flutter speed and at flow speed that is slightly higher than the critical

one. At critical flutter speed the response was found to possess more than one attractor which is obtained from a certain domain of initial conditions. As the excitation amplitude increases, the response experiences a cascade of period doubling and eventually chaotic motion. At critical excitation amplitude the response exhibits stabilization state to the zero equilibrium attractor over a wide range of initial conditions. The stabilization effect was also manifested at a flow speed that is slightly higher than the critical flutter speed. However, the stabilization effect was preceded by new phenomena such as firing and recovery states. The original nonlinear equations of motion were numerically integrated in order to validate the multiple scales results. The numerical simulations confirmed the multiple scales findings.

Another problem that has been analyzed in this thesis is the influence of uncertainties on the flutter behavior of a nonlinear aeroelastic wing. In order to accomplish that, an aerodynamic model based on unsteady vortex lattice method was adopted and a finite element model which includes uncertainty in bending and stiffness was developed. Also, an interpolation matrix was used to combine the models and treat the airflow and the wing structure as a single system. The system is then solved by an adapted Hamming's fourth order predictor-corrector method. The uncertainties are modeled using a modified first order stochastic perturbation method which uses truncated Karhunen-Loeve expansion to discretize the random field. Four cases were analyzed: (1) the system in the absence of uncertainties; (2) the influence of bending stiffness uncertainty; (3) the influence of torsion stiffness uncertainty; (4) the influence of combination

bending-torsion stiffness uncertainty. The results of the perturbation approach are then compared with those predicted by Monte Carlo simulation. The following conclusions have been taken:

- There is a good correlation between the perturbation method and Monte Carlo simulation for low values of stiffness uncertainty levels.
- As the uncertainty level increases, the perturbation method loses accuracy.
- For the prediction of LCO, the perturbation method is very accurate for all levels of bending stiffness uncertainty examined, but the method loses its accuracy at upper levels of torsion stiffness uncertainty.
- The stability boundary in the flow speed versus stiffness uncertainty reveals the appearance of LCOs below the flutter speed. Further increase of uncertainty level produces instability.
- The uncertainties in torsion stiffness induce a significant disturbance in the system. A smaller level of torsion stiffness uncertainty induces instability in the system.
- The results presented in Chapter 3 are pertaining to material properties listed in page 154. The algorithm can be used for any other material properties.

One last remark pertaining to the CPU time in generating the results of the perturbation method and Monte Carlo simulation. The CPU, on a PC of 3.2 GHz, for a single Monte Carlo simulation (based on assuming ergodicty of the response) requires 8 hours which is the CPU time required for perturbation analysis. Even though for Monte Carlo simulation, 7 equations are necessary to be solved and for the perturbation method 21 equations, the computational time

is approximately the same. In the case of Monte Carlo simulation the equations must be solved for each value of airflow speed and each value of uncertainty level. In the case of perturbation method, the $\xi_n^0$ order equations (3.41a) are necessary to be solved only once for each value of air-flow speed regardless of level of uncertainty. For the same airflow speed and different levels of uncertainty, only equations (3.41b) need to be solved. The equations (3.41b), if they are solved simultaneously, will take less computational time than a single Monte Carlo simulation.

A very important problem that has not been analyzed in the present work is the influence of the boundary condition relaxation together with the wing structure uncertainties. The problem is important because, in reality, the joints in the clamped end can relax with time and can change the boundary conditions which at the extreme will become simply-supported. Because this problem involves the evolution of system frequencies in time, it can be analyzed using time-frequency techniques such as short time Fourier transform (STFT) or wavelet transform (WT). Since in reality the wing structure is not linear, a nonlinear finite element model of the wing will be proposed. This will complicate the problem because the nonlinear finite element involves different computational schemes that have to be correlated with Hamming's method. Also the modeling of the aerodynamic loads using the unsteady vortex lattice method can include gust, ground effect, stores inclusion, or aileron. Because the vortex lattice method is valid only for incompressible flow and viscosity is present only in the

boundary and wakes, the effect of compressibility and turbulence must be analyzed by different computational fluid dynamics techniques.

# APPENDIX A

Elements of equation (2.22)

$$AA(k_\alpha,\bar{\omega})=\bar{\omega}^2\left(A_R+iA_I\right)+2ir\zeta_u\bar{\omega}+r^2,\quad BB(k_\alpha,\bar{\omega})=\bar{\omega}^2\left(B_R+iB_I\right),$$

$$DD(k_\alpha,\bar{\omega})=\bar{\omega}^2\left(D_R+iD_I\right),\ EE(k_\alpha,\bar{\omega})=\bar{\omega}^2\left(E_R+iE_I\right)+2ir_\alpha\zeta_\alpha\bar{\omega}+{r_\alpha}^2$$

where

$$A_R=-\left(1+\mu+\frac{2\mu G(k)}{k_\alpha\bar{\omega}}\right),\ A_I=\frac{2\mu F(k)}{k_\alpha\bar{\omega}},$$

$$B_R=c_6\left[-x_\alpha+\left(a+\frac{2F(k)}{\left(k_\alpha\bar{\omega}\right)^2}-(1-2a)\frac{G(k)}{k_\alpha\bar{\omega}}\right)\mu\right],\ B_I=\frac{c_6\mu}{k_\alpha\bar{\omega}}\left[1+\frac{2G(k)}{\left(k_\alpha\bar{\omega}\right)}-(1-2a)F(k)\right],$$

$$D_R=c_7\left[-x_\alpha+\left(a+(1+2a)\frac{G(k)}{k_\alpha\bar{\omega}}\right)\mu\right],\ D_I=-c_7(1+2a)\frac{\mu F(k)}{k_\alpha\bar{\omega}},$$

$$E_R=-r_\alpha^2+\mu\left[-\left(\frac{1}{8}+a^2\right)+\left(\frac{1}{2}-2a^2\right)\frac{G(k)}{k_\alpha\bar{\omega}}-(1+2a)\frac{F(k)}{\left(k_\alpha\bar{\omega}\right)^2}\right],$$

$$E_I=\frac{\mu}{k_\alpha\bar{\omega}}\left[\frac{1}{2}-a-\left(\frac{1}{2}-2a^2\right)F(k)-(1+2a)\frac{G(k)}{k_\alpha\bar{\omega}}\right],$$

$$F\left(k_\alpha\bar{\omega}\right)=1-\frac{0.165\left(k_\alpha\bar{\omega}\right)^2}{\left(k_\alpha\bar{\omega}\right)^2+0.00207}-\frac{0.335\left(k_\alpha\bar{\omega}\right)^2}{\left(k_\alpha\bar{\omega}\right)^2+0.09},\ \text{and}$$

$$G\left(k_\alpha\bar{\omega}\right)=-\frac{0.000883735k_\alpha\bar{\omega}+0.108008\left(k_\alpha\bar{\omega}\right)^3}{0.000186323+0.0920702\left(k_\alpha\bar{\omega}\right)^2+\left(k_\alpha\bar{\omega}\right)^4}.$$

## APPENDIX B

The parameters $p_i, i=1,2,3,4$ in equations (2.27) and (2.28)

$$p_1(k)=\frac{16c_7r^2\left(x_\alpha-a\mu\right)}{8r_\alpha^2\left(1+\mu-r^2\right)-\mu p_5\left(k\right)+\sqrt{p_4(k)}},\quad p_2(k)=\frac{16c_7r^2\left(x_\alpha-a\mu\right)}{8r_\alpha^2\left(1+\mu-r^2\right)-\mu p_5\left(k\right)-\sqrt{p_4(k)}},$$

$$p_3(k)=8r_\alpha^2\left(1+r^2+\mu\right)+\mu\left[r^2\left(1+8a^2\right)-\frac{8B(k)}{k_\alpha^2}\left(1+\mu\left(1+2a\left(1-c_6c_7\right)\right)+2\left(a+c_6c_7x_\alpha\right)\right)\right],$$

$$p_4(k)=p_3^2-32r^2\left[r_\alpha^2-\frac{B(k)\mu}{k_\alpha^2}\left(1+2a\right)\right]\left[8r_\alpha^2\left(1+\mu\right)+\mu\left(1+\mu\right)\left(1+8a^2\right)-8c_6c_7\left(x_\alpha-a\mu\right)^2\right].$$

$$p_5\left(k\right)=\left[r^2\left(1+8a^2\right)+\frac{8B(k)}{k_\alpha^2}\left(1+\mu+2c_6c_7x_\alpha+2a\left(1+\mu-c_6c_7\right)\mu\right)\right]$$

## APPENDIX C

Coefficients $C_i$ in equations (43)

$$C_1 = 3q_{15} + q_{11}\bar{\omega}_2^2,\ C_2 = q_7\bar{\omega}_1 + q_{18}\bar{\omega}_2,\ C_3 = q_{16} + 3q_9\bar{\omega}_1^2 - q_6\bar{\omega}_2\bar{\omega}_1$$

$$C_4 = -q_{19} + q_8\frac{\bar{\omega}_2}{\bar{\omega}_1},\ C_5 = \frac{q_3}{\bar{\omega}_1} + q_{10}\bar{\omega}_2 - q_5\frac{\bar{\omega}_2^2}{\bar{\omega}_1},\ C_6 = 3s_{14} + s_4\bar{\omega}_1^2,\ C_7 = s_{19}\bar{\omega}_1 + s_8\bar{\omega}_2,$$

$$C_8 = s_3 + 3s_5\bar{\omega}_2^2 - s_{10}\bar{\omega}_1\bar{\omega}_2,\ C_9 = -s_7 + s_{18}\frac{\bar{\omega}_2}{\bar{\omega}_1},\ C_{10} = \frac{s_{16}}{\bar{\omega}_2} + s_6\bar{\omega}_1 - s_9\frac{\bar{\omega}_1^2}{\bar{\omega}_2},\ C_{11} = 6s_{14} + 2s_4\bar{\omega}_1^2,$$

$$C_{12} = 6q_{15} + 2q_{11}\bar{\omega}_2^2,\ C_{13} = 2\left(3s_3\bar{\omega}_1 + 3q_{16}\bar{\omega}_2 + \left(q_9 + s_{10}\right)\bar{\omega}_1^2\bar{\omega}_2 + \left(q_6 + s_5\right)\bar{\omega}_1\bar{\omega}_2^2\right)$$

$$C_{14} = 2\left[3s_{19}\bar{\omega}_1^2 + \left(q_7 - s_8\right)\bar{\omega}_1\bar{\omega}_2 - 3q_{18}\bar{\omega}_2^2\right],\ C_{15} = \left(2s_{16}\bar{\omega}_1 + 2s_9\bar{\omega}_1^3 + 3q_{14}\bar{\omega}_2 + q_4\bar{\omega}_1^2\bar{\omega}_2\right)$$

$$C_{16} = s_{16}\bar{\omega}_1 - s_9\bar{\omega}_1^3 + s_6\bar{\omega}_1^2\bar{\omega}_2,\quad C_{17} = s_7\bar{\omega}_1^2 - s_{18}\bar{\omega}_1\bar{\omega}_2,$$

$$C_{18} = 2q_3\bar{\omega}_2 + 2q_5\bar{\omega}_2^3 + 3s_{15}\bar{\omega}_1 + s_{11}\bar{\omega}_2^2\bar{\omega}_1,\ C_{19} = q_3\bar{\omega}_2 - q_5\bar{\omega}_2^3 + q_{10}\bar{\omega}_2^2\bar{\omega}_1,\ C_{20} = q_8\bar{\omega}_2^2 - q_{19}\bar{\omega}_1\bar{\omega}_2,$$

$$C_{21} = s_2\bar{\omega}_1 b_1^2 + q_1\bar{\omega}_2 b_2^2,\ C_{22} = 6s_{14} + 2s_4\bar{\omega}_1^2,\ C_{23} = 6q_{15} + 2q_{11}\bar{\omega}_2^2,$$

$$C_{24} = 2\left[-3s_3\bar{\omega}_1 + 3q_{16}\bar{\omega}_2 + \left(q_9 - s_{10}\right)\bar{\omega}_1^2\bar{\omega}_2 + \left(q_6 - s_5\right)\bar{\omega}_1\bar{\omega}_2^2\right],$$

$$C_{25} = 2\left[-3s_{19}\bar{\omega}_1^2 + \left(q_7 + s_8\right)\bar{\omega}_1\bar{\omega}_2 - 3q_{18}\bar{\omega}_2^2\right],\ C_{26} = \left[-2s_{16}\bar{\omega}_1 - 2s_9\bar{\omega}_1^3 + 3q_{14}\bar{\omega}_2 + q_4\bar{\omega}_1^2\bar{\omega}_2\right]$$

$$C_{27} = -s_{16}\bar{\omega}_1 + s_9\bar{\omega}_1^3 - s_6\bar{\omega}_1^2\bar{\omega}_2,\quad C_{28} = -s_7\bar{\omega}_1^2 + s_{18}\bar{\omega}_1\bar{\omega}_2,$$

$$C_{29} = 2q_3\bar{\omega}_2 + 2q_5\bar{\omega}_2^3 - 3s_{15}\bar{\omega}_1 - s_{11}\bar{\omega}_2^2\bar{\omega}_1,\ C_{30} = q_3\bar{\omega}_2 - q_5\bar{\omega}_2^3 + q_{10}\bar{\omega}_2^2\bar{\omega}_1,\ C_{31} = q_8\bar{\omega}_2^2 - q_{19}\bar{\omega}_1\bar{\omega}_2,$$

$$C_{32} = s_2\bar{\omega}_1 b_1^2 - q_1\bar{\omega}_2 b_2^2.$$

# APPENDIX D

## D.1 THE NAVIER-STOKES EQUATIONS

The purpose of this Appendix is to provide detailed analysis of the fluid equations that are used to determine the aerodynamic loading on the wing. The fluid dynamics equations constitute the momentum and continuity equations. These equations are given in Cartesian coordinates as follow [24].

The continuity equation:

$$\frac{D\rho}{Dt} + \rho \nabla \cdot \mathbf{V} = 0 \tag{D.1}$$

where the material derivative $D/Dt$ represents the rate of change following a fluid particle, $\rho$ is fluid density, $\mathbf{V}$ is the fluid velocity vector, and $\nabla = \frac{\partial}{\partial x}\hat{i} + \frac{\partial}{\partial x}\hat{j} + \frac{\partial}{\partial x}\hat{k}$, where $\hat{i}$, $\hat{j}$, $\hat{k}$ are the unit vectors of Cartesian coordinates $x$, $y$, and $z$ respectively.

Momentum equation:

$$\frac{D\mathbf{V}}{Dt} = \frac{\partial \mathbf{V}}{\partial t} + (\mathbf{V} \cdot \nabla)\mathbf{V} = \mathbf{f} - \frac{1}{\rho}\nabla p + \nu \nabla^2 \mathbf{V} + \frac{\nu}{3}\nabla(\nabla \cdot \mathbf{V}) \tag{D.2}$$

where $\nu$ is kinematic viscosity, $p$ is the pressure, $\mathbf{f}$ represents the body forces per unit mass.

In the case of subsonic flow at speeds below $0.45c$ (where $c$ is the speed of sound) the fluid can be considered incompressible and inviscid. In this case

the Navier-Stokes equations become the Euler equations in which the continuity equation will be

$$\nabla \cdot \mathbf{V} = 0 \tag{D.3}$$

and the momentum equation:

$$\frac{D\mathbf{V}}{Dt} = \frac{\partial \mathbf{V}}{\partial t} + (\mathbf{V} \cdot \nabla)\mathbf{V} = \mathbf{f} - \frac{1}{\rho}\nabla p \tag{D.4}$$

## D.2 VORTICITY AND CIRCULATION

The motion of the fluid consists of translation, rotation, and deformation. The rotation of the fluid is represented by the angular velocity which in terms of the fluid velocity will be [24]:

$$\boldsymbol{\omega} = \frac{1}{2}\nabla \times \mathbf{V} \tag{D.5}$$

The vorticity vector $\boldsymbol{\Omega}$ is defined as twice the angular velocity:

$$\boldsymbol{\Omega} = 2\boldsymbol{\omega} = \nabla \times \mathbf{V} \tag{D.6}$$

Figure D.1 represents an open surface $S$ enclosed by the curve $C$. Using the Stokes theorem, the vorticity on the surface $S$ is related to the line integral around $C$ by the following formula:

$$\int_S \nabla \times \mathbf{V} \cdot \mathbf{n} dS = \int_S \boldsymbol{\Omega} \cdot \mathbf{n} dS = \oint_C \mathbf{V} \cdot d\vec{l} \tag{D.7}$$

where $\mathbf{n}$ is the normal vector to the surface $S$, and $d\vec{l}$ is the differential vector length on the curve $C$.

The right hand side of the equation (D.7) defines the circulation and is represented by:

$$\Gamma = \oint_C \mathbf{V} \cdot d\vec{l} = \int_S \mathbf{\Omega} \cdot \mathbf{n} dS \tag{D.8}$$

The circulation is tied to the rotation of the fluid. If the viscous force is very large, the fluid rotates like a rigid body. In this case $\nabla \times \mathbf{V} \neq 0$ and the flow is considered *rotational*. In the case of negligible fluid viscosity, the shear forces in the fluid will be small and they will not rotate the fluid. In this case $\nabla \times \mathbf{V} = 0$ and the flow is considered *irrotational*.

## D.3 IRROTATIONAL FLOW AND THE VELOCITY POTENTIAL

At high Reynolds number flow-fields, the flow outside the boundary layer is irrotational while the flow inside is rotational. For the irrotational region of the flow, vorticity is zero, $\mathbf{\Omega} = \nabla \times \mathbf{V} = curl(\mathbf{V}) = 0$.

If the velocity vector is determined by a gradient of a scalar function,

$$\mathbf{V} = \nabla \Phi \tag{D.9}$$

the flow is irrotational (because $\nabla \times \nabla \Phi = 0$). $\Phi$ is called the velocity potential function of the flow field. In this case the continuity equation will take the form of Laplace's equation:

$$\nabla^2 \Phi = 0 \tag{D.10}$$

Equation (D.10) is the governing equation for the velocity for an inviscid, irrotational and incompressible flow. It is a linear elliptic partial differential equation[14]. Regarding fluid-structure boundary (see Figure D.2), the boundary conditions require [24]:

1. The normal component of the relative velocity between the fluid and the solid surface is zero at the boundary:

$$\left(\mathbf{V} - \mathbf{V}_S\right) \cdot \mathbf{n} = 0 \tag{D.11a}$$

where $\mathbf{V}_S$ is the velocity of the solid surface and $\mathbf{n}$ is the normal unit vector.

2. At infinity (far from the solid boundary) the disturbance $\mathbf{V}$ decays to zero:

$$\lim_{r \to \infty} \mathbf{V} = 0 \tag{D.11b}$$

where $r$ represents the distance from the boundary.

## D.4 KELVIN'S THEOREM

---

[14] A differential equation of the form: $A\frac{\partial^2 \phi}{\partial x^2} + B\frac{\partial^2 \phi}{\partial x \partial y} + C\frac{\partial^2 \phi}{\partial x^2} + D\frac{\partial \phi}{\partial x} + E\frac{\partial \phi}{\partial y} + F = 0$ is called elliptic if $AC - B^2/4 > 0$.

The Kelvin's theorem (e.g. [23, 24]) states that in an inviscid, homogeneous flow (in a homogeneous flow the density depends only on the pressure) with conservative body forces, the circulation around a closed fluid line remains constant with respect to time.

The time rate of the circulation along a closed curve $C$ (see Figure D.1) is:

$$\frac{D\Gamma}{Dt} = \frac{D}{Dt}\oint_C \mathbf{V}\cdot d\vec{l} = \oint_C \frac{D\mathbf{V}}{Dt}\cdot d\vec{l} + \oint_C \mathbf{V}\cdot\frac{D}{Dt}d\vec{l} \tag{D.12}$$

The expression for $\frac{D\mathbf{V}}{Dt}$ is given by equation (D.4) restated below:

$$\frac{D\mathbf{V}}{Dt} = \mathbf{f} - \frac{1}{\rho}\nabla p \tag{D.4}$$

If the body forces (the gravity forces) are considered conservative, they can be expressed by a body-force potential, $F$ :

$$\mathbf{f} = \nabla F \tag{D.13}$$

Since a particular fluid particle is followed, the order of differentiation does not mater:

$$\frac{D}{Dt}d\vec{l} = d\frac{D\vec{l}}{Dt} = d\mathbf{V} \tag{D.14}$$

Introducing equations (D.4), (D.13), and (D.14) into equation (D.12) yields

$$\frac{D}{Dt}\oint_C \mathbf{V}\cdot d\vec{l} = \oint_C dF - \oint_C \frac{1}{\rho}dp + \oint_C \mathbf{V}\cdot d\mathbf{V} \tag{D.15}$$

Because the density is a function only of the pressure, all right hand side terms in equation (D.15) form exact differentials. The integral of an exact differential around a closed path is zero. So,

$$\frac{D\Gamma}{Dt} = \frac{D}{Dt}\oint_C \mathbf{V}\cdot d\vec{l} = 0 \tag{D.16}$$

Equation (D.16) is known as *Kelvin's theorem*. Consider the flow around an airfoil which it is initially at rest and then suddenly is in constant forward motion. As a consequence of Kelvin's theorem, in addition to the circulation developed around the airfoil, a starting wake vortex must exist such that the total circulation around a line surrounding both airfoil and wake remains unchanged:

$$\frac{D\Gamma}{Dt} = \frac{1}{\Delta t}\left(\Gamma_{airfoil} + \Gamma_{wake}\right) = 0 \tag{D.17}$$

where $\Gamma_{airfoil}$ is the circulation around the airfoil and $\Gamma_{wake}$ is the circulation of the wake.

## D.5 HELMHOLTZ'S VORTEX THEOREMS [24]

At this point it is necessary to define various quantities for the vorticity vector, quantities which will be necessary for modeling the lifting flow. The *vortex lines* are the field lines parallel to the vorticity vector and these lines have the following property:

$$\Omega \times d\vec{l} = 0 \tag{D.18}$$

The vortex lines passing through an open curve in space form a *vortex surface* and the vortex lines passing through a closed curve in space form a *vortex tube*. A vortex tube having an infinitesimal cross-sectional surface is named *vortex filament*.

A volume $Vol$ enclosed by a surface $S$ is considered. Applying the divergence theorem on the vorticity on the surface $S$ yields:

$$\int_S \mathbf{\Omega} \cdot \mathbf{n} dS = \int_{Vol} \nabla \cdot \mathbf{\Omega} dV = \int_{Vol} \nabla \cdot \left( \nabla \times \mathbf{V} \right) dV = 0 \tag{D.19}$$

because the divergence of the curl of any vector is identically zero.

Figure D.3 represents a vortex tube enclosed by the surfaces $S_1$, $S_2$, and $S_3$. Applying (D.19) to the vortex tube yields:

$$\int_S \mathbf{\Omega} \cdot \mathbf{n} dS = \int_{S_1} \mathbf{\Omega} \cdot \mathbf{n} dS - \int_{S_2} \mathbf{\Omega} \cdot \mathbf{n} dS = 0 \tag{D.20}$$

because the surface $S_3$ is parallel to the vorticity its contribution vanishes and $\mathbf{n}$ is considered positive in the direction of vorticity. The equation (D.20) can be written as:

$$\int_{S_1} \mathbf{\Omega} \cdot \mathbf{n} dS = \int_{S_2} \mathbf{\Omega} \cdot \mathbf{n} dS = constant \tag{D.21}$$

If $C_1$ is a curve that encloses the surface $S_1$ (see Figure D.3), the circulation around $C_1$ is given by equation (D.8) as:

$$\Gamma_{C_1} = \oint_{C_1} \mathbf{V} \cdot d\vec{l} = \int_{S_1} \boldsymbol{\Omega} \cdot \mathbf{n} dS = constant \tag{D.22}$$

If the tube is reduced to a filament then equation (D.22) becomes

$$\Gamma_{C_1} = \left|\boldsymbol{\Omega}\right| dS = constant \tag{D.23}$$

where $\left|\boldsymbol{\Omega}\right|$ is the magnitude of $\boldsymbol{\Omega}$.

Based on the above results and the Kelvin's theorem, the following theorems were developed by Helmholtz:

1. The strength of a vortex filament is constant along its length.
2. A vortex filament cannot start or end in a fluid.
3. The fluid that forms a vortex tube continues to form a vortex tube and its strength remains constant as the tube moves

D.6 THE BIOT-SAVART LAW [24]

An incompressible fluid having the continuity equation (D.3) is considered. There is the possibility that vorticity can exist in the fluid. The aim is to find the velocity field as a function of vorticity distribution. The velocity field can be expressed as a curl of the vector field $\mathbf{B}$ such that:

$$\mathbf{V} = \nabla \times \mathbf{B} \tag{D.24}$$

Since the curl of a gradient vector is zero, the vector field $\mathbf{B}$ can be selected such that:

$$\nabla \cdot \mathbf{B} = 0 \tag{D.25}$$

Inserting (D.24) into the vorticity expression (D.5) and making use of vector/tensor identity[15], gives:

$$\boldsymbol{\Omega} = \nabla \times \mathbf{V} = \nabla \times \left( \nabla \times \mathbf{B} \right) = \nabla \left( \nabla \cdot \mathbf{B} \right) - \nabla^2 \mathbf{B} \tag{D.26}$$

Inserting equation (D.25) into equation (D.26), the vorticity becomes:

$$\boldsymbol{\Omega} = -\nabla^2 \mathbf{B} \tag{D.27}$$

The solution of equation (D.27) obtained using Green's theorem is (e.g. [24, 193]):

$$\mathbf{B} = \frac{1}{4\pi} \iiint_V \frac{\boldsymbol{\Omega}}{\left| \mathbf{R}_0 - \mathbf{R}_1 \right|} dV \tag{D.28}$$

where $\mathbf{B}$ is estimated at point $P$ (see Figure D.4), $\mathbf{R}_0$ is the distance from the origin $O$ to $P$, and $\mathbf{R}_1$ is the distance from the origin to the point of integration of vorticity as seen in Figure D.4. Introducing (D.28) into expression (D.24), the velocity field is obtained as:

---

[15] $\mathbf{F} \times \left( \mathbf{G} \times \mathbf{H} \right) = \left( \mathbf{F} \times \mathbf{H} \right) \mathbf{G} - \left( \mathbf{F} \times \mathbf{G} \right) \mathbf{H}$ is true for any arbitrary vectors $\mathbf{F}$, $\mathbf{G}$, and $\mathbf{H}$

$$\mathbf{V} = \frac{1}{4\pi}\iiint_V \nabla \times \frac{\mathbf{\Omega}}{|\mathbf{R}_0 - \mathbf{R}_1|} dV \tag{D.29}$$

An infinitesimal section of the vorticity filament is shown in Figure D.5. The cross-sectional surface $dS$ is selected in the way that it is normal to the vorticity $\mathbf{\Omega}$, $d\vec{l} = \frac{\mathbf{\Omega}}{|\mathbf{\Omega}|} dl$, $\Gamma = |\mathbf{\Omega}| dS$, and $dV = dSdl$. For a vortex filament the velocity field is:

$$\mathbf{V} = \frac{1}{4\pi}\iiint_V \nabla \times \frac{\mathbf{\Omega}}{|\mathbf{R}_0 - \mathbf{R}_1|} dV = \frac{1}{4\pi}\iiint_V \nabla \times \frac{\mathbf{\Omega}}{|\mathbf{R}_0 - \mathbf{R}_1|} dSdl = \frac{1}{4\pi}\iiint_V \Gamma \frac{\nabla \times d\vec{l}}{|\mathbf{R}_0 - \mathbf{R}_1|}$$

Carrying out the curl operation, the final expression for velocity is:

$$\mathbf{V} = \frac{1}{4\pi}\iiint_V \Gamma \frac{\nabla \times d\vec{l}}{|\mathbf{R}_0 - \mathbf{R}_1|} = \frac{\Gamma}{4\pi}\iiint_V \frac{d\vec{l} \times (\mathbf{R}_0 - \mathbf{R}_1)}{|\mathbf{R}_0 - \mathbf{R}_1|^3} \tag{D.30}$$

The expression (D.30) is called Biot-Savart law.

## D.7 BIOT-SAVART LAW FOR A STRAIGHT VORTEX SEGMENT

Based on Biot-Savart law, the expression for the velocity induced by a straight vortex segment will be obtained. According to Helmholtz second theorem a vortex line cannot begin or end in a fluid and the vortex segment is a section of continuous vortex line. A vortex element $d\vec{l}$ is shown in Figure D.6. The velocity induced by the element $d\vec{l}$ at point $P$ is given by Biot-Savart law and is shown below:

$$\Delta \mathbf{V}_{\varphi} = \frac{\Gamma}{4\pi} \frac{d\vec{l} \times \mathbf{R}}{|\mathbf{R}|^3} \tag{D.31}$$

where $\mathbf{R}$ represents the distance between point $P$ and vortex element $d\vec{l}$. The above expression can be written in the scalar form as:

$$\Delta |\mathbf{V}_{\varphi}| = \frac{\Gamma}{4\pi} \frac{\sin\varphi}{|\mathbf{R}|^2} dl \tag{D.32}$$

From the Figure D.6 we can conclude that:

$$|\mathbf{R}| = \frac{h}{\sin\varphi}, \text{ and } \tan(\pi - \varphi) = -\tan(\varphi) = \frac{h}{l}$$

So

$$dl = -\frac{\partial}{\partial\varphi}\left(\frac{h}{\tan(\varphi)}\right) d\varphi = \frac{h}{\sin^2(\varphi)} d\varphi$$

where $dl$ is the magnitude of $d\vec{l}$. Inserting the above expressions into equation (D.32), the velocity induced by the vortex element $d\vec{l}$ in scalar form is:

$$\Delta |\mathbf{V}_{\varphi}| = \frac{\Gamma}{4\pi} \frac{\sin^3\varphi}{h^2} \frac{h}{\sin^2(\varphi)} d\varphi = \frac{\Gamma}{4\pi h} \sin\varphi d\varphi \tag{D.33}$$

Considering a vortex segment as shown in Figure D.7 the velocity induced by this segment will be the integration of equation (D.33) over the entire segment $(1 \to 2)$:

$$\left|\mathbf{V}_{\varphi_{1,2}}\right| = \frac{\Gamma}{4\pi h}\int_{\varphi_1}^{\varphi_2} \sin\varphi d\varphi = \frac{\Gamma}{4\pi h}\left(\cos\varphi_1 - \cos\varphi_2\right) \tag{D.34a}$$

And in vectorial form [25]:

$$\mathbf{V}_{\varphi_{1,2}} = \frac{\Gamma}{4\pi h}\left(\cos\varphi_1 - \cos\varphi_2\right)\hat{\mathbf{e}} \tag{D.34b}$$

where $\hat{\mathbf{e}}$ is a unit vector pointed in the direction of $\mathbf{V}_{\varphi_{1,2}}$ (see Figure D.7).

The expression (D.34) is called the Biot-Savart law for a straight vortex segment. For computational purpose, equation (D.34) will be modified in the following way [25]. The nomenclature is given in Figure D.7.

$$\vec{l}\times\mathbf{r}_1 = l\left|\mathbf{r}_1\right|\sin\left(\varphi_1\right)\hat{\mathbf{e}} = lh\hat{\mathbf{e}}$$
$$\left|\vec{l}\times\mathbf{r}_1\right| = l\left|\mathbf{r}_1\right|\sin\left(\varphi_1\right) = lh$$
$$h = \left|\mathbf{l}\times\mathbf{r}_1\right|/\left|\mathbf{l}\right|,\ \hat{\mathbf{e}} = \vec{l}\times\mathbf{r}_1/\left|\vec{l}\times\mathbf{r}_1\right|$$
$$\vec{l}\cdot\mathbf{r}_1 = l\left|\mathbf{r}_1\right|\cos\varphi_1 \text{ from where } \cos\varphi_1 = \vec{l}\cdot\mathbf{r}_1/\left(l\left|\mathbf{r}_1\right|\right)$$
$$\vec{l}\cdot\mathbf{r}_2 = l\left|\mathbf{r}_2\right|\cos\varphi_2 \text{ from where } \cos\varphi_2 = \vec{l}\cdot\mathbf{r}_2/\left(l\left|\mathbf{r}_2\right|\right)$$
$$\hat{\mathbf{e}}_1 = \mathbf{r}_1/\left|\mathbf{r}_1\right|,\ \hat{\mathbf{e}}_2 = \mathbf{r}_2/\left|\mathbf{r}_2\right|$$

Introducing the above expressions into equation (D.34b), gives

$$\mathbf{V}_{\varphi_{1,2}} = \frac{\Gamma}{4\pi}\frac{\vec{l}}{\left|\vec{l}\times\mathbf{r}_1\right|}\left(\frac{\vec{l}\cdot\mathbf{r}_1}{l\left|\mathbf{r}_1\right|} - \frac{\vec{l}\cdot\mathbf{r}_2}{l\left|\mathbf{r}_2\right|}\right)\frac{\vec{l}\times\mathbf{r}_1}{\left|\vec{l}\times\mathbf{r}_1\right|}$$

$$= \frac{\Gamma}{4\pi}\frac{\vec{l}\times\mathbf{r}_1}{\left|\vec{l}\times\mathbf{r}_1\right|^2}\left[\vec{l}\cdot\left(\frac{\mathbf{r}_1}{\left|\mathbf{r}_1\right|} - \frac{\mathbf{r}_2}{\left|\mathbf{r}_2\right|}\right)\right] = \frac{\Gamma}{4\pi}\frac{\vec{l}\times\mathbf{r}_1}{\left|\vec{l}\times\mathbf{r}_1\right|^2}\left[\vec{l}\cdot\left(\hat{\mathbf{e}}_1 - \hat{\mathbf{e}}_2\right)\right]$$

$$\mathbf{V}_{\varphi_{1,2}} = \frac{\Gamma}{4\pi} \frac{\vec{l} \times \mathbf{r}_1}{\left|\vec{l} \times \mathbf{r}_1\right|^2} \left[\vec{l} \cdot \left(\hat{\mathbf{e}}_1 - \hat{\mathbf{e}}_2\right)\right] \tag{D.35}$$

## D.8 UNSTEADY VORTEX LATTICE METHOD

The unsteady vortex method used here follows the work of Preidikman [25]. The method is applicable to two-dimensional or three-dimensional flows and it is not limited by platform, camber, twist, or angle of attack. Also the method is valid for incompressible and irrotational flows over the entire flow-field except near the boundaries and in the wakes. The method accounts for aerodynamic nonlinearities associated with the angle of attack, static deformation, vorticity-dominated flow, and unsteady behavior. It is also not limited to small periodic motion. The general unsteady vortex-lattice model imitates the boundary layers and the wakes as vortex sheets [36]. The vortex sheets are of two types, bound-vortex sheet, and free vortex sheet. The bound-vortex sheets create the boundary layer on the surface of the wing while free-vortex sheets represent the wakes. In order to simplify the problem the wing is considered thin. In this case, the vortex sheets on the upper and lower surfaces of the wing merge into a single sheet on the camber surface. Figure D.8 shows the position of an arbitrary point $P$ in the airflow near the wing structure. The airflow is having the undisturbed velocity field $\mathbf{V}_\infty$. The wing structure is moving with velocity $\mathbf{V}_S$, $\mathbf{n}$ represents the vector normal to the lifting surface, the disturbance created by the body is given by the velocity field $\mathbf{V}_D$ which is associated with wakes and boundary layers, and $\mathbf{V}_F$ is the fluid velocity field. Two systems of coordinate are

chosen: B-frame is the coordinate system which moves with the body and N-frame is the inertial coordinate system which is not moving in time. At rest the two coordinate systems coincide. The position vector of a point $P$ in the N-frame is:

$$\mathbf{R} = \mathbf{R}_B + \mathbf{r} \tag{D.36}$$

where $\mathbf{R}_B$ is the position of the origin $O_B$ relative to N-frame and $\mathbf{r}$ is the position of the point $P$ relative to B-frame. Differentiating (D.36) with respect to time, the velocity of a point $P$ in the N-frame is obtained:

$$\mathbf{V}_F = \mathbf{V}_B + {}^N\boldsymbol{\omega}^B \times \mathbf{r} + \mathbf{v} \tag{D.37}$$

where $\mathbf{V}_B = \frac{d\mathbf{R}_B}{dt}$ is the absolute velocity of the origin $O_B$ relative to N-frame, ${}^N\boldsymbol{\omega}^B$ is the angular velocity of the B-frame relative to N-frame, and $\mathbf{v} = \frac{d\mathbf{r}}{dt}$ is the velocity of the point $P$ relative to B-frame.

For incompressible fluid at high Reynolds number, the flow is governed by the Euler's equations:

$$\nabla \cdot \mathbf{V}_F = 0 \tag{D.38a}$$

$$\frac{\partial \mathbf{V}_F}{\partial t} + \left(\mathbf{V}_F \cdot \nabla\right)\mathbf{V}_F = -\frac{1}{\rho}\nabla p \tag{D.38b}$$

where $\rho$ is fluid density, $p$ is the fluid pressure. Equations (D.38) are valid for the region outside to the boundary surfaces, boundary layers and wakes. The boundary conditions for the above equations are[16]:

$$\left(\mathbf{V}_F - \mathbf{V}_S\right)\cdot\mathbf{n} = 0 \tag{D.39a}$$

$$\lim_{|\mathbf{r}|\to\infty} \mathbf{V}_F = 0 \tag{D.39b}$$

The velocity field $\mathbf{V}_F$ is given by the sum of two velocity components:

$$\mathbf{V}_F = \mathbf{V}_\infty + \mathbf{V}_D \tag{D.40}$$

The velocity $\mathbf{V}_D$ is generated by the vorticity in the boundary layers on the structure surface and by the wakes. Outside the boundary layers and wakes, $\mathbf{V}_D$ is irrotational and can be expressed as the gradient of a potential function $\Psi$:

$$\mathbf{V}_D = \nabla\Psi \tag{D.41}$$

Since the flow is incompressible, both $\mathbf{V}_\infty$ and $\mathbf{V}_D$ satisfy the continuity equation (D.38a) which for $\mathbf{V}_D$ will become:

$$\nabla\cdot\mathbf{V}_D = \nabla^2\Psi = 0 \tag{D.42}$$

with the no-penetration boundary condition given by the equation:

---

[16] Equation (D.39a) is called no-penetration condition.

$$\nabla\Psi \cdot \mathbf{n} = \left(\mathbf{V}_S - \mathbf{V}_\infty\right) \cdot \mathbf{n} \tag{D.43}$$

which is valid on the surface. Another boundary condition must be satisfied. This is the infinity condition generated by the equation:

$$\lim_{|\mathbf{r}|\to\infty} \nabla\Psi = 0 \tag{D.44}$$

This condition requires that the flow remains undisturbed at a distance far from the body. The velocity disturbance $\mathbf{V}_D$ is computed with Biot-Savart law in which the distance $|\mathbf{R} - \mathbf{R}_B| = |\mathbf{r}|$ appears in the denominator, so equation (D.44) is satisfied.

The velocity field of the fluid is computed by the equation of continuity (D.43). Once the velocity is calculated, the pressure is obtained from the momentum equation (D.38b) which is integrated to produce Bernoulli's equation. The aerodynamic loads are then obtained by integrating the pressure. Besides the boundary conditions, Kutta condition, which states that the pressure at the wing leading edge must be the same as the pressure at the wing trailing edge, and Kelvin and Helmholtz theorems must be used to determine the wakes.

In the frame of the unsteady vortex-lattice method, the bound-vortex sheets are replaced by lattices of short segments of constant circulation. Each area element in the lattice is enclosed by a loop of vortex segments. The leading segment of the vortex loop is located at the panel's quarter chord line. Because of the approximation of the sheets with lattices, the boundary condition (D.43) is satisfied at a finite number of points named control or collocation points. Also at

control points, velocities and aerodynamic loads are calculated. The control points are located at the lattice center.

An example of lattice of $3\times4$ elements is shown in Figure D.9. The circulation around each segment is unknown. In this example there are 31 unknowns. The size of the problem can be reduced by considering that each element is enclosed by a closed loop of vortex segments with the same circulation. In this way the spatial conservation of circulation is automatically satisfied. The circulations loops are represented by $G_i(t)$, with $i=1...12$, and are represented in Figure D.10. As we can see the number of unknowns is reduced from 31 to 12. The circulation of a segment is then given by the difference of the circulation loops of the two elements that are separated by that segment, for example:

$$\Gamma_{12}=G_5(t)-G_4(t) \text{ or } \Gamma_{11}=G_4(t)$$

The nodes in the lattice are called *aerodynamic nodes* in order to distinguish them from the structural nodes obtained by discretization of the wing structure. The next step is to find the circulations loops $G_i(t)$ in the way that velocity field $\mathbf{V}_F$ satisfies the boundary condition (D.43) at control points.

The wing starts to move with a constant speed through a fluid which would be at rest otherwise. All circulations are set to zero before the wing starts to move. Then at each time step the circulations are calculated. Along the trailing edge and tip of the wing, the vortex segments are convected into the wake at the

local particle velocity in order to satisfy the Kutta condition [25]. No wake exists in the beginning of the motion.

In order to calculate the circulations, a matrix of influence coefficients $A_{i,j}$, for $i, j = 1, 2, ..., NP$ ($NP$ is the total number of elements in the bound lattice), must be developed. The coefficient $A_{i,j}(t)$ is the normal component of the velocity $\mathbf{V}_{D,i}$ at the control point of the $i$-th element generated by the vortex loop of element $j$ (see Figure D.11) and it is a function of time. The normal component of the velocity at the control point of the $i$-th element associated with all bound vortices is given by:

$$\mathbf{V}_{bound,i}(\mathbf{r}_i, t) \cdot \mathbf{n}_i(\mathbf{r}_i, t) = \sum_{j=1}^{NP} A_{i,j}(t) G_j(t) \tag{D.45}$$

where $\mathbf{r}_i$ represents the position vector in the B-frame and $\mathbf{n}(\mathbf{r}_i, t)$ is the normal unit vector at the control point of $i$.

At the initial time $t = 0$, the no-penetration boundary condition (D.43) for the $i$-th element becomes:

$$\sum_{j=1}^{NP} A_{i,j}(0) G_j(0) = \left(\mathbf{V}_S(\mathbf{r}_i, 0) - \mathbf{V}_\infty\right) \cdot \mathbf{n}(\mathbf{r}_i, 0) \tag{D.46}$$

Knowing $A_{i,j}$, $\mathbf{V}_S(\mathbf{r}_i, 0)$, and $\mathbf{V}_\infty$, the circulations $G_j(0)$ can be solved using $LU$ decomposition[17] or Gauss elimination.

At the next time step $t = \Delta t$, the starting vortex has to be convected at the local particle velocity. Along the wing tip and trailing edge the local velocity relative to B-frame is calculated at each aerodynamic node from the expression:

$$\mathbf{v} = \mathbf{V}_F - \mathbf{V}_B \tag{D.47}$$

where $\mathbf{V}_F$ is the absolute velocity of the fluid particle and it is calculated using Biot-Savart law.

In order to obtain the displacements of the aerodynamic nodes in the B-frame, the equation (D.47) is integrated:

$$\Delta\mathbf{r} = \int_0^{\Delta t} \mathbf{v}\,dt \tag{D.48}$$

Referring to the Figure D.12, the vortex segment between the nodes 22 and 23 has the circulation $\Gamma_{14}(t - \Delta t)$ which is the circulation of the vortex segment between the nodes 8 and 12 at the previous time step $t - \Delta t$. In this way the spatial conservation of circulation is satisfied.

The length and direction between the nodes 8 → 22 and 12 →23 is determined by an approximation of equation (D.48):

[17] According to www.wikipedia.com the LU decomposition is a matrix decomposition which writes a matrix as the product of a lower and upper triangular matrix. This decomposition is used in numerical analysis to solve systems of linear equations or find the inverse of a matrix

$$\mathbf{r}_{22} - \mathbf{r}_{8} = \mathbf{v}\left(\mathbf{r}_{8}, t - \Delta t\right) t \tag{D.49a}$$

$$\mathbf{r}_{23} - \mathbf{r}_{12} = \mathbf{v}\left(\mathbf{r}_{12}, t - \Delta t\right) t \tag{D.49b}$$

for $t = \Delta t$ .

Next, the bound circulations of the $i$-th element at the time step $t = \Delta t$ are calculated using the no-penetration condition:

$$\sum_{j=1}^{NP} A_{i,j}\left(\Delta t\right) G_{j}\left(\Delta t\right) = \left(\mathbf{V}_{S}\left(\mathbf{r}_{i}, \Delta t\right) - \mathbf{V}_{W}\left(\mathbf{r}_{i}, \Delta t\right) - \mathbf{V}_{\infty}\right) \cdot \mathbf{n}\left(\mathbf{r}_{i}, \Delta t\right) \tag{D.50}$$

where $\mathbf{V}_{W}\left(\mathbf{r}_{i}, \Delta t\right)$ is the velocity field associated to the vorticity in the wake. The purpose of the vortex lattice method is to find the velocity field $\mathbf{V}_{F}$ needed in the Bernlulli's equation formulated in Chapter 3 to calculate the airflow pressure necessary to compute the aerodynamic loads.

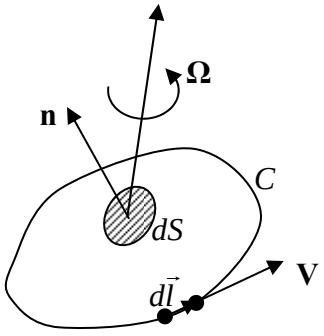


Figure D.1. The relationship between line and surface integrals

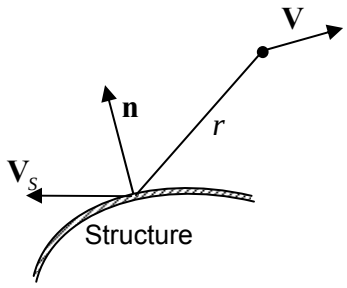


Figure D.2. Fluid-structure boundary

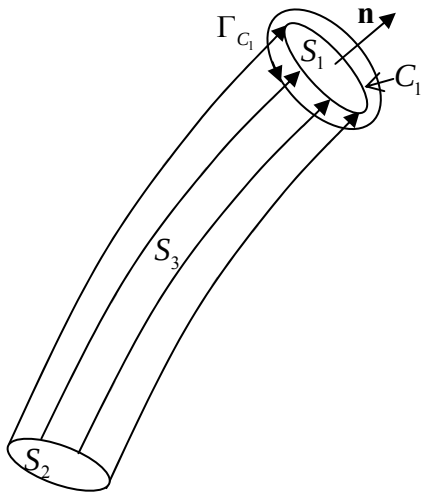


Figure D.3. Vortex tube

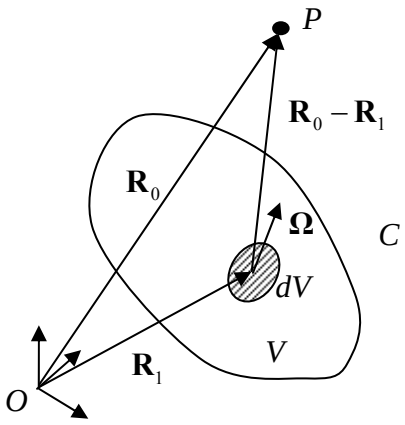


Figure D.4. Velocity estimated at point $P$ due to vorticity distribution

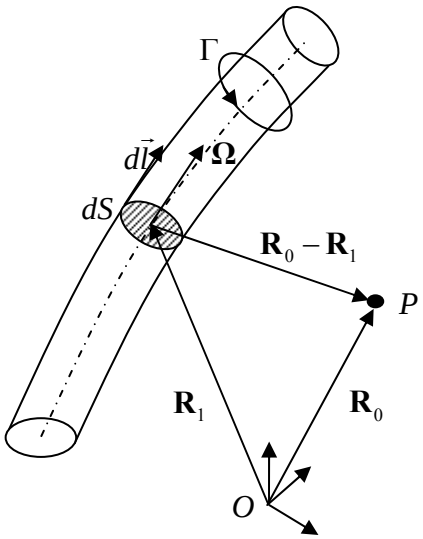


Figure D.5. Velocity estimated at point $P$ due to a vortex filament

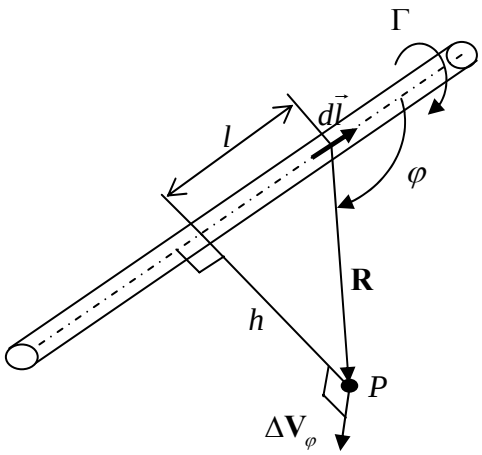


Figure D.6. Velocity induced by a straight vortex element

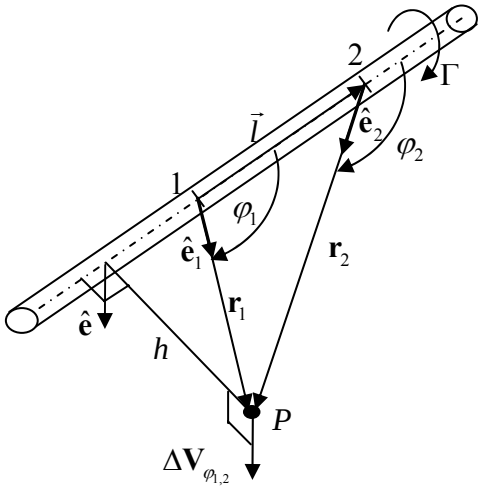


Figure D.7. Velocity induced by a straight vortex segment

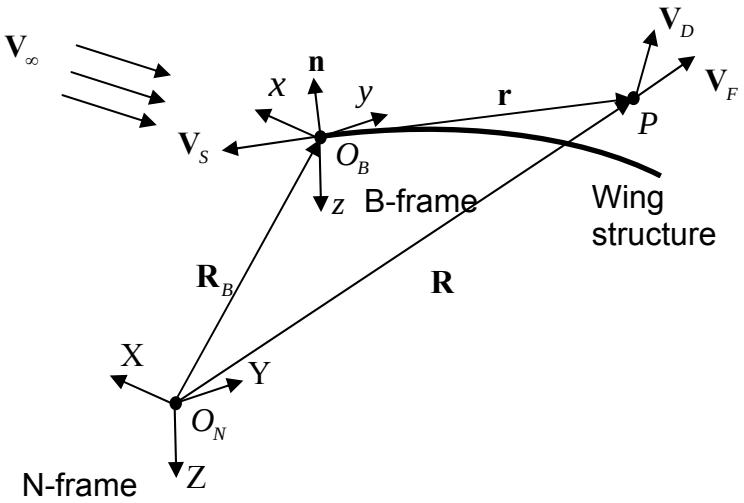


Figure D.8. The position of an arbitrary point $P$ in the airflow

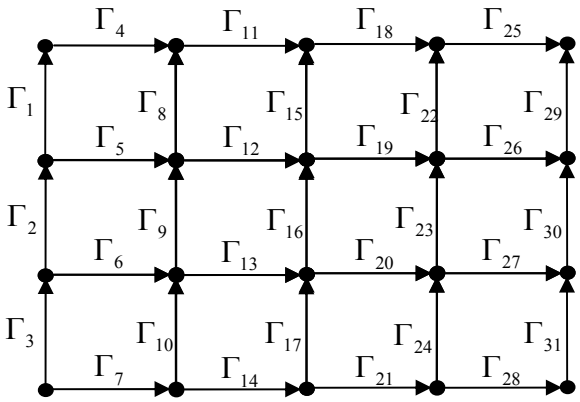


Figure D.9. A $3\times4$ elements lattice

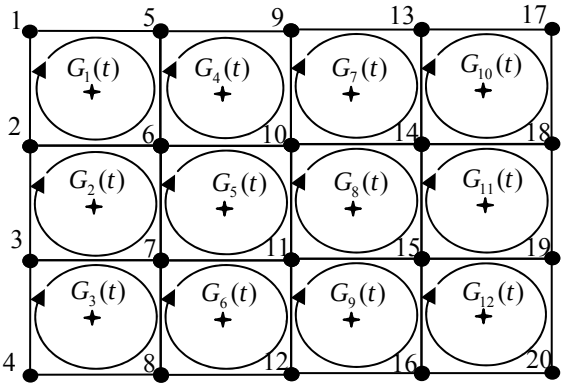


Figure D.10. Vortex loops

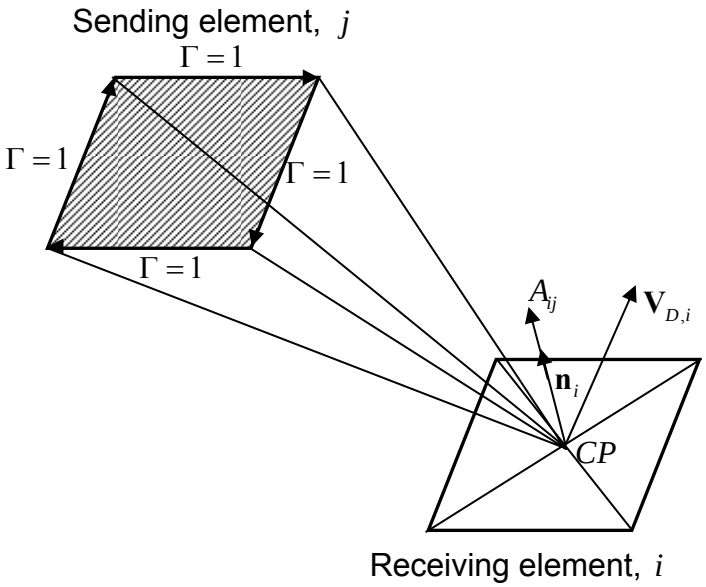


Figure D11. Influence coefficients interpretation

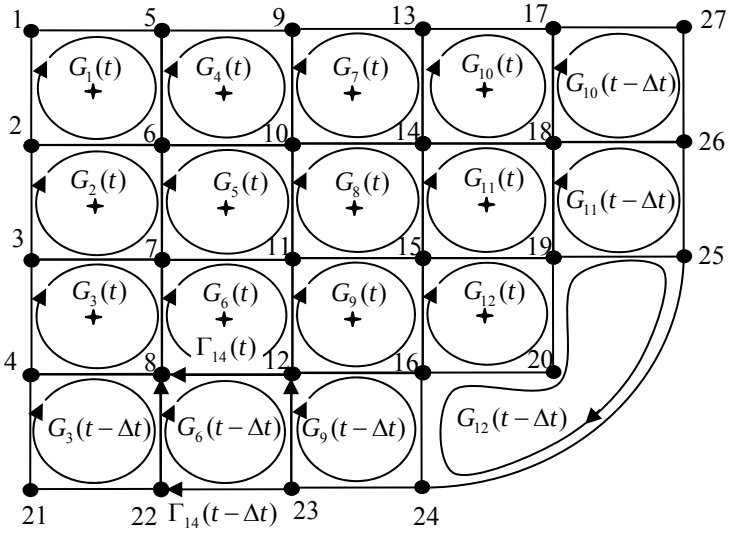


Figure D.12. Vortex loops at time $t = \Delta t$

## APPENDIX E

The detailed structures of $\boldsymbol{Y}_{ij}$

$$\mathbf{Y}_{11}=\begin{bmatrix} Y_3 & 0 & 0 \\ 0 & Y_1 & 0 \\ 0 & 0 & Y_3 \end{bmatrix}, \quad \mathbf{Y}_{12}=\begin{bmatrix} 0 & 0 & -Y_5 \\ 0 & 0 & 0 \\ Y_5 & 0 & 0 \end{bmatrix}, \quad \mathbf{Y}_{13}=\begin{bmatrix} Y_4 & 0 & 0 \\ 0 & Y_2 & 0 \\ 0 & 0 & Y_4 \end{bmatrix}, \quad \mathbf{Y}_{14}=\begin{bmatrix} 0 & 0 & -Y_6 \\ 0 & 0 & 0 \\ Y_6 & 0 & 0 \end{bmatrix},$$

$$\mathbf{Y}_{21}=\begin{bmatrix} 0 & 0 & -Y_3' \\ 0 & 0 & 0 \\ Y_3' & 0 & 0 \end{bmatrix}, \quad \mathbf{Y}_{22}=\begin{bmatrix} Y_5' & 0 & 0 \\ 0 & Y_1 & 0 \\ 0 & 0 & Y_5' \end{bmatrix}, \quad \mathbf{Y}_{23}=\begin{bmatrix} 0 & 0 & -Y_4' \\ 0 & 0 & 0 \\ Y_4' & 0 & 0 \end{bmatrix}, \quad \mathbf{Y}_{24}=\begin{bmatrix} Y_6' & 0 & 0 \\ 0 & Y_2 & 0 \\ 0 & 0 & Y_6' \end{bmatrix}$$

$Y_i$ are the finite element shape functions given by equations (3.18), and a prime denotes a derivative with respect to $y$.

The matrices $\mathbf{G}_{AS}$, $\mathbf{F}_A$, and $\mathbf{F}_S$ of equation (3.35)

$$\mathbf{G}_{AS}=\begin{bmatrix}
\mathbf{G}_{1,1} & \mathbf{G}_{1,2} & \mathbf{0} & \mathbf{0} & \mathbf{0} & \mathbf{0} & \mathbf{0} & \mathbf{0} \\
\mathbf{0} & \mathbf{G}_{2,2} & \mathbf{G}_{2,3} & \mathbf{0} & \mathbf{0} & \mathbf{0} & \mathbf{0} & \mathbf{0} \\
\mathbf{0} & \mathbf{0} & \mathbf{G}_{3,3} & \mathbf{G}_{3,4} & \mathbf{0} & \mathbf{0} & \mathbf{0} & \mathbf{0} \\
\mathbf{0} & \mathbf{0} & \mathbf{0} & \mathbf{G}_{4,4} & \mathbf{G}_{4,5} & \mathbf{0} & \mathbf{0} & \mathbf{0} \\
\mathbf{0} & \mathbf{0} & \mathbf{0} & \mathbf{0} & \mathbf{0} & \mathbf{G}_{5,6} & \mathbf{G}_{5,7} & \mathbf{0} \\
\mathbf{0} & \mathbf{0} & \mathbf{0} & \mathbf{0} & \mathbf{0} & \mathbf{0} & \mathbf{G}_{6,7} & \mathbf{G}_{6,8} \\
\mathbf{0} & \mathbf{G}_{7,2} & \mathbf{G}_{7,3} & \mathbf{0} & \mathbf{0} & \mathbf{0} & \mathbf{0} & \mathbf{0} \\
\mathbf{0} & \mathbf{0} & \mathbf{G}_{8,3} & \mathbf{G}_{8,4} & \mathbf{0} & \mathbf{0} & \mathbf{0} & \mathbf{0} \\
\mathbf{0} & \mathbf{0} & \mathbf{0} & \mathbf{G}_{9,4} & \mathbf{G}_{9,5} & \mathbf{0} & \mathbf{0} & \mathbf{0} \\
\mathbf{0} & \mathbf{0} & \mathbf{0} & \mathbf{0} & \mathbf{G}_{10,5} & \mathbf{G}_{10,6} & \mathbf{0} & \mathbf{0} \\
\mathbf{0} & \mathbf{0} & \mathbf{0} & \mathbf{0} & \mathbf{0} & \mathbf{0} & \mathbf{G}_{11,7} & \mathbf{G}_{11,8} \\
\mathbf{0} & \mathbf{0} & \mathbf{0} & \mathbf{0} & \mathbf{0} & \mathbf{0} & \mathbf{0} & \mathbf{G}_{12,8} \\
\mathbf{0} & \mathbf{G}_{13,2} & \mathbf{G}_{13,3} & \mathbf{0} & \mathbf{0} & \mathbf{0} & \mathbf{0} & \mathbf{0} \\
\mathbf{0} & \mathbf{0} & \mathbf{G}_{14,3} & \mathbf{G}_{14,4} & \mathbf{0} & \mathbf{0} & \mathbf{0} & \mathbf{0} \\
\mathbf{0} & \mathbf{0} & \mathbf{0} & \mathbf{G}_{15,4} & \mathbf{G}_{15,5} & \mathbf{0} & \mathbf{0} & \mathbf{0} \\
\mathbf{0} & \mathbf{0} & \mathbf{0} & \mathbf{0} & \mathbf{0} & \mathbf{G}_{16,6} & \mathbf{G}_{16,7} & \mathbf{0} \\
\mathbf{0} & \mathbf{0} & \mathbf{0} & \mathbf{0} & \mathbf{0} & \mathbf{0} & \mathbf{G}_{17,7} & \mathbf{G}_{17,8} \\
\mathbf{0} & \mathbf{0} & \mathbf{0} & \mathbf{0} & \mathbf{0} & \mathbf{0} & \mathbf{0} & \mathbf{G}_{18,8}
\end{bmatrix}, \quad \mathbf{F}_S=\begin{Bmatrix} \mathbf{F}_{S_1} \\ \mathbf{F}_{S_2} \\ \vdots \\ \mathbf{F}_{S_8} \end{Bmatrix}, \quad \mathbf{F}_A=\begin{Bmatrix} \mathbf{F}_{A_1} \\ \mathbf{F}_{A_2} \\ \vdots \\ \mathbf{F}_{A_{18}} \end{Bmatrix}$$

References

1 Ashley, H., 'Some observations on four current subjects related to aeroelastic stability,' *Israel Journal of Technology*, 1978, **16**, 3-22.

2 Wagner, H., 'Uber die entstehung des dynamischen auftriebes von tragflugeln,' *Zeitschrift fur angewandte Mathematik und Mechanik*, 1925, **5**(1).

3 Bisplinghoff, R.L. and Ashley, H., *Principles of aeroelasticity*, John Wiley and Sons, Inc., New York, 1962.

4 Fung, Y.C., *An introduction to the theory of aeroelasticity*, Dover, New York, 1969.

5 Yates, E.C., Jr., *Calculation of flutter characteristics for finite span swept or unswept wings at subsonic and supersonic speeds by a modified strip analysis*, NACA RM L47L10, 1958.

6 Garrick, I.E. and Rabinow, S.I., *Flutter and oscillating air force calculations for an airfoil in a two-dimensional supersonic flow*, NACA Rept No. 846, 1946.

7 Watkins, C.E., Woolston, D.S. and Cunningham, H.J., *A systematic kernel function procedure for determining aerodynamic forces on oscillating or steady finite wings at subsonic speeds*, NASA TR R-48, 1959.

8 Lesing, H.C., Troutman, J.L. and Menees, G.P., *Experimental determination of the pressure distribution on a rectangular wing oscillating in the first bending mode for mach numbers from 0.24 to 1.3*, NASA TN D-344, 1960.

9 Theodorsen, T., *General theory of aerodynamic instability and mechanism of flutter*, NACA Rept No. 496, 1935.

10 Theodorsen, T. and Garrick, I.E., *Mechanics of flutter: A theoretical and experimental investigation of flutter problem*, NACA Rept. No. 685, 1940.

11 Jones, R.T., *The unsteady lift of a wing of finite aspect ratio*, NACA Report 681, 1940.

12 Hess, J.L., 'Review of integral-equation techniques for solving potential-flow problems with emphasis on the surface-surface method,' *Computer Methods in Applied Mechanics and Engineering*, 1975, **5**(2), 145-196.

13 Hess, J.L., 'Analytic solutions for potential flow over a class of semi-infinite two-dimensional bodies having circular-arc noses,' *Journal of Fluid Mechanics*, 1973, **60**, 225-239.

14 Latta, G.E. and Hess, G.B., 'Potential flow past a sphere tangent to a plane,' *Physics of Fluids*, 1973, **16**(7), 974-976.

15 Hess, J.L., 'The problem of three-dimensional lifting potential flow and its solution by means of surface singularity distribution,' *Computer Methods in Applied Mechanics and Engineering*, 1974, **4**(3), 283-219.

16 Hess, J.L., 'Improved solution for potential flow about arbitrary axisymmetric bodies by the use of a higher-order surface source method,' *Computer Methods in Applied Mechanics and Engineering*, 1975, **5**(3), 297-308.

17 Hess, J.L., 'Review of integral-equation techniques for solving potential-flow problems with emphasis on the surface-source method,' *Computer Methods in Applied Mechanics and Engineering*, 1975, **5**(2), 145-196.

18 Hess, J.L., 'The use of higher-order surface singularity distributions to obtain improved potential flow solutions for two-dimensional lifting airfoils,' *Computer Methods in Applied Mechanics and Engineering*, 1975, **5**(1), 11-35.

19 Hess, J.L., 'Higher order panel method for three-dimensional potential flow,' pp. 517-520, Inst of Eng, Aust, Barton, Brisbane, Aust, 1980.

20 Hess, J.L., 'Use of higher-order surface singularity distributions to obtain improved potential flow solutions for two-dimensional lifting airfoils,' *Computer Methods in Applied Mechanics and Engineering*, 1975, **5**(1), 11-35.

21 Hess, J.L. and Smith, A.M.O., 'Calculation of nonlifting potential flow about arbitrary three-dimensional bodies,' *Journal of Ship Research*, 1964, **8**(2), 22-44.

22 Bauer, A.B., Smith, A.M.O. and Hess, J.L., 'Potential flow and boundary layer theory as design tools in aerodynamics,' 1970, **16**(2), 53-69.

23 Bertin, J.J. and Smith, M.L., *Aerodynamics for engineers*, Prentice Hall, New Jersey, 1989.

24 Katz, J. and Plotkin, A., *Low speed aerodynamics*, Cambridge University Press, New York, 2001.

25 Preidikman, S., 'Numerical simulations of interactions among aerodynamics, structural dynamics, and control systems.' *Engineering Mechanics*, Virginia Polytechnic Institute and State University, Blacksburg, 1998.

26 Mook, D.T. and Maddox, S.A., 'Extension of a vortex-lattice method to include the effects of leading-edge separation,' *Journal of Aircraft*, 1974, **11**(2), 127-128.

27 Kandil, O.A., Mook, D.T. and Nayfeh, A.H., 'Nonlinear prediction of aerodynamic loads on lifting surfaces,' 1976, **13**(1), 22-28.

28 Asfar, K.R., Mook, D.T. and Nayfeh, A.H., 'Application of the vortex-lattice technique to arbitrary bodies,' 1979, **16**(7), 421-424.

29 Konstadinopoulos, P., Thrasher, D.F., Nayfeh, A.H., Watson, L. and Mook, D.T., 'A vortex-lattice method for general, unsteady aerodynamics,' *Journal of Aircraft*, 1985, **22**(1), 43-49.

30 Elzebda, J., Mook, D.T. and Nayfeh, A.H., 'Steady and unsteady aerodynamic interference in closely coupled canard/wing configurations,' pp. 37-44, ASME, New York, NY, USA, Cincinnati, OH, Engl, 1987.

31 Strganac, T. and Mook, D.T., 'A new method to predict unsteady aeroelastic behavior.' *AIAA/ASME/ASCE/AHS 27th Structures, Structural*

*Dynamics, and Materials Conference*, AIAA Paper No 86-0867-CP, San-Antonio, TX, 1987.

32 Strganac, T. and Mook, D.T., 'The numerical simulation of subsonic flutter.' *AIAA 19th Fluid Dynamics, Plasma Dynamics and Laser Conference*, AIAA Paper No. 87-1428, Honolulu, Hawaii, 1987.

33 Strganac, T.W. and Mook, D.T., 'Application of the unsteady vortex-lattice method to the nonlinear two-degree-of-freedom aeroelastic equations,' pp. 201-210, AIAA (CP864), New York, NY, USA, San Antonio, TX, USA, 1986.

34 Strganac, T.W. and Mook, D.T., 'Numerical model of unsteady subsonic aeroelastic behavior,' *AIAA Journal*, 1990, **28**(5), 903-909.

35 Nuhait, A.O. and Mook, D.T., 'Numerical simulation of wings in steady and unsteady ground effects,' *Journal of Aircraft*, 1989, **26**(12), 1081-1089.

36 Preidikman, S. and Mook, D., 'Time-domain simulations of linear and nonlinear aeroelastic behavior,' *Journal of Vibration and Control*, 2000, **6**, 1135-1175.

37 Luton, J.A. and Mook, D.T., 'Numerical simulations of flutter and its supression by active control ' *AIAA Journal*, 1993, **31**(12), 2312-2319.

38 Hall, B.D., 'Numerical simulations of the aeroelastic response of an actively controlled flexible wing.' *Engineering Mechanics*, Virginia Polytechnic Institute and State University, Blacksburg, 1999.

39 Soviero, P.A.O. and Bortolus, M.V., 'Generalized vortex lattice method for oscillating lifting surfaces in subsonic flow,' *AIAA Journal*, 1992, **30**(11), 2723-2729.

40 Soviero, P.A.O., 'Generalized vortex lattice method for oscillating thin airfoil in subsonic flow,' *AIAA Journal*, 1993, **31**(12), 2380-2382.

41 Kalman, T.P., Rodden, W.P. and Giesing, J.P., 'Application of the doublet-lattice method to nonplanar configurations in subsonic flow,' 1971, **8**(6), 406-413.

42 Yurkovich, R., 'Status of unsteady aerodynamic prediction for flutter of high-performance aircraft,' *Journal of Aircraft*, 2003, **40**(5), 832-842.

43 Albano, E. and Rodden, W.P., 'Doublet-lattice method for calculating lift distributions on oscillating surfaces in subsonic flows,' *AIAA Journal*, 1969, **7**(2), 279-285.

44 Rodden, W.P., Taylor, P.F. and McIntosh, S.C., Jr., 'Further refinement of the subsonic doublet-lattice method,' *Journal of Aircraft*, 1998, **35**(5), 720-727.

45 Eversman, W. and Pitt, D.M., 'Hybrid doublet lattice/doublet point method for lifting surfaces in subsonic flow,' *Journal of Aircraft*, 1991, **28**(9), 577-578.

46 Ando, S. and Ichikawa, A., 'Quasi-doublet-lattice method for oscillating thin airfoils in subsonic flow,' *Transactions of the Japan Society for Aeronautical and Space Sciences*, 1983, **26**(73), 163-173.

47 van Zyl, L.H., 'Application of the subsonic doublet lattice method to delta wings,' *Journal of Aircraft*, 1999, **36**(3), 609-611.

48 Edwards, J.W. and Wieseman, C.D., 'Flutter and divergence analysis using the generalized aeroelastic analysis method,' pp. 788-802, American Inst. Aeronautics and Astronautics Inc., Norfolk, VA, United States, 2003.

49 Lee, B.H.K., Price, S.J. and Wong, Y.S., 'Nonlinear aeroelastic analysis of airfoils: Bifurcation and chaos,' *Progress in Aerospace Sciences*, 1999b, **35**, 205-334.

50 Ashley, H., 'On the role of shock waves in the "Sub-transonic" Flutter phenomenon.' *AIAA 79-0765, AIAA/ASME/ASCE/AHS 20th Structures, Structural Dynamics, and Material Conf*, St. Louis, 1979.

51 Barnard, R.H. and Philpott, D.R., *Aircraft flight: A description of the physical principles of aircraft flight*, Longman Scientific & Technical, Singapore, 1995.

52 Gilliatt, H.C., Strganac, T.W. and Kurdila, A.J., 'An investigation of internal resonance in aeroelastic systems,' *Nonlinear Dynamics*, 2003, **31**, 1-22.

53 Abdel-Rahim, A., Sisto, F. and Thangam, S., 'Computational study of stall flutter in linear cascades,' *Journal of Turbomachinery*, 1993, **115**(1), 157-166.

54 Hwang, C.J. and Fang, J.M., 'Transonic stall/choke flutter analysis of cascades by a navier-stokes solution-adaptive approach,' p. 9, ASME, New York, NY, USA, Burmingham, UK, 1996.

55 Dunn, P. and Dugundji, J., 'Nonlinear stall flutter and divergence analysis of cantilevered graphite/epoxy wings,' *AIAA Journal*, 1992, **30**(1), 153-162.

56 Liu, X.-N. and Xiang, J.-W., 'Stall flutter analysis of high-aspect-ratio composite wing,' *Chinese Journal of Aeronautics*, 2006, **19**(1), 36-43.

57 Sisto, F., Thangam, S. and Chen, T., 'Analysis and prediction of stall flutter in spanwise finite airfoil cascades,' pp. 93-108, Publ by ASME, New York, NY, USA, Anaheim, CA, USA, 1992.

58 Sarkar, S. and Bijl, H., 'Stall induced vibration and flutter in a symmetric airfoil,' American Society of Mechanical Engineers, New York, NY 10016-5990, United States, Vancouver, BC, Canada, 2006.

59 Whiting, R.J., Delamore-Sutcliffe, D.W. and Greenwell, D., 'Experimental and numerical study of gust loads on stall flutter initiation,' pp. 1225-1232, American Institute of Aeronautics and Astronautics Inc., Reston, VA 20191, United States, Toronto, ON, Canada, 2005.

60 Delamore-Sutcliffe, D.W., Whiting, R.J. and Greenwell, D., 'Experimental and numerical study of stall flutter,' pp. 1215-1224, American Institute of Aeronautics and Astronautics Inc., Reston, VA 20191, United States, Toronto, ON, Canada, 2005.

61 Yamasaki, M., Isogai, K., Uchida, T. and Yukimura, I., 'Shock-stall flutter of a two-dimensional airfoil,' *AIAA Journal*, 2004, **42**(2), 215-219.

62 Thomas, J.P., Dowell, E.H. and Hall, K.C., 'Nonlinear inviscid aerodynamic effects on transonic divergence, flutter, and limit-cycle oscillations,' *AIAA Journal*, 2002, **40**(4), 638 - 646.

63 Yang, S. and Lee, I., 'Aeroelastic analysis for flap of airfoil in transonic flow,' *Computers and Structures*, 1996, **61**(3), 421 430.

64 Breitbach, E.J., *Effect of structural nonlinearities on aircraft vibration*, Advisory Group for Aerospace Research and Development of NATO, AGARD Report No. 665, 1977.

65 De Ferrari, G., Chesta, L., Sensburg, O. and Lotze, A., *Effects of nonlinearity of wing-store flutter*, Advisory Group for Aerospace Research and Development of NATO, AGARD Report No. 687, 1980.

66 Peloubet, R.P., Jr., Haller, R.L. and M., B.R., 'F-16 flutter suppression system investigation.' *Proc of the AIAA/ASME/ASCE/AHS 21st Structures, Structural Dynamics & Materials Conference*, pp. 620-634, Seattle, Washington, 1980.

67 Reed, W.H.I., Foughner, J.T., Jr. and Runyan, H.L., 'Decoupler pylon: A simple effective wing/store suppressor,' *Journal of Aircraft*, 1980, **17**(3), 206-211.

68 Desmarais, R.N. and Reed, W.H.I., 'Wing/store flutter with nonlinear pylon stiffness,' *Journal of Aircraft*, 1981, **19**(11), 984-987.

69 Alighanbari, H., 'Aeroelastic response of an airfoil-aileron combination with freeplay in aileron hinge,' *Journal of Aircraft*, 2002, **39**(4), 711 - 713.

70 Kim, S.H. and Lee, I., 'Aeroelastic analysis of a flexible airfoil with a free-play non-linearity,' *Journal of Sound and Vibration*, 1996, **193**(4), 823-846.

71 Laurenson, R.M. and Trn, R.M., 'Flutter analysis of missile control surfaces containing structural nonlinearities,' *AIAA Journal*, 1980, **18**(10), 1245-1251.

72 Woolston, D.S., Runyan, H.W. and Andrews, R.E., 'An investigation of effects of certain type of structural nonlinearities on wing and control surface flutter,' *Journal of Aeronautical Sciences*, 1957, **24**, 57-63.

73 Yang, Z.C. and Zhao, L.C., 'Analysis of limit cycle flutter of an airfoil in incompressible flow,' *Journal of Sound and Vibration*, 1988, **123**(1), 1-13.

74 Bae, J.S. and Lee, I., 'Limit cycle oscillation of mistle control fin with structural non-linearity,' *Journal of Sound and Vibration*, 2004, **269**, 669-687.

75 Bae, J.S., Yang, S.M. and Lee, I., 'Linear and nonlinear aeroelastic analysis of fighter-type wing with control surface,' *Journal of Aircraft*, 2002, **39**, 697-708.

76 Bae, J.S., Inman, D.J. and Lee, I., 'Effects of structural nonlinearity on subsonic aeroelastic characteristics of an aitcraft wing with control surface,' *Journal of Fluids and Structures*, 2004, **19**, 747-763.

77 Bae, J.S., Kim, D.K., Shin, W.H., Lee, I. and Kim, S.H., 'Nonlinear aeroelastic analysis of deployable missile control fin,' *Journal of Spacecraft and Rockets*, 2004, **41**(2), 264-271.

78 Ueda, T. and Dowell, E.H., 'A new solution method for lifting surfaces in subsonic flow,' *AIAA Journal*, 1982, **20**, 348-355.

79 Zhao, Y.H. and Hu, H.Y., 'Aeroelastic analysis of a nonlinear airfoil based on unsteady vortex lattice model,' *Journal of Sound and Vibration*, 2004, **276**, 491-510.

80 Lee, B.H.K., Jiang, L.Y. and Wong, Y.S., 'Flutter of an airfoil with a cubic restoring force,' *Journal of Fluids and Structures*, 1999a, **13**, 75-101.

81 Lee, B.H.K., Liu, L. and Chung, K.W., 'Airfoil motion in subsonic flow with strong cubic nonlinear restoring forces,' *Journal of Sound and Vibration*, 2005, **281**, 699-717.

82 Liu, L., Wong, Y.S. and Lee, B.H.K., 'Application of the centre manifold theory in non-linear aeroelasticity,' *Journal of Sound and Vibration*, 2000, **234**(4), 641-659.

83 Liu, L. and Dowell, E.H., 'The secondary bifurcation of an aeroelastic airfoil motion: Effects of high harmonics,' *Nonlinear Dynamics*, 2004, **37**, 31-49.

84 Zhao, L.C. and Yang, Z.C., 'Chaotic motions of an airfoil with non-linear stiffness in incompressible flow,' *Journal of Sound and Vibration*, 1990, **138**(2), 245-254.

85 Price, S.J., Alighanbari, H. and Lee, B.H.K., 'The aeroelastic response of a two-dimensional airfoil with bilinear and cubic structural nonlinearities,' *Journal of Fluids and Structures*, 1995, **9**, 175-193.

86 Singh, S.N. and Brenner, M., 'Limit cycle oscillation and orbital stability in aeroelastic systems with torsional nonlinearity,' *Nonlinear Dynamics*, 2003, **31**, 435-450.

87 Dessi, D. and Mastroddi, F., 'Limit-cycle stability reversal via singular perturbation and wing-flap flutter,' *Journal of Fluids and Structures*, 2004, **19**, 765-783.

88 Coller, B.D. and Chamara, P.A., 'Structural non-linearities and the nature of the classic flutter instability,' *Journal of Sound and Vibration*, 2004, **277**, 711-739.

89 Shahrzad, P. and Mahzoon, M., 'Limit cycle flutter of airfoils in steady and unsteady airfoils,' *Journal of Sound and Vibration*, 2002, **256**(2), 213 - 225.

90 Marzocca, P., Librescu, L. and Silva, W., 'Aeroelastic response of nonlinear wing sections using a functional series technique,' *AIAA Journal*, 2002, **40**(5), 813-824.

91 Tang, D.M. and Dowell, E.H., 'Effects of geometric structural nonlinearity on flutter and limit cycle oscillations of high-aspect-ratio wings,' *Journal of Fluids and Structures*, 2004, **19**, 291-306.

92 Sheta, F.E. and Harrand, V.J., 'Computational and experimental investigation of limit cycle oscillations of nonlinear aeroelastic systems,' *Journal of Aircraft*, 2002, **39**(1), 133 - 141.

93 Patil, M.J., Hodges, D.H. and Cesnik, C.E.S., 'Limit-cycle oscillations in high-aspect-ratio wings,' *Journal of Fluids and Structures*, 2001, **15**, 107 - 132.

94 Ghanem, G.G. and Spanos, P.D., *Stochastic finite elements: A spectral aproach*, Springer-Verlag New York, 1991.

95 Lin, Y.K., *Probabilistic theory of structural dynamics*, McGraw-Hill, New York, 1967.

96 Lin, Y.K., Kozin, F., Wen, Y.K., Casciati, F., Schueller, G.I., Der Kiureghian, A., Ditlevsen, O. and Vanmarcke, E.H., 'Methods of stochastic structural dynamics,' *Structural Safety*, 1986, **3**, 167-194.

97 Yang, T.Y. and Kapania, R.K., 'Finite element random response analysis of cooling tower,' *Journal of Engineering Mechanics, ASCE*, 1984, **110**(EM4), 589-609.

98 Shinozuka, M. and Astill, C.J., 'Random eigenvalue problems in structural analysis,' *AIAA Journal*, 1972, **10**(4), 456-462.

99 Shinozuka, M. and Lenoe, E., 'Probabilistic model for spatial distribution of material properties,' *Engineering Fracture Mechanics*, 1976, **8**(1), 217-227.

100 Shinozuka, M., 'Structural response variability,' *Journal of Engineering Mechanics*, 1987, **113**(6), 825-842.

101 Polhemus, N.W. and Cakmak, A.S., 'Simulation of earthquake ground motions using autoregressive moving average (arma) models,' *Earthquake Engineering & Structural Dynamics*, 1981, **9**(4), 343-354.

102 Spanos, P.D. and Mignolet, M.P., 'Z-transform modeling of p-m wave spectrum,' *Journal of Engineering Mechanics*, 1986, **112**(8), 745-759.

103 Cambou, B., 'Application of first-order uncertainty analysis in the finite element method in linear elasticity.' *Proceedings of the 2nd International Conference on Application of Statistics and Probability in Soil and Structural Engineering*, pp. 67-87, Aachen, West Germany, 1975.

104 Nakagiri, S. and Hisada, T., 'Stochastic finite element method applied to structural analysis with uncertain parameters.' *Proc. Intl. Conference on FEM*, pp. 206-211, 1982.

105 Shinozuka, M. and Yamazaki, F., Stochastic finite element analysis: An introduction, In Ariaratnam, S.T., Schueller, G.I. and Elishakoff, I., eds. *Stochastic structural dynamics: Progress in theory and applications* (Elsevier Applied Science, London 1988).

106 Liu, W.K., Belytschko, T. and Mani, A., 'Probabilistic finite elements for nonlinear structural dynamics,' *Computer Methods in Applied Mechanics and Engineering*, 1986, **56**(1), 61-81.

107 Kleiber, M., Tran, D.H. and Hien, T.D., *The stochastic finite element method*, Chichester: John Wiley, 1992.

108 Yamazaki, F., Shinozuka, M. and Dasgupta, G., 'Neumann expansion for stochastic finite element analysis,' *Journal of Engineering Mechanics*, 1988, **114**(8), 1335-1354.

109 Shinozuka, M. and Nomoto, T., *Response variability due to spatial randomness of material properties*, Technical Report, Dept. of Civil Engineering, Columbia University, New York, 1980.

110 Adomian, G. and Malakian, K., 'Inversion of stochastic partial diferential operators -the linear case,' *J. Math. Anal. Appl.*, 1980, **77**, 309-327.

111 Loeve, M., *Probability theory*, Springer-Verlag, Berlin, 1977.

112 Nayfeh, A.H. and Mook, D., *Nonlinear oscillations*, Wiley Interscience, New York, 1979.

113 Nieuwenhof, B.V.d. and Coyette, J.-P., 'A perturbation stochastic finite element method for the time-harmonic analysis of structures with random mechanical properties.' *Fifth World Congress on Computational Mechanics*, Vienna, Austria, 2002.

114 Mikhlin, S.G., *Integral equations*, Pergamon Press, Oxford, 1957.

115 Fredholm, I., 'Sur une class d'equations fonctionnelles,' *Acta Mathematica*, 1903, **27**, 365-390.

116 Nashed, Z., Editor, *Generalized inverses and aplications, proceedings of an advanced seminar*, The University of Wisconsin-Madison, Academic Press, New York, 1976.

117 Bharrucha-Reid, A.T., 'On random operator equations in banach space,' *Bull. Acad. Polon. Sci., Ser. Sci. Math. Astr. Phys.*, 1959, **7**, 561-564.

118 Adomian, G., *Stochastic systems*, Academic Press, New York, 1983.

119 Yamazaki, F., Shinozuka, M. and Dasgupta, G., *Neumann expansion for stochastic finite element analysis*, Technical Report, Department of Civil Engineering, Columbia University, New York, 1985.

120 Ibrahim, R.A., 'Structural dynamics with parameter uncertainties,' *Appl Mech Rev*, 1987, **40**(3), 309-328.

121 Manohar, C.S. and Ibrahim, R.A., 'Progress in structural dynamics with stochastic parameter variations: 1987–1998,' *Trans. ASME Appl. Mech. Rev.*, 1999, **52**(5), 177–196.

122 Kapur, J.N. and Kesavan, H.K., *Entropy optimization principles with applications*, Academic Press, San Diego, 1992.

123 Soize, C., 'A non-parametric model of random uncertainties for reduced matrix models in structural dynamics,' *Probabilistic Engineering Mechanics*, 2000, **15**(3), 277-294.

124 Soize, C., 'Nonlinear dynamical systems with non-parametric model of random uncertainties,' *Uncertainties in Engineering Mechanics*, 2001, **1**(1), 1-38.

125 Soize, C., 'Maximum entropy approach for modeling random uncertainties in transient elastodynamics,' *Journal of the Acoustical Society of America*, 2001, **109**(5), 1979-1996.

126 Soize, C., 'Transient responses of dynamical systems with random uncertainties,' *Probabilistic Engineering Mechanics*, 2001, **16**(4), 363-372.

127 Soize, C., 'Random matrix theory and non-parametric model of random uncertainties in vibration analysis,' *Journal of Sound and Vibration*, 2002, **263**(3), 893-916.

128 Ibrahim, R.A. and Pettit, C.L., 'Uncertainties and dynamic problems of bolted joints and other fasteners,' *Journal of Sound and Vibration*, 2004, **279**, 857-936.

129 Jensen, H.A., 'Dynamic response of structures with uncertain parameters,' California Institute of Technology, Pasadena, California, 1990.

130 Lei, Z. and Chen, Q., 'Neumann dynamic stochastic finite element method of vibration for structures with stochastic parameters to random excitation,' *Computers and Structures*, 2000, **77**, 651 - 657.

131 Oh, D.H. and Librescu, L., 'Free vibration and reliability of composite cantilevers featuring uncertain properties,' *Reliability Engineering and System Safety*, 1997, **56**, 265 - 272.

132 Klosner, J.M., Haber, S.F. and Voltz, P., 'Response of nonlinear systems with parameter uncertainties,' *International Journal of Nonlinear Mechanics*, 1992, **27**(4), 647-653.

133 Liaw, D.G. and Yang, H.T.Y., 'Reliability of uncertain laminated shells due to buckling and supersonic flutter,' *AIAA Journal*, 1991, **29**(10), 1698 - 1708.

134 Liaw, D.G. and Yang, H.T.Y., 'Reliability of initially compressed uncertain laminated plates in supersonic flow,' *AIAA Journal*, 1991, **29**(6), 952 - 960.

135 Kuttenkeuler, J. and Ringertz, U., 'Aeroelastic tailoring considering uncertainties in material properties,' *Structural Optimization*, 1998, **15**, 157 - 162.

136 Lindsley, N.J., Beran, P.S. and Pettit, C.L., 'Effects of uncertainty on the aerothermoelastic flutter boundary of a nonlinear plate,' *AIAA Paper 2002-5136*, 2002.

137 Lindsley, N.J., Beran, P.S. and Pettit, C.L., 'Effects of uncertainty on nonlinear plate aeroelastic response,' *AIAA Paper 2002-1271*, 2002.

138 Pettit, C.L. and Beran, P.S., 'Effects of parametric uncertainty on airfoil limit cycle oscillation,' *Journal of Aircraft*, 2003, **40**(5), 1004-1006.

139 Pettit, C.L. and Beran, P.S., 'Polynomial chaos expansion applied to airfoil limit cycle oscillations.' *AIAA 2004-1691*, pp. 1975-1985, Palm Springs, CA, 2004.

140 Ueda, T., 'Aeroelastic analysis considering structural uncertainty,' *Aviation*, 2005, **9**(1), 3-7.

141 Attar, P.J. and Dowell, E.H., 'A stochastic analysis of the limit cycle behavior of a nonlinear aeroelastic model using the response surface method,' pp. 2318-2338, American Inst. Aeronautics and Astronautics Inc., Reston, VA 20191-4344, United States, Austin, TX, United States, 2005.

142 Ostenfeld-Rosenthal, P., Madsen, H.O. and Larsen, A., 'Probabilistic flutter criteria for long span bridges,' *Journal of Wind Engineering and Industrial Aerodynamics*, 1992, **42**(1-3), 1265-1276.

143 Ge, Y.J., Xiang, H.F. and Tanaka, H., 'Application of the reliability analysis model to bridge flutter under extreme winds,' *Journal of Wind Engineering and Industrial Aerodynamics*, 2000, **86**, 155-167.

144 Jakobsen, J.B. and Tanaka, H., 'Modeling uncertainties in prediction of aeroelastic bridge behavior,' *Journal of Wind Engineering and Industrial Aerodynamics*, 2003, **91**, 1485-1498.

145 Potter, S. and Lind, R., *Developing uncertainty models for robust flutter analysis using ground vibration test data*, AIAA 2001-1585, also as NASA/TM-2001-210392, 2001.

146 Lind, R. and Brenner, M., 'Flutterometer: An on-line tool to predict robust flutter margins,' *Journal of Aircraft*, 2000, **37**(6), 1105-1112.

147 Brenner, M.J., 'Aerosevoelastic uncertainty model identification from flight data,' *Journal of Guidance, Control, and Dynamics*, 2002, **25**(4), 748-754.

148 Prazenica, R.J., Lind, R. and Kurdila, A.J., 'Uncertainty estimation from volterra kernels for robust flutter analysis,' *Journal of Guidance, Control, and Dynamics*, 2003, **26**(2), 331-339.

149 Rao, S.S., Chen, L. and Mulkay, E., 'Unified finite element method for engineering system with hybrid uncertainties,' *AIAA Journal*, 1998, **36**(7), 1291 - 1299.

150 Reddy, T.S.R., Mital, S.K. and Stefko, G.L., 'Probabilistic aeroelastic analysis of turbomachinery components.' *42nd AIAA/ASME/ASCE/AHS/ASC Structures, Structural Dynamics and Materials Conference*, pp. 2027-2036, American Inst. Aeronautics and Astronautics Inc., Seattle, WA, 2001.

151 Ibrahim, R.A., 'Excitation-induced stability and phase transition: A review,' *JVC/Journal of Vibration and Control*, 2006, **12**(10), 1093-1170.

152 Ibrahim, R.A., Stabilization and stochastic bifurcation with application to nonlinear ocean structures, In Shlesinger, M.F. and Swean, T., eds. *Stochastically excited nonlinear ocean structures* (World Scientific Publishing Company, 1998).

153 Lumbantobing, H. and Haaker, T.I., 'On the parametric excitation of some nonlinear aeroelastic oscillators,' *Journal of Fluids and Structures*, 2004, **19**, 221-237.

154 Chin, C., Nayfeh, A.H. and Mook, D.T., *Supression of flutter by parametric excitations* AIAA-94-1425-CP, 1994.

155 Chin, C., Nayfeh, A.H. and Mook, D.T., 'The response of a nonlinear system with a non-semisimple one-to-one resonance to a combination resonance,' *International Journal of Bifurcation and Chaos*, 1995, **5**(1), 971-982.

156 Young, T.H., Tseng, T.C. and Song, L.S., 'Dynamic stability of fluttered systems subjected to parametric random excitations,' *JVC/Journal of Vibration and Control*, 2002, **8**(3), 291-310.

157 Poirel, D. and Price, S.J., 'Random binary (coalescence) flutter of a two-dimensional linear airfoil,' *Journal of Fluids and Structures*, 2003, **18**, 23-42.

158 Poirel, D. and Price, S.J., 'Response probability structure of a structurally nonlinear fluttering airfoil in turbulent flow,' *Probabilistic Engineering Mechanics*, 2003, **18**, 185-202.

159 Stephenson, A., 'On a new type of dynamical stability,' *Memoirs and Proceedings of the Manchester Literary and Philosophical Society*, 1908, **52**, 1-10.

160 Acheson, D.J., *From calculus to chaos, an introduction to dynamics*, Oxford University Press, 1997.

161 Bogdanoff, J.L., 'Influence on the behavior of a linear dynamical systems of some imposed motion of small amplitude,' *Journal of Acoustical Society of America*, 1962, **34**, 1055-1062.

162 Chelomi, V.N., 'The possibility of increasing the stability of elastic systems using vibrations,' *Doklady Akademii Nauk SSSR*, 1956, **110**(3), 345-347.

163 Kapitsa, P.L., 'Dynamic stability of a pendulum with a vibrating suspension axis,' *Zhurnal Exsperimental'noi i Teoreticheskoi Fiziki (ZhETF)*, 1951, **21**, 588-597.

164 Kapitsa, P.L., 'Pendulum with vibrated suspension,' *Uspekhi Pizicheskikh Nauk*, 1951, **44**, 7-20.

165 Stoker, J.J., *Nonlinear vibrations in mechanical and electrical systems*, Wiley & Sons, New York, 1950.

166 Bogdanoff, J.L. and Citron, S.J., 'Experiments with inverted pendulum subject to random parametric excitation,' *Acoustical Society of America -- Journal*, 1965, **38**(3), 447-452.

167 Michaelis, M.M., 'Stroposcopic study of the inverted pendulum,' *American Journal of Physics*, 1985, **53**, 1079-1083.

168 Kalmus, H.P., '1970,' *American Journal of Physics*, The inverted pendulum, **38**, 874-878.

169 Smith, H.J.T. and Blackburn, K.A., 'Experimental study of an inverted pendulum,' *American Journal of Physics*, 1992, **60**, 909-911.

170 Sudor, D.J. and Bishop, S.R., 'Inverted dynamics of tilted parametric pendulum,' *European Journal of Mechanics A/Solids*, 1996, **18**, 517-526.

171 Weibel, S., Taper, J. and Baillieul, U., 'Global dynamics of a rapidly forced cart pendulum,' *Nonlinear Dynamics*, 1997, **13**, 131-170.

172 Yabuno, H., Miura, M. and Aoshima, N., 'Bifurcation in an inverted pendulum with tilted high-frequency excitation: Analytical and experimental investigations on the symmetry-breaking of the bifurcation,' *Journal of Sound and Vibration*, 2004, **273**, 493-513.

173 Tso, W.K. and Asmis, K.G., 'Parametric excitation of a pendulum with bilinear hysteresis,' *Transactions of the ASME. Series E, Journal of Applied Mechanics*, 1970, **37**(4), 1061-1068.

174 Agafonov, S.A., 'Stabilization of the equilibrium of ziegler's pendulum by parametric excitation,' *Mechanics of Solids*, 1997, **32**(6), 29-33.

175 Agafonov, S.A., 'Stabilization of motion of nonconservative systems by parametric excitation,' *Mechanics of Solids*, 1998, **33**(2), 170-173.

176 Agafonov, S.A. and Shcheglov, G.A., 'On the stabilization of a double pendulum acted upon by a follower force by means of parametric excitation,' *Mechanics of Solids*, 2003, **38**(3), 27-35.

177 Otterbein, S., 'Stabilisierung des n-pendels und der indische seiltrick,' *Arch. Ration. Mech. Analysis*, 1982, **78**, 381-393.

178 Acheson, D.J., 'A pendulum theorem,' *Proceedings of the Royal Society of London, Series A (Mathematical, Physical and Engineering Sciences)*, 1993, **443**, 239-245.

179 Acheson, D.J. and Mullin, T., 'Upside-down pendulums,' *Nature*, 1993, **366**, 215-216.

180 Hurst, C.A., 'The indian rope trick explained,' *Australian Mathematical Society Gazette*, 1996, **23**, 154-159.

181 Acheson, D.J. and Mullen, T., 'Ropy magic,' *New Scientist*, 1998, **21**, 32-33.

182 Galán, J., Fraser, W. B., Acheson, D. J., and Champneys, A. R., 'The parametrically excited upside-down rod: An elastic joint pendulum model,' *Journal of Sound and Vibration*, 2005, **280**, 359-377.

183 Lee, B.H.K., 'Oscillatory shock motion caused by transonic shock-boundary-layer interaction,' *AIAA Journal*, 1990, **28**, 942-944.

184 Ibrahim, R.A. and Hijawi, M., 'Deterministic and stochastic response of nonlinear coupled bending-torsion modes in a cantilever beam,' *Nonlinear Dynamics*, 1998, **16**(3), 259-292.

185 Lindner, B., Garcia-Ojalvo, J., Neiman, A. and Schimansky-Geier, L., 'Effects of noise in excitable systems,' *Physics Reports*, 2004, **329**, 321-424.

186 FitzHugh, R.A., 'Impulses and physiological states in theoretical models of nerve membrane,' *Biophysics Journal*, 1961, **1**, 445-466.

187 Nagumo, J., Arimoto, S. and Yoshitzawa, S., 'An active pulse transmission line simulating nerve axon,' *Proceedings of the Institute of the Radio Engineering (IRE)*, 1962, **50**, 2061-2070.

188 Morris, C. and Lecar, H., 'Voltage oscillations in the barnacle giant muscle fiber,' *Biophysics Journal*, 1981, **35**, 193-213.

189 Ibrahim, R.A. and Castravete, S.C., 'Flutter suppression of a plate-like wing via parametric excitation,' *Nonlinear Dynamics*, 2006, **46**(4), 387-426.

190 Love, A.E.H., *A treatise on the mathematical theory of elasticity*, Dover, New York, 1944.

191 Boccaletti, S., Grebogi, C., Lai, Y.-C., Mancini, H. and Maza, D., 'The control of chaos: Theory and applications,' *Physics Reports*, 2000, **329**, 103-197.

192 Chandrupatla, T.R. and Belegundu, A.D., *Introduction to finite elements in engineering* Prentice Hall, Upper Saddle River, N.J, 2002.

193 Karamcheti, K., *Principles of ideal-fluid aerodynamics*, R. E. Krieger Publishing Co., 1980.

## ABSTRACT

NONLINEAR FLUTTER OF A CANTILEVER WING INCLUDING THE INFLUENCE OF STRUCTURE UNCERTAINTIES

by

STEFAN CRISTIAN CASTRAVETE

May 2007

Advisor: Dr. Raouf A. Ibrahim

Major: Mechanical Engineering

Degree: Doctor of Philosophy

The present work deals with the effect of parametric excitation and uncertainties on the flutter characteristics of an aeroelastic wing. The work is structured in two parts. First part explores the possibility of suppressing wing flutter via parametric excitation along the plane of highest rigidity in the neighborhood of combination resonance. The aerodynamics of the wing is modeled using Theodorsen's theory and the equations are obtained using Hamilton's principle. The domains of attraction and bifurcation diagrams are obtained to reveal the conditions under which the parametric excitation can provide stabilizing effect. The basins of attraction for different values of excitation amplitude reveal the stabilizing effect that takes place above a critical excitation level. Below that level, the response experiences limit cycle oscillations, cascade of period doubling, and chaos. For flow speed slightly higher than the critical flutter speed, the response experiences a train of spikes, known as "*firing,*" a

term that is borrowed from neuroscience, followed by "*refractory*" or *recovery* effect, up to an excitation level above which the wing is stabilized.

The second part of the paper investigates the influence of stiffness uncertainties on the flutter behavior of an aeroelastic wing using a stochastic finite element approach. A numerical algorithm to simulate unsteady, nonlinear, incompressible flow (based on the unsteady vortex lattice method) interacting with linear aeroelastic wing in the presence of uncertainties was developed. The air flow and the wing structure are treated as elements of a single dynamical system. In order to implement this algorithm in the presence of uncertainties, a random field representing bending or torsion stiffness parameters is introduced using a truncated Karhunen-Love expansion. Both perturbation technique and Monte Carlo simulation are used to establish the boundary of stiffness uncertainty level at which the wing exhibits LCO and above which the wing experiences dynamic instability. The analysis also includes the limitation of perturbation solution for a relatively large level of stiffness uncertainty. It was found that the presence of the uncertainties in bending and torsion stiffness can lower the flutter speed and the effect of torsion stiffness uncertainty induce greater disturbance in the system.

## AUTOBIOGRAPHICAL STATEMENT

STEFAN CRISTIAN CASTRAVETE

Stefan C. Castravete was born in Calafat, a small and beautiful town on the shore of the Danube River in Romania. At the age of 5, he moved into a bigger city named Craiova where he completed his primary, middle, and high school. He spent the vacations to his grandparents' farm where he learned many different things like how to work the land or ride a horse. His grandfather gave him the passion for mechanics and his father the passion for automobiles. Because of that, in 1992 he was admitted to the Mechanical Engineering Department of the University of Craiova, the Automotive Engineering Section. In 1997 he graduated with bachelor degree. After graduation he worked for Daewoo Automotive Craiova for four years. In August 2001 he was admitted to Wayne State University where he completed a MS program and fulfilled the requirements for a Ph.D. program. The author currently lives in Detroit with his wife Liliana, his daughter Daria, and a new baby girl to be. Among his hobbies includes reading, skiing, hiking, listening to classical and jazz music, playing guitar and drums.